

Evaluating cerium (IV) oxide nanoparticles membrane behaviour and related toxicity

Natalia Domenech-Garcia

Submitted in accordance with the requirements for the
degree of PhD

The University of Leeds
School of Chemical and Process Engineering
School of Chemistry



March 2020

The candidate confirms that the work submitted is her own and that appropriate credit has been given where reference has been made to the work of others.

This copy has been supplied on the understanding that it is copyright material and that no quotation from the thesis may be published without proper acknowledgement.

The right of Natalia Domenech-Garcia to be identified as Author of this work has been asserted by Natalia Domenech-Garcia in accordance with the Copyright, Designs and Patents Act 1988.

Acknowledgements

First of all, I am extramly gratefull to prof. Rik Brydson and prof. Andrew Nelson for their guidance and support during my PhD. Besides my advisors, I would like to thank Dr Nicole Hondow for her insightful comments which always helped me so much. In addition, I would like to thank the ICN2 for giving me access to their research facilities.

Secondly, I would like to thank my parents, Jose Antonio and Antonia, because without their help and sacrifice, I would not be where I am now. I would like to also thank my sister Ana Belen for always being the main role model in my life. In addition, I will always be extremely grateful to my grandma Anita, my second mother, who raised me to be the best version of myself I could be. I hope one day I could be just a ten per cent of the person she was. I will always remember you. You will always be with me wherever I am.

Finally, I would like to thank my family of choice. Thank you, Julio, for your patience and your support in bad moments. Thank you, Angela, for your wisdom, support and encouragement. Thank you, Rosa, because having you close makes Leeds feel like home. Thank you, Alberto, for being there from day one. Thank you, Javi, for your guidance. Lastly, I would like to mention Josh, Silvia, Clara, Jesus, Andrea, Paula, Cristina O. and Cristina T. because without them, this PhD would not have been the same.

Abstract

Cerium (IV) oxide nanoparticles (CeO₂ NPs or nano-ceria) are one of the most popular NPs used in both industry and medicine. Nowadays, CeO₂ NPs could be considered as one of the NPs with better prospects for future applications in medicine. CeO₂ NPs have the ability to change between oxidation states Ce(IV) and Ce(III) creating oxygen vacancies in their structure. This ability, in theory, could regulate oxidative stress (OS). However, there are many contradictory reports regarding the beneficial or adverse effects CeO₂ NPs produce when internalised in the body. In addition, the mechanisms through which CeO₂ NPs interact once internalised in the body are not yet totally understood.

This thesis analyses the interaction between CeO₂ NPs and phospholipids (DOPC, DOPG, DOPE, DOPA and DOPS) using a biosensor able to mimic the cellular membrane. The working electrode of the electrochemical sensing device (ESD) consists of a mercury coated platinum electrode (Hg/Pt electrode) where phospholipids are deposited. CeO₂ NPs with different size and shapes (spheres, cubes, needles and dots) are synthesised using wet-chemical and hydrothermal methods. Also, coated CeO₂ NPs were synthesised using PVP, PEG, dextran and the CeO₂ NPs were treated with PBS. The NPs were characterised using TEM, SAED, EDX, XRD, DLS and Z-Potential.

Results show the chemical behavior of the CeO₂NPs is related to a large extent to the characteristics of the NPs surface, the characteristics of their dispersion media and the size of the NPs. CeO₂ NPs (spheres, cubes, needles and dots) did not show an interaction with the phospholipid membrane (DOPC) when the system was under a continuous flow of phosphate saline buffer (PBS, pH 7.4) and citric-citrate buffer (CCB, pH 4.0, 5.0, 6.0). Nevertheless, an interaction was observed when the system was under a continuous flow of CCB (pH 3.0) and GLY (3.0). It was concluded that Ce³⁺ on the NPs surface can bind to the phosphate group of the phospholipid polar heads when the NPs are in GLY 3.0. Results also showed that citrate on the CeO₂ NPs surface hampers the interaction with the phospholipid monolayer at pHs above 3.0. Additionally, at

acidic pH (pH 3.0), the CeO₂ NPs (spheres and cubes) were able to cross the phospholipid monolayer and directly interact with the Hg/Pt electrode showing a semiconductor effect. Needles, which were bigger in size, did not produce a semiconductor effect under the same conditions. The semiconductor effect decreases as size increases. The interaction of the coated CeO₂ NPs with DOPC was found to be dependent on the coating agent. In this way, the interaction between DOPC and the NPs was produced by the coating agent, not the NPs. Finally, CeO₂ showed to be inert when interacting with DOPA, DOPG and DOPE under a continuous flow of PBS. The only exception was the dots, which produced a significant interaction with DOPA under the same conditions.

Table of Contents

Table of Figures.....	XII
List of Tables.....	XXVI
Abbreviations.....	XXVIII
CHAPTER 1. INTRODUCTION.....	1
CHAPTER 2. LANTHANIDES NANOPARTICLES: PROPERTIES AND APPLICATIONS	6
2.1 Nanoparticles.....	6
The NP surface	7
2.1.1 Chemical properties of the nanoparticles and NPs activity	8
2.1.2 Industrial and biological application of nanoparticles	10
2.2 Lanthanides and lanthanide nanoparticles.....	12
2.3 Cerium	14
2.3.1 Ceria at the nanoscale	16
2.3.2 Synthesis of ceria nanoparticles.....	18
2.3.3 Applications of nano-ceria	22
2.3.4 Toxicity studies of nano-ceria.....	24
2.3.5 Chemical characteristics of ceria-nanoparticles	28
CHAPTER 3. CHARACTERISATION TECHNIQUES, MATERIALS AND SYNTHESIS METHODS	30
3.1 Characterisation techniques.....	30
3.1.1 Transmission electron microscopy	30
3.1.1.1 The design of a TEM	31
3.1.1.2 Specimen-beam interactions.....	33
3.1.1.2.1 X-Rays	35
3.1.1.3 The resolution in the TEM	36

3.1.1.3.1	Imaging in the TEM.....	38
3.1.1.4	EDX.....	40
3.1.1.5	EELS.....	40
3.1.1.6	TEM experimental conditions and methods	42
3.1.2	X-Ray diffraction (XRD)	43
3.1.2.1	Basics in XRD.....	43
3.1.2.2	The XRD machine.....	44
3.1.2.3	XRD experimental conditions and methods	46
3.1.3	Dynamic light scattering (DLS)	47
3.1.3.1	How a DLS machine works.....	47
3.1.3.2	The theory behind the DLS machine.....	48
3.1.3.3	Limitations of the DLS	50
3.1.3.4	Zeta-Potential (Z-Potential).....	51
3.1.3.5	DLS and Z-Potential experimental conditions and methods	52
3.2	The nanoparticles under study. Materials and synthesis methods....	53
3.2.1	Materials.....	53
3.2.2	Methods. Synthesis of CeO ₂ NPs.....	54
3.2.2.1	Needles.....	54
3.2.2.2	Cubes.....	54
3.2.2.3	Spheres.....	54
3.2.2.4	Coatings.....	55
3.2.2.4.1	PVP-40 coated CeO ₂ NPs.....	55
3.2.2.4.2	Dextran coated CeO ₂ NPs	55
3.2.2.4.3	PEG-coated CeO ₂ NPs.....	55
3.2.2.4.4	PBS-coated CeO ₂ NPs	55

CHAPTER 4. CHARACTERISATION OF CERIA NANOPARTICLES	56
Synthesised ceria NPs	58
4.1.1 Hydrothermal method using NaOH. Needles	58
4.1.2 Cubes.....	63
4.1.3 Spheres.....	66
4.2 Commercial CeO ₂ NPs.....	69
4.3 Coated-CeO ₂ NPs.....	72
4.3.1 40-PVP coated CeO ₂ NPs.....	72
4.3.2 PEG-coated CeO ₂ NPs	74
4.3.3 Dextran- coated NPs.....	76
4.3.4 PBS-treated CeO ₂ NPs (PBS-CeO ₂ NPs).....	78
4.4 Chapter 4. Summary.	82
CHAPTER 5. HIGH-THROUGHPUT ELECTROCHEMICAL DETECTION OF SUBSTANCES	85
5.1 Voltammetry and Rapid Cyclic Voltammetry.....	85
5.1.1 Cyclic voltammetry.....	88
5.2 The electrified interface	90
5.2.1 The electric double layer.....	90
5.2.2 Capacitance and the RC-circuit.	92
5.2.3 Biological membranes, the double layer and the RC-Circuit.....	95
5.3 Adsorption.....	97
5.4 Relationship between the electrical interface, capacitance, current phospholipids, adsorption and RCV.	98
5.5 The electrochemical sensor device (ESD).....	100
5.5.1 The device	100
5.5.1.1 The flow cell	100

5.5.2	The ESD and the RCV response. What is it?	103
5.5.3	Uses and limitations	104
5.6	Methods.	106
5.6.1	The ESD start-up.....	106
5.6.2	RCV measurements	107
CHAPTER 6. ELECTROCHEMICAL BEHAVIOUR OF DIFFERENT LIPIDS.		
STABILITY OF PHOSPHOLIPIDS ON THE Hg/Pt.....		
6.1	Materials and methods.....	114
6.1.1	Materials.....	114
6.1.2	Buffer preparation.....	114
6.2	DOPC	115
6.2.1	DOPC stability in PBS (pH 7.4)	116
6.2.2	DOPC stability in HCl-Glycine buffer. pH 3.0	121
6.2.3	DOPC stability in citric/citrate buffer	125
6.2.3.1	Citric/citrate buffer pH 3.0	125
6.2.3.2	Citric/citrate buffer pH 4.0	128
6.2.3.3	Citric/citrate buffer pH 5.0	131
6.2.3.4	Citric/citrate buffer pH 6.0	134
6.3	DOPE.....	137
6.4	DOPS.....	141
6.5	DOPA	146
6.6	DOPG	156
6.7	Chapter 6. Summary.....	161
CHAPTER 7. INTERACTION OF CERIA NANOPARTICLES WITH A		
MODEL MEMBRANE		
		163

7.1	The effects on the voltammogram derived from interactions with phospholipids.....	164
7.2	Interactions of CeO ₂ NPs with model membranes of different lipids	168
7.2.1	DOPE.....	168
7.2.2	DOPA.....	170
7.2.3	DOPG.....	175
7.2.4	DOPC.....	177
7.2.5	Summary and discussion.....	179
7.3	Interactions of CeO ₂ NPs with DOPC. Effect of pH and dispersant medium	180
7.3.1	Interaction of CeO ₂ NPs with DOPC under a flow of HCl-Glycine buffer at pH 3.0 (GLY 3.0).....	181
7.3.1.1	Different concentration of spheres in GLY 3.0.....	181
7.3.1.2	Different concentration of cubes in GLY 3.0	184
7.3.1.3	Different concentrations of ceria needles in GLY 3.0.....	186
7.3.2	Interaction of CeO ₂ NPs with DOPC under a flow of citric/citrate buffer at pH 3.0 (CCB 3.0).....	188
7.3.2.1	Different concentration of ceria spheres in CCB 3.0	188
7.3.2.2	Different concentration of ceria cubes in CCB 3.0	190
7.3.2.3	Different concentration of ceria needles in CCB 3.0	192
7.3.3	Interaction of CeO ₂ NPs with DOPC under a flow of citric/citrate buffer at pH 4.0 (CCB 4.0)	194
7.3.3.1	Different concentration of ceria spheres in CCB 4.0.....	194
7.3.3.2	Different concentration of ceria cubes in CCB 4.0.....	196
7.3.3.3	Different concentration of ceria needles in CCB 4.0.....	198

7.3.4	Interaction of CeO ₂ NPs with DOPC under a flow of citric/citrate buffer at pH 5.0 (CCB 5.0).....	200
7.3.4.1	Different concentrations of ceria spheres in CCB 5.0.....	200
7.3.4.2	Different concentrations of ceria cubes in CCB 5.0.....	202
7.3.4.3	Different concentration ceria needles in CCB 5.0	204
7.3.5	Interaction of CeO ₂ NPs with DOPC under a flow of citric/citrate buffer at pH 6.0 (CCB 6.0)	206
7.3.5.1	Different concentration of ceria spheres in CCB 6.0	206
7.3.5.2	Different concentration of ceria cubes in CCB 6.0	208
7.3.5.3	Different concentrations of ceria needles in CCB 6.0	210
7.3.6	Summary and discussion.....	212
7.4	The cerium response in the RCV measurements.....	215
7.4.1	The effect of the buffer in Ce ³⁺ interaction	216
7.4.1.1	Ce(NO ₃) ₃ in GLY 3.0.....	216
7.4.1.2	Ce(NO ₃) ₃ in CCB at different pH values	219
7.4.1.3	Ce(NO ₃) ₃ in PBS (pH7.4).....	222
7.4.1.4	Summary and discussion.....	224
7.4.2	Evaluating the presence of Ce(III) in solution. ICP-MS results	226
7.4.3	Evaluating the presence of Ce(III) in the particle surface. EELS results	230
7.5	The effect of coating in the interaction of CeO ₂ NPs with model membranes.....	232
7.5.1	PVP-coated NPs	233
7.5.2	PEG-coated NPs	236
7.5.3	Dextran-coated NPs.....	238
7.5.4	PBS-coated NPs in acidic pH.....	240
7.5.5	Summary and discussion.....	242



7.6	Conclusions of Chapter 7.....	243
CHAPTER 8.	CONCLUSIONS AND FUTURE WORK.....	249
Bibliography	243
Appendix. Chapter 4.....		248

Table of figures:

FIGURES CHAPTER 2

Figure 2. 1 Diagram showing the different factors governing NP activity in a dispersion. Arrows show the direction of effect. 8

Figure 2. 2: CeO₂ fluorite structure and oxygen vacancy formation during a doping with a metal Mⁿ⁺ process [62]..... 14

Figure 2. 3: Pourbaix diagram for the Ce(III)/(IV)-H₂O-H₂O₂ systems. Copied from [61]..... 15

FIGURES CHAPTER 3

Figure 3. 1: Scheme of a TEM with an EDX and an EELS devices. Copied from [1]..... 31

Figure 3. 2: Specimen- beam interactions..... 33

Figure 3. 3: Scheme of X-Rays production..... 35

Figure 3. 4: Diagram of a XRD machine..... 44

Figure 3. 5 Table 3. 2: Experimental conditions of XRD experiments..... 46

Figure 3. 6: Diagram of a DLS machine..... 47

FIGURES CHAPTER 4

Figure 4. 1: BFTEM images of CeO₂ NPs synthesised using an hydrothermal method and NaOH. A and B: before sonication. C and D: after sonication 58

Figure 4. 3: Red bars: number of CeO₂ NPs (needles) of a certain the length (A) and width (B). Black line: log-normal distribution curve of the length (A) and width of CeO₂ (needles). 59

Figure 4. 2: BFTEM image of CeO₂ NPs needles indicating length and width of one of the needles.... 59

Figure 4. 4: Red bars: number of CeO₂ NPs (needles) of a certain size after sonication for 30min, black line: log-normal distribution curve of the size of CeO₂ NPs (needles) after sonication for 30min. 60

Figure 4. 5: A: XRD pattern of: Black line: CeO₂ (needles), red line: theoretical pattern of CeO₂ (ICDD file:00-004-0593), blue line: theoretical pattern of Ce₂O₃ (ICDD file: 00-023-1048). B: SAED pattern of CeO₂ NPs (needles) 61

Figure 4. 6: A: Graph showing the size of CeO₂ NPs (needles) from DLS when they are dispersed in different media. Black bars: Z-Average, associated error and Pdl index from DLS data. Red bars: Size of the CeO₂ NPs (needles) as 'mean number' from DLS data. B: Z-Pot values (mV) from DLS obtained from CeO₂ NPs (needles) in different media. 62

Figure 4. 7: BFTEM images of CeO₂ NPs synthesised using HMT and a wet chemical method 63

Figure 4. 8: Red bars: number of NPs of a certain size. Black line: log-normal distribution curve of the side of the CeO₂ NPs synthesised using HMT 64

Figure 4. 9: A: XRD pattern of: Black line: CeO ₂ NPs synthesised using HMT, Red line: theoretical pattern of CeO ₂ NPs (ICDD file: 00-004-0593), Blue line: theoretical pattern of Ce ₂ O ₃ (ICDD file: 00-023-1048). B: SAED pattern of CeO ₂ NPs synthesised using HMT.	64
Figure 4. 10: A: Graph showing the size of CeO ₂ NPs (cubes) from DLS when they are dispersed in different media. Black bars: Z-Average, associated error and Pdl index from DLS data. Red bars: Size of the CeO ₂ NPs (cubes) as 'mean number' from DLS data. B: Z-Pot values (mV) from DLS obtained from CeO ₂ NPs (cubes) in different media.	65
Figure 4. 11: BFTEM images of CeO ₂ NPs synthesised using a wet chemical method and TMAOH.	66
Figure 4. 12: Red bars: number of CeO ₂ NPs (synthesised using TMAOH and a wet chemical method) of a certain size. Black line: log-normal distribution curve of the CeO ₂ NPs synthesised using TMAOH.	67
Figure 4. 13: A: XRD pattern of: Black line: CeO ₂ NPs synthesised using TMAOH and a wet chemical method, Red bars: Theoretical pattern of CeO ₂ NPs (ICDD file: 00-004-05936), Blue bars: theoretical pattern of Ce ₂ O ₃ NPs (ICDD file: 00-023-1048)	67
Figure 4. 14: A: Graph showing the size of CeO ₂ NPs (spheres) from DLS when they are dispersed in different media. Black bars: Z-Average, associated error and Pdl index from DLS data. Red bars: Size of the CeO ₂ NPs (spheres) as 'mean number' from DLS data. B: Z-Pot values (mV) from DLS obtained from CeO ₂ NPs (spheres) in different media.	68
Figure 4. 15: BFTEM images of comertical CeO ₂ NPs, purchased from sigma Aldrich.	69
Figure 4. 16: Red bars: Number of CeO ₂ NPs of a certain size of commertially purchased from Sigma Aldrich. Black line: log-normal distribution curve of CeO ₂ NPs purchased from Sigma Aldrich.	70
Figure 4. 17: A: XRD pattern of: Black line: CeO ₂ commercial, Red line: theoretical pattern of CeO ₂ NPs (ICDD file: 00-004-0593), Blue line: theoretical pattern of Ce ₂ O ₃ (ICDD file: 00-023-1048). B: SAED pattern of CeO ₂ NPs synthesised using HMT.....	71
Figure 4. 18: BFTEM images of 40-PVP coated CeO ₂ NPs.....	72
Figure 4. 20: Red bars: Number of 40PVP coated CeO ₂ NPs of a certain size. Black line: log-normal distribution curve of the size of 40PVP coated CeO ₂ NPs.....	73
Figure 4. 20: SAED pattern of 40PVP coated CeO ₂ NPs.	73
Figure 4. 21: BFTEM images of PEG coated CeO ₂ NPs.....	74
Figure 4. 23: SAED pattern of PEG coated CeO ₂ NPs.	75
Figure 4. 23: Red bars: Number of PEG coated CeO ₂ NPs of a certain size. Black line: log-normal distribution curve of the size of PEG coated CeO ₂ NPs.	75
Figure 4. 24: BFTEM images of dextran coated CeO ₂ NPs.....	76
Figure 4. 25: Red bars: Number of dextran coated CeO ₂ NPs of a certain size. Black line: log-normal distribution curve of the size of dextran coated CeO ₂ NPs.....	77
Figure 4. 26: BFTEM images of PBS-CeO ₂ NPs (spheres).....	78
Figure 4. 27: Red bars: Number of PBS-CeO ₂ NPs (spheres) of a certain size. Black line: log-normal distribution curve of the size of PBS-CeO ₂ NPs (spheres).....	79

Figure 4. 28: SAED pattern of PBS-CeO ₂ NPs (spheres)	79
Figure 4. 29: BFTEM images of PBS coated CeO ₂ NPs (cubes).....	80
Figure 4. 30: SAED pattern of PBS-CeO ₂ NPs (cubes).....	81
Figure 4. 31: Red bars: Number of PBS-CeO ₂ NPs (cubes) of a certain size. Black line: log-normal distribution curve of the size of PBS-CeO ₂ NPs (cubes).....	81

FIGURES CHAPTER 5

Figure 5. 1: Voltammetry circuit.....	85
Figure 5. 2: Current variation at an increasing lineal potential.	87
Figure 5. 3: Left graph: cyclical potential variation with time. Right graph: Current variation in function of an applied cyclical potential.	88
Figure 5. 4: EDL structure showing the arrangement of solvated anions and cations according to: (a) the Helmholtz model. (b) the Gouy-Chapman model. (c) the Gouy-Chapman-Stern model. Copied from [131].	91
Figure 5. 5: RC-circuit.....	92
Figure 5. 6: Left graph: RC-circuit in a phospholipid bilayer. Right graph: Equivalent RC-circuit in a cellular membrane	96
Figure 5. 7: ESD diagram. The ESD device is composed by a buffer reservoir, a pump, a flow cell and a computer	100
Figure 5. 8: Left image: EDS electrochemical cell with the micro-fabricated electrode and the Ag/Cl reference electrode. Right image: Micro-fabricated electrode with the eight working electrodes and the auxiliary electrodes.....	101
Figure 5. 9: Diagram of the working electrode with the deposited Hg and the phospholipid layer over it.	101
Figure 5. 10: RCV voltammograms of the un-coated Hg/Pt before phospholipid deposition. Left graph: RCV voltammogram recorded at 100Vs ⁻¹ with a potential excursion from -0.4V to -3.0V. Right graph: RCV voltammogram recorded at 40Vs ⁻¹ with a potential excursion from -0.4V to -1.2V.....	107

FIGURES CHAPTER 6

Figure 6. 1: Diagram of a phospholipid.....	109
Figure 6. 2: Preferred supramolecular structure depending on steric factors.	110
Figure 6. 3: Chemical structure of: (a) 1,2-dioleoyl-sn-glycero-3-phosphocholine, (DOPC), (b) 1,2-dioleoyl-sn-glycero-3-phosphoethanolamine, (DOPE), (c) 1,2-dioleoyl-sn-glycero-3-phosphate (sodium salt), (DOPA), (d) 1,2-dioleoyl-sn-glycero-3-phospho-(1'-rac-glycerol) (sodium salt), (DOPG), (e) 1,2-dioleoyl-sn-glycero-3-phospho-L-serine (sodium salt), (DOPS).....	113

<i>Figure 6. 4: RCV profile of DOPC and related phase of the phospholipids on the Hg/Pt at a certain potential. Zone A: The phospholipids form a mono-layer over the electrode that hampers the passage of ions or water through the membrane. Zone B: Phospholipid polar heads join allowing the passage of ions and water which creates a current. Zone C: correspond to a growth process that ends in a bilayer with patches formation.....</i>	<i>116</i>
<i>Figure 6. 5: RCV profile of DOPC in PBS (pH 7.4) recorded at 40V s⁻¹ using potential cycles from -0.4V to -1.2V at time: (a): t=0s, (b): t=25s, (c):t=50s, (d): t=75s, (e): t=100s, (f):t=125s, (g): t=150s, (h):t=175s, (i): t=200s, and (j) t=225s.....</i>	<i>118</i>
<i>Figure 6. 6: Current variation with time of 10 different DOPC depositons in PBS (pH 7.4) of (a) Peak 1. Black dots: PBS 1, red dots: PBS 2, light blue: PBS 3, pink dots: PBS 4, dark green: PBS 5, dark blue: PBS 6, light purple: PBS 7, dark purple: PBS 8, brown: PBS 9, and light green: PBS 10, (b) Peak 2. Black dots: PBS 1, red dots: PBS 2, light blue: PBS 3, pink dots: PBS 4, dark green: PBS 5, dark blue: PBS 6, light purple: PBS 7, dark purple: PBS 8, brown: PBS 9, and light green: PBS 10.....</i>	<i>119</i>
<i>Figure 6. 7: Average peak suppression of the current peaks of the RCV voltammograms with time of DOPC in PBS (pH 7.4). Black dots: Peak 1 of the voltammogram. Red dots: Peak 2 of the voltammogram.....</i>	<i>120</i>
<i>Figure 6. 8: RCV profile of DOPC in GLY (pH 3.0) recorded at 40V s⁻¹ using potential cycles from -0.4V to -1.2V at time: (a): t=0s, (b): t=25s, (c):t=50s, (d): t=75s, (e): t=100s, (f):t=125s, (g): t=150s, (h):t=175s, (i): t=200s, and (j) t=225s.....</i>	<i>121</i>
<i>Figure 6. 9: Current variation with time of 10 different DOPC depositons in GLY (pH 3.0) of (a) Peak 1. Black dots: GLY 1, red dots: GLY 2, light blue: GLY 3, pink dots: GLY 4, dark green: GLY 5, dark blue: GLY 6, light purple: GLY 7, dark purple: GLY 8, brown: GLY 9, and light green: GLY 10, (b) Peak 2. Black dots: GLY 1, red dots: GLY 2, light blue: GLY 3, pink dots: GLY 4, dark green: GLY 5, dark blue: GLY 6, light purple: GLY 7, dark purple: GLY 8, brown: GLY 9, and light green: GLY 10</i>	<i>122</i>
<i>Figure 6. 10: Average peak suppression of the current peaks of the RCV voltammograms with time of DOPC in GLY (pH 3.0). Black dots: Peak 1 of the voltammogram. Red dots: Peak 2 of the voltammogram.....</i>	<i>123</i>
<i>Figure 6. 11: Current at -0.6V when DOPC in GLY (pH 3.0) when the RCV profile is recorded at 40Vs⁻¹ using potential cycles from -0.4V to -1.2V.....</i>	<i>124</i>
<i>Figure 6. 12: RCV profile of DOPC in CCB (pH 3.0) recorded at 40V s⁻¹ using potential cycles from -0.4V to -1.2V at time: (a): t=0s, (b): t=25s, (c):t=50s, (d): t=75s, (e): t=100s, (f):t=125s, (g): t=150s, (h):t=175s, (i): t=200s, and (j) t=225s.....</i>	<i>125</i>
<i>Figure 6. 13: Current variation with time of 10 different DOPC depositons in CCB (pH 3.0) of (a) Peak 1. Black dots: CCB 1, red dots: CCB 2, light blue: CCB 3, pink dots: CCB 4, dark green: CCB 5, dark blue: CCB 6, light purple: CCB 7, dark purple: CCB 8, brown: CCB 9, and light green: CCB 10, (b) Peak 2. Black dots: CCB 1, red dots: CCB 2, light blue: CCB 3, pink dots: CCB 4, dark green: CCB 5, dark blue: CCB 6, light purple: CCB 7, dark purple: CCB 8, brown: CCB 9, and light green: CCB 10.....</i>	<i>126</i>

Figure 6. 14: Average peak suppression of the current peaks of the RCV voltammograms with time of DOPC in CCB (pH 3.0). Black dots: Peak 1 of the voltammogram. Red dots: Peak 2 of the voltammogram. 127

Figure 6. 15: Current at -0.8V when DOPC in CCB (pH 3.0) when the RCV profile is recorded at 40Vs⁻¹ using potential cycles from -0.4V to -1.2V. 127

Figure 6. 16: RCV profile of DOPC in CCB (pH 4.0) recorded at 40V s⁻¹ using potential cycles from -0.4V to -1.2V at time: (a): t=0s, (b): t=25s, (c):t=50s, (d): t=75s, (e): t=100s, (f):t=125s, (g): t=150s, (h):t=175s, (i): t=200s, and (j) t=225s..... 128

Figure 6. 17: Current variation with time of 10 different DOPC depositons in CCB (pH 4.0) of (a) Peak 1. Black dots: CCB 1, red dots: CCB 2, light blue: CCB 3, pink dots: CCB 4, dark green: CCB 5, dark blue: CCB 6, light purple: CCB 7, dark purple: CCB 8, brown: CCB 9, and light green: CCB 10, (b) Peak 2. Black dots: CCB 1, red dots: CCB 2, light blue: CCB 3, pink dots: CCB 4, dark green: CCB 5, dark blue: CCB 6, light purple: CCB 7, dark purple: CCB 8, brown: CCB 9, and light green: CCB 10. 129

Figure 6. 18: Average peak suppression of the current peaks of the RCV voltammograms with time of DOPC in CCB (pH 4.0). Black dots: Peak 1 of the voltammogram. Red dots: Peak 2 of the voltammogram. 130

Figure 6. 19: Current at -0.8V when DOPC in CCB (pH 4.0) when the RCV profile is recorded at 40Vs⁻¹ using potential cycles from -0.4V to -1.2V. 130

Figure 6. 20: RCV profile of DOPC in CCB (pH 5.0) recorded at 40V s⁻¹ using potential cycles from -0.4V to -1.2V at time: (a): t=0s, (b): t=25s, (c):t=50s, (d): t=75s, (e): t=100s, (f):t=125s, (g): t=150s, (h):t=175s, (i): t=200s, and (j) t=225s..... 131

Figure 6. 21: Average peak suppression of the current peaks of the RCV voltammograms with time of DOPC in CCB (pH 5.0). Black dots: Peak 1 of the voltammogram. Red dots: Peak 2 of the voltammogram. 132

Figure 6. 22: Current variation with time of 10 different DOPC depositions in CCB (pH 5.0) of (a) Peak 1. Black dots: CCB 1, red dots: CCB 2, light blue: CCB 3, pink dots: CCB 4, dark green: CCB 5, dark blue: CCB 6, light purple: CCB 7, dark purple: CCB 8, brown: CCB 9, and light green: CCB 10, (b) Peak 2. Black dots: CCB 1, red dots: CCB 2, light blue: CCB 3, pink dots: CCB 4, dark green: CCB 5, dark blue: CCB 6, light purple: CCB 7, dark purple: CCB 8, brown: CCB 9, and light green: CCB 10. 132

Figure 6. 23: Current at -0.8V when DOPC in CCB (pH 5.0) when the RCV profile is recorded at 40Vs⁻¹ using potential cycles from -0.4V to -1.2V. 133

Figure 6. 24: RCV profile of DOPC in CCB (pH 6.0) recorded at 40V s⁻¹ using potential cycles from -0.4V to -1.2V at time: (a): t=0s, (b): t=25s, (c):t=50s, (d): t=75s, (e): t=100s, (f):t=125s, (g): t=150s, (h):t=175s, (i): t=200s, and (j) t=225s..... 134

Figure 6. 25: Current variation with time of 10 different DOPC depositions in CCB (pH 6.0) of (a) Peak 1. Black dots: CCB 1, red dots: CCB 2, light blue: CCB 3, pink dots: CCB 4, dark green: CCB 5, dark blue: CCB 6, light purple: CCB 7, dark purple: CCB 8, brown: CCB 9, and light green: CCB 10, (b) Peak 2.

Black dots: CCB 1, red dots: CCB 2, light blue: CCB 3, pink dots: CCB 4, dark green: CCB 5, dark blue: CCB 6, light purple: CCB 7, dark purple: CCB 8, brown: CCB 9, and light green: CCB 10.....	135
Figure 6. 26: Current at -0.8V when DOPC in CCB (pH 6.0) when the RCV profile is recorded at 40Vs ⁻¹ using potential cycles from -0.4V to -1.2V.....	136
Figure 6. 27: Average peak suppression of the current peaks of the RCV voltammograms with time of DOPC in CCB (pH 6.0). Black dots: Peak 1 of the voltammogram. Red dots: Peak 2 of the voltammogram.....	136
Figure 6. 28: RCV profile of DOPE in PBS (pH 7.4.0) recorded at 40V s ⁻¹ using potential cycles from -0.4V to -1.2V at time: (a): t=0s, (b): t=25s, (c):t=50s, (d): t=75s, (e): t=100s, (f):t=125s, (g): t=150s, (h):t=175s, (i): t=200s, and (j) t=225s.....	138
Figure 6. 29: Current variation with time of 4 different DOPC depositions in PBS (pH 7.4) of (a) Peak 1: Black dots: DOPE 1, red dots: DOPE 2, light blue: DOPE 3, pink dots: DOPE 4 and (b) Peak 2. Black dots: DOPE 1, red dots: DOPE 2, light blue: DOPE 3, pink dots: DOPE 4,.....	139
Figure 6. 30: Current at -0.8V when DOPE in PBS (pH 7.4) when the RCV profile is recorded at 40Vs ⁻¹ using potential cycles from -0.4V to -1.2V.....	140
Figure 6. 31: Average peak suppression of the current peaks of the RCV voltammograms with time of DOPE in PBS (pH 7.4). Black dots: Peak 1 of the voltammogram. Red dots: Peak 2 of the voltammogram.....	140
Figure 6. 32: RCV profile of DOPS in PBS (pH 7.4) recorded at 40V s ⁻¹ using potential cycles from -0.4V to -1.2V at time: (a): t=0s, (b): t=25s, (c):t=50s, (d): t=75s, (e): t=100s, (f):t=125s, (g): t=150s, (h):t=175s, (i): t=200s, and (j) t=225s.....	142
Figure 6. 33: RCV profile of DOPS in PBS (pH 7.4) recorded at 40Vs ⁻¹ using potential cycles from -0.4V to -1.2V at: Black line: t=0s and red line: t=225s.	143
Figure 6. 34: Current variation with time of 10 different DOPS depositions in PBS (pH 7.4) of (A) Peak 1. Black dots: DOPS 1, red dots: DOPS 2, light blue: DOPS 3, pink dots: DOPS 4, dark green: DOPS 5, dark blue: DOPS 6, light purple: DOPS 7, dark purple: DOPS 8, brown: DOPS 9.	143
Figure 6. 35: RCV profile current at -0.8V of DOPS in PBS (pH 7.4) when the RCV profile is recorded at 40Vs ⁻¹ using potential cycles from -0.4V to -1.2V.	144
Figure 6. 36: RCV profile of DOPA in PBS (pH 7.4) using potential cycles from: (A): -0.4V to -1.2V recorded at 40V s ⁻¹ and (B): -0.4V to -1.4V recorded at 46V s ⁻¹	148
Figure 6. 37: RCV profile of DOPA in PBS (pH 7.4.0) recorded at 40V s ⁻¹ using potential cycles from -0.4V to -1.2V at time: (a): t=0s, (b): t=25s, (c):t=50s, (d): t=75s, (e): t=100s, (f):t=125s, (g): t=150s, (h):t=175s, (i): t=200s, and (j) t=225s.....	150
Figure 6. 38: Average peak suppression of the current peaks of the RCV voltammograms with time of DOPA in PBS (pH=7.4). Black dots: Peak 1 of the voltammogram. Red dots: Peak 2 of the voltammogram.....	151

Figure 6. 39: RCV profile of DOPA in PBS (pH 7.4.0) recorded at 40V s⁻¹ using potential cycles from -0.4V to -1.4V at time: (a): t=0s, (b): t=25s, (c):t=50s, (d): t=75s, (e): t=100s, (f):t=125s, (g): t=150s, (h):t=175s, (i): t=200s, and (j) t=225s..... 152

Figure 6. 40: Current variation with time of 10 different DOPA depositions in PBS (pH 7.4) of **(a) Peak 1**: Black dots: DOPA in PBS 1, red dots: DOPA in PBS 2, light blue: DOPA in PBS 3, pink dots: DOPA in PBS 4, dark green: DOPA in PBS 5, dark blue: DOPA in PBS 6, light purple: DOPA in PBS 7, dark purple: DOPA in PBS 8, brown: DOPA in PBS 9, and light green: DOPA in PBS 10, **(b) Peak 2**: Black dots: DOPA in PBS 1, red dots: DOPA in PBS 2, light blue: DOPA in PBS 3, pink dots: DOPA in PBS 4, dark green: DOPA in PBS 5, dark blue: DOPA in PBS 6, light purple: DOPA in PBS 7, dark purple: DOPA in PBS 8, brown: DOPA in PBS 9, and light green: DOPA in PBS 10, **(c) Peak 3**: Black dots: DOPA in PBS 1, red dots: DOPA in PBS 2, light blue: DOPA in PBS 3, pink dots: DOPA in PBS 4, dark green: DOPA in PBS 5, dark blue: DOPA in PBS 6, light purple: DOPA in PBS 7, dark purple: DOPA in PBS 8, brown: DOPA in PBS 9, and light green: DOPA in PBS 10. **(d) Peak 4**: Black dots: DOPA in PBS 1, red dots: DOPA in PBS 2, light blue: DOPA in PBS 3, pink dots: DOPA in PBS 4, dark green: DOPA in PBS 5, dark blue: DOPA in PBS 6, light purple: DOPA in PBS 7, dark purple: DOPA in PBS 8, brown: DOPA in PBS 9, and light green: DOPA in PBS 10 **(e) Peak 5**: Black dots: DOPA in PBS 1, red dots: DOPA in PBS 2, light blue: DOPA in PBS 3, pink dots: DOPA in PBS 4, dark green: DOPA in PBS 5, dark blue: DOPA in PBS 6, light purple: DOPA in PBS 7, dark purple: DOPA in PBS 8, brown: DOPA in PBS 9, and light green: DOPA in PBS 10..... 153

Figure 6. 41: Average peak suppression of the current peaks of the RCV voltammograms with time of DOPA in PBS (pH=7.4) of **(a) Stable Peak 1**: Black dots: Peak 1 of the voltammogram. Red dots: Peak 2 of the voltammogram. Blue dots: Peak 3 of the voltammogram. Green dots: Peak 4 of the voltammogram. **(b) Unstable Peak 1**: Black dots: Peak 1 of the voltammogram. Red dots: Peak 2 of the voltammogram. Blue dots: Peak 3 of the voltammogram. Green dots: Peak 4 of the voltammogram 154

Figure 6. 42: Current at -0.8V when DOPA in PBS (pH 7.4) when the RCV profile is recorded at 40Vs⁻¹ using potential cycles from -0.4V to -1.2V. 155

Figure 6. 43: RCV profile of DOPG in PBS (pH 7.4.0) recorded at 40V s⁻¹ using potential cycles from -0.4V to -1.2V at time: (a): t=0s, (b): t=25s, (c):t=50s, (d): t=75s, (e): t=100s, (f):t=125s, (g): t=150s, (h):t=175s, (i): t=200s, and (j) t=225s..... 157

Figure 6. 44: Current variation with time of 10 different DOPG depositions in PBS (pH 7.4) of (A) Peak 1. Black dots: DOPG 1, red dots: DOPG 2, light blue: DOPG 3, pink dots: DOPG 4, dark green: DOPG 5, dark blue: DOPG 6, light purple: DOPG 7, dark purple: DOPG 8, brown: DOPG 9, and light green: DOPG 10, (b) Peak 2. Black dots: DOPG 1, red dots: DOPG 2, light blue: DOPG 3, pink dots: DOPG 4, dark green: DOPG 5, dark blue: DOPG 6, light purple: DOPG 7, dark purple: DOPG 8..... 158

Figure 6. 45: Current at -0.8V when DOPG in PBS (pH 7.4) when the RCV profile is recorded at 40Vs⁻¹ using potential cycles from -0.4V to -1.2V. 159

Figure 6. 46: Current at -0.8V when DOPG in PBS (pH 7.4) when the RCV profile is recorded at 40Vs⁻¹ using potential cycles from -0.4V to -1.2V..... 160

FIGURES CHAPTER 7

Figure 7. 1: RCV voltammograms recorded at 40Vs⁻¹ with a potential excursion from -0.4V to -1.20V of DOPC (black lines) under a continuous flow of PBS in the presence of (red lines): A: 0.01M Ce(NO₃)₃, B: 40mM TMAOH and C: 0.5M HMT. RCV voltammograms recorded at 40Vs⁻¹ with a potential excursion from -0.4V to -1.20V of DOPC (black lines) under a continuous flow of PBS in the presence of (red lines): A: 0.01M Ce(NO₃)₃, B: 40mM TMAOH and C: 0.5M HMT. 166

Figure 7. 2: RCV voltammograms recorded at 40Vs⁻¹ with a potential excursion from -0.4V to -1.20V of DOPC (black lines) under a continuous flow of GLY 3.0 in the presence of (red lines): A: 0.01M dots in GLY 3.0, B: 0.01M spheres in GLY 3.0, C: 0.01M cubes in GLY 3.0 and D: 0.01M needles in GLY 3.0. 167

Figure 7. 3: RCV voltammogram recorded at 40Vs⁻¹ with a potential excursion from -0.4V to -1.2V in a continuous flow of PBS of: black line: DOPE, red line: DOPE vs 0.01M of CeO₂ NPs (spheres) **Table:** Average peak suppression (%) and peak shift (V) of the peaks of the voltammograms produced when 0.01M of CeO₂ NPs (spheres) are in contact with DOPE..... 169

Figure 7. 4: RCV voltammogram recorded at 40Vs⁻¹ with a potential excursion from -0.4V to -1.2V in a continuous flow of PBS of: black line: DOPE, red line: DOPE vs 0.01M of commercial CeO₂ NPs (dots) **Table:** Average peak suppression (%) and peak shift (V) of the peaks of the voltammograms produced when 0.01M of commercial CeO₂ NPs (dots) are in contact with DOPE..... 169

Figure 7. 5: **Graph:** RCV voltammogram recorded at 46Vs⁻¹ with a potential excursion from -0.4V to -1.4V in a continuous flow of PBS of: black line: DOPA, red line: DOPA vs 0.01M of CeO₂ NPs synthesised using TMAOH (spheres) **Table:** Average peak suppression (%) and peak shift (V) of the peaks of the voltammograms produced when 0.01M of CeO₂ NPs synthesised with TMAOH (spheres) are in contact with DOPA 170

Figure 7. 6: **Graph:** RCV voltammogram recorded at 46Vs⁻¹ with a potential excursion from -0.4V to -1.4V in a continuous flow of PBS of: black line: DOPA, red line: DOPA vs 0.01M of CeO₂ NPs synthesised using HMT(cubes) **Table:** Average peak suppression (%) and peak shift (V) of the peaks of the voltammograms produced when 0.01M of CeO₂ NPs synthesised with HMT (cubes) are in contact with DOPA..... 171

Figure 7. 7: **Graph:** RCV voltammogram recorded at 46Vs⁻¹ with a potential excursion from -0.4V to -1.4V in a continuous flow of PBS of: black line: DOPA, red line: DOPA vs 0.01M of commercial CeO₂ NPs (dots), blue line: DOPA vs 0.01M commercial CeO₂ NPs . **Table:** Average peak suppression (%) and peak shift (V) of the peaks of the voltammograms produced when 0.01M of commercial CeO₂ NPs (dots) are in contact with DOPA..... 172

Figure 7. 8: RCV voltammogram recorded at 46Vs^{-1} with a potential excursion from -0.4V to -1.4V in a continuous flow of PBS of: black line: DOPA, blue line: interaction of DOPA with milli-Q water, red line: DOPA recovery after the interaction. 173

Figure 7. 9: **Graph:** RCV voltammogram recorded at 40Vs^{-1} with a potential excursion from -0.4V to -1.2V in a continuous flow of PBS of: black line: DOPG, red line: DOPG in contact with 0.01M of CeO_2 NPs synthesised using TMAOH (spheres) **Table:** Average peak suppression (%) and peak shift (V) of the peaks of the voltammograms produced when 0.01M of CeO_2 NPs synthesised with TMAOH (spheres) are in contact with DOPC 175

Figure 7. 10: : **Graph:** RCV voltammogram recorded at 40Vs^{-1} with a potential excursion from -0.4V to -1.2V in a continuous flow of PBS of: black line: DOPG, red line: DOPG in contact with 0.01M of CeO_2 NPs synthesised using HMT (cubes) **Table:** Average peak suppression (%) and peak shift (V) of the peaks of the voltammograms produced when 0.01M of CeO_2 NPs synthesised with HMT (cubes) are in contact with DOPC..... 176

Figure 7. 11: **Graph:** RCV voltammogram recorded at 40Vs^{-1} with a potential excursion from -0.4V to -1.2V in a continuous flow of PBS of: black line: DOPG, red line: DOPG in contact with 0.01M of CeO_2 NPs synthesised using HMT (cubes) **Table:** Average peak suppression (%) and peak shift (V) of the peaks of the voltammograms produced when 0.01M of CeO_2 NPs synthesised with HMT (cubes) are in contact with DOPC..... 176

Figure 7. 12: **Graph:** RCV voltammogram recorded at 40Vs^{-1} with a potential excursion from -0.4V to -1.2V in a continuous flow of PBS of: black line: DOPC, red line: DOPC vs 0.01M of CeO_2 NPs synthesised using TMAOH (spheres) **Table:** Average peak suppression (%) and peak shift (V) of the peaks of the voltammograms produced when 0.01M of CeO_2 NPs synthesised with TMAOH (spheres) are in contact with DOPC..... 177

Figure 7. 13: RCV voltammogram recorded at 40Vs^{-1} with a potential excursion from -0.4V to -1.2V in a continuous flow of PBS of: black line: DOPC, red line: DOPC vs 0.01M of CeO_2 NPs synthesised using HMT (cubes) **Table:** Average peak suppression (%) and peak shift (V) of the peaks of the voltammograms produced when 0.01M of CeO_2 NPs synthesised with HMT (cubes) are in contact with DOPC..... 178

Figure 7. 14: RCV voltammogram recorded at 40Vs^{-1} with a potential excursion from -0.4V to -1.2V in a continuous flow of PBS of: black line: DOPC, red line: DOPC vs 0.01M of CeO_2 NPs synthesised using HMT (cubes) **Table:** Average peak suppression (%) and peak shift (V) of the peaks of the voltammograms produced when 0.01M of CeO_2 NPs synthesised with HMT (cubes) are in contact with DOPC..... 178

Figure 7. 15: RCV voltammograms recorded at 40Vs^{-1} with a potential excursion from -0.4V to -1.20V of DOPC (black lines) under a continuous flow of GLY 3.0 in the presence of (red lines): A: 0.01M of CeO_2 NPs (spheres) in GLY 3.0, B: 0.006M of CeO_2 NPs (spheres) in GLY 3.0, C: 0.002M of CeO_2 NPs (spheres) in GLY 3.0, D: 0.0004M of CeO_2 NPs (spheres) in GLY 3.0. 181

Figure 7. 16: Behaviour of the Peak 1 (black dots) and Peak 2 (red dots) of the voltammograms obtained from the ESD when a varying concentration of CeO ₂ NPs (spheres) in GLY 3.0 interact with DOPC under a continuous flow of GLY 3.0. A: Graph showing the suppression, in percentage (%), of the peaks. B: Graph showing the shift (V), in potential, of the peaks.	182
Figure 7. 17: RCV voltammograms recorded at 40Vs ⁻¹ with a potential excursion from -0.4V to -1.20V of DOPC (black lines) under a continuous flow of GLY 3.0 in the presence of (red lines): A: 0.01M of CeO ₂ NPs (cubes) in GLY 3.0, B: 0.006M of CeO ₂ NPs (cubes) in GLY 3.0, C: 0.002M of CeO ₂ NPs (cubes) in GLY 3.0, D: 0.0004M of CeO ₂ NPs (cubes) in GLY 3.0.	184
Figure 7. 18: Behaviour of the Peak 1 (black dots) and Peak 2 (red dots) of the voltammograms obtained from the ESD when a varying concentration of CeO ₂ NPs (cubes) in GLY 3.0 interact with DOPC under a continuous flow of GLY 3.0. A: Graph showing the suppression, in percent age (%), of the peaks. B: Graph showing the shift (V), in potential, of the peaks.	185
Figure 7. 19: : RCV voltammograms recorded at 40Vs ⁻¹ with a potential excursion from -0.4V to -1.2V of DOPC (black lines) under a continuous flow of GLY 3.0 in the presence of (red lines): A: 0.01M of CeO ₂ NPs (needles) in GLY 3.0, B: 0.006M of CeO ₂ NPs (needles) in GLY 3.0, C: 0.002M of CeO ₂ NPs (needles) in GLY 3.0, D: 0.0004M of CeO ₂ NPs (needles) in GLY 3.0.	186
Figure 7. 20: Behaviour of the Peak 1 (black dots) and Peak 2 (red dots) of the voltammograms obtained from the ESD when a varying concentration of CeO ₂ NPs (cubes) in GLY 3.0 interact with DOPC under a continuous flow of GLY 3.0. A: Graph showing the suppression, in percentage (%), of the peaks. B: Graph showing the shift (V), in potential, of the peaks.	187
Figure 7. 21: RCV voltammograms recorded at 40Vs ⁻¹ with a potential excursion from -0.4V to -1.20V of DOPC (black lines) under a continuous flow of CCB 3.0 in the presence of (red lines): A: 0.01M of CeO ₂ NPs (spheres) in CCB 3.0, B: 0.006M of CeO ₂ NPs (spheres) in CCB 3.0, C: 0.002M of CeO ₂ NPs (spheres) in CCB 3.0, D: 0.0004M of CeO ₂ NPs (spheres) in CCB 3.0.....	188
Figure 7. 22: Behaviour of the Peak 1 (black dots) and Peak 2 (red dots) of the voltammograms obtained from the ESD when a varying concentration of CeO ₂ NPs (spheres) in CCB 3.0 interact with DOPC under a continuous flow of CCB 3.0. A: Graph showing the suppression, in percentage (%), of the peaks. B: Graph showing the shift (V), in potential, of the peaks.	189
Figure 7. 23: RCV voltammograms recorded at 40Vs ⁻¹ at a cycling potential that ranges from -0.4V to -1.20V of DOPC (black lines) under a continuous flow of CCB 3.0 in the presence of (red lines): A: 0.01M of CeO ₂ NPs (cubes) in CCB 3.0, B: 0.006M of CeO ₂ NPs (cubes) in CCB 3.0, C: 0.002M of CeO ₂ NPs (cubes) in CCB 3.0, D: 0.0004M of CeO ₂ NPs (cubes) in CCB 3.0.....	190
Figure 7. 24: Behaviour of the Peak 1 (black dots) and Peak 2 (red dots) of the voltammograms obtained from the ESD when a varying concentration of CeO ₂ NPs (cubes) in CCB 3.0 interact with DOPC under a continuous flow of CCB 3.0. A: Graph showing the suppression, in percentage (%), of the peaks. B: Graph showing the shift (V), in potential, of the peaks.	191
Figure 7. 25: RCV voltammograms recorded at 40Vs ⁻¹ at a cycling potential that ranges from -0.4V to -1.20V of DOPC (black lines) under a continuous flow of CCB 3.0 in the presence of (red lines): A:	

0.01M of CeO ₂ NPs (needles) in CCB 3.0, B: 0.006M of CeO ₂ NPs (needles) in CCB 3.0, C: 0.002M of CeO ₂ NPs (needles) in CCB 3.0, D: 0.0004M of CeO ₂ NPs (needles) in CCB 3.0.	192
<i>Figure 7. 26: Behaviour of the Peak 1 (black dots) and Peak 2 (red dots) of the voltammograms obtained from the ESD when a varying concentration of CeO₂ NPs (broken needles) in CCB 3.0 interact with DOPC under a continuous flow of CCB 3.0. A: Graph showing the suppression, in percentage (%), of the peaks. B: Graph showing the shift (V), in potential, of the peaks.</i>	
.....	193
<i>Figure 7. 27: RCV voltammograms recorded at 40Vs⁻¹ with a potential excursion from -0.4V to -1.20V of DOPC (black lines) under a continuous flow of CCB 4.0 in the presence of (red lines): A: 0.01M of CeO₂ NPs (spheres) in CCB 4.0, B: 0.006M of CeO₂ NPs (spheres) in CCB 4.0, C: 0.002M of CeO₂ NPs (spheres) in CCB 4.0, D: 0.0004M of CeO₂ NPs (spheres) in CCB 4.0.</i>	
.....	194
<i>Figure 7. 28: Behaviour of the Peak 1 (black dots) and Peak 2 (red dots) of the voltammograms obtained from the ESD when a varying concentration of CeO₂ NPs (spheres) in CCB 4.0 interact with DOPC under a continuous flow of CCB 4.0. A: Graph showing the suppression, in percentage (%), of the peaks. B: Graph showing the shift (V), in potential, of the peaks.</i>	
.....	195
<i>Figure 7. 29: RCV voltammograms recorded at 40Vs⁻¹ with a potential excursion from -0.4V to -1.20V of DOPC (black lines) under a continuous flow of CCB 4.0 in the presence of (red lines): A: 0.01M of CeO₂ NPs (cubes) in CCB 4.0, B: 0.006M of CeO₂ NPs (cubes) in CCB 4.0, C: 0.002M of CeO₂ NPs (cubes) in CCB 4.0, D: 0.0004M of CeO₂ NPs (cubes) in CCB 4.0.</i>	
.....	196
<i>Figure 7. 30: Behaviour of the Peak 1 (black dots) and Peak 2 (red dots) of the voltammograms obtained from the ESD when a varying concentration of CeO₂ NPs (cubes) in CCB 4.0 interact with DOPC under a continuous flow of CCB 4.0. A: Graph showing the suppression, in percentage (%), of the peaks. B: Graph showing the shift (V), in potential, of the peaks.</i>	
.....	197
<i>Figure 7. 31: RCV voltammograms recorded at 40Vs⁻¹ with a potential excursion from -0.4V to -1.20V of DOPC (black lines) under a continuous flow of CCB 4.0 in the presence of (red lines): A: 0.01M of CeO₂ NPs (needles) in CCB 4.0, B: 0.006M of CeO₂ NPs (needles) in CCB 4.0, C: 0.002M of CeO₂ NPs (needles) in CCB 4.0, D: 0.0004M of CeO₂ NPs (needles) in CCB 4.0.</i>	
.....	198
<i>Figure 7. 32: Behaviour of the Peak 1 (black dots) and Peak 2 (red dots) of the voltammograms obtained from the ESD when a varying concentration of CeO₂ NPs (needles) in CCB 4.0 interact with DOPC under a continuous flow of CCB 4.0. A: Graph showing the suppression, in percentage (%), of the peaks. B: Graph showing the shift (V), in potential, of the peaks.</i>	
.....	199
<i>Figure 7. 33: RCV voltammograms recorded at 40Vs⁻¹ with a potential excursion from -0.4V to -1.20V of DOPC (black lines) under a continuous flow of CCB 5.0 in the presence of (red lines): A: 0.01M of CeO₂ NPs (spheres) in CCB 5.0, B: 0.006M of CeO₂ NPs (spheres) in CCB 5.0, C: 0.002M of CeO₂ NPs (spheres) in CCB 5.0, D: 0.0004M of CeO₂ NPs (spheres) in CCB 5.0.</i>	
.....	200
<i>Figure 7. 34: Behaviour of the Peak 1 (black dots) and Peak 2 (red dots) of the voltammograms obtained from the ESD when a varying concentration of CeO₂ NPs (spheres) in CCB 5.0 interact with DOPC under a continuous flow of CCB 5.0. A: Graph showing the suppression, in percentage (%), of the peaks. B: Graph showing the shift (V), in potential, of the peaks.</i>	
.....	201

Figure 7. 35: RCV voltammograms recorded at 40Vs^{-1} with a potential excursion from -0.4V to -1.20V of DOPC (black lines) under a continuous flow of CCB 5.0 in the presence of (red lines): A: 0.01M of CeO_2 NPs (cubes) in CCB 5.0, B: 0.006M of CeO_2 NPs (cubes) in CCB 5.0, C: 0.002M of CeO_2 NPs (cubes) in CCB 5.0, D: 0.0004M of CeO_2 NPs (cubes) in CCB 5.0.	202
Figure 7. 36: Behaviour of the Peak 1 (black dots) and Peak 2 (red dots) of the voltammograms obtained from the ESD when a varying concentration of CeO_2 NPs (cubes) in CCB 5.0 interact with DOPC under a continuous flow of CCB 5.0. A: Graph showing the suppression, in percentage (%), of the peaks. B: Graph showing the shift (V), in potential, of the peaks.	203
Figure 7. 37: RCV voltammograms recorded at 40Vs^{-1} with a potential excursion from -0.4V to -1.20V of DOPC (black lines) under a continuous flow of CCB 5.0 in the presence of (red lines): A: 0.01M of CeO_2 NPs (needles) in CCB 5.0, B: 0.006M of CeO_2 NPs (needles) in CCB 5.0, C: 0.002M of CeO_2 NPs (needles) in CCB 5.0, D: 0.0004M of CeO_2 NPs (needles) in CCB 5.0.....	204
Figure 7. 38: Behaviour of the Peak 1 (black dots) and Peak 2 (red dots) of the voltammograms obtained from the ESD when a varying concentration of CeO_2 NPs (needles) in CCB 5.0 interact with DOPC under a continuous flow of CCB 5.0. A: Graph showing the suppression, in percentage (%), of the peaks. B: Graph showing the shift (V), in potential, of the peaks.	205
Figure 7. 39: RCV voltammograms recorded at 40Vs^{-1} with a potential excursion from -0.4V to -1.20V of DOPC (black lines) under a continuous flow of CCB 6.0 in the presence of (red lines): A: 0.01M of CeO_2 NPs (spheres) in CCB 6.0, B: 0.006M of CeO_2 NPs (spheres) in CCB 5.0, C: 0.002M of CeO_2 NPs (spheres) in CCB 6.0, D: 0.0004M of CeO_2 NPs (spheres) in CCB 6.0.....	206
Figure 7. 40: Behaviour of the Peak 1 (black dots) and Peak 2 (red dots) of the voltammograms obtained from the ESD when a varying concentration of CeO_2 NPs (spheres) in CCB 6.0 interact with DOPC under a continuous flow of CCB 6.0. A: Graph showing the suppression, in percentage (%), of the peaks. B: Graph showing the shift (V), in potential, of the peaks.	207
Figure 7. 41: RCV voltammograms recorded at 40Vs^{-1} with a potential excursion from -0.4V to -1.20V of DOPC (black lines) under a continuous flow of CCB 6.0 in the presence of (red lines): A: 0.01M of CeO_2 NPs (cubes) in CCB 6.0, B: 0.006M of CeO_2 NPs (cubes) in CCB 5.0, C: 0.002M of CeO_2 NPs (cubes) in CCB 6.0, D: 0.0004M of CeO_2 NPs (cubes) in CCB 6.0.	208
Figure 7. 42: Behaviour of the Peak 1 (black dots) and Peak 2 (red dots) of the voltammograms obtained from the ESD when a varying concentration of CeO_2 NPs (cubes) in CCB 6.0 interact with DOPC under a continuous flow of CCB 6.0. A: Graph showing the suppression, in percentage (%), of the peaks. B: Graph showing the shift (V), in potential, of the peaks.	209
Figure 7. 43: RCV voltammograms recorded at 40Vs^{-1} with a potential excursion from -0.4V to -1.20V of DOPC (black lines) under a continuous flow of CCB 6.0 in the presence of (red lines): A: 0.01M of CeO_2 NPs (needles) in CCB 6.0, B: 0.006M of CeO_2 NPs (needles) in CCB 5.0, C: 0.002M of CeO_2 NPs (needles) in CCB 6.0, D: 0.0004M of CeO_2 NPs (needles) in CCB 6.0.....	210
Figure 7. 44: Behaviour of the Peak 1 (black dots) and Peak 2 (red dots) of the voltammograms obtained from the ESD when a varying concentration of CeO_2 NPs (needles) in CCB 6.0 interact with	

DOPC under a continuous flow of CCB 6.0. A: Graph showing the suppression, in percentage (%), of the peaks. B: Graph showing the shift (V), in potential, of the peaks.	211
Figure 7. 45: RCV voltammograms recorded at 40Vs^{-1} with a potential excursion from -0.4V to -1.20V of DOPC (black lines) under a continuous flow of GLY 3.0 in the presence of (red lines): A: $3.95 \cdot 10^{-3}$, B: $3.95 \cdot 10^{-4}$, C: $3.95 \cdot 10^{-5}$, D: $3.95 \cdot 10^{-6}$, E: $3.95 \cdot 10^{-7}$, F: $3.95 \cdot 10^{-8}$	216
Figure 7. 46: Behaviour of the Peak 1 (black dots) and Peak 2 (red dots) of the voltammograms obtained from the ESD when a varying concentration of $\text{Ce}(\text{NO}_3)_3$ in GLY 3.0 interact with DOPC under a continuous flow of GLY 3.0. A: Graph showing the suppression, in percentage (%), of the peaks. B: Graph showing the shift (V), in potential, of the peaks.	217
Figure 7. 47: RCV voltammograms recorded at 40Vs^{-1} with a potential excursion from -0.4V to -1.20V of DOPC (black lines) under a continuous flow of CCB 3.0 in the presence of (red lines): A: $3.95 \cdot 10^{-3}$, B: $3.95 \cdot 10^{-4}$, C: $3.95 \cdot 10^{-5}$, D: $3.95 \cdot 10^{-6}$, E: $3.95 \cdot 10^{-7}$, F: $3.95 \cdot 10^{-8}$	219
Figure 7. 48: Behaviour of the Peak 1 (black dots) and Peak 2 (red dots) of the voltammograms obtained from the ESD when a varying concentration of $\text{Ce}(\text{NO}_3)_3$ in CCB 3.0 interact with DOPC under a continuous flow of CCB 3.0. A: Graph showing the suppression, in percentage (%), of the peaks. B: Graph showing the shift (V), in potential, of the peaks.	220
Figure 7. 49: Behaviour of the Peak 1 (black dots) and Peak 2 (red dots) of the voltammograms obtained from the ESD when a varying concentration of $\text{Ce}(\text{NO}_3)_3$ interact with DOPC under a continuous flow of different buffers: A: peak suppression versus concentration of $\text{Ce}(\text{NO}_3)_3$ under a continuous flow of CCB 4.0, B: peak shift versus concentration of $\text{Ce}(\text{NO}_3)_3$ under a continuous flow of CCB 4.0, C: peak suppression versus concentration of $\text{Ce}(\text{NO}_3)_3$ under a continuous flow of CCB 5.0, D: peak shift versus concentration of $\text{Ce}(\text{NO}_3)_3$ under a continuous flow of CCB 5.0, E: peak suppression versus concentration of $\text{Ce}(\text{NO}_3)_3$ under a continuous flow of CCB 6.0, and F: peak shift versus concentration of $\text{Ce}(\text{NO}_3)_3$ under a continuous flow of CCB 6.0.	221
Figure 7. 50: Behaviour of the Peak 1 (black dots) and Peak 2 (red dots) of the voltammograms obtained from the ESD when a varying concentration of $\text{Ce}(\text{NO}_3)_3$ in PBS (pH 7.4) interact with DOPC under a continuous flow of CCB 3.0. A: Graph showing the suppression, in percentage (%), of the peaks. B: Graph showing the shift (V), in potential, of the peaks.	222
Figure 7. 51: RCV voltammogram recorded at 40Vs^{-1} potential excursion from -0.4V to -1.20V of DOPC (black lines) under a continuous flow of PBS in the presence of (red line) 0.01M $\text{Ce}(\text{NO}_3)_3$	223
Figure 7. 52: Average percentage of dissolved cerium from dispersions of the metal in different matrixes (GLY 3.0, CCB 3.0, CCB 4.0, CCB 5.0, CCB 6.0, PBS 7.4) of: CeO_2 NPs (spheres) and B: CeO_2 NPs (cubes)	227
Figure 7. 53: A: Suppression of the peak 1 (black dots) and peak 2 (red dots) of the voltammogram when different concentrations of $\text{Ce}(\text{NO}_3)_3$ (M) interact with DOPC under a constant flow of GLY 3.0. Orange lines: average cerium in solution from ICP-MS experiments (continuous line) and its associated error (dashed line) produced from 0.01M of CeO_2 NPs (spheres). Blue lines: average cerium in solution from ICP-MS experiments (continuous line) and its associated error (dashed line)	

produced from 0.01M of CeO ₂ NPs (Cubes). B : Suppression of the peak 1 (black dots) and peak 2 (red dots) of the voltammogram when different concentrations of Ce(NO ₃) ₃ (M) interact with DOPC under a constant flow of CCB 3.0. Orange lines: average cerium in solution from ICP-MS experiments (continuous line) and its associated error (dashed line) produced from 0.01M of CeO ₂ NPs (spheres). Blue lines: average cerium in solution from ICP-MS experiments (continuous line) and its associated error (dashed line) produced from 0.01M of CeO ₂ NPs (Cubes).....	229
Figure 7. 54: EELS spectra of: Black line: Ce(IV) reference material, red line: Ce(III) reference material, blue line: spheres in PBS (pH 7.4), light green line: spheres in CCB at pH 3.0, dark green line: spheres in glycine pH 3.0	231
Figure 7. 55: Average suppression of the peak 1 (black dots) and peak 2 (red dots) versus concentration of 40-PVP wof the voltammograms produced when DOPC interacts witj 40-PVP.....	233
Figure 7. 56: RCV voltammograms recorded at 40Vs ⁻¹ at a cycling potential that ranges from -0.4V to -1.20V of DOPC (black lines) under a continuous flow of PBS in the presence of (red lines): A: 2.5·10 ⁻⁴ M 40-PVP and B: 1·10 ⁻³ M.....	233
Figure 7. 57: RCV voltammograms recorded at 40Vs ⁻¹ at a cycling potential that ranges from -0.4V to -1.20V of DOPC (black lines) under a continuous flow of PBS in the presence of (red lines): A: Supernatant 2 and B: supernatant 3.....	234
Figure 7. 58: RCV voltammogram recorded at 40Vs ⁻¹ at a cycling potential that ranges from -0.4V to -1.20V of DOPC (black line) under a continuous flow of PBS in the presence of (red line) 40 PVP CeO ₂ NPs.....	235
Figure 7. 59: RCV voltammograms recorded at 40Vs ⁻¹ at a cycling potential that ranges from -0.4V to -1.20V of DOPC (black line) under a continuous flow of PBS in the presence of PEG-CeO ₂ NPs.....	236
Figure 7. 60: RCV voltammograms recorded at 40Vs ⁻¹ at a cycling potential that ranges from -0.4V to -1.20V of DOPC (black line) under a continuous flow of PBS in the presence of the supernatant 0 from the synthesis of PEG-coated CeO ₂ NPs. B: Graph showing peak suppression versus concentration of PEG.	236
Figure 7. 61: RCV voltammograms recorded at 40Vs ⁻¹ at a cycling potential that ranges from -0.4V to -1.20V of DOPC (black line) under a continuous flow of PBS in the presence of 1.6% dextran at 5s (red line) and 1.6% dextran at 1.5min. B: Graph showing peak suppression versus concentration of dextran.....	238
Figure 7. 62: A: RCV voltammograms recorded at 40Vs ⁻¹ at a cycling potential that ranges from -0.4V to -1.20V of DOPC (black lines) under a continuous flow of PBS in the presence of (red lines): A: the supernatant 1 and B: dextran-CeO ₂ NPs.	239
Figure 7. 63: RCV voltammograms recorded at 40Vs ⁻¹ at a cycling potential that ranges from -0.4V to -1.20V of DOPC (black line) in the presence of (red line): A: PBS-CeO ₂ (spheres) in GLY 3.0, B: PBS-CeO ₂ (cubes) in GLY 3.0, C: PBS-CeO ₂ (spheres) in CCB 3.0 and D: PBS-CeO ₂ (cubes) in CCB 3.0.....	240
Figure 7. 64: The left image shows how CeO ₂ spheres, cubes and needles NPs interact with a DOPC monolayer in the Hg/Pt electrode in different buffers (GLY 3.0, CCB 3.0, CCB 4.0, CCB 5.0, CCB 6.0 and	

PBS 7.4). The light green colour surrounding the NPs represent a citrate coating in CCB 3.0, the dark green colour surrounding the NPs represent a citrate coating in CCB 4.0, CCB 5.0 and CCB 6.0 and the purple colour surrounding the NPs represent a phosphate coating. The right graphs show the RCV response the CeO₂ NPs generate in different buffes. The black line of the RCV voltammograms indicate the RCV of DOPC. The red line of the RCV voltammograms indicate the interaction with the CeO₂ NPs (spheres, cubes and needles) when in contact with DOPC under a continuous flow of: A: GLY 3.0, B: CCB 3.0, C: CCB 4.0, CCB 5.0 and CCB 6.0, and D: PBS 7.4. 247

Figure 7. 66: The top left image shows the interaction of PBS-CeO₂ NPs (spheres and cubes) in GLY 3.0 with a monolayer of DOPC under a continuous flow of GLY 3.0. The top right image shows the interaction of PBS-CeO₂ NPs (spheres and cubes) in CCB 3.0 with a monolayer of DOPC under a continuous flow of CCB 3.0. The purple colour surrounding the NPs represents the PBS coating the NPs. The bottom graphs The bottom graphs are the RCV profiles that coated CeO₂ NPs produce when in contact with a DOPC monolayer. The black lines are the RCV profile of the monolayer of DOPC. The red lines are the RCV response which is produced when DOPC interacts with: PBS-CeO₂ NPs (spheres and needles)in: A: GLY 3.0 under a continuous flow of GLY 3.0 and B: CCB 3.0 under a continuous flow of CCB 3.0. 248

Figure 7. 65: The top image shows the interaction of coated CeO₂ NPs (blue spheres) with a monolayer of DOPC under a continuous flow of PBS. The pink colour surrounding the NPs represents the PVP coating. The yellow colour surrounding the NPs represent the dextran coating. The orange colour surrounding the NPs represent the PEG coating. The bottom graphs are the RCV profiles that coated CeO₂ NPs produce when in contact with a DOPC monolayer. The black lines are the RCV profile of the monolayer of DOPC. The red lines are the RCV response which is produced when DOPC interacts with: A: PVP-CeO₂ NPs, B: Dextran-CeO₂ NPs and C: PEG-CeO₂ NPs 248

List of tables:

TABLES CHAPTER 2

Table 2. 1: Summary of CeO₂ NPs synthesis methods 21

TABLES CHAPTER 3

Table 3. 1: Experimental conditions of XRD experiments..... 46

Figure 3. 5 Table 3. 2: Experimental conditions of XRD experiments..... 46

Table 3. 3: Experimental conditions of DLS and z-Potential analysis..... 52

TABLES CHAPTER 4

<i>Table 4. 1: Summary of the CeO₂ experimental conditions in this thesis.....</i>	<i>57</i>
<i>Table 4. 2: Description of CeO₂ NPs in H₂O.....</i>	<i>82</i>

TABLES CHAPTE 5

<i>Table 5. 1: Potential, charge and current variations in a RC-circuit with time</i>	<i>93</i>
---	-----------

TABLES CHAPTE 6

<i>Table 6. 1: pK value of different phospholipids.....</i>	<i>111</i>
<i>Table 6. 2: Volume of citric acid and sodium citrate tribasic needed to make a buffer solution of a certain pH.....</i>	<i>114</i>
<i>Table 6. 3: Summary of the time at which the RCV profiles were taken and their associated errors of phospholipids in different media</i>	<i>162</i>

TABLES CHAPTER 7


<i>Table 7. 1: Summary table of the interaction between different CeO₂ NPs and a DOPC monolayer under the influence of different buffers</i>	<i>212</i>
<i>Table 7. 2: Table showing data obtained from ICP-MS experiments</i>	<i>226</i>
<i>Table 7. 3: Summary of the findings of 8.5. Table showing 'YES or NO' interaction of coated-CeO₂ NPs and free coating agents with a monolayer of DOPC.....</i>	<i>242</i>
<i>Table 7. 4: Table showing the type of interaction and its cause when CeO₂ NPs interact with different phospholipids under a continuous flow of PBS.....</i>	<i>243</i>
<i>Table 7. 5: Table showing the effect and the cause of the effect CeO₂ NPs have on the RCV voltammogram when they interact with a DOPC monolayer under different buffers</i>	<i>244</i>
<i>Table 7. 6: Table showing the effect and cause of the effect produced when Ce³⁺ interact with the phospholipid monolayer in different buffers.</i>	<i>245</i>

TABLES CHAPTER 8

<i>Table 8. 1: A literature review of papers which show the effect coated-CeO₂ NPs have on biological activity</i>	<i>252</i>
---	------------

Abbreviations:

- BFTEM: Bright field transmission electron microscopy
- CCB: citric acid and trisodium citrate dehydrate buffer
- Ceria NPs: Cerium (IV) oxide nanoparticles
- DOPA: 1,2-dioleoyl-sn-glycero-3-phosphate (sodium salt)
- DOPC: 1,2-dioleoyl-sn-glycero-3-phosphocholine
- DOPG: 1,2-dioleoyl-sn-glycero-3-phospho-(1'-rac-glycerol) (sodium salt)
- DOPS: 1,2-dioleoyl-sn-glycero-3-phospho-L-serine (sodium salt)
- DLS: Dynamic light scattering
- EDL: Electron double layer
- EDX: Energy-dispersive X-Ray spectroscopy
- EELS: Electron energy loss spectroscopy
- ESD: Electrochemical sensing device
- GLY: Glycine buffer
- HI: micelle organisation
- HII: hexagonal organisation
- HMT: Hexamethylenetetramine or methenamine
- ICN2: Catalan Institut of Nanoscience and Nanotechnology
- L: lamellar organisation
- MFE: Micro-fabricated electrode
- Nano-Ceria: Cerium (IV) oxide nanoparticles
- NP: nanoparticle

- 
- OS: Oxidative stress
 - PBS: Phosphate buffered saline
 - RI: Refractive index
 - ROS: Reactive oxygen species
 - RNS: Reactive nitrogen species
 - SAED: Selected area electron diffraction
 - SAR: Structure-activity relationship
 - SOFC: Solid oxide fuel cells
 - TMAOH: Tetramethylammonium hydroxide
 - TWC: Three way catalyst
 - TEM: Transmission electron microscopy
 - vdW: Van der Waals forces
 - WBD: Wafer-based device
 - XANES: Near edge X-Ray absorption
 - XPS: X-Ray photoelectron spectroscopy

CHAPTER 1. INTRODUCTION

Even though the concept of a ‘nanoparticle’ is relatively new, nanoparticles (NPs) have always existed in the environment. These range from inorganic nanoparticles produced by atmospheric phenomena, such as volcanos or fires, to nano-organic compounds like proteins and viruses, etc., produced by biological activity [1, 2]. However, real progress in this field was not possible until the development of new tools and techniques that allowed both the controlled synthesis and characterisation of nanoparticles.


In 1938 the first transmission electron microscope (TEM) was launched onto the market and, since then, electron microscopes have continued to develop and current scanning electron microscopes (SEMs) and TEMs are not only used to take images of nanoparticles and characterize them in terms of size and shape, but they also can offer information about the exact atomic structure and elemental composition using associated techniques such as energy-dispersive X-Ray spectroscopy (EDX) and electron energy loss spectroscopy (EELS).

In addition to the creation of imaging and analytical tools, another key point for the development of ‘nanoscience and nanotechnology’ was the discovery of so-called quantum size effects [3]. It was found that nanoscale particles had different properties from bulk particles: with both optical and electronic properties dependent on size and shape. This discovery revolutionized the way the world saw NPs and they started to be used in many applications. Material properties could be changed and often improved by decreasing the particle size; when the size is reduced to the nanoscale, the surface-area, the surface hardness, the electronic bandgap, the electronic properties, chemical properties and the magnetic properties of NPs can all be drastically altered. In addition, NPs can be doped with other elements and molecules to change their surface properties. By attaching a group of ligands to their surface, NPs can be functionalized with complex organic molecules in order to exert a property or group of properties corresponding to this functional group.

Traditionally, chemistry has used organic or inorganic compounds to create new substances or materials which are able to satisfy a particular requirement by providing the substance or material with a specific property. In many cases, synthesis processes are expensive and are not suitable for industrial applications because of a high cost-price ratio. Reactants are too expensive, the cost to purify the products is too high, and the method used is too complex (e.g. high pressures and temperature needed). In this way, processes, projects and scientific development are closely tied to economic profitability. The use of nanoparticles offers a convenient and elegant solution to this problem. They are able to supply a substance or material with a specific property not easily achievable by common means at a reasonable price. Industry does not need to invest in the creation of new substances and materials from scratch, which would be expensive. Instead, they can opt for the modification of existing products to achieve new and improved properties and functions. In this way, thanks to industry, the use of nanoparticles has advanced to what we currently know as nanoscience and, more specifically, nanotechnology.

Currently, nanoparticles surround us on a daily basis, not necessarily with our explicit knowledge; for instance, they are present in cosmetic products. They are used in a wide variety of industrial applications. They are used as food stabilisers and as antimicrobial agents and slowly they are being used for medical purposes. Initially, nanoparticles in health care were used to study sustained drug release in vaccines [4] and now, they are being used in cancer therapy [5]. This all implies that the potential risk of exposure to NPs is higher than it was some years ago. Nanoparticle exposure has been related to injury or different biological responses [6]. The highest risk of exposure to nanoparticles arises in the workplace. It is generally produced from hand to mouth contact or inhalation among industry workers, engineers and scientists [7].

Nanoparticles can be released into the environment as well. For example, from industrial waste [7] or from the combustion of industrial products which release NPs to the air [8]. At the same time, many studies are considering nanoparticles for environmental remediation [9]. Nevertheless, even if the chemical and



physical characteristics of the NPs are well known, there is little knowledge of how the NPs behaves once released into the environment and the associated risk this implies.

In addition to the many biomedical applications of nanoparticles, considering the potential exposure of both the population and environment to nanoparticles, an understanding of nanoparticulate behaviour and activity is essential. Not only to prevent their damaging effects, but also to create new and safer nanomaterials.

Cerium dioxide (ceria, CeO_2) nanoparticles are currently of considerable interest. Their distinctive chemical behaviour makes them of use in both industrial and biological applications. Ceria at the nanoscale forms stable particles that are able to change between cerium oxidation state (IV) and (III) by eliminating or storing oxygen from within its structure. This property makes nano-ceria have an important oxygen storage capacity.

CeO_2 NPs are used as a three-way catalyst in vehicle exhaust systems to reduce contaminant gases. More recently, they have been used for biological purposes. The high oxygen storage capacity appears to control reactive oxygen species (ROS) and reduce oxidative stress (OS). ROS and reactive nitrogen species (RNS) are produced as a by-product of O_2 metabolism. Under conditions where OS is promoted by, for example, increasing the concentration of H_2O_2 , they can decompose membrane lipids and other structures causing even cell death. However, the potential toxic effects of nano-ceria remain unclear, with many controversial reports about the biological behaviour of cerium (IV) oxide NPs.

Classic toxicity tests analyse the dose-response relationship between a chemical and cell culture or organism. However, cells are complex systems and it is often extremely difficult to determine the leading cause of toxicity. Current toxicity tests are not capable of determining the exact cause and type of the interaction between a cell and a particular type of nanoparticle. In comparison, the model electrochemical technique described and used in this research is, in principle,

capable of providing information about the interaction between nanoparticles and phospholipids, which could potentially lead to toxicity.

This current study uses a biosensor based on rapid cyclic voltammetry (RCV) [10, 11] to measure the membrane activity of CeO₂ NPs. The electrochemical sensing device (ESD) consists of a mercury-coated platinum electrode (Hg/Pt) upon which phospholipids can be deposited. Deposited phospholipids on the Hg/Pt electrode produce a voltammogram as a function of an applied potential which exhibit current peaks characteristic of the type of phospholipid. When NPs interact with the phospholipids, changes in the voltammogram are produced which are indicative of the type of interaction [12].

This thesis is structured into seven chapters. The first and second chapters provide a review of the topic addressed in this thesis. Chapter 3 corresponds to a review of the synthesis methods and characterisation techniques for the NPs produced in the following chapter (Chapter 4). Chapter 5 provides an overview of the RCV technique and in Chapter 6 the stability of different lipids on the Hg/Pt electrode is analysed. Finally, in chapter 7, the interaction of CeO₂ NPs with the model membrane is studied in detail.

The principal aim of this thesis is to explore the interaction behaviour of CeO₂ NPs with bio-membranes, using a biosensor able to mimic a model cell membrane. The interaction between phospholipids and the CeO₂ nanoparticles are analysed in order to clarify the mechanisms in detail. The following objectives are investigated:

- A. Synthesis of coated and un-coated CeO₂ NPs using different methods.
 - a.1. Nanoparticles with different shape and size are synthesized using both wet chemical and hydrothermal methods. NP activity depends primarily on particle size, shape and surface characteristics. Commercial NPs often present different characteristics (shape and size) than those provided in their specifications, in addition, coatings, stabilisers or reactants from poor cleaning processes can also be

present. For this reason, the synthesis of NPs is the best option for controlling NPs characteristics.

a.2. CeO₂ NP surface modification. To improve the colloidal stability of NP dispersions, coatings or stabilisers are commonly employed. So as to mimic real-case scenarios, the activity of coated-CeO₂ NPs will be analysed.

a.3. Characterisation of the NPs are undertaken using TEM, SAED, EDX, XRD, DLS and Zeta-Potential measurements.

B. Investigation of the interaction of CeO₂ NPs with phospholipid monolayers using RCV.

b.1. Investigation of the stability of different phospholipids on the Hg/Pt electrode. Cell membranes are complex matrixes formed from a combination of proteins and phospholipids with different chemical characteristics. For this reason, the interaction of CeO₂ NPs with different phospholipids is investigated. However, first, the stability of the phospholipids on the Hg/Pt must be evaluated to avoid false-positive results.

b.2. Investigation of the interaction between CeO₂ NPs and different phospholipids (DOPE, DOPA, DOPG, DOPS and DOPC)

b.3. Investigation of the effect of the synthesis reactants or possible contaminants could have on the interaction between CeO₂ NPs and phospholipid monolayers of DOPC.

b.4. Investigation of the effect pH has on the interaction between CeO₂ NPs and phospholipid monolayers of DOPC.

b.5. Investigation of the effect the dispersion media has on the interaction between CeO₂ NPs and phospholipid monolayers of DOPC.

b.6. Investigation of the role Ce³⁺ plays in terms of the interaction of CeO₂ NPs with the model phospholipid membranes.

CHAPTER 2. LANTHANIDES NANOPARTICLES: PROPERTIES AND APPLICATIONS

2.1 Nanoparticles

A nanoparticle (NP) can be defined as a particulate material with varying composition and structure that ranges in dimension up to 100 nm. A NP dispersion is a subcategory of colloids. Colloids size ranges up to 1000 nm. There are 1D, 2D and 3D nanomaterials (NMs) depending on the number of dimensions which are measured in the nanoscale [13].

A colloidal system (also called a colloidal suspension or colloidal dispersion) is a two-phase system which consists of a dispersed medium in a dispersion media. They can consist of a combination of either gas, liquid or solid [14, 15]. For example, solid particles in a liquid are referred to as dispersions, solid particles in a gas are called aerosols, liquid in liquid colloidal systems are commonly known as emulsions, etc. However, gas in gas colloidal systems do not exist.

Dispersions have different origins. They can naturally occur [1, 2, 16], have an unintended anthropogenic origin (for example, NPs formed from industrial processes) [8, 17] or be synthesised for different purposes [18]. This last group of NPs are commonly known as engineered nanoparticles (ENPs). In addition, NPs can be inorganic or organic.

NPs are complex materials and can often be formed from two or three layers of different chemical composition or structure:

- A **surface layer** - the outer part of the NP, which is in contact with the medium.
- A **shell** which may have a different chemical composition to **the core** of the NP itself.

The NP surface

NPs are often functionalised with surfactants, polymers, small molecules or ions to increase stability against agglomeration which can be achieved via either electrostatic (i.e. charge) or steric (i.e. long chain molecules) stabilisation. The strength of the interaction between the coating and the NP depends on the chemical structure and composition of both. Coatings with specific functional groups such as thiols, carboxylates, phosphines or amines can covalently bound to specific sites on the NP surface. For example, long-chain surfactants such as polyethene glycol (PEG) or polyvinylpyrrolidone (PVP), can form covalent bonds with metal NPs and coat and stabilise NPs [19, 20]. The use of PEG or PVP to synthesise PVP-Au NPs [21], PVP-Ag NPs [22], PVP-Cu NPs [23], is well known. NPs with a charged surface can be stabilised by ions attached to the NPs surface by electrostatic interactions [24, 25]. PEGylation is used in pharmacy with different objectives [25]. Recently, PEG has been used to coat the NPs surface by forming covalent bonds which improve the stability of the NP dispersion [26].

NPs can also stabilise by adding substances that adsorb into the NPs surface without creating a chemical bond with it. Citric acid is an excellent example of this kind of compounds. Citric acid usually adsorbs in the NPs surface and stabilise them by electrostatic repulsion [27]. For instance; citric acid is used to synthesise citrate stabilised Au NPs [28], citrate stabilised Ag NPs [29] or citrate-Fe NPs [30].

2.1.1 Chemical properties of the nanoparticles and NPs activity

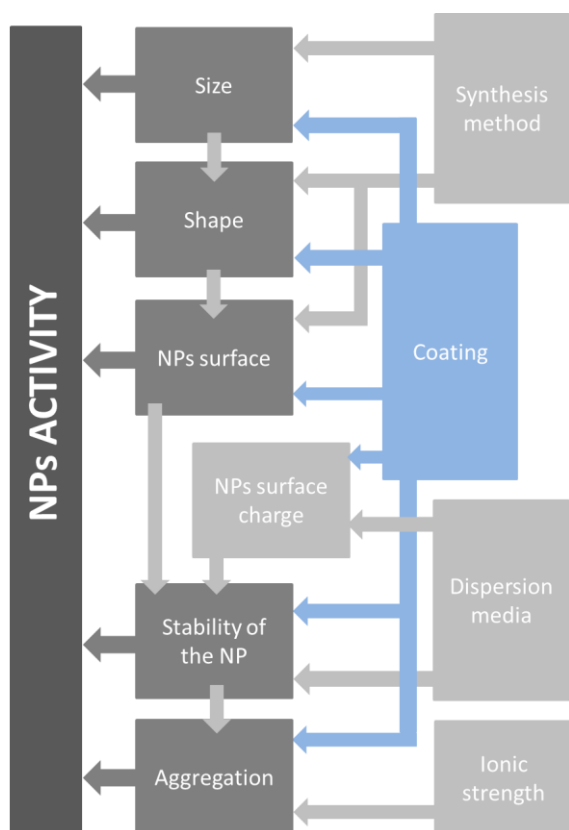



Figure 2.1 Diagram showing the different factors governing NP activity in a dispersion. Arrows show the direction of effect.

The properties of the NPs are very much related to size. Because of the small size, NPs have a high surface area to volume ratio, which provides a large proportion of surface atoms. For this reason, NPs can have different properties to their bulk materials. As the size decreases, the energy associated with the surface increases, which can affect the chemical, physical, thermal, optical, electrical and magnetic properties [31]. Due to the large surface area in the NP, the chemical characteristics of the

surface are of vital importance and will affect the way the NPs interact with their surroundings.

NPs in dispersion are complex systems. Their chemical behaviour depends on their size, shape and surface characteristics. However, other factors, such as the stability of the NPs and their aggregation, also affects their chemical and biochemical activity. Again, as a result of the large surface area, NPs can dissolve in a particular medium. Some reports suggest Ag NPs can dissolve once internalised in cells generating OS [32] [33]. Nevertheless, other reports relate toxicity as a direct effect of the Ag NPs presence [34]. Additionally, aggregated NPs do not behave in the same manner as their counterpart dispersed NPs. Since aggregated NPs do not have all their surface in contact with the medium, the surface area to volume ratio is correspondingly smaller, which often results in a change in the activity.



In addition, other factors can indirectly affect NP activity. The synthesis method directly affects the particle size, shape and nanoparticle surface chemistry. The dispersion media affects both the surface charge and the stability of the NPs. The ionic strength of the dispersion directly affects aggregation. The use of a coating in the synthesis of NPs can change the chemical characteristics of the surface affecting the stability of the NPs and the aggregation and the activity.

In conclusion, there are many interdependent factors that affect NP activity and, for this reason, the study of NP activity is challenging.

2.1.2 Industrial and biological application of nanoparticles


NPs are tremendously common. NPs can be naturally occurring, have an anthropogenic origin or can be incidental. They have been used for hundreds of years without necessarily the knowledge that they were, indeed, nanoscale. Nanoparticles have different behaviour to their bulk materials and, for this reason, they are used as additives to enhance properties or to provide new functions and properties to materials.

Chemically inert nanoparticles have been used since ancient times as pigments. For example, unconsciously, copper was added to glass to obtain a red colour thousands of years ago [35].

Nowadays, nanoparticles are used in a wide range of applications. TiO₂ NPs are used to reduce UV absorption. TiO₂ has a high refractive index ($n=2.6$) and, for this reason, it is commonly used as a whitener in paints. Under 50nm, the optical properties of TiO₂ change, and it becomes transparent but its refractive index remains the same. For this reason, TiO₂ NPs have been used in UV protection creams [36]. Additionally, TiO₂ NPs have been used in solar cells to improve photovoltaic performance [37].

NPs have an active surface because of their large surface area to volume ratio and, for this reason, NPs are also commonly used in heterogeneous catalysis [38] to improve the efficiency of chemical processes. The catalytic properties of NPs are both size and surface dependant. Smaller NPs have stronger catalytic properties which are dependant on the characteristics of its surface. NPs can play a role in many catalytic reactions such as hydrogenations [39], oxidations [40] and cross-coupling reactions [41].

NPs are also used as sensors and biosensors [42]. They can be used to immobilise biomolecules. For example, Au NPs can immobilise proteins [43, 44] and enzymes [45] on their surface. [45] created enzyme electrodes which retain the enzymatic activity by using electrodeposition. NPs can also be used to catalyse a reaction with a sensing purpose. For example, to create a sensor able to detect dopamine in ascorbic acid. Au NPs in ascorbic acid decreased the



oxidation overpotential of the acid, which allowed separation of the oxidation potentials of ascorbic acid and dopamine [46]. In addition, NPs can be used to enhance the electron transfer process. NPs can be used to facilitate the electrical connection between proteins [47] or enzymes [48] with electrodes for sensing. NPs can be used to label other biomolecules: Au NPs [49] or ZnS NPs, CdS NPs and PbS NPs [50] being used to analyse the concentration of the molecule they are linked to.

NPs are also used in a wide range of applications in biomedicine and pharmacy. For example, NPs are used in drug delivery [51] and in cancer therapy and diagnosis. For example, Au NPs are used in photothermal [52, 53] and radiofrequency [53] therapy. Au NPs are heated up by using light or alternating current to destroy tumours. Additionally, they are used because of their antimicrobial activity [54].


2.2 Lanthanides and lanthanide nanoparticles

Both the physical and chemical properties of substances are, to a large extent, determined by their valence electron configuration. In this case, the lanthanide group, also called the Rare Earth elements, are formed by fifteen elements that go from lanthanum with atomic number 57 to lutetium with atomic number 71.

The electronic configuration of lanthanum (57), the first of the lanthanides, is $[\text{Xe}] 6s^2 5d^1$. The addition of an additional proton renders the 4f orbitals more stable and penetrating than 5d orbitals so that the electronic configuration for cerium (atomic number 58 atom) is $[\text{Xe}] 4f^1 5d^1 6s^2$. Following the period, from Nd to Eu the configuration is $[\text{Xe}] 6s^2 4f^n$. Where 'n' is a number between 4 and 7 depending on the element. Once the f orbital has been half filled, its stability increases in such a way that the next electron is added to the 5d orbital as happens with Gd ($[\text{Xe}] 6s^2 5d^1 4f^7$). After this, the $[\text{Xe}] 6s^2 4f^n$ (n=10-14) configuration continues until the end of the period where Lu has its 4f shell completely full and its electronic configuration is $[\text{Xe}] 6s^2 5d^1 4f^{14}$.

Lanthanide 4f orbitals are filled with electrons across the period as the atomic number increases. 4f orbitals are very penetrating (they are very close to the nucleus) and have a core-like behaviour; their electrons are 'inside' the 5s and 5p orbitals. These orbitals penetrate into the 4f subshell and thus they cannot be affected by shielding. This behaviour can be translated into a radius reduction as the atomic number increases [55]. This effect, characteristic of the group, is called the lanthanide contraction. In addition, because of the large nuclear penetration of the 4f orbitals, they are stable to environmental conditions. Lanthanides are able to form strong bonds with other ligands but cannot form complexes with multiple bonds as other transition metals do.

The oxidation state three is the most stable for all the elements of the lanthanide period. When electrons are removed, increasing the ionic charge, an orbital stabilization is produced so that 4f orbitals become more penetrating towards the nucleus rather than 5d and 6s orbitals. In this way, the electrons fill 4f



orbitals first, lower in energy, and the 5d and 6s orbitals remain empty, stabilising the +3. One exception is cerium, which has 4f orbitals with higher energy and can thus lose another electron to increase stability ($\text{Ce}^{3+}=[\text{Xe}] 4f^1$, $\text{Ce}^{4+}=[\text{Xe}]$) [55].

Lanthanides have excellent luminescent properties. The lanthanides can produce sharp bands with narrow band width, which emit in the visible close to the UV region (biological region) [56]. In addition, they have large Stokes or anti-Stokes shifts, durable luminescence, low photobleaching and the absence of blinking [57]. For this reason, lanthanides are commonly used as contrast agents for imaging or as biosensors.

Eu(III) emits in the visible region, has a long luminescent lifetime and low sensitivity to quenching by singlet oxygen [58]. For this reason, Eu_2O_3 NPs are one of the most popular lanthanides for immunoassay and imaging. Eu_2O_3 NPs are used in the detection of HIV [59], are used in the fluorescence imaging of cervical carcinoma cells [60, 61] and are used in MRI imaging [62, 63].

2.3 Cerium

As mentioned before, due to its special chemical configuration with a 4f orbital lowered in energy, cerium has a peculiar behaviour different from the other elements in its period. Cerium can exhibit a change in valence state between two oxidation states (Ce^{3+} and Ce^{4+}).

Trivalent cerium has a non-bonding electron in its valence layer. Its behaviour is similar to the other lanthanide elements. Nevertheless, when cerium has an oxidation state +4, an isostructural volume collapse is produced due to the elimination of the last valence electron. Ce^{4+} bonds are formed by the hybridisation of 4f orbitals with the orbitals of the ligand as happens with oxygen orbitals in CeO_2 . For this reason, cerium (IV) could be described as a group 4 element [55]. Titanium, zirconium and hafnium belong to this group while Ce^{3+} can be described as a lanthanide.

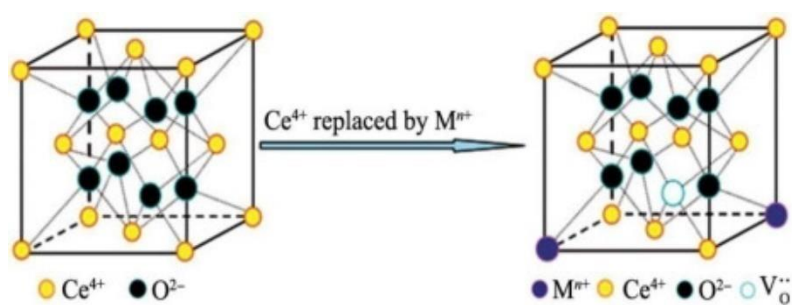


Figure 2. 2: CeO_2 fluorite structure and oxygen vacancy formation during a doping with a metal M^{n+} process [62]

Cerium (IV) oxide, commonly called ceria, usually crystallizes with a fluorite structure ($\text{Fm}\bar{3}\text{m}$) as shown in Figure 2. 2. It is a face centred cubic structure with Ce atoms at vertexes and faces of a cube and oxygen ions occupying tetrahedral sites inside the structure. Cerium (IV) ions have coordination number eight, while oxygen anions have coordination number four [64, 65]. There are 4 Ce atoms and 8 O atoms per unit cell. Bulk Ceria has high thermal and chemical stability. Nevertheless, when the size decreases, oxygen vacancies are generated in the fluorite structure leading to CeO_{2-x} assembly [66]. Cerium (III) oxide (Ce_2O_3), unlike ceria, crystallises with a hexagonal structure.

CeO₂ is a good oxidising agent. The coordination sphere around cerium affects its redox behaviour [67]. Ce³⁺ is able to form complexes with certain anions and, for this reason, the standard potential of reduction (^oE) for the pair Ce⁴⁺/Ce³⁺ is dependent on the anion present [68]. ^oE (Ce⁴⁺/Ce³⁺) is 1.74V in SO₄²⁻ [68], 1.3V in acetonitrile [69], 1.418V in glacial acetic acid [69] and 1.47V in HCl [70], 1.61V in nitric acid solution [71]. The following figure shows a Pourbaix diagram for the Ce(III/IV)-H₂O-H₂O₂ system [72]. It relates the potential with respect to the standard hydrogen electrode versus pH for a certain system. As observed, at acidic pH, the formation of Ce³⁺ is preferred to Ce⁴⁺.

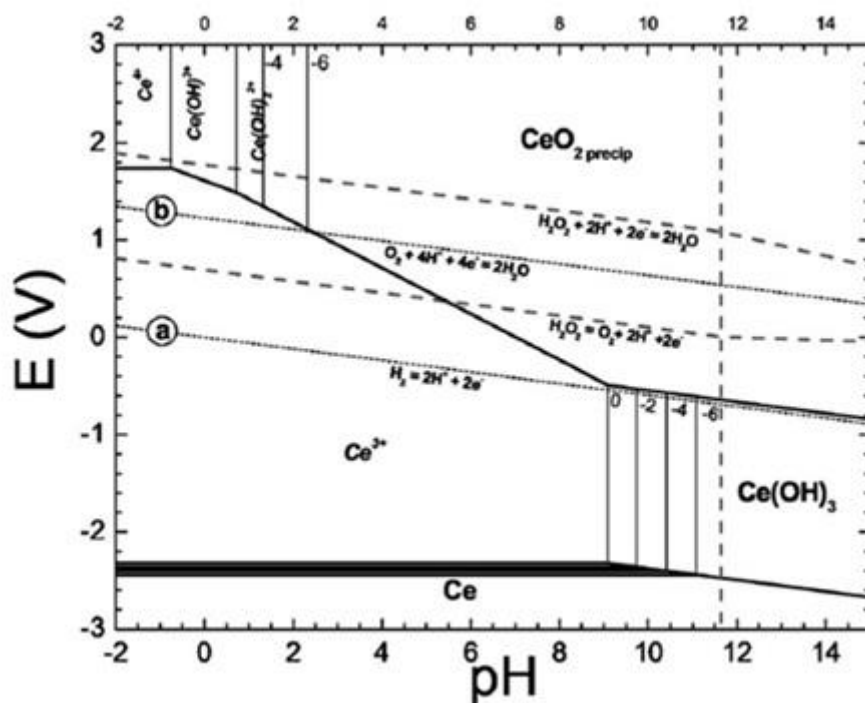


Figure 2. 3: Pourbaix diagram for the Ce(III)/(IV)-H₂O-H₂O₂ systems. Copied from [61]

2.3.1 Ceria at the nanoscale

A decrease in particle size to the nano-scale imposes a very large surface area/volume ratio. This produces an increase in free energy and stress that generate structural irregularities [73] which could act as active sites for chemical reactions [64]. In this way, CeO₂ NPs are expected to possess a bigger percentage of Ce³⁺ at the surface relative to bulk ceria [74]. The reduction of Ce⁴⁺ to Ce³⁺ causes the creation of oxygen vacancies in the fluorite structure to maintain the charge neutrality and reduce the structural tension of the cell [75]. When oxygen is eliminated from the structure, it generates an increase in entropy that produces a decrease in Gibbs free energy providing stability to the structure [64]. Oxygen vacancy generation provides new surface structures (irregularities) that along with corners and edges offers active sites where different chemical reactions can take place. In addition, at very low particle sizes, quantum confinement must be considered. The electron mobility becomes impeded, resulting in a change of the energy levels and in consequence, a change in electrical and optical properties.

One of the most interesting properties of cerium (IV) oxide is the relatively easy transformation between Ce⁴⁺ and Ce³⁺ oxidation states [76, 77]. Bulk ceria can be reduced at high temperatures, creating non-stoichiometric oxides with oxygen deficiencies (CeO_{2-x}), and re-oxidized even at room temperature [74] ($E^\circ(\text{Ce}^{4+}/\text{Ce}^{3+}) = 1.61\text{V}$). Ceria can act as an oxygen scavenger retaining oxygen and losing it when cerium is reduced. In addition, reduced ceria can change between different phases [78-80] although it can still retain the fluorite structure with 25% of the lattice oxygen eliminated [80].

The chemical activity of Ceria nanoparticles depends on the characteristics of the surface. In this way, both experimental and computational studies have been carried out to understand better its behaviour. However, almost all studies are based on ideal bulk-like structures, which is the reason why the results cannot always be extrapolated to the nanoscale. The initial studies revolved around stoichiometric ({111}, {110} and {310}) and non-stoichiometric ({100} and {211}) ideal surfaces. Sayle [81] and Conesa [82] related the oxygen vacancy

formation to the surface structure in different planes and concluded that structures with {1 1 1} planes were more stable. Sayle concluded that oxygen vacancy occurred preferentially at the surface rather than in the bulk. This assumption was questioned by Skorodumova [83] who found that oxygen deficiencies were located in the bulk. In addition, they showed that conversion between Ce_2O_3 and CeO_2 was related with the electro-delocalization from 5p state (oxygen) to 4f state (cerium). They proved that additional electrons, arising when an oxygen is eliminated from the structure, were located in the 4f orbitals of the four nearest neighbour cerium atoms to the oxygen vacancy. This associated oxygen vacancy formation with the Ce^{3+} presence.

Oxygen vacancies were found to be dependent on particle size. In this way, it was found that nanoparticles relaxed at {1 1 1} planes [84, 85]. In addition, oxygen vacancy formation was more favourable to occur in small particles and clusters rather than in bulk ceria. A bigger concentration of Ce^{3+} can be found in nanoparticles, affecting its reactivity and its use in industry [86].

A more recent study has considered octahedral {1 1 1} surfaces with oxygen vacancies at the corners and edges [74]. They found:

1. Oxygen with low coordination numbers are easier to eliminate;
2. Ce^{4+} atoms favour highly coordinated bulk-like sites while Ce^{3+} tend to occupy corners and edges;
3. As the particle size decreases, is more favourable to form oxygen vacancies and subsequently, the $\text{Ce}^{3+}/\text{Ce}^{4+}$ ratio increases.

2.3.2 Synthesis of ceria nanoparticles

There exist two pathways for NP synthesis: top-down and bottom-up. The first pathway uses mechanical methods as for example, milling, to reduce the size of the NPs to the nano-scale. It uses mechanical equipment to produce large volumes of nanomaterials (NMs). Unlike top-down methods, bottom-up methods cannot generate big volumes of NPs. However, they are used when the physico-chemical characteristic of the NPs are important, and this is achieved by controlled synthesis of NMs using reactants from which the NPs are synthesised by chemical reactions. In this case, the chemical product depends on the synthesis reaction and is determined by the synthesis conditions (e.g. temperature and pH). Bottom-up methods are ideal to synthesise small amounts of NPs. Nevertheless, the physical thus chemical characteristics of the NPs can change while scaling up the synthesis because the reaction can vary.

The following section consists of a review of bottom-up synthesis methods for CeO₂ NPs. A summary table can be found in **Error! Reference source not found.**

Precipitation methods use a salt or an oxide of the metal of interest, an oxidiser and a stabiliser that can sometimes, play the role of the redox agent to form colloids in a continuous phase. The reactants are dissolved and interact to form NPs with different characteristics depending on the synthesis conditions (e.g. reactant concentration, pH, temperature, media, etc.). Many use a cerium (III) salt and a base. The use of a base can change the redox potential of both oxidising and reducing agents and can hamper or favour the reaction. Examples of the synthesis of CeO₂ NPs using precipitation methods can be found in [77, 87-89].

Hydrothermal and solvothermal methods work similarly but often use different solvent systems and high temperatures and pressures to increase the solubility of substances. The reaction flask contains a salt of the element of interest, the solvent and other species known as mineralizers that are added to change the solution properties. They can be basic, acidic, oxidizers, reducers,

complexants, etc. [90]. In addition, at temperatures $>600^{\circ}\text{C}$, water is strongly dissociated and its amphoteric behaviour is increased. Water could act as a reducing agent (producing O_2) provoking changes in the oxidation state of metals [90]). Some examples of nano-Ceria particle synthesis using this method are given in [91-93]. In general, they use cerium nitrate as a precursor but change the mineralizer agent to increase pH (ammonium nitrate, sodium hydroxide) or the oxidant (H_2O_2) to vary redox conditions

Sol-Gel processes use metal chlorides or alkoxides, which are hydrolysed to form a colloidal dispersion that is then polymerised to produce a gel. Gels are colloidal systems where the continuous phase is solid and the disperse phase is liquid. The solvent is trapped in the macromolecular net of particles so that it gives consistency to the gel. NPs are obtained when the gel is dehydrated [90]. A study that uses this technique to synthesise CeO_2 NPs is [94]. They use cerium (III) nitrate, europium (III) nitrate, polyethylene glycol (PEG) and citric acid to synthesise Eu^{3+} doped CeO_2 .

Micro-emulsions are a type of transparent colloidal solutions where both hydrophilic and hydrophobic solutions can co-exist in equilibrium. They are formed by surfactants that self-organise to form micelles or inverse micelles, able to contain a liquid that would not be miscible with the solvent. In the microemulsion method, reactants are trapped inside nanodroplets that interact with each other and produce and interchange substances. The nucleation and growth processes of NPs take place inside the droplet. An example of CeO_2 NPs synthesis using micro-emulsions is [95].

Sonochemical methods use ultrasound to improve the reaction speed, reagents or catalyst reactivity and control the precipitation process in order to optimize particle shape and size. When ultrasound is applied, molecular vibrations are produced and thus a rise in temperature. Reference [96] used this method to synthesise CeO_2 NPs; a mix of cerium (III) nitrate and azodicarbonamide was ultrasonically processed for 3h at room temperature with the solution temperature rising up to 80°C during the process.

Other bottom-up methods employ gas-phase synthesis. They produce NP nucleation in the gas phase by supersaturating a vapour using either physical or chemical methods. The first one changes the environmental conditions by cooling a monomer or transferring heat to the surroundings. The second one uses decomposition reactions catalysed by temperature. High purity particles are produced since there are no secondary species involved:

Spray pyrolysis methods use small drops that contain the reactant which is atomised and passed through a flame causing solvent evaporation and supersaturation that causes the precipitation of the oxide. Reference [97] an example of ceria NPs synthesis using Ce(III) 2-ethylhexanoate in xylene as precursors.

Combustion methods consist of heating precursors at high temperatures to initiate a reaction and produce an oxide of the metal of interest. Reference [98] uses cerium (III) nitrate in nitric acid. Reference [99] uses thermal decomposition of a cerium salt, oleic acid, oleyamine and 1-octadecene.

This thesis uses precipitation and hydrothermal methods to synthesise CeO₂ NPs. Contrary to spray pyrolysis and combustion methods, hydrothermal and precipitation methods do not need expensive synthesis equipment and can be used at low temperature. A hydrothermal autoclave reactor is used in hydrothermal methods but the synthesis temperature is usually below 300°C, which decreases the energetic costs compared with combustion methods. In addition, precipitation and hydrothermal methods use commoner and a lower amount of reactants compared to Sol-Gel, microemulsion or sonochemical methods. For this reason, the probability of formation of secondary species during the synthesis is lower. In addition, hydrothermal and precipitation methods allow the synthesis of well defined structures by varying experimental conditions.

Table 2. 1: Summary of CeO₂ NPs synthesis methods

Method	Reactants	Sphape	Size (nm)	Reference
Precipitation	Ce(NO ₃) ₃ + NH ₄ OH	spheres	5-8	89
	Ce(NO ₃) ₃ + Eu(NO ₃) ₃ + NH ₄ OH	polymorphous	5-30	87
	Ce(NO ₃) ₃ + NH ₄	spheres	5	88
Hydrothermal	Ce(NO ₃) ₃ + H ₂ O ₂ + NH ₄ OH	spheres	7-9	90
	Ce(NO ₃) ₃ + NH ₄ OH+NaOH	spheres	8-10	91
	Ce(NO ₃) ₃ + NaOH	cubes and needles	N/A	93
Sol-Gel	Ce(NO ₃) ₃ + Eu(NO ₃) ₃ + Citric acid + PEG	N/A	23-28	94
Microemulsion	Cerium(III) 2-ethylhexanoate + surfactant + hexane	spheres	3	95
Sonochemical	Ce(NO ₃) ₃ + H ₂ NCON==NCONH ₂	spheres	2-5	96
Spray Pyrolysis	Ce(III) 2-ethylhexanoate + xylene	polymorphous	8	97
Combustion	Ce(NO ₃) ₃ + nitric acid	polymorphous	24-37	98
	Oleyamine + oleic acid + Ce(CH ₃ CO ₂) ₃	Rods and plates	N/A	97


2.3.3 Applications of nano-ceria

As already mentioned, one of the most important properties of CeO₂ NPs is their oxygen storage capacity. Industries have exploited this property and have used ceria as an oxygen buffer or as catalyser in redox reactions. The commonly accepted theory is based on a four step mechanism [74] which is valid for ideal surface structures:

1. Reduction of Ce⁴⁺ to Ce³⁺ and formation of lattice oxygen vacancies: oxygen loss and cerium reduction can be considered part of the same process. In a well-defined structured with a fixed charge, the elimination of an oxygen atom for every two Ce³⁺ is necessary in order to maintain charge neutrality;
2. Ce³⁺ migration from the bulk to the surface. This supposes only Ce³⁺ with Oxygen vacancies sites are active sites for chemical reactions and thus stable ceria does not present Ce³⁺ on its surface. This assumption is well supported for ideal surface structures;
3. Oxygen adsorption by Ce³⁺;
4. Reaction of adsorbed molecules with reactants to form the reaction product and oxidation of Ce³⁺ to regenerate the catalyst surface.

Ceria has been used as a three-way catalysts (TWCs) help to transform hydrocarbons, carbon monoxide and nitrogen oxides toxic fumes, produced by automobiles and other means of transport, to less dangerous gases such as H₂O, CO₂ and N₂ [30]. TWCs are made of Rhodium or Platinum and CeO₂ as an oxygen scavenger. The use of CeO₂ presupposes an advantage against the use of other compounds as it can auto-regenerate taking advantage of its relatively easy transformation between Ce⁴⁺/Ce³⁺ under specific conditions [17] In addition, both storage capacity properties and thermal stability can be improved by coating the particles with other nanoparticles oxides such as ZrO₂ [30].

Ceria is also used as a ceramic electrolyte in solid oxide fuel cells (SOFCs) [31]. This type of cell oxidizes fuel to produce electricity. Doped ZnO or CaO particles



with CeO₂ exhibit good UV-absorption; this is why it has been used in optical films [32]. In addition, ceria has been used as a polishing material [33, 34].

In the last few years, ceria has expanded into the medical field. CeO₂ NPs are used as reactive oxygen and nitrogen scavengers to modulate oxidative stress and cause or reduce cytotoxicity. It has been used as an anti-inflammatory agent [35], in cancer therapy [8], as an anti-obesity drug [36], or to repair bones and to influence neuronal growth [37].

2.3.4 Toxicity studies of nano-ceria

Many properties can be enhanced by reducing particle size to the nano-scale owing to their large surface volume/ratio providing greater surface activity. However, there is little information about their toxicity or environmental impact and it is necessary to create databases and protocols to regulate safe use of these materials.

There are many contradictory reports about nano-ceria toxicity. However, a common theme is that the damage or protective effect of CeO₂ NPs depends on the ability to produce or control oxidative stress (OS), respectively. OS is produced when the reactive oxygen species (ROS) and reactive nitrogen species (RNS) on the cell cannot be controlled and free radicals are generated. These substances are very oxidising and can produce cell necrosis or apoptosis. Free radicals are produced as part of the electron transport chain in mitochondria. Usually, electrons produced by the oxidation of NADH to NAD⁺ (nicotinamide adenine dinucleotide), pass through the electron chain to an electron-acceptor oxygen that is reduced to water. Meanwhile, thanks to the electron transfer process, protons cross the membrane and produce the transformation of ADP (adenosine diphosphate) into ATP (adenosine triphosphate) by the ATP synthase. In oxygen-deficient situations, there is insufficient oxygen molecules to accept the electrons resulting from the NADH and they accumulate in the electron chain and ultimately are transposed to other reactive molecules that can accept them producing 'reactive oxygen species'.

ROS or RNS are produced as a sub-product of O₂ metabolism. In regular conditions, they can help in signal transduction, but in abnormal conditions, these highly reactive species can decompose membrane lipids or other substances even causing cell death. The most important species are: superoxide radicals, hydroxyl radicals, hydrogen peroxide, lipid radicals, nitric oxide and peroxyxynitrite.

In order to control reactive species, the body contains a series of antioxidant substances that maintain the concentration of ROS or RNS. The superoxide

dismutase enzyme (SOD) transform superoxide radicals to hydrogen peroxide. However, H₂O₂ is an oxidising agent that can decompose to form highly reactive hydroxyl radicals able to cause OS. Thereby, the catalase enzyme works with the SOD and decomposes hydrogen peroxide to oxygen and water. Together, SOD and catalase can degrade superoxide radicals to non-dangerous molecules and they are the principal defence mechanism against oxidative stress. CeO₂ NPs, as well as the previously mentioned enzymes, seem to have an antioxidant effect. Nano ceria takes advantage of its oxygen scavenging capacity to capture superoxide anions, hydrogen peroxide and peroxy nitrite and reduce oxidative stress [38, 39].

Several studies have been carried out to demonstrate the multi-enzyme mimetic properties of nano-ceria. In general, the studies are based on measuring cell growth in the presence and absence of CeO₂ NPs under oxidative stress. Many articles confirm a SOD behaviour and relate the chemical activity with surface chemical composition. CeO₂ NPs with a higher Ce³⁺/Ce⁴⁺ ratio have a higher SOD mimetic activity [20, 38-41]. In addition, nano-Ceria has mimetic catalase activity which seems to be inversely proportional to the Ce³⁺/Ce⁴⁺ ratio [42].

However, the presence of Ce(III) in CeO₂ NPs surface is still under discussion. Oxygen free sites and thus cerium in oxidation state (III) could be formed due to the experimental conditions when measurement [43] (e.g. under high vacuum conditions in electron microscopes or in surface spectroscopic techniques such as X-ray photoelectron spectroscopy (XPS)). In addition, the mechanism by which nano-ceria scavenges both ROS and RNS is still unknown and many processes, based on the enzymes that they mimic, have been proposed [40].

However, there are also many other articles that suggest the toxic properties of CeO₂ NPs. In contrary to the previously mentioned articles, they assert that nano-ceria is actually able to exert cytotoxicity. When nano-ceria is internalised by the cell cytotoxicity can be caused due to lysosomal injury [44, 45] or an increase of the oxidative stress [46].


In 2006 [8], the relationship between exposure time and Ceria NPs dose was reported. CeO₂ NPs exerted bigger cytotoxicity as the dose and exposure time increases. Park [47] studied the toxicity of different size Ceria NPs in cells; all particles showed cytotoxicity. Asati [44] reported a selective toxic behaviour of CeO₂ NPs. Positive, negative and neutral coated NPs (poly-(acrylic acid), aminated poly(acrylic acid) and dextran respectively) were exposed to different cell cultures. Once nano-ceria particles were in the cell, they were internalised at the lysosomes of cancer cells (where there is an acidic environment) showing an oxidase effect. An oxidase enzyme is able to catalyse the oxidation of O₂ to form H₂O or H₂O₂ and thus produce toxicity. However, in healthy cells, where the pH was neutral, CeO₂ NPs were located at the cytoplasm and did not show toxicity.

Other articles confirm that nano-Ceria presents both toxic and non-toxic behaviours depending on the particle structure. Pulido-Reyes studies [12] related Ce³⁺ surface ratio with pro-oxidant or anti-oxidant effects. In this way, particles with higher Ce³⁺/Ce⁴⁺ ratios presented higher toxicities. Forest [48] associated the toxic or non-toxic effect with the shape. Cubes and spheres did not present any toxicity; meanwhile rods did show a toxic effect.

The study of NPs toxicological behaviour is not an easy task. NP activity not only depends on shape, size and surface characteristics but also on particle concentration, exposure time and the medium in which they are dispersed.

The solvent media (e.g. ionic strength, pH, the presence of proteins etc.) can change aggregation by increasing or decreasing intermolecular forces between the particles and changing their activity. In addition, some substances can remain attached to the particle surface and cause toxicity. It gives false-positive results in bio-toxicity tests of NPs. The toxicity could be produced by attached substances to the particle surface instead of by the particle itself. Thus it is necessary to clean the NPs in order to avoid possible contaminant effects.

On the other hand, bio-toxicity tests are usually done in biological laboratories. NPs are usually synthesised in other places, or they are purchased from




commercial suppliers. NPs are stable under certain conditions (e.g. temperature, presence of stabilisers etc.). However, they can easily become unstable and change in size and shape, or they can even degrade with time. It is often the case that purchased nanoparticles do not have the characteristics of those that are written on their bottle labels. It is necessary to have regular access to characterization techniques such as TEM to guarantee that the particle physical characteristics remain stable. Otherwise, the toxicological results will not correspond to the particles that are measured.

2.3.5 Chemical characteristics of ceria-nanoparticles

The biological activity of nano-ceria has been related to the surface chemistry of the NPs. Nano-ceria particles have been reported to have free radical scavenging properties which in theory, are related to the $\text{Ce}^{3+}/\text{Ce}^{4+}$ ratio on the NP surface. However, the redox mechanism underlying the change of oxidation state in CeO_2 NPs is based on ideal bulk ceria systems [74] and assumes NPs behave in the same manner as bulk materials. This mechanism implies that any reduction at the NP surface self-regenerates showing a SOD and catalase mimetic activity [100]. However, reference [89] showed an absence of chemically active Ce^{3+} during nano-ceria-induced catalase mimetic activity. In addition, the study of the nano-ceria redox mechanism is usually based in abiotic systems and, for this reason, they cannot totally mimic biological conditions.

Nevertheless, there are many papers which report the presence of Ce^{3+} on the surface of ceria NPs. However, different studies have shown that the amount of $\text{Ce}^{3+}/\text{Ce}^{4+}$ ratio in the NPs is reliant on the technique used. Techniques like XPS (X-Ray photoelectron spectroscopy), EELS (electron energy loss spectroscopy) or XANES (X-ray absorption near the edge spectroscopy) can distinguish between the different oxidation states of many elements and, for this reason, they are the most typically used techniques to analyse the $\text{Ce}^{3+}/\text{Ce}^{4+}$ ratio on the surface of CeO_2 NPs [101-106]. Reference [107] showed that the amount of Ce^{3+} in the CeO_2 NPs was larger when measured using the ultra surface-sensitive technique of XPS than when it was measured by XANES. However, they reported that the amount of Ce^{3+} increased with the time that the sample was in the vacuum chamber of the XPS machine, perhaps suggesting that maybe the vacuum environment required for surface analysis was causing surface reduction. In addition, reference [108] showed that the X-Ray radiation from the XPS could lead to the reduction of the surface of bulk CeO_2 . Reference [109] studied the dose rate dependent formation of oxygen deficiencies using EELS in the STEM and showed that below a dose rate of $2.97 \times 10^5 \text{ e nm}^{-2} \text{ s}^{-1}$ there was no observable reduction of the surface cerium ions.



All these analytical techniques usually use dried NPs and do not take into account how the liquid media affects the NPs. However, reference [110] found that CeO₂ particles could undergo shifts in oxidation state once internalised in cells and that the exact localisation of the NPs, when internalised, depended on the Ce³⁺/Ce⁴⁺ ratio. From previous studies, it can be concluded that the presence of Ce³⁺ on the surface of CeO₂ NPs is dependent on the environmental conditions. Thus the presence of ultra-high vacuum or high energy radiation can induce the reduction of Ce⁴⁺ to Ce³⁺ and produce false-positive results for the determination of Ce³⁺/Ce⁴⁺ ratios. In addition, many studies show that the modification of the nano-ceria surface affects the biological response of the NPs. References [111, 112] relate the surface charge of the nanoparticles, produced by the coating (polyacrylic acid and dextran), with the NP distribution once internalised in the cell.

From another point of view, references [113, 114] report that CeO₂ NPs, despite being known as a refractory and highly insoluble material, can dissolve in acidic conditions (the stability of Ce³⁺ ion increases at acidic conditions (Figure 2. 3)). Dissolution has been proposed as the main factor for toxicity associated with other NPs, such as for example, Ag NPs [32]. For this reason, the impact of the dissolution of CeO₂ NPs in toxicity has also been analysed. Reference [115] showed that PVP coated CeO₂ NPs maintained at pH 4.0 for 24h dissolved by 40% of the initial mass; however, the ionic Ce³⁺ was not found to be the main driver of toxicity in *Daphnia magna* juveniles.

CHAPTER 3. CHARACTERISATION TECHNIQUES, MATERIALS AND SYNTHESIS METHODS

3.1 Characterisation techniques

3.1.1 Transmission electron microscopy

The first electron microscope was invented by Max Knoll and Ernest Ruska in 1931. It surpassed conventional transmission light microscopes and permitted an increase in resolution to the nano-scale. By 1944, they had increased its theoretical resolution from 10nm (in 1931) to 2nm. This was a considerable improvement on the 200nm theoretical resolution of its optical counterparts had. To do so, they did not just improve the voltage stability of the electron beam, but they also upgraded lens and vacuum systems to decrease aberrations. In this way, in 1938 the first transmission electron microscope (TEM) was launched into the market.

Since then, electron microscopes have continued to develop and nowadays, scanning electron microscopes (SEMs) and TEMs are not only used to obtain morphological information (size and shape) of the sample at atomic resolution. They also can offer information about the atomic structure or elemental composition using other devices such as an energy-dispersive X-Ray spectrometer (EDX) or an electron energy loss spectrometer (EELS) which can be connected to the SEM or TEM and provide additional information.

3.1.1.1 The design of a TEM

In general, a TEM is formed by an illumination system, where the electron gun and the condenser lenses are located, a specimen, an objective lens and a magnification system (Figure 3. 1)[116].

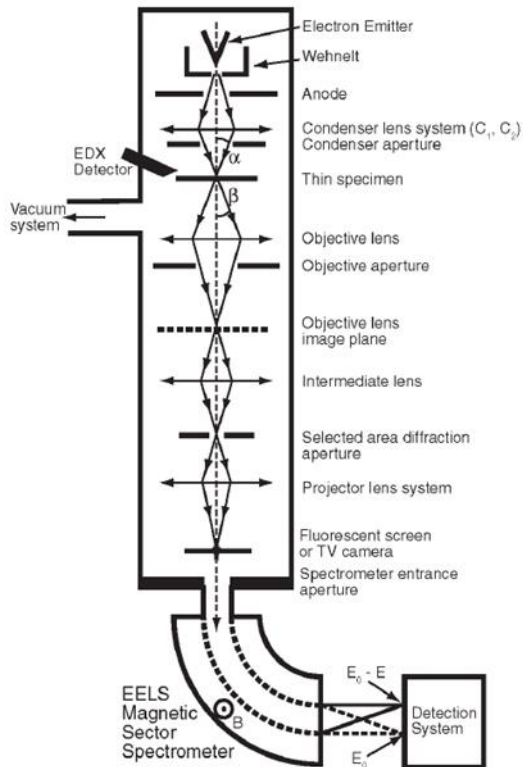


Figure 3. 1: Scheme of a TEM with an EDX and an EELS devices. Copied from [1]

The electron gun produces a high-energy beam of electrons which allows visualisation of the sample. It is composed of a source of electrons, an anode and focusing structure under vacuum. A thermionic electron gun uses heat to remove electrons from a metal filament. Then, the electrons pass through the Wehnelt cylinder, which focuses them to crossover. It directs them to the anode where they are accelerated by a difference in potential. A field emission electron gun (FEG) can operate at room temperature. It uses an

electric field to remove electrons from a metal tip. These electrons pass through a Wehnelt cylinder to a sequence of anodes that connected generate an electrostatic field, which accelerates and focuses them.

The generated electron beam passes through the condenser lenses. Their function is to control the beam diameter (C1) and the beam divergence/convergence angle (C2). Then, the beam reaches the specimen. Next, the first real image from the illuminated area of the specimen is formed by the electromagnetic objective lens that generates a magnified image in the objective lens image plane. The electron beam then passes through the intermediate lenses and projector lenses, which magnify the image, to the viewing screen and finally, to the camera.

When a TEM operates in the selected area electron diffraction (SAED) mode (as opposed to image mode), the first image (of the diffraction pattern) is created after the objective lenses in the back focal plane. At this point, in the back focal plane, an objective aperture can be inserted to limit the beam divergence. Then, the image is magnified by the intermediate lenses and pass through the selected area diffraction aperture, which is usually located in one of the projector lenses, to the viewing screen and then, to the camera.

3.1.1.2 Specimen-beam interactions

When an electron beam hits a sample, the electrons interact with the atoms of the sample in different ways as is observed in Figure 3. 2.

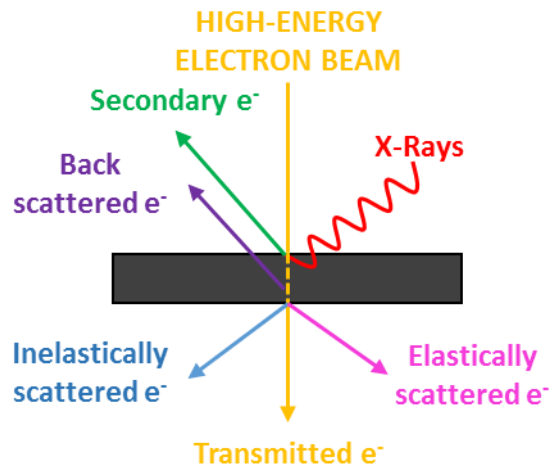


Figure 3. 2: Specimen- beam interactions

SCATTERED ELECTRONS

Elastic scattering is used to form images. It takes place when the transmitted electrons are scattered in the same direction and preserve the phase of the incident phase.

- The **coherent elastic scattering** is used to form images in bright field imaging. In this case, electrons directly interact with the electrons of the sample and diffract them, forming angles from 1° to 10° .
- **High-angle incoherent elastic scattering or backscattering** is produced when electrons are scattered at higher angles (10° - 180°). The number of back-scattered electrons is produced varies with the atomic number of the element. In this way, higher atomic number elements appear brighter than those with small atomic number. In this case, the beam of electrons directly interacts with the nucleus of the atoms to create, for example, dark field images in scanning electron microscopy (STEM).

Inelastic scattering is when the beam in contact with a solid is reflected in many directions with different phases because an energy loss is produced. There are four major mechanisms of this phenomenon:

- The **plasmon scattering** takes place in electron-solid interactions; where the incident electrons excite plasmons in the valence electrons of the solid sample.
- The **phonon scattering** takes place when an electron directly interacts with a photon and decreases its energy (increase in wavelength and decrease in frequency).
- A **single electron-excitation** produces **secondary electrons**. When a high energy incident electron ionises an electron of the sample, the incident electron loses some of its charge and changes its path while the excited electron leaves the atom.
 - o If the excited electron is excited from the valence bond of the material, it can be ejected and escape from the surface of the sample producing what it is called secondary electrons. These electrons are used to form images in scanning electron microscopy (SEM).
 - o If inner shell electrons are those which are excited and escape from the atom, X-Rays are produced. Techniques such as the energy dispersive X-Ray spectroscopy (EDX) or the electron energy loss spectroscopy (EELS) use these secondary emissions to obtain analytical information.
- Lastly, **direct radiation losses** take place when X-Rays suffer a deceleration due to the solid sample. They form the background of EDX spectra.

UN-SCATTERED ELECTRONS

When a high energy electron beam hits the sample, the beam can pass through the sample without interacting with its atoms. The produced electrons are

called transmitted electrons and are used to form images in bright field transmission electron microscopy (BFTEM). The number of transmitted electrons is inversely proportional to the thickness of the sample. In this way, the thicker the sample, the lower transmitted electrons it will produce.

3.1.1.2.1 X-Rays

When a high-energy electron beam hits a sample, it can ionise an electron in such a way it can escape from the atom. It generates a un-stable empty state that tends to be filled by an electron of a higher energy level. In order to allow the electron to change between states, energy is lost in the form of a photon, usually an X-Ray.

The photon energy released depends on the energy between the electron shells and hence the element. The photon is classified in terms of the initial electron level (E_0) which is ionised (K, L, M, etc) and the level (E_1) from which electron drops to fill the hole created by the ionisation process (Figure 3. 3).

$$E_1 - E_0 = h \cdot \nu \quad (3.1)$$

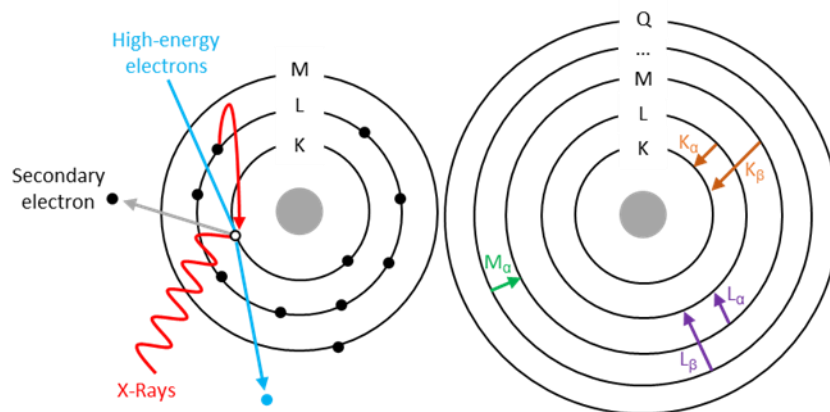


Figure 3. 3: Scheme of X-Rays production

3.1.1.3 The resolution in the TEM

A TEM uses a beam of high-energy electrons to create images with high enough resolution to distinguish between two points closely spaced and visualise a sample. The resolution depends on three related mathematical concepts factors: the Airy disks, Abbe's diffraction limit and the Raleigh criterion.

When an image of the specimen is formed, each object point is not a single point in the image; instead, it consists of a dot surrounded by concentric circles with diminishing intensity, which are known as Airy disks. When a sample is being observed under the TEM, many Airy disks are created from each point in the object. In this way, the closer two disks are from each other, the more difficult is to distinguish between them. However, if two Airy disks are in a distance greater than the Rayleigh limit (minimum resolvable detail a TEM can distinguish) from one to another, then, the two points can be distinguished and details in the sample can be observed. This is what it is known as the Rayleigh criterion.

Abbe's diffraction limit is a related concept and refers to the diffraction-limited resolution, in an optical system, if all aberrations and distortions were eliminated. It can be described in equation 3.1:

$$d = \frac{0.612 \cdot \lambda}{n \cdot \sin \alpha} = \frac{0.612 \cdot \lambda}{NA} \quad (3.2)$$

Where:

- d= resolution
- λ = wavelength
- n= index of refraction of a medium through light passes
- α = half aperture angle
- NA=numerical aperture

Basically, it states that, in order for a spacing "d" in an object to be resolved, the lens must capture the scattered (diffracted) ray from that spacing.

In addition, Louis de Broglie demonstrated that electrons have a dual character. They behave like a particle and a wave and their wavelength can be calculated according to equation 3.2.

$$\lambda = h/mv \quad (3.3)$$

Where:

- h = Planck constant= $6.63 \cdot 10^{-34}$ J·s
- v = speed
- λ = wavelength
- m = mass of an electron= $9.1 \cdot 10^{-31}$ Kg

In a TEM, electrons are accelerated by a difference of potential (V). In this way, their kinetic energy, or work needed to be done to accelerate a body of a certain mass from a resting position to a certain speed, can be described by following equation 3.3

$$E = eV = \frac{1}{2}mv^2 \quad (3.4)$$

$$v = \sqrt{\frac{2eV}{m}} \quad (3.5)$$

When equations 3.3 and 3.5 are combined, it can be observed that the use of high- energy electrons generates smaller wavelengths and hence higher resolution.

$$\lambda = \frac{h}{m\sqrt{\frac{2eV}{m}}} = \frac{h}{\sqrt{2emV}} = 1.23/\sqrt{V} \quad (\text{nm}) \quad (3.6)$$

Where:

- e = electron charge= $1.6 \cdot 10^{-19}$ C

However, in a TEM, the practical limit of resolution is determined by distortions, aberrations and how well aligned are its optical components (high numerical aperture values).

3.1.1.3.1 Imaging in the TEM

A TEM has two imaging modes. Bright field imaging (BFTEM) and Dark Field Imaging (DFTEM).

BFTEM principally utilises the un-diffracted electron beam to form an image. The contrast of the image depends on the electrons that are blocked by the selected objective aperture. It gives information about size, morphology, lattice spacing and line defects.

When an electron beam hits a sample, the electrons interact with it and are able to give information about the system. TEM uses transmitted electrons to form an image. However, the resolution of the image depends on the contrast. TEM uses different mechanisms to create contrast:

- **Mass-thickness contrast:** The quantity of transmitted electrons depends to a large extent on sample thickness. Images of the regions where the volume or atomic weight of the sample are higher (higher electron density) appear darker (more electrons are scattered) providing mass-thickness contrast. Unlike in the scanning electron microscope (SEM), the TEM needs very thin samples and sometimes, complex sample preparation processes (e.g. polishing).
- The **diffraction contrast** is produced when electrons are excluded from the image because they are scattered through the Bragg angle by diffraction gratings formed by the periodic arrangement of atoms in crystalline regions. When an electron beam hits a sample, electrons are scattered with a certain angle and can diffract out of the objective aperture producing dark zones in the image. Both thickness and diffraction contrast help to give information about particle size shape and crystallinity.
- **Phase contrast** is based on the difference in phase of electrons that are scattered from a sample. Un-diffracted electron waves and different diffracted waves all have different phase shifts and can create constructive and destructive interactions originating contrast. Waves

with constructive interactions appear bright while waves with destructive interactions appear darker. Phase contrast gives information at nanometre resolution (lattice spacing). However, to obtain phase contrast images, it is necessary to allow un-diffracted and diffracted beams to interfere; hence contrast images are taken without an objective aperture.

DFTEM imaging uses an objective aperture in the diffraction plane to exclude un-diffracted electrons in such a way that only diffracted electrons pass through and form the image. The DFTEM mode can give information about variations in crystallinity.

On the other hand, the TEM is able to provide crystallographic information using selected area diffraction (SAED). When a parallel electron beam passes through a sample, electrons are diffracted by the atomic planes following the Bragg equation and creating diffraction patterns that depend on the characteristics of the sample. The region of the sample from which the diffraction pattern is formed can be defined by the intersection of a selected area aperture in the image plane of one of the project lenses further down in the microscope column, below the objective lens. Diffraction patterns with dots are created when the sample is monocrystalline. Diffraction patterns made of rings appear when the sample is polycrystalline and diffraction patterns with diffuse rings are created when the sample is amorphous.

3.1.1.4 EDX

EDX devices can be found in SEMs and TEMs. However, the level of information they can provide is different. First, the spatial resolution in TEMs is higher than in SEMs. This is due to the higher beam energy in TEM and the fact that SEMs samples are thick compared to TEMs samples (around 200nm). A bigger volume of sample generates more X-Rays while at the same time, it generates more scattering. For this reason, the detection limit in SEMs is smaller but the count rate is bigger than in TEMs. A thinner sample generates less beam spreading and, since the volume of the sample is smaller, the interaction of the X-Rays with the atoms of the sample decreases. This means that the X-Ray absorption and fluorescence effect is negligible so the peaks of the spectra are proportional to the concentration and specimen thickness. For these reasons, EDX on TEMs allows for quantitative and qualitative analysis. EDX can detect substances up to 1000ppm of concentration. In addition, EDX is not able to detect substances lighter than C.

3.1.1.5 EELS

An EELS device can be coupled to a TEM or a scanning TEM (STEM). It measures the energy lost by the incident electrons to create an EELS spectra. When a high energy electron hits a sample and interacts with it, an inelastic scattering event can take place. The incident electron ionises an electron of the inner shells of the atom and loses energy on its way. Once they have passed through the sample, these electrons enter the optic axes to a magnetic spectrometer that separates the electrons as a function of their kinetic energy. The magnetic spectrometer classically has an angle of 90° and applies magnetic fields of 0.01T [117]. When the electrons enter the magnetic chamber, the magnetic field causes the electrons to spread according to their energy following the equation:

$$F = Bev = \frac{mv^2}{r} \quad (3.7)$$

Where:

- F = magnetic force of an electron;
- B = magnetic field= 0.01T;
- e = electronic charge;
- v = electron speed;
- m = relativistic mass;
- r = change of direction. Modulus of the position vector \hat{r} , which is produced when an electron moves from its initial position to a point 'P' under the presence of a magnetic field.

Once the electrons pass into the magnetic field and are separated according to their kinetic energy, the spread electrons are focused again with the help of small curvatures in the magnetic chamber which condense the electron beams to create a spectrum which relates counts with electron energy loss (eV) [117].

An EELS spectrum can be divided into two differentiated areas [117]: the low loss region (<100eV) and the high loss region (>100eV). The zero-loss peak is in the low loss region. It is produced by the elastically scattered electrons; thus, the energy loss of the electrons is close to 0eV. The plasmon peak is visible from 3eV to 30eV. The energy of the plasmon peak has been related to the mechanical properties of metal alloys, semiconductors, and ceramics [118]. In addition, in thicker samples, an electron can excite more than one plasmon producing several plasmon peaks of different energy. The ionisation edges are located in the high energy loss region (>100eV). In this zone, the intensity of the spectra drops abruptly but peaks, produced by the excitation of core electrons from inner shells of the atom, are visible and provide elemental level information [117]. EELS is able to distinguish between two elements or between the oxidation states of an element and, for this reason, it is an excellent technique to analyse the Ce^{3+}/Ce^{4+} ratio on the CeO_2 NPs surface.

3.1.1.6 TEM experimental conditions and methods

In this thesis, TEM is used to analyse CeO₂ NPs structure and composition with BFTEM imaging mode. Due to their small size, it is not necessary to do special sample preparation. A drop of the sample (in water) was cast over a holey carbon film-copper grid, 300 mesh (Agar Scientific), a day before the analysis to avoid the contamination of the column. TEM analysis were performed using A FEI Tecnai F20 field emission gun TEM equipped with a Gatan Orius SC600A charge coupled device (CCD) camera. The Image J software was used to analyse the images.

3.1.2 X-Ray diffraction (XRD)

XRD is a materials characterisation technique that provides information about the crystalline structure of materials such as crystallite size, crystal structure, lattice cell parameters, analysis of phase composition and also detection of defects.

3.1.2.1 Basics in XRD

X-rays are electromagnetic radiation approximately 1Å in wavelength. X-rays are formed when a metal (for example copper) emits radiation after being bombarded by electrons from a pre-heated metal filament. When the electrons ionise the copper k electrons, a transition of electrons from the 2p orbitals of the L shell to the K shell results in K α and K β X-Ray emissions [119, 120]. The emitted radiation is then mono-chromatied in such a way only K α radiation hits the sample. When an X-ray beam hits a crystalline sample, X-rays are scattered depending on the crystallographic structure and form destructive or constructive interferences at certain angles. When the interactions between scattered rays are constructive, they follow Bragg's Law, which relates the distance between the planes (d) of the crystal lattice and the angle of diffraction of the incident X-Ray:

$$n\lambda = 2d \sin \theta \quad (3.8)$$

The peaks of a diffraction pattern can be associated with different planes of atoms (miller indices) and their intensities can be related to their structural arrangement [121].

3.1.2.2 The XRD machine

Figure 3. 4 shows a diagram of an XRD machine. It is formed by five main components:

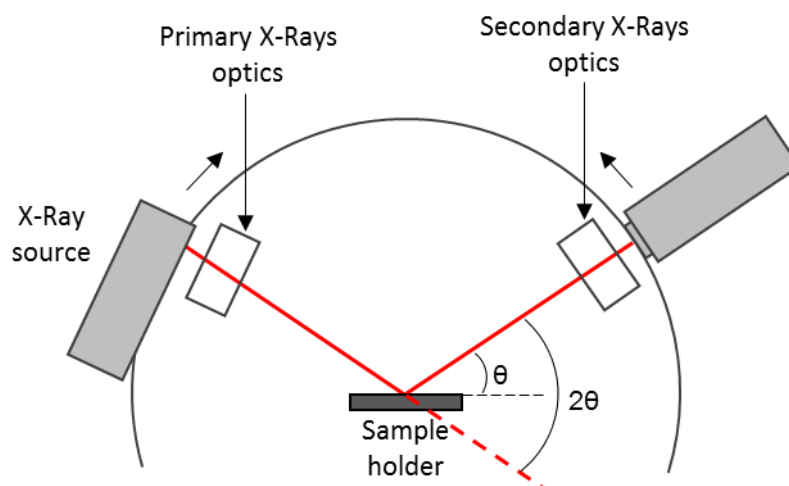


Figure 3. 4: Diagram of a XRD machine


- The **X-Ray tube**, as its name suggests, is the main source of X-Rays. This is a ceramic or glass container which uses tungsten cathode as the source of electrons. Then, these electrons are accelerated by a difference in potential and hit an anode target material, usually made of cobalt (Co) or (Cu).

- The **primary optics** are in charge of adjusting the X-Rays before they hit the sample and increase the resolution of the data when it is collected. It is formed by three main parts:

Slits keep the beam in position and correct the angular divergence, the divergence slit controls the beam spread (or beam width) and the monochromators allow the pass of $K\alpha_1$ and $K\alpha_2$ radiation while hampering the passage of $K\beta$ or any other radiation.

- The **sample holder** consists of a static arm where the sample can be located.

- The **secondary optics** components retrieve the X-Rays from the sample and condition them before reaching the detector. It is formed by four parts: The selection slit reduces the scattered X-Rays produced by air or amorphous



scattering, the height-limiting slit limits the beam height, the receiving slit limit diffuse scattered X-Rays and finally there is another monochromator which filters the $K\beta$ radiation.

- In **the detector**, X-rays are transformed into visible light by a scintillator material. Then a photomultiplier detects the photons and outputs a voltage which is proportional to the original X-Ray intensity.

3.1.2.3 XRD experimental conditions and methods

The crystal structure of the samples was analysed using XRD. To obtain the particulate material, the synthesised NPs were centrifuged to separate them from the dispersion media. Then, the NPs were air dried to obtain the dried solid sample. All samples were mounted using top-loading on a zero background silicon holder with a cavity.

To obtain the solid from the commercial sample of CeO₂ NPs, which was highly dispersed, NaOH was used. CeO₂ NPs, in contact with a basic solution, tend to aggregate and precipitate. Then the particulate material was separated from the solution with centrifugation and they were let to dry to obtain the solid.

Table 3. 1: Experimental conditions of XRD experiments

Parameter	Value
Scan Axis	Gonio
Start Position (2 θ)	10-20
End Position (2 θ)	90
Step size (2 θ)	0.033
Scan step time (s)	310.4918
Scan type	continuous
Specimen length (mm)	10
Temperature (°C)	25
Anode Material	Cu
K α -1 wavelength (Å)	1.5406
K α -2 wavelength (Å)	1.5443
K β wavelength (Å)	1.39225
K-A2/K-A1 Intensity ratio	0.5
Generator settings	40mA, 45kV

3.1.3 Dynamic light scattering (DLS)

The measurement of particles size is essential in both industry and science as the properties of the materials are related to size. For this reason, the control of the particle size is essential. Microscopy is able to provide information about the size of the particles in two (TEM) or even three dimensions (SEM). SEM uses secondary electrons to produce two dimensions image with image depth.

However, the use of TEMs and SEMs are expensive and they do not provide data about the stability of the particles in dispersion. The Dynamic Light Scattering (DLS) or Photo Correlation Spectroscopy is a good technique for this matter. It records a physical value and translates it to the size of the sphere that could produce the data.

3.1.3.1 How a DLS machine works

A diagram of a DLS device is shown in Figure 3. 6. DLS machine is formed mainly by six parts: a laser, an attenuator, a cell, a detector, a correlator and the computer.

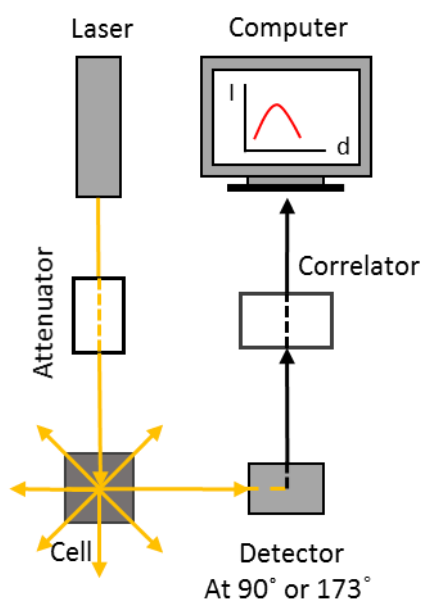


Figure 3. 6: Diagram of a DLS machine

The laser produces a beam of light that passes through the attenuator to the cell where the sample is located. The attenuator diminishes the intensity of the beam of light so the detector does not saturate. Then, the beam of light travels to the cell where the sample is located. At this point, the beam of light hits the particles of the sample and the light scatters in different directions and reach the correlator, which is situated at either 90 or 173 degrees from the cell. The correlator processes the digital

signal. It transforms the intensity of the scattered light at a certain time to data able to be processed by the computer by deriving the rate of change at which the light varies. This rate of change of intensity is related to the movement of

particles in the liquid, which is related to the hydrodynamic diameter of the particles. Finally, the computer produces a signal in terms of intensity, volume or number versus size.

3.1.3.2 The theory behind the DLS machine

DLS [122-124] is a light scattering technique that relates the speed of particles under Brownian motion with particle size (in diameter) at a certain temperature. These particles (usually smaller than 1 μ m in size) are un-soluble colloids suspended in a certain media.


The Brownian motion refers to the random movement of the particles as a consequence of the collision of those particles with the solvent molecules. The speed at which particles move depends on the translational diffusion coefficient (D) and it can be used to calculate particle size using Stokes-Einstein equation:

$$d(H) = \frac{kT}{3\pi\eta D} \quad (3.9)$$

Where:

- d(H): the hydrodynamic diameter of the particle
- k: Boltzmann's constant= $1.38064852 \cdot 10^{-23} \text{ m}^2 \text{ kg s}^{-2} \text{ K}^{-1}$
- T: absolute temperature / K
- η : viscosity / $\text{kg}\cdot\text{m}^{-1}\cdot\text{s}^{-1}$
- D: diffusion constant / $\text{m}^2\cdot\text{s}$

DLS uses the diffusion of the NPs to estimate the hydrodynamic diameter of a theoretical solvated\hydrated spherical particle in a dispersion medium. The hydrodynamic diameter is different from the hard-sphere diameter. The hard-sphere diameter refers to the actual diameter of the NPs while the hydrodynamic diameter corresponds to the diameter formed by the NPs plus the layer of solvated molecules and ions surrounding it. For this reason, anything that affects the diffusion constant will affect the particle size measurement because it can change the layer of molecules and ions surrounding the NP thus can change the electrical double layer (ELD). For



example, ionic strength can expand or shrink the EDL in such a way that diffusion of a particle changes and it affects particle speed. It could affect final measurements giving media specific values for a certain speed. Standards, as NaCl, are used to verify DLS good operation. They contract the EDL as much as possible to ensure that the reported hydrodynamic diameter corresponds to the actual size value. In addition, anything that affects particle surface characteristics will affect diffusion. Coatings (e.g. polymers) can affect movement and ionic strength can affect the coating conformation altering diffusion.

DLS uses a beam of diffracted light to estimate the size of the particles. Large particles in solution move slower than small particles. When a beam of light hits a particle under Brownian motion, the light is scattered in different directions with different phases and fluctuates with time at different rates. It produces constructive and destructive waves that result in an increase or decrease of the intensity when the light reaches the detector. In addition, the intensity of that light depends on the particle size. In this way, bigger particles scatter more light than smaller particles according to the Rayleigh scattering theory.

The correlator translates the signal in intensity to a correlation function. It measures the difference of intensity for really short periods of time, in fact, milliseconds or tens of milliseconds. In this way, for short periods of time, the difference in intensity is very small and the correlation is 1. However, in a long period of time ($t \rightarrow \infty$) the difference in intensity is higher and the correlation is 0. In this way, by measuring the difference in intensity for short times with time, a sigmoidal correlation function is created. When the light hits large particles, the amount of the scattered light and thus its the intensity is bigger. The signal it produces in the correlator will vary less and will persist with time. If particles are small, the correlation decreases quicker.

The correlation function gives information about the particle size. The diffusion coefficient can be calculated by fitting the correlation curve to an exponential function. The DLS uses different algorithms to obtain the Z-average (Z-Ave)

diameter, the polydispersity index (Pdl) and an intensity size distribution from the correlation function. The Z-Average is defined as the intensity weighted harmonic mean size and it is a good approximation of the average size of the particle size distribution. This information together with the Pdl is usually taken into account when establishing the main hydrodynamic size of particles in the dispersion. However, Z-Ave and Pdl should only be taken into account in samples with particles of narrow size distribution where the Pdl is below 0.2. If the Pdl is higher than 0.2 the Z-Ave is not a good approximation to the size of the NPs. For this reason, the DLS uses different algorithms to obtain the result in number of particles and volume of particles. The Mie theory is used to translate intensity into volume [123]. It relates the relative scattering intensity with particle size in volume with respect to a detection angle (90° or 173°).

3.1.3.3 Limitations of the DLS

As mentioned before, DLS uses the diffusion and the Brownian motion of spherical colloids to calculate their size in diameter. For this reason, non-spherical particles in DLS are treated as spheres what can produce an error in the estimation of its real size. Also, DLS is sensitive to agglomerates. Agglomerates move slower than disperse particles due to their volume and mass and are treated as spherical particles in DLS. DLS is not able to distinguish in between particles moving together at a certain speed because they diffuse in the same way. Nevertheless, the DLS can detect agglomeration and inform about it when agglomeration is happening while taking a measurement.

3.1.3.4 Zeta-Potential (Z-Potential)

DLS machines can also measure Z-Potential or electrokinetic potential. In general terms, Z-Potential could be described as the difference in potential between the oppositely charged ions attached to the dispersed particle and the medium (slipping/shear plane) [125]. The DLS machine uses electrophoresis to measure the Z-Potential. Electrophoresis is a technique which uses an electric field (E) to separate ions of opposite charge [126]. The separation speed (v) depends on the strength of E and the mobility of the particles ($v=m \cdot E$). Also, as mentioned before, the mobility of the particles depends on particle size, shape, charge and the temperature.

When a charged particle is dispersed in any medium, it generates an electrical double layer (EDL). Ions and molecules with the opposite charge to the particle tend to group around the particle due to electrostatic forces following the Gouy-Chapman-Stern model. In general terms, this model states that a charged particle in dispersion is surrounded by static opposite charge ions or molecules that form the Stern layer and that this layer is surrounded by other positively and negatively charged molecules and ions which moves to create a diffuse layer. In this way, ions generate an EDL that goes from the particle to the solution. In-depth information about the EDL can be found in section 5.2.1.

When applying an electric field in electrophoresis, charged particles tend to go to the oppositely charged electrode. The slipping/shear plane is the thin zone which separates the static ions and molecules of the Stern layer from the diffuse layer. The charge at the slipping/shear plane is known as ZP [126].

The operation of a DLS machine with Z-Potential mode is really similar to the functioning of a DLS. When doing a Z-Potential measurement, the laser is split in two. One part is the reference beam, and the other part hits the sample. Under the effect of an incident laser during electrophoresis, particles move and the scattered light has a different frequency than the original frequency. Then, the scattered beam from the sample is combined with the reference beam and the Z-Potential is determined through some mathematical equations [126].

3.1.3.5 DLS and Z-Potential experimental conditions and methods

As mentioned before, dynamic light scattering is mainly used to figure out the hydrodynamic size and Z-Potential of the NPs. Nevertheless, CeO₂ NPs quickly aggregate. For this reason, the data obtained from DLS correspond to the diameter of ideal spherical aggregates and cannot be used to measure the diameter of individual particles.

Because the NPs aggregate, the polydispersity index (Pdl) is too high and the Z-average is not a good approximation of the size of the aggregates. For this reason, in addition to Z-Average, the results are given as a number. All the errors are calculated by doing the standard deviation of the sample (n=3).

The Z-Potential average was calculated from the result of three measurements. The error between the measurements was calculated by doing the standard deviation of the sample (n=3).

Table 3. 3: Experimental conditions of DLS and z-Potential analysis

Parameter	Value
Temperature (°C)	25
Refractive Index _{dispersant}	1.33
Viscosity (mPa•s) _{dispersant}	0.8872
Dielectric constant _{dispersant}	78.5
Refractive Index _{CeO2}	2.2
Absorption _{CeO2}	0.1
Sample holder	Disposable Cuvettes

3.2 The nanoparticles under study. Materials and synthesis methods

3.2.1 Materials

Synthesis reactants, commercial nanoparticles and buffer preparation

Cerium (III) nitrate hexahydrate 99.99%, tetramethylammonium hydroxide (TMAOH), IM, ACS reagent and hexamethylenetetramine (HMT), ACS reagent (>99%) were bought from Sigma Aldrich. Sodium hydroxide pellets, analytical reagent grade were obtained from Fisher Scientific. Cerium (IV) oxide, 20% in H₂O nanoparticles dispersion was obtained from Alfa Aesar.

Phosphate buffered saline (PBS), pH 7.4 (powder), citric acid monohydrated, ACS reagent, ≥99.0%, sodium citrate tribasic dehydrate, BioUltra, ≥99.5% were purchased from Sigma Aldrich, Glycine-HCl buffer, 10mM, pH 3.0 was obtained from Bio-Rad.

Dextran from *Leuconostoc* spp., Mr ~7000 was bought from Sigma Aldrich. Polyvinylpyrrolidone, K40, was purchased from MP Biomedicals and Polyethylene glycol, 50%, soln. was purchased from Alfa Aesar.

Phospholipids for RCV experiments

1,2-dioleoyl-sn-glycero-3-phosphocholine (DOPC), 1,2-dioleoyl-sn-glycero-3-phosphate (sodium salt) (DOPA), 1,2-dioleoyl-sn-glycero-3-phosphoethanolamine (DOPE), and 1,2-dioleoyl-sn-glycero-3-phospho-L-serine (sodium salt) (DOPS) were bought from Avanti Polar Lipids. 1,2-dioleoyl-sn-glycero-3-phospho-(1'-rac-glycerol) (sodium salt) (DOPG) was purchased from Sigma Aldrich.

Additional materials

Potassium chloride, ACS grade, Cerium (III) phosphate 99% was obtained from Alfa Aesar, Cerium standard, 2% in HNO₃, 1000µg/mL was bought from SPEX CertiPrep.

3.2.2 *Methods. Synthesis of CeO₂ NPs.*

3.2.2.1 Needles

CeO₂ nano-needles synthesis was based on the procedure described in [93]. In general, a solution of 0.0115M of cerium (III) nitrate hexahydrate was prepared by dissolving 0.9777g of the salt in 10mL of milli-Q water. Then, a solution of 5M of sodium hydroxide was prepared by dissolving 4.0860g of sodium hydroxide in 20mL of milli-Q water. After that, the cerium (III) nitrate solution was poured, dropwise and under continuous stirring, into the sodium hydroxide solution. At this point, the colour of the dissolution changes from transparent to white. Finally, the solution is transferred into a hydrothermal autoclave reactor and it is heated up to 150°C for two hours.

The synthesised cerium (IV) oxide NPs consisted of a dense white dispersion. The NPs were cleaned using centrifugation at 10000G for 15min. The NPs were sonicated for 5 min after the end of every centrifugation step. Then, the supernatant was separated from the particles and the particles were dispersed in milli-Q water. The cycle was repeated 3 times to obtain clean particles. Finally, the solid particles were let to dry to obtain the pellet.

3.2.2.2 Cubes

CeO₂ nano-cubes were synthesised using a wet chemical method following a personal communication with the Catalan Institute of Nanoscience and Nanotechnology (ICN2). They were synthesised by mixing 37.5M of cerium (III) nitrate hexahydrate with 0.5M of HMT in milli-Q water, dropwise and under continuous stirring during 48h. The solution was cleaned by centrifugation and it was suspended with milli-Q water three times before use. Then, it was dried to obtain the pellet.

3.2.2.3 Spheres

CeO₂ nano-spheres were synthesised following a personal communication with the ICN2. The NPs were synthesised by mixing 37.5mM of cerium (III) nitrate hexahydrate with 40mM of TMAOH in milli-Q water, dropwise and under continuous stirring during 48h. The solution was cleaned by centrifugation, and

it was resuspended with milli-Q water three times before use. Then, it was dried to obtain the pellet.

3.2.2.4 Coatings

3.2.2.4.1 PVP-40 coated CeO_2 NPs

A solution containing 37.5mM of $Ce(NO_3)_3$ was poured into the same volume of a solution containing 0.5% of 40-PVP and 40mM of TMAOH. Then, the synthesis mixture was left to stir for 48h. Milli-Q water was used in the synthesis.

3.2.2.4.2 Dextran coated CeO_2 NPs

First, a solution containing 37.5mM of $Ce(NO_3)_3$ was poured into the same volume of a solution containing 0.5% dextran under continuous stirring. Then, this solution was poured into the same volume of a solution containing 40mM of TMAOH. Finally, the synthesis mixture was left under continuous stirring for 48h. It is important to notice that the whole synthesis was made using milli-Q water.

3.2.2.4.3 PEG-coated CeO_2 NPs

A solution containing 37.5mM of $Ce(NO_3)_3$ was poured into the same volume of a solution containing 0.5% of PEG and 40mM of TMAOH. Then, the synthesis mixture was left to stir for 48h. Milli-Q water was used in the synthesis

3.2.2.4.4 PBS-coated CeO_2 NPs

CeO_2 NPs were phosphate coated using PBS. The CeO_2 NPs were dispersed in PBS and sonicated for 30min. Then, the NPs were left in dispersion in PBS for 24h before using them for the experiments.

CHAPTER 4. CHARACTERISATION OF CERIA NANOPARTICLES

The interaction of synthesised and commercial CeO₂ NPs with model membranes is studied in this thesis. Chapter 4 provides information about the physical and chemical characteristics of the nine different CeO₂ NPs used in future chapters. Eight of the nine coated and uncoated CeO₂ NPs samples with different shape and size were synthesised using wet and hydrothermal methods. The last CeO₂ NPs sample was commercially obtained. The size and the shape of the CeO₂ NPs were analysed using BFTEM. The sample preparation method for taking the BFTEM images can be found in 3.1.1.6. XRD and SAED were used to confirm the presence of CeO₂ NPs. The experimental conditions for XRD can be found in 3.1.2.3. Additionally, DLS was used to assess the stability of the NPs in dispersion and their Z-Potential. The experimental conditions used in DLS can be found in 3.1.3.5. It is important to notice that all synthesised NPs were cleaned with milli-Q water and centrifugation before carrying out any experiment. BFTEM images were taken from the CeO₂ NPs in milli-Q water. After the washing process, the NPs were left to dry to obtain a powder to carry out the XRD experiments. The CeO₂ NPs powder obtained from the synthesis is later dispersed in different buffers to meet the experimental conditions required in future experiments (CHAPTER 7). Table 4. 1 summarises the conditions of the CeO₂ NPs in the experiments of this thesis. The NPs were dispersed in H₂O, Glycine-HCl buffer at pH 3.0 (GLY 3.0), citric/citrate buffer at pH 3.0 (CCB 3.0), pH 4.0 (CCB 4.0), pH 5.0 (CCB 5.0), pH, 6.0 (CCB 6.0) and phosphate saline buffer at pH 7.4 (PBS 7.4).

Table 4. 1: Summary of the CeO₂ experimental conditions in this thesis

Sample name	Used in experimental section:	Cleaning procedure	NPs dispersed in:
Spheres	7.2	centrifugation 30min + sonication 30min (x3 times)	H ₂ O
	7.3		GLY 3.0, CCB 3.0, CCB 4.0, CCB 5.0, CCB 6.0 and PBS 7.4
Cubes	7.2	Centrifugation 15min + sonication 5min (x3 times)	H ₂ O
	7.3		GLY 3.0, CCB 3.0, CCB 4.0, CCB 5.0, CCB 6.0 and PBS 7.4
Needles	7.3	Centrifugation 15min + sonication 5min (x3 times)	GLY 3.0, CCB 3.0, CCB 4.0, CCB 5.0, CCB 6.0 and PBS 7.4
Dots	7.2	N/A	N/A
PVP-CeO ₂	7.5	N/A	H ₂ O
PEG-CeO ₂	7.5	N/A	H ₂ O
Dextran- CeO ₂	7.5	N/A	H ₂ O
PBS-CeO ₂ (spheres)	7.5	N/A	H ₂ O
PBS-CeO ₂ (cubes)	7.5	N/A	H ₂ O

Synthesised ceria NPs

4.1.1 Hydrothermal method using NaOH. Needles

Figure 4. 1 shows the synthesised NPs using the hydrothermal method described in section 3.2.2.1. As observed, the sample consisted of thin needles of different lengths (Figure 4. 1 A and B) that breaks after sonication for 30min (Figure 4. 1 C and D). In order to match the experimental conditions followed in CHAPTER 7, the NPs had to be sonicated for 30min which provokes breakage. It is important to notice that the needles were washed before taking the BFTEM images. In-depth about the cleaning procedure of the needles can be found in 3.2.2.1.

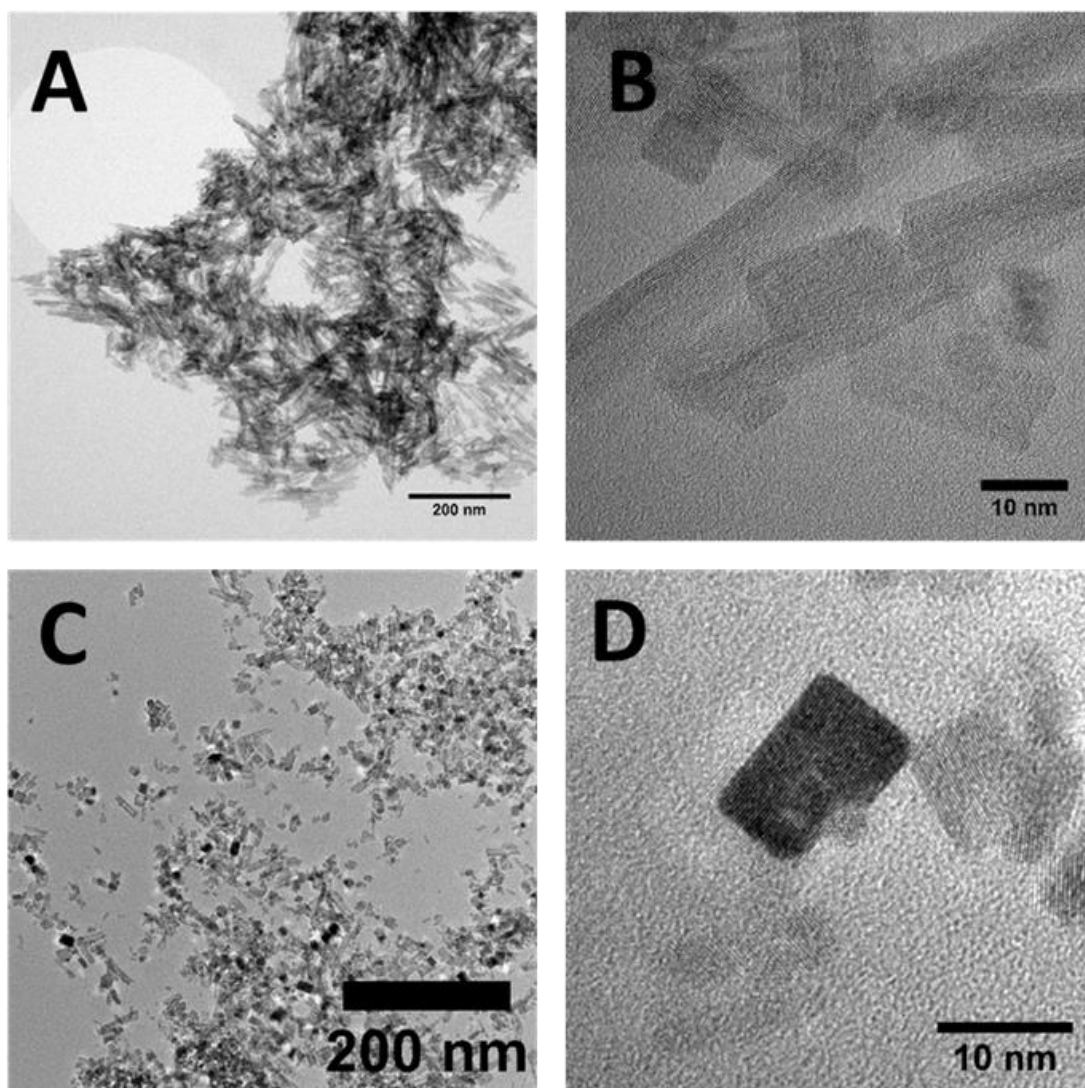


Figure 4. 1:BFTEM images of CeO_2 NPs synthesised using an hydrothermal method and NaOH. A and B: before sonication. C and D: after sonication

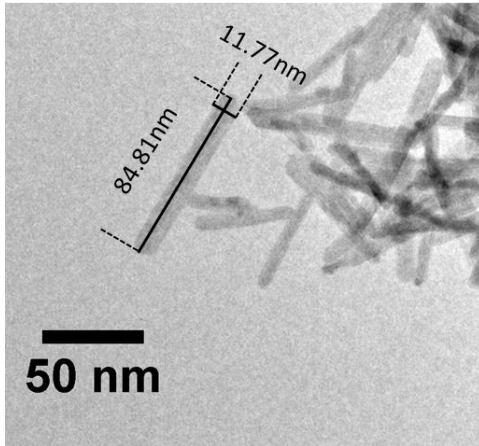


Figure 4. 3: BFTEM image of CeO₂ NPs needles indicating length and width of one of the needles.

Figure 4. 3 shows how the length and width of the needles were measured to create the log-normal distribution curves displayed in Figure 4. 2 A and B. The log-normal distribution curve was calculated by measuring the length (A) and width (B) of more than 300 NPs from BRTEM images. The result shows the sample is

formed by needles of around 75.6nm in length and 5nm in width. However, the length of the NPs ranges between 20nm and 200nm and their width ranges between 3nm and 15nm.

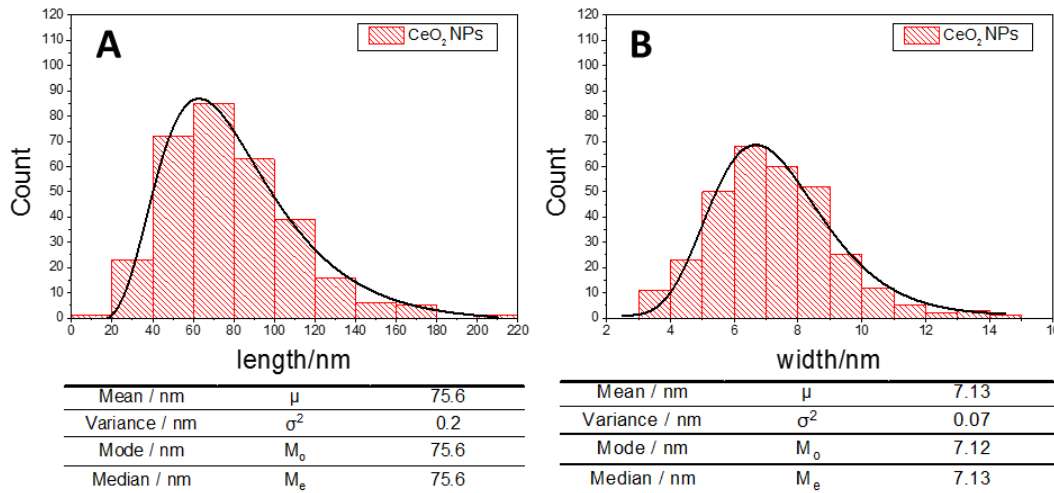


Figure 4. 2: Red bars: number of CeO₂ NPs (needles) of a certain the length (A) and width (B). Black line: log-normal distribution curve of the length (A) and width of CeO₂ (needles).

Figure 4. 4 displays the log-normal distribution curve of the needles after the sonication for 30min. It was calculated by measuring the size of more than 300 NPs from BFTEM images. As observed in Figure 4. 1 and corroborated in Figure 4. 4 the long rods break after sonication to form a mixture of cubes (of around 10nm) and short rodes (with a maximum length of 40nm).

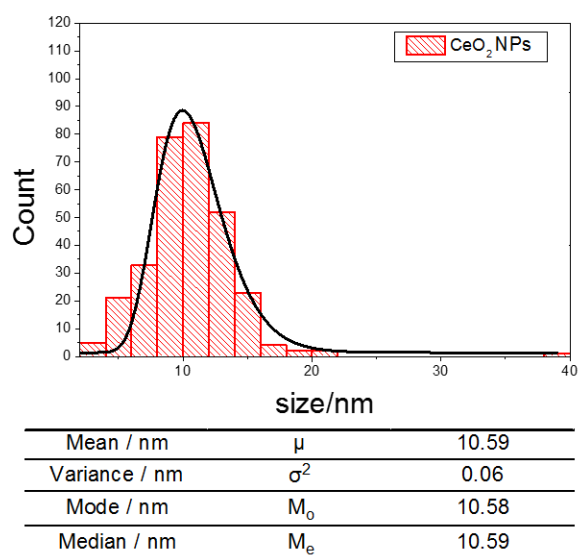


Figure 4. 4: Red bars: number of CeO₂ NPs (needles) of a certain size after sonication for 30min, black line: log-normal distribution curve of the size of CeO₂ NPs (needles) after sonication for 30min.

The XRD pattern taken from the sample was indexed against the ICDD database and it was found to be pure ceria according to ICDD file 00-004-0593 (Figure 4. 5) with a crystalline cubic structure (Fm-3m) with $a=b=c= 5.4110 \text{ \AA}$. However, the peak at 33 degrees $\{0\ 0\ 2\}$ has a bigger intensity than expected. The CeO_2 NPs sample consists of needles that probably sit on the XRD holder in an organised manner. In this way, the orientation parallel to the x-axes is preferred due to the shape of the NPs and so the $\{0\ 0\ 2\}$ peak is bigger than expected. The presence of needle-shaped particles is, as well, confirmed by the different width of the XRD peaks, which indicate an anisotropic particle morphology. Also, SAED patterns showed as well, confirm the sample is formed by cerium (IV) oxide as the SAED rings can be indexed against ICDD 00-004-0593 (Figure 4. 5).

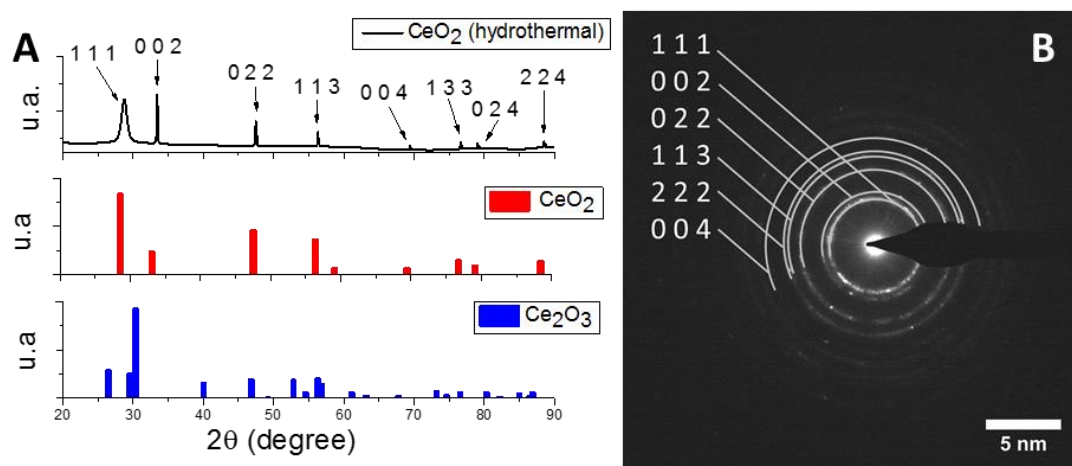


Figure 4. 5: A: XRD pattern of: Black line: CeO_2 (needles), red line: theoretical pattern of CeO_2 (ICDD file: 00-004-0593), blue line: theoretical pattern of Ce_2O_3 (ICDD file: 00-023-1048). B: SAED pattern of CeO_2 NPs (needles)

For later experiments, CeO₂ NPs (needles) were dispersed in different media. DLS was used to study the size of the aggregates. In this way, 0.01M of needles in various media were tested using DLS. As observed in Figure 4. 6, the Pdl indexes of the measurements are high and, for this reason, the Z-Ave is not a good approximation of the size of the particles. Instead, the result is also presented in number mean. As observed from the DLS results and corroborated by BFTEM images, the samples are formed by aggregated broken needles. The needles break with sonication and, for this reason, it is impossible to know if what is being measured is the size of the aggregates or the length of long needles. The DLS graphs will be plotted in the appendix of chapter 4. In Figure 4. 6B the Z-Pot value from DLS can be observed for the NPs in different media. The NPs in GLY have a positive value, while the NPs in citrate have a negative value produced by the presence of citrate.

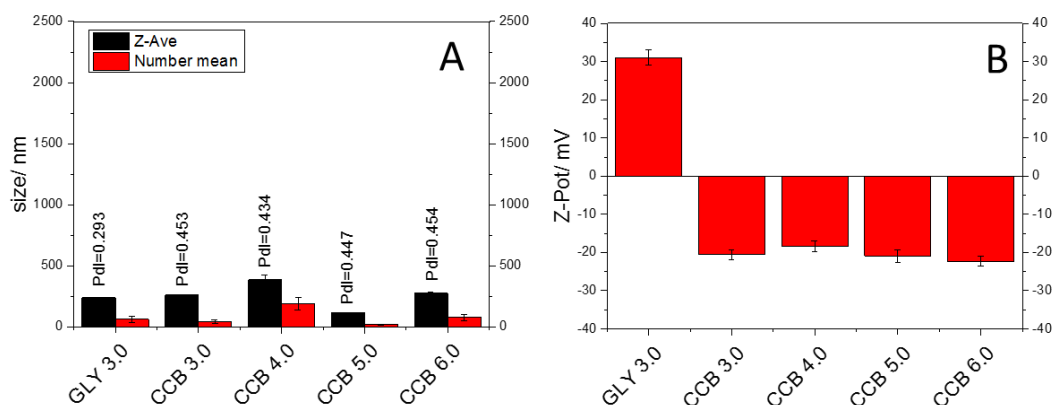


Figure 4. 6: **A:** Graph showing the size of CeO₂ NPs (needles) from DLS when they are dispersed in different media. Black bars: Z-Average, associated error and Pdl index from DLS data. Red bars: Size of the CeO₂ NPs (needles) as 'mean number' from DLS data. **B:** Z-Pot values (mV) from DLS obtained from CeO₂ NPs (needles) in different media.

4.1.2 Cubes

As observed in Figure 4. 7 the sample, synthesised by the procedure described in 3.2.2.2, is formed by cubes of around 10 nm side that tend to aggregate forming agglomerates. Log-Normal distribution of the NPs size is displayed in Figure 4. 8. The distribution curve was done by measuring the size of more than 300 NPs (Figure 4. 7) in BFTEM images. It concludes the average particle size is 10.57nm with a variation between 4nm and 18nm.

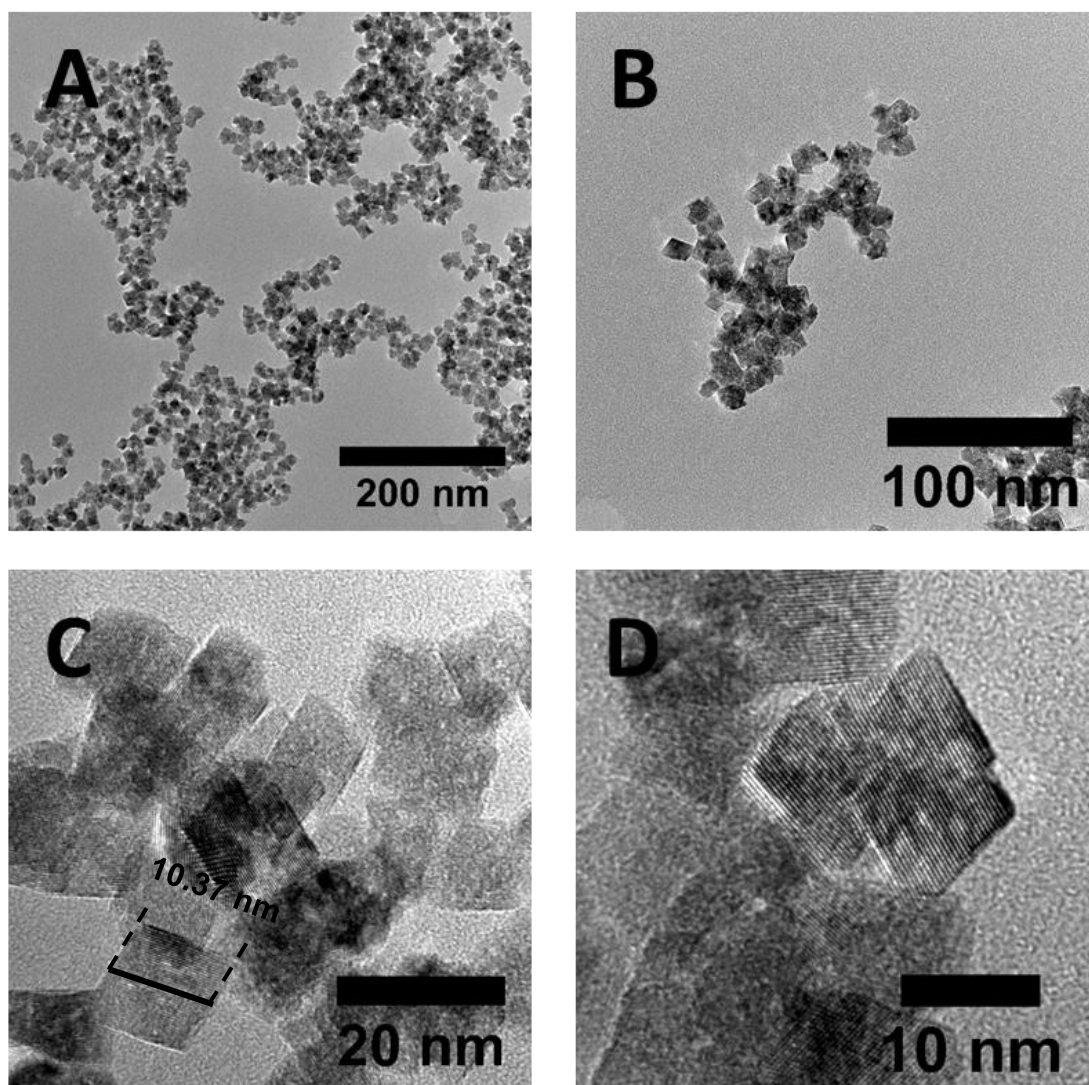
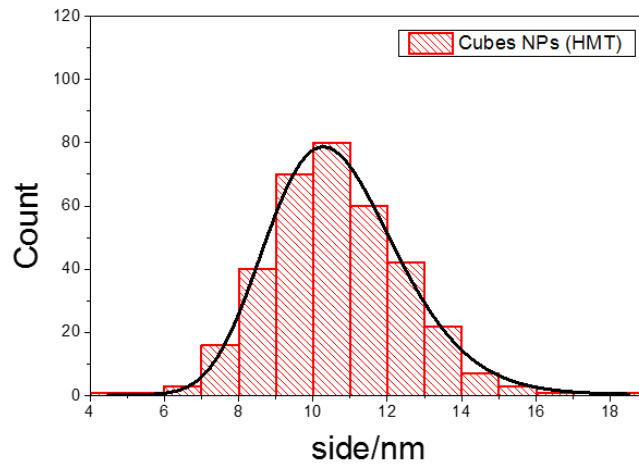


Figure 4. 7: BFTEM images of CeO₂ NPs synthesised using HMT and a wet chemical method



Mean / nm	μ	10.57
Variance / nm	σ^2	0.03
Mode / nm	M_0	10.56
Median / nm	M_e	10.56

Figure 4. 8: Red bars: number of NPs of a certain size. Black line: log-normal distribution curve of the side of the CeO_2 NPs synthesised using HMT

The XRD pattern taken from the sample was indexed against the ICDD database and it was found to be pure ceria according to ICDD file 00-004-0593 with a crystalline cubic structure (Fm-3m) with $a=b=c= 5.4110 \text{ \AA}$. In addition, SAED patterns, confirm the sample is formed by cerium (IV) oxide as the SAED rings can be indexed against ICDD 00-004-0593 (Figure 4. 9)

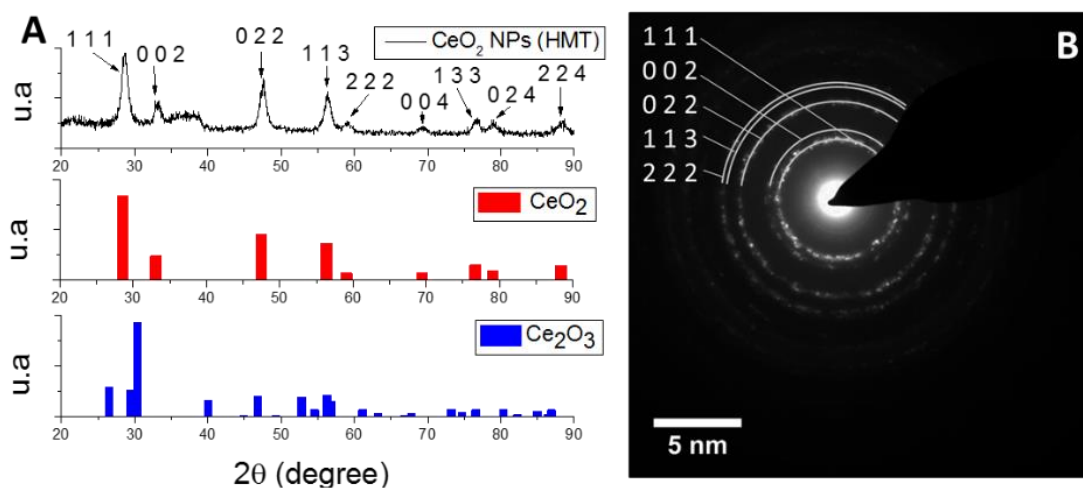


Figure 4. 9: A: XRD pattern of: Black line: CeO_2 NPs synthesised using HMT, Red line: theoretical pattern of CeO_2 NPs (ICDD file: 00-004-0593), Blue line: theoretical pattern of Ce_2O_3 (ICDD file: 00-023-1048). B: SAED pattern of CeO_2 NPs synthesised using HMT.

For later experiments, CeO₂ NPs (cubes) were dispersed in different media. DLS was used to study the size of the aggregates. In this way, 0.01M of cubes in various media were tested using DLS. As observed in Figure 4. 10 A the Pdl indexes of the measurements are high and, for this reason, the Z-Ave is not a good approximation of the size of the aggregates. Instead, the result is also presented as ‘number. It can be concluded that the NPs aggregate more in PBS than in GLY and CCB. Also, cubes in GLY 3.0 have a slightly lower aggregation than in CCB. The DLS plots can be consulted in the appendix of chapter 4. The Z-Pot values of the NPs dispersed in different media are displayed in Figure 4. 10 B. As observed, the NPs in GLY have a positive Z-Pot while the NPs in CCB and PBS have a negative Z-Pot probably produce by the presence of citrate and phosphate.

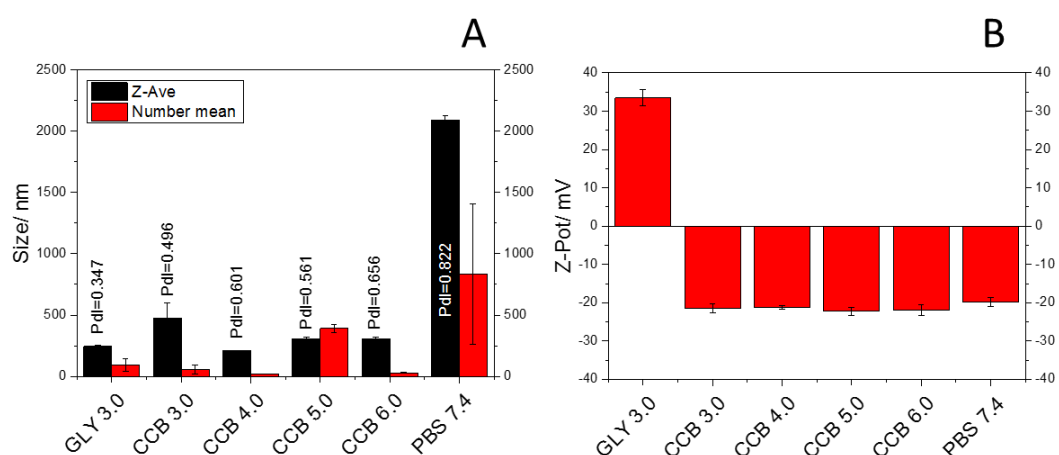


Figure 4. 10: **A:** Graph showing the size of CeO₂ NPs (cubes) from DLS when they are dispersed in different media. Black bars: Z-Average, associated error and Pdl index from DLS data. Red bars: Size of the CeO₂ NPs (cubes) as ‘mean number’ from DLS data. **B:** Z-Pot values (mV) from DLS obtained from CeO₂ NPs (cubes) in different media.

4.1.3 Spheres

Figure 4. 11 shows BFTEM images of CeO₂ NPs synthesised using TMAOH and a wet chemical method. The synthesis procedure can be found in section 3.2.2.3. As observed, the sample consists of little spheres smaller than 5nm in diameter. The distribution curve (Figure 4. 12), obtained by measuring the size of more than 300NPs from BFTEM images, concludes the average NP size is 4.28nm in diameter. However, the suspension is formed by NPs that range in diameters between 1-10nm.

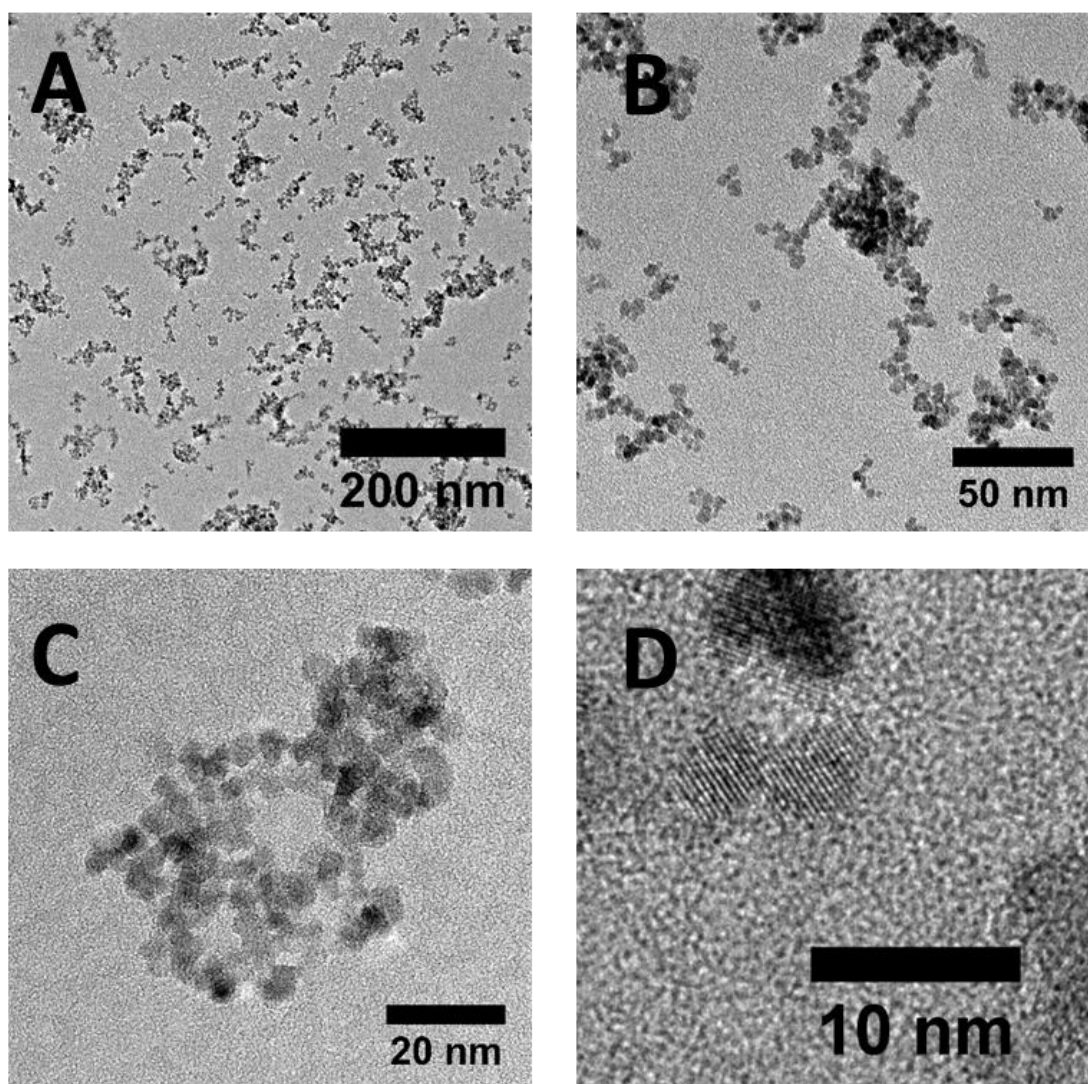


Figure 4. 11: BFTEM images of CeO₂ NPs synthesised using a wet chemical method and TMAOH.

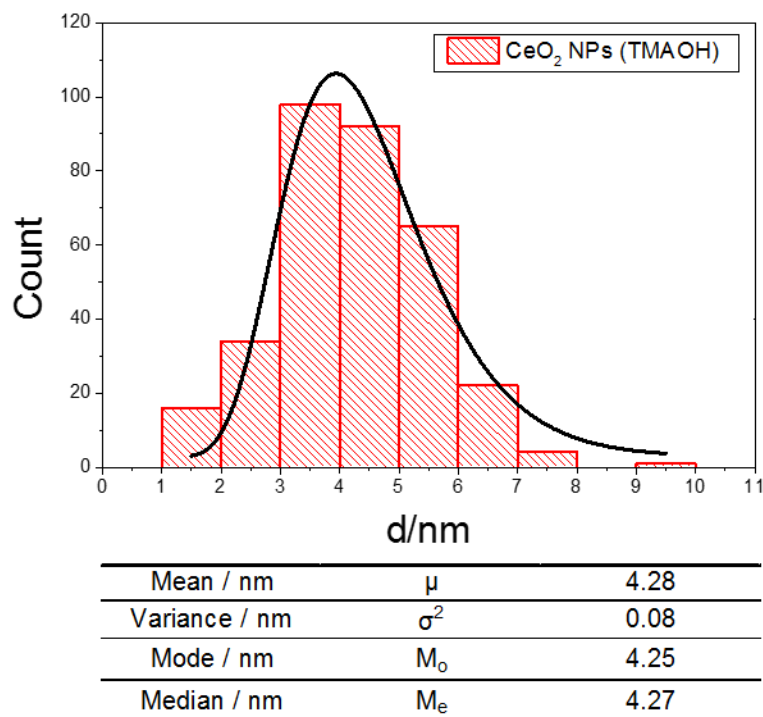


Figure 4. 12: Red bars: number of CeO_2 NPs (synthesised using TMAOH and a wet chemical method) of a certain size. Black line: log-normal distribution curve of the CeO_2 NPs synthesised using TMAOH.

In addition, The XRD pattern taken from the sample was indexed against the ICDD database, and it was found to be pure ceria according to ICDD file 00-004-0593 with a crystalline cubic structure (Fm-3m) with $a=b=c= 5.4110 \text{ \AA}$. In addition, SAED patterns, confirm the sample is formed by cerium (IV) oxide as the SAED rings can be indexed against ICDD 00-004-0593 (Figure 4. 13B)

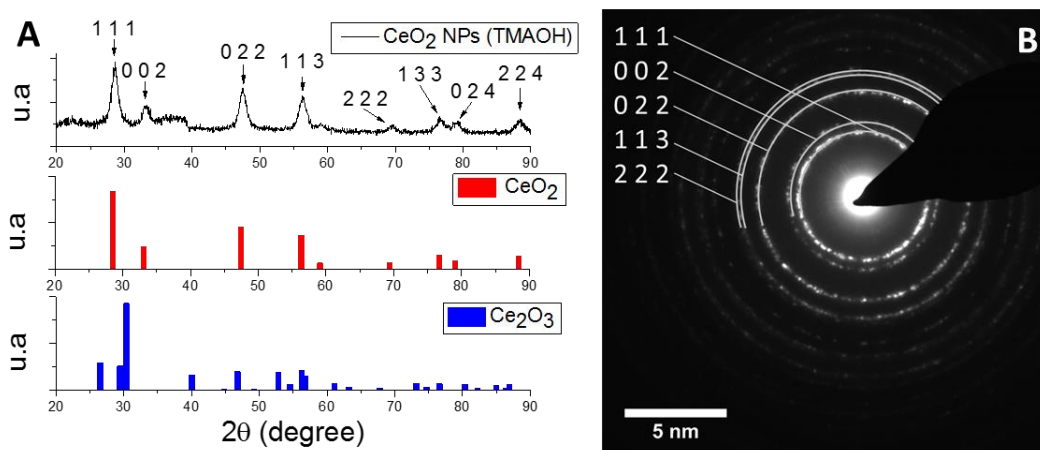


Figure 4. 13: A: XRD pattern of: Black line: CeO_2 NPs synthesised using TMAOH and a wet chemical method, Red bars: Theoretical pattern of CeO_2 NPs (ICDD file: 00-004-05936), Blue bars: theoretical pattern of Ce_2O_3 NPs (ICDD file: 00-023-1048)

For later experiments, CeO₂ NPs (spheres) were dispersed in different media. DLS was used to study the size of the aggregates. In this way, 0.01M of spheres in various media were tested using DLS. As observed in Figure 4. 14 the Pdl indexes of the measurements are high and, for this reason, the Z-Ave is not a good approximation of the size of the aggregates. Instead, the result is also presented as ‘number. A similar trend than the observed before with cubes can be observed. NPs aggregate more in PBS than in GLY and CCB. In addition, spheres in GLY 3.0 present a slight lower aggregation than in CCB. The DLS plots can be consulted in the appendix of chapter 4. The Z-Pot values of the NPs dispersed in different media are displayed in Figure 4. 14 B. The NPs in GLY, have a positive Z-Pot while the NPs in CCB and PBS have a negative Z-Pot probably produce by the presence of citrate and phosphate.

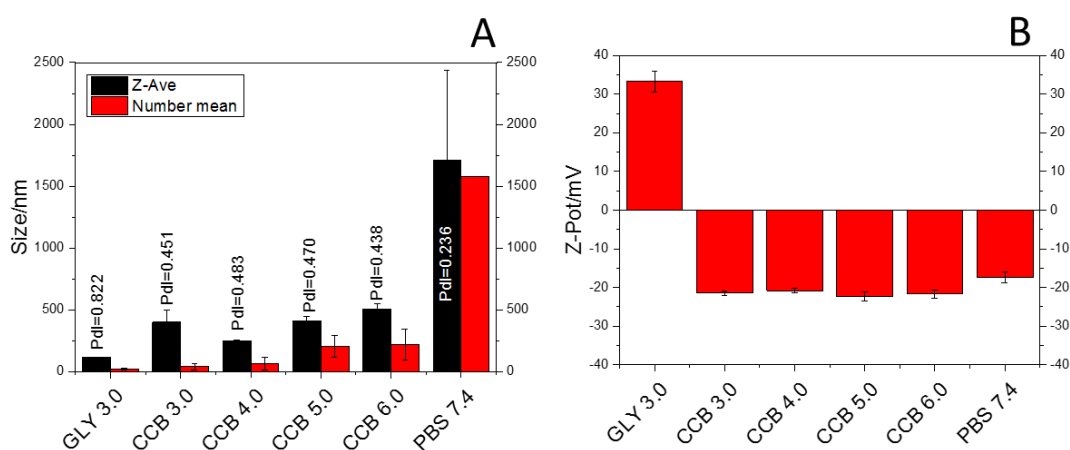


Figure 4. 14: **A:** Graph showing the size of CeO₂ NPs (spheres) from DLS when they are dispersed in different media. Black bars: Z-Average, associated error and Pdl index from DLS data. Red bars: Size of the CeO₂ NPs (spheres) as ‘mean number’ from DLS data. **B:** Z-Pot values (mV) from DLS obtained from CeO₂ NPs (spheres) in different media.

4.2 Commercial CeO₂ NPs

Figure 4. 15 corresponds to images of commercially purchased and un-coated CeO₂ NPs. As it can be observed, the NPs size is very small and they can be found both forming aggregates and dispersed. Later communications with the NPs supplier confirmed that citrate was used to synthesise the NPs so it is possible the NPs are citrate coated. This fact could explain the higher stability of the dispersion in comparison with the synthesised ones. DLS results show the commercial sample of NPs is highly dispersed. The Z-Ave of the CeO₂ NPs is 3.8 ± 0.1 nm and the Z-Pot is -25 ± 3 mV.

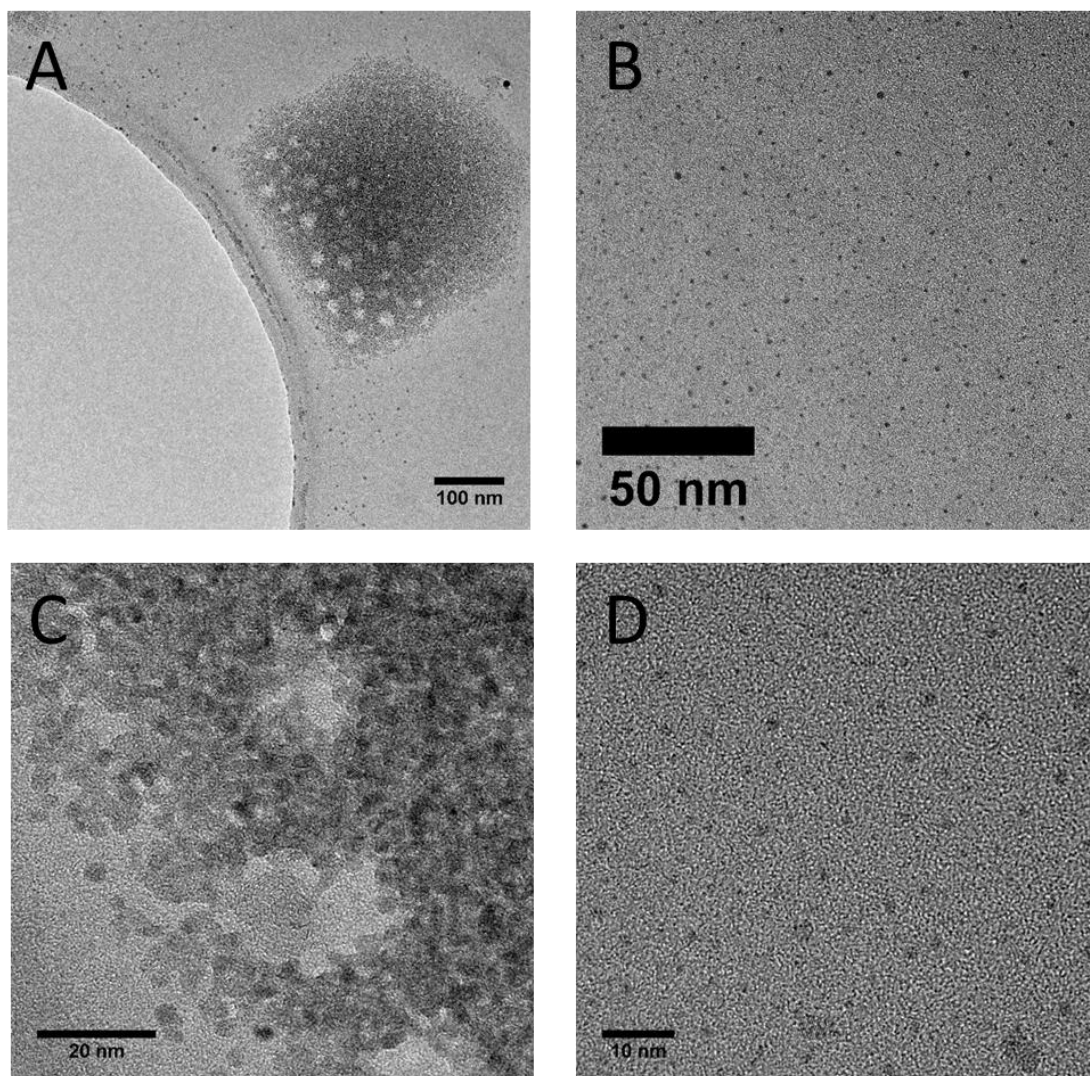


Figure 4. 15: BFTEM images of commercial CeO₂ NPs, purchased from sigma Aldrich.

The average size of the NPs was obtained by calculating a log-normal distribution curve from the histogram obtained by counting more than 300 NPs from BFTEM images (Figure 4. 16). It can be concluded the sample is formed mainly by NPs of 3.2nm in diameter. However, the NPs could be found in a range of size from 1.5-5.5nm.

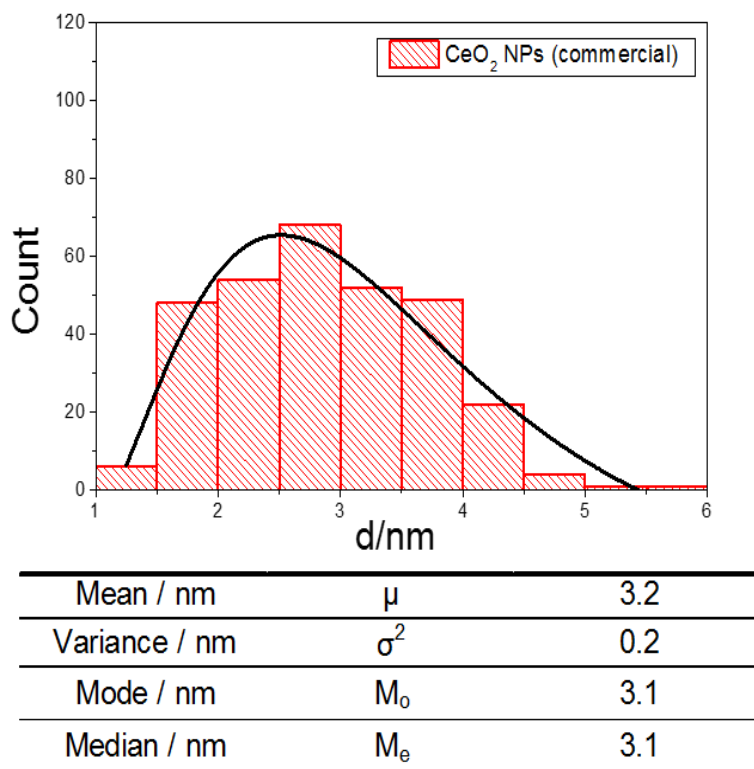


Figure 4. 16: Red bars: Number of CeO₂ NPs of a certain size of commercially purchased from Sigma Aldrich. Black line: log-normal distribution curve of CeO₂ NPs purchased from Sigma Aldrich.

To obtain a powder for the XRD experiments, aggregation thus sedimentation was promoted by adding 5 drops of 3M NaOH to the CeO₂ NPs dispersion. Then, the NPs were separated from the dispersion using centrifugation at 10G for 30min. Finally, the NPs were left to air dry before carrying out the XRD experiments. The XRD pattern which was taken from the sample (Figure 4. 17A) was indexed against the ICDD database, and it was found to be pure ceria according to ICDD file 00-004-0593 with a crystalline cubic structure (Fm-3m) with a=b=c= 5.4110 Å. In addition, SAED patterns (Figure 4. 17B), confirm the sample is formed by cerium (IV) oxide as the SAED rings can be indexed against ICDD 00-004-0593.

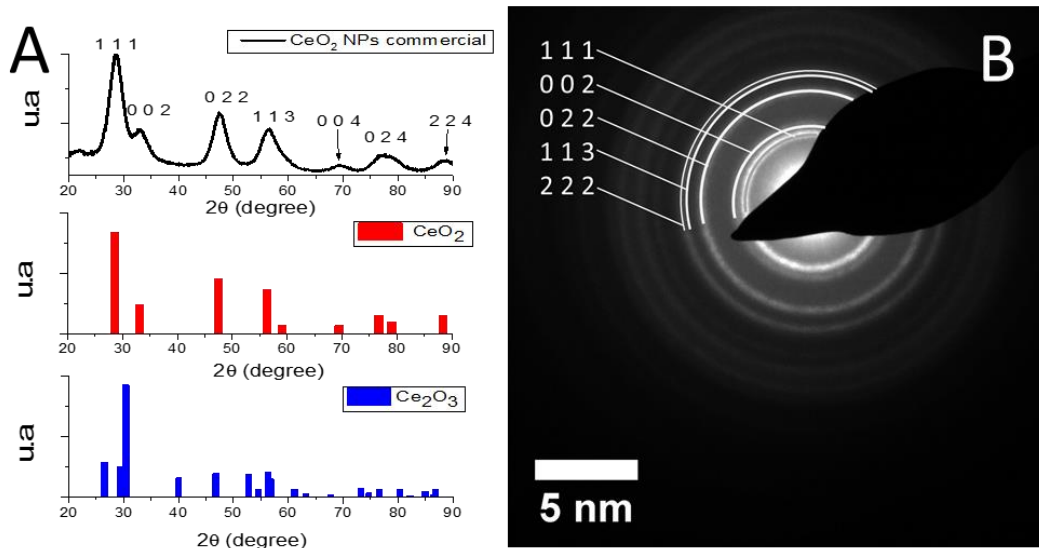


Figure 4. 17: **A**: XRD pattern of: Black line: CeO₂ commercial, Red line: theoretical pattern of CeO₂ NPs (ICDD file: 00-004-0593), Blue line: theoretical pattern of Ce₂O₃ (ICDD file: 00-023-1048). **B**: SAED pattern of CeO₂ NPs synthesised using HMT.

4.3 Coated-CeO₂ NPs

4.3.1 40-PVP coated CeO₂ NPs

40PVP coated CeO₂ NPs were synthesised following the procedure described in 3.2.2.4.1. The TEM images of the synthesis product displayed in Figure 4. 18 show the sample is formed by spheres smaller than 5nm. This fact is also confirmed by Figure 4. 19. The log-normal curve distribution shows the average particle size is 3.36nm with a variation between 1.5nm and 6.5nm. It was calculated by measuring the size of more than 300NPs of BFTEM images. SAED pattern of Figure 4. 20 shows the NPs are cerium (IV) oxide as they can be indexed against ICDD 00-004-0593.

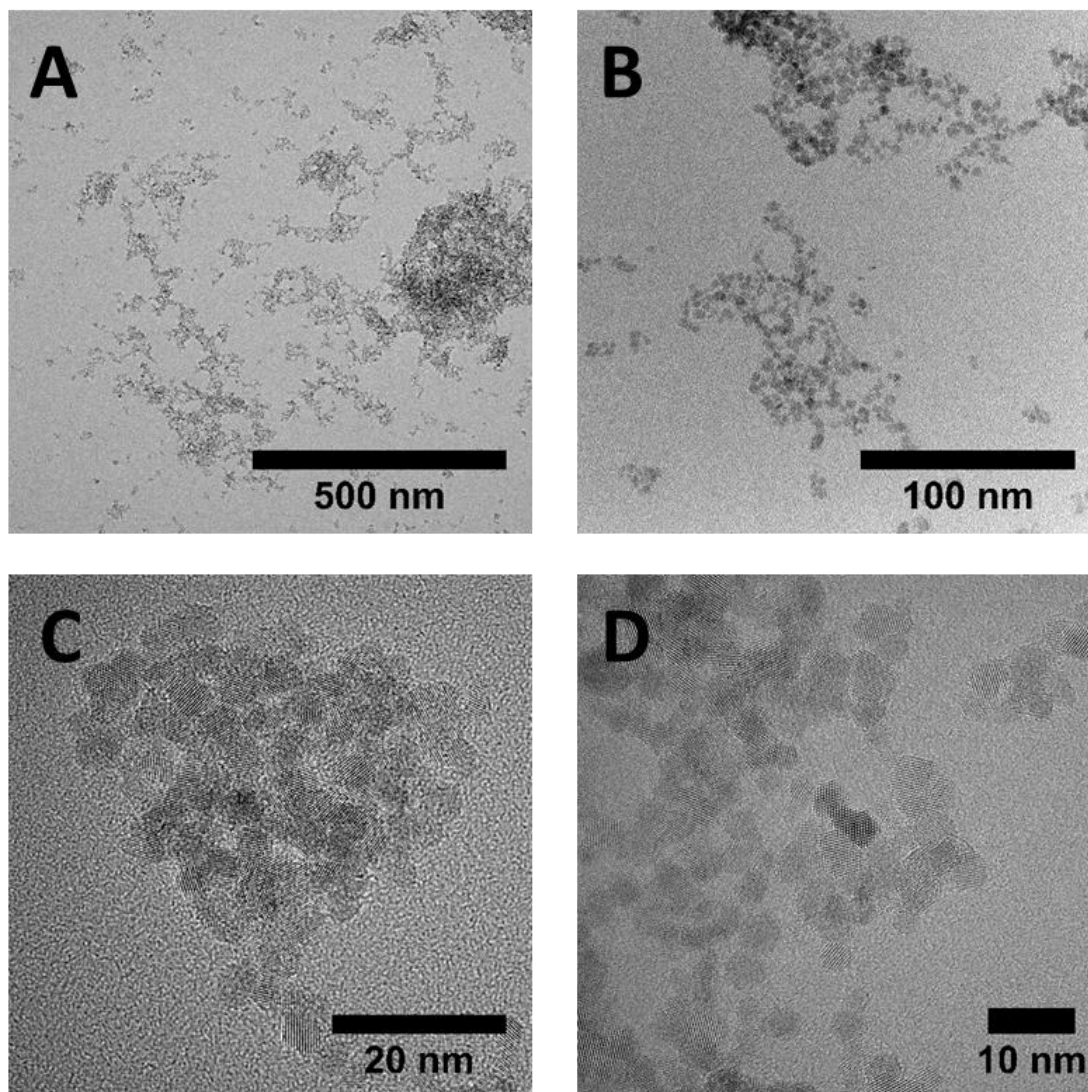


Figure 4. 18: BFTEM images of 40-PVP coated CeO₂ NPs.

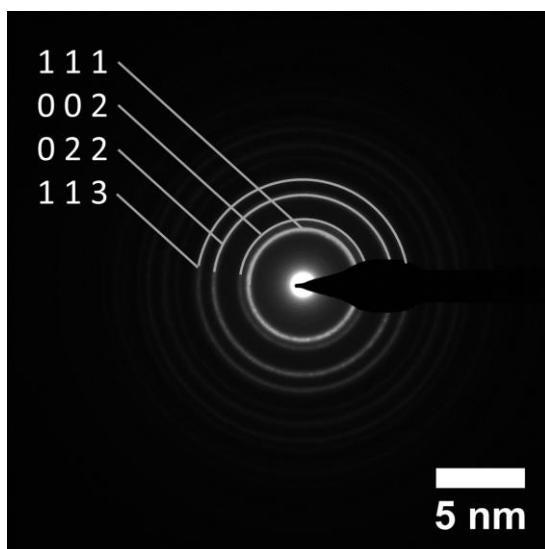


Figure 4. 20: SAED pattern of 40PVP coated CeO_2 NPs.

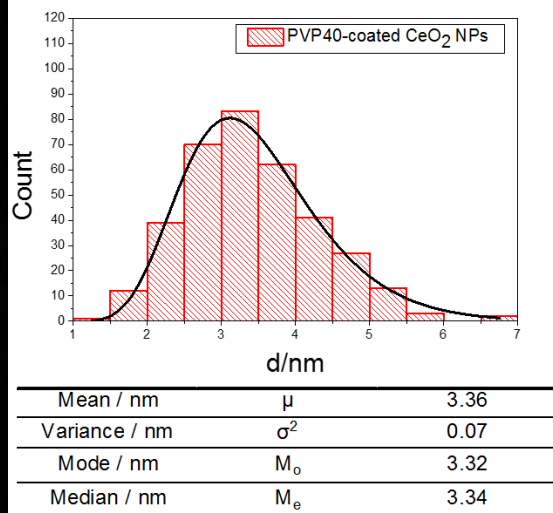


Figure 4. 19: Red bars: Number of 40PVP coated CeO_2 NPs of a certain size. Black line: log-normal distribution curve of the size of 40PVP coated CeO_2 NPs.

4.3.2 PEG-coated CeO₂ NPs

PEG-coated CeO₂ NPs were synthesised following the procedure described in chapter 4.3.2. Figure 4. 21 show the sample is formed by spheres smaller than 10nm. The log-normal distribution curve of Figure 4. 23, obtained by counting 160 NPs, shows the size of the NPs is 3.66nm with a variation in size between 1.5nm and 8nm. The SAED pattern (Figure 4. 22) can be indexed against ICDD 00-004-0593. For this reason, it is concluded the sample is pure ceria

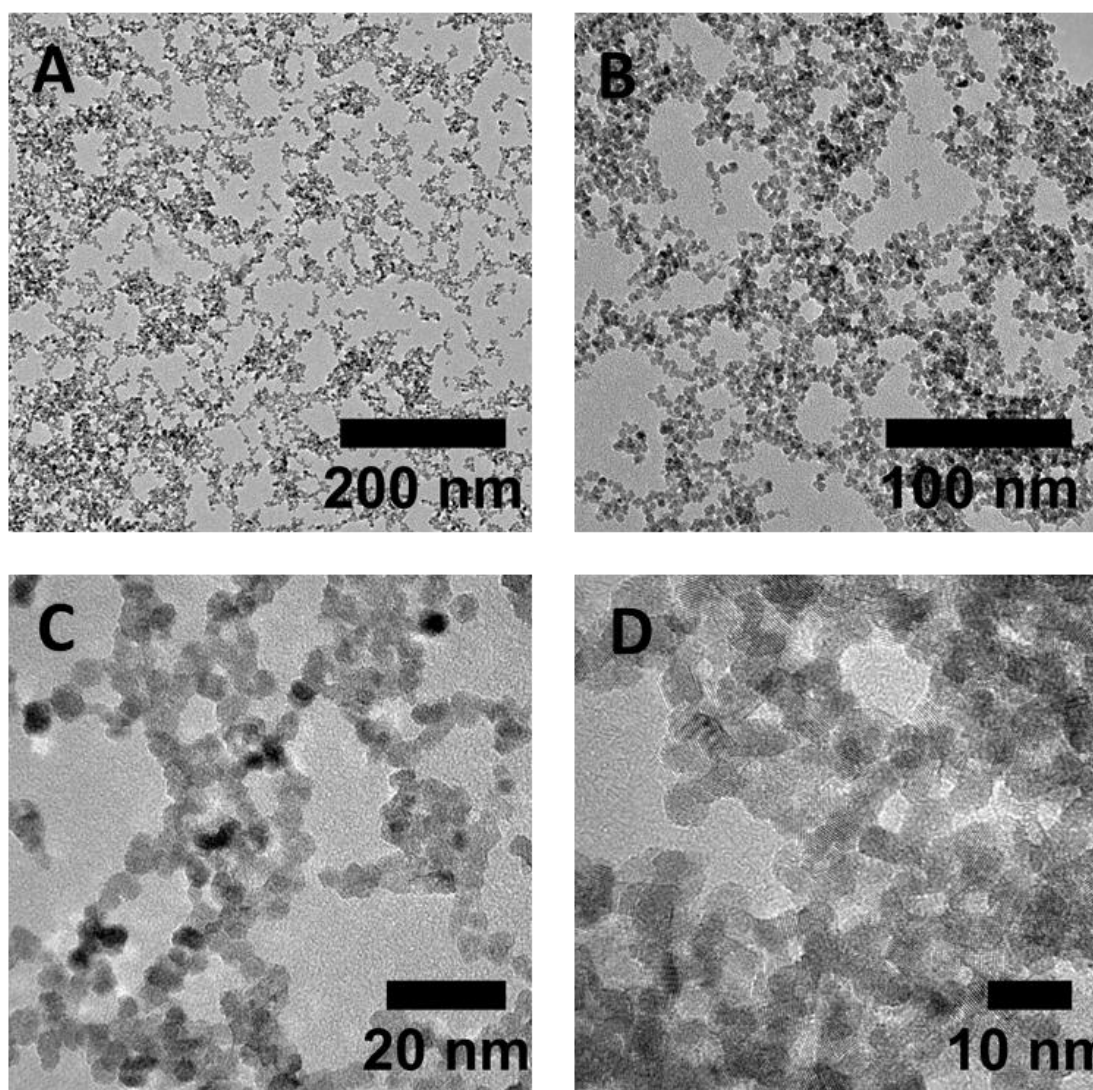
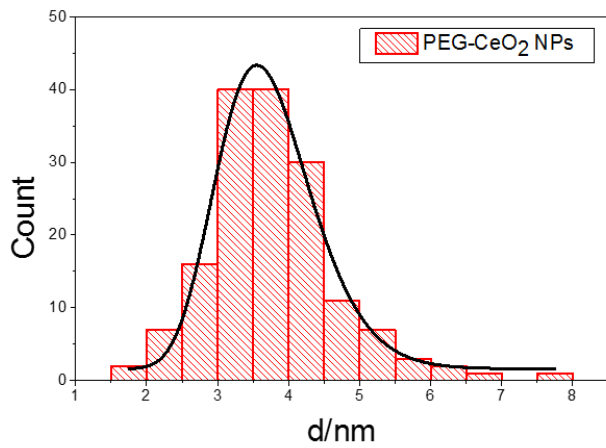


Figure 4. 21: BFTEM images of PEG coated CeO₂ NPs



Mean / nm	μ	3.67
Variance / nm	σ^2	0.03
Mode / nm	M_0	3.66
Median / nm	M_e	3.67

Figure 4. 23: Red bars: Number of PEG coated CeO₂ NPs of a certain size. Black line: log-normal distribution curve of the size of PEG coated CeO₂ NPs.

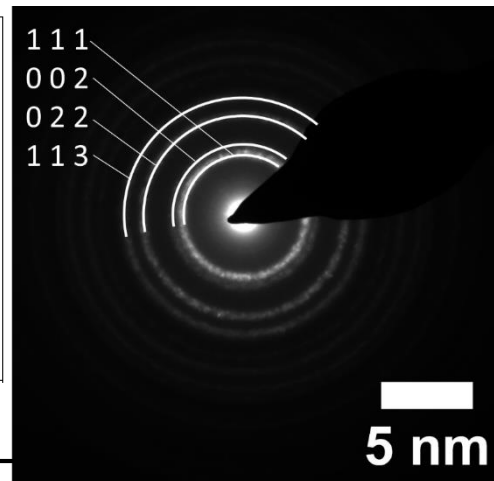


Figure 4. 22: SAED pattern of PEG coated CeO₂ NPs.

4.3.3 Dextran- coated NPs

Dextran coated CeO_2 NPs were synthesised following the procedure described in 0. As observed, the sample is formed by dots smaller than 2nm in diameter. Figure 4. 25 shows the log-normal distribution curve obtained by counting 206 NPs from BFTEM images. As observed, the size of the NPs in the sample ranges between 1nm to 4nm.

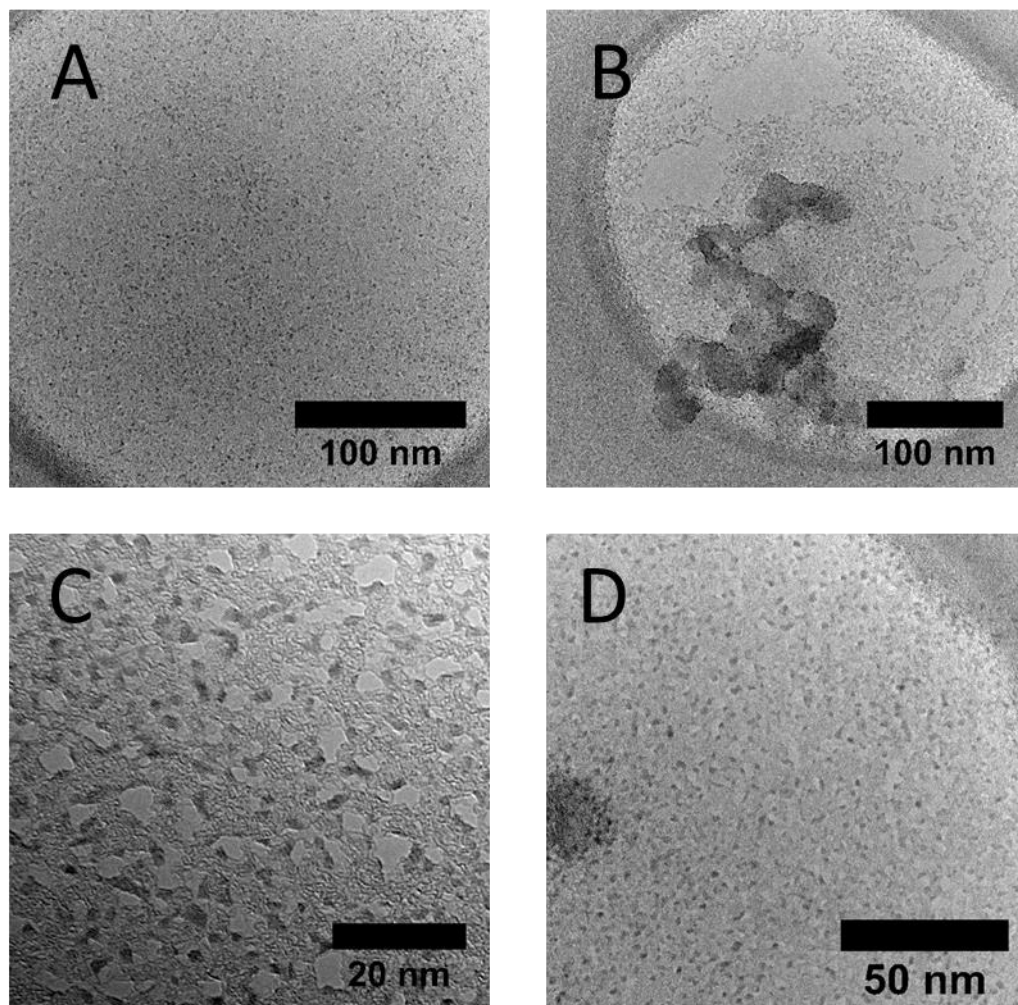
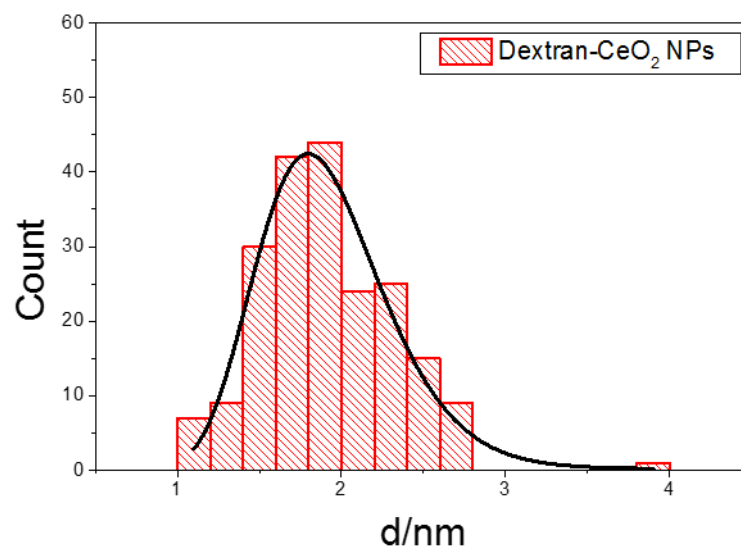


Figure 4. 24: BFTEM images of dextran coated CeO_2 NPs



Mean / nm	μ	1.88
Variance / nm	σ^2	0.04
Mode / nm	M_o	1.84
Median / nm	M_e	1.87

Figure 4. 25: Red bars: Number of dextran coated CeO₂ NPs of a certain size. Black line: log-normal distribution curve of the size of dextran coated CeO₂ NPs.

4.3.4 PBS-treated CeO_2 NPs (PBS- CeO_2 NPs)

Figure 4. 26 shows TEM images of the PBS- CeO_2 NPs (spheres). As observed, the sample is formed by spheres of 4.71 nm of average side. However, the NPs in the sample ranges in sizes from 2nm to 10 nm. Figure 4. 28 shows the log-normal distribution curve obtained from counting 206 nanoparticles from TEM images. The SAED pattern (Figure 4. 27) can be indexed against ICDD 00-004-0593. For this reason, it is concluded the sample is pure ceria

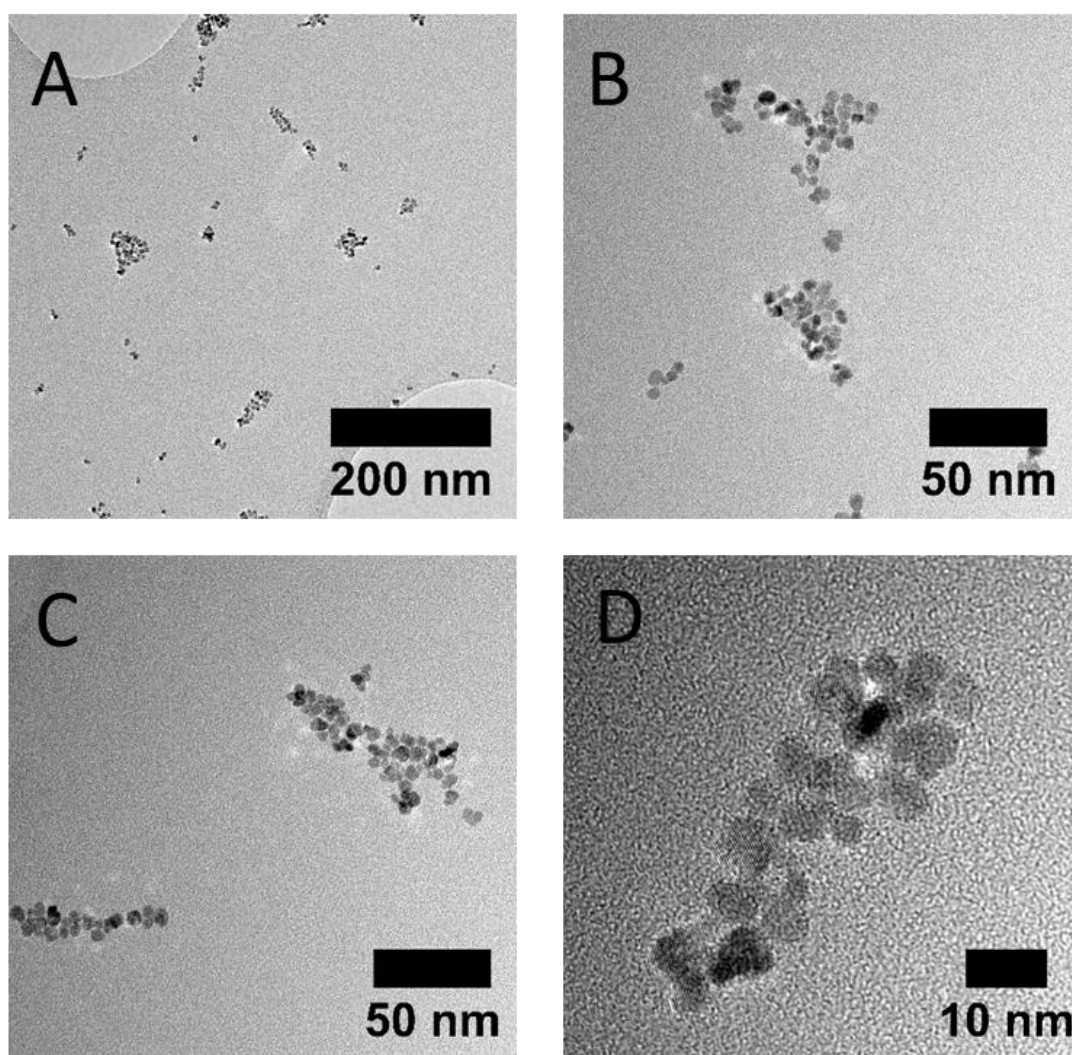
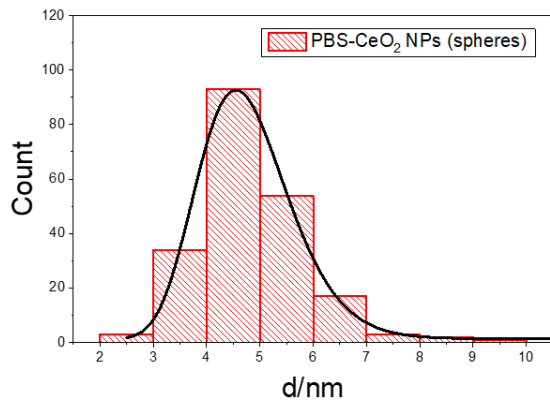


Figure 4. 26: BFTEM images of PBS- CeO_2 NPs (spheres)



Mean / nm	μ	4.71
Variance / nm	σ^2	0.03
Mode / nm	M_o	4.70
Median / nm	M_e	4.70

Figure 4. 28: Red bars: Number of PBS-CeO₂ NPs (spheres) of a certain size. Black line: log-normal distribution curve of the size of PBS-CeO₂ NPs

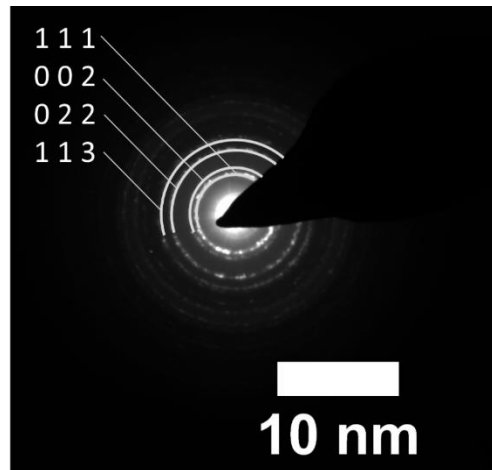


Figure 4. 27: SAED pattern of PBS-CeO₂ NPs

Figure 4. 29 shows BFTEM images of the PBS-CeO₂ NPs (cubes). The log-normal distribution curve (Figure 4. 31), obtained by measuring the size of 201 NPs from BFTEM images, concludes the average NP size is 11.98nm in length. However, the suspension is formed by NPs that range in length of the sides between 5-20nm. The SAED pattern (Figure 4. 30) can be indexed against ICDD 00-004-0593. For this reason, it is concluded the sample is pure ceria.

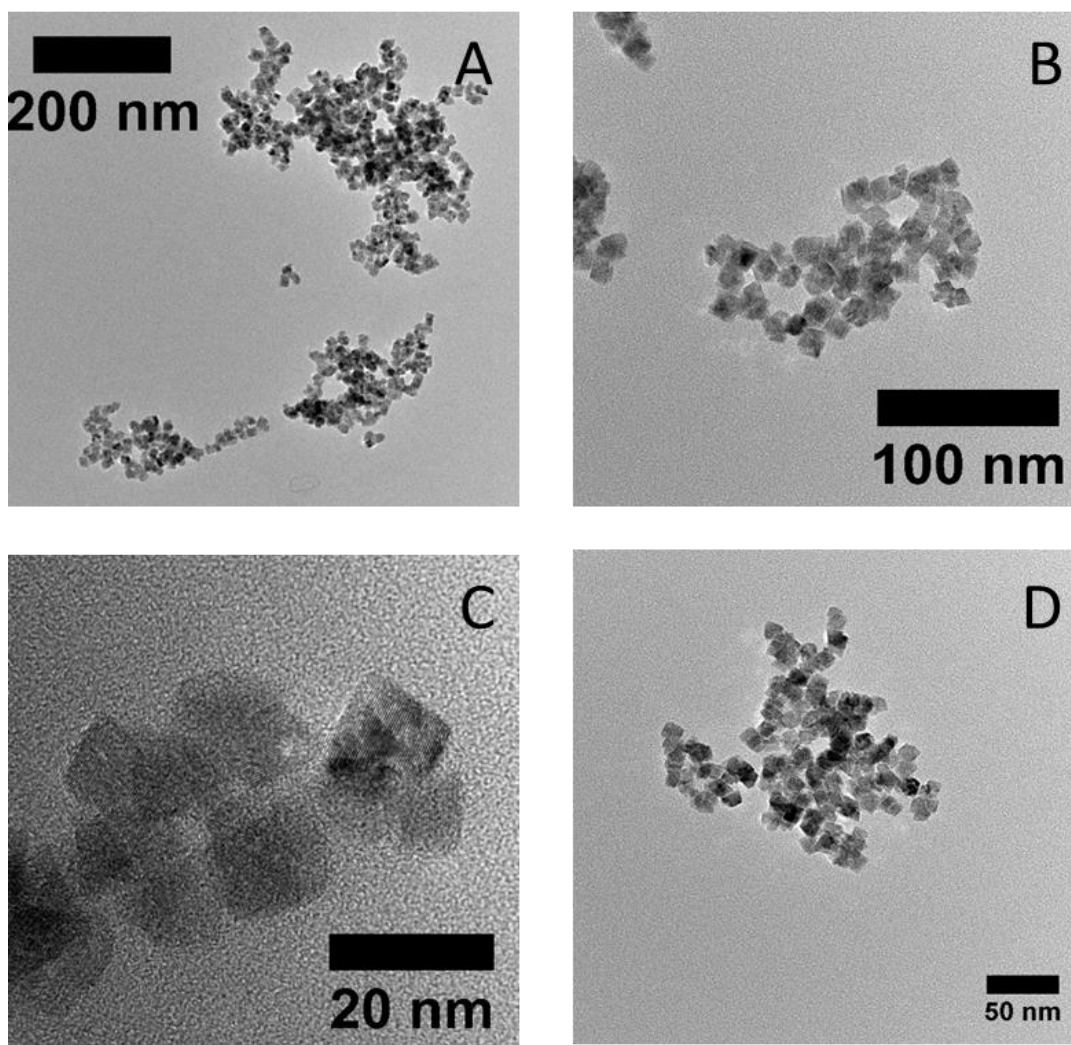


Figure 4. 29: BFTEM images of PBS coated CeO₂ NPs (cubes)

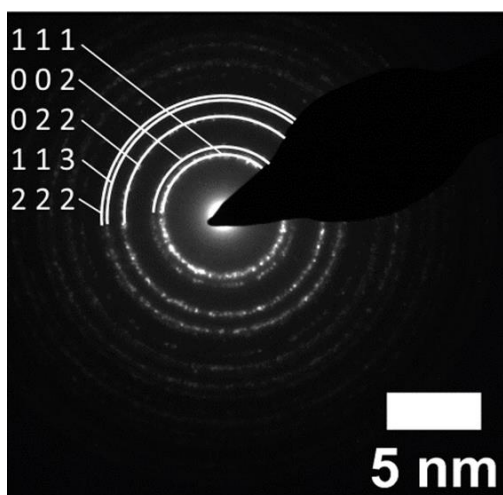
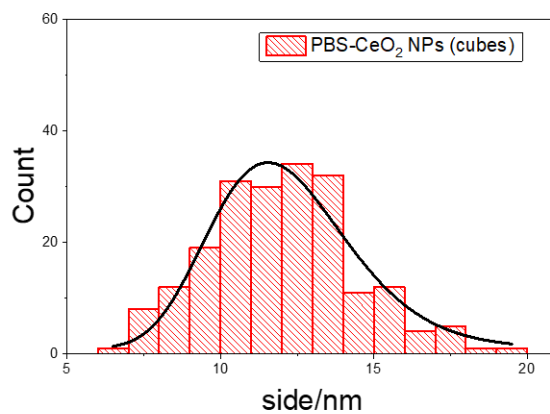


Figure 4. 30: SAED pattern of PBS-CeO₂ NPs



Mean / nm	μ	11.98
Variance / nm	σ^2	0.04
Mode / nm	M_o	11.98
Median / nm	M_e	11.98

Figure 4. 31: Red bars: Number of PBS-CeO₂ NPs (cubes) of a certain size. Black line: log-normal

4.4 Chapter 4. Summary.

Table 4. 2: Description of CeO₂NPs in H₂O

Sample name	Coating	Synthesis method	Synthesis reactants	Origin	Size (nm) EM	Z-Ave (nm)	PdI	Z-Potential (mV)	Main lattice plane
Spheres	N/A	Precipitation	Ce(NO ₃) ₃ , TMAOH	Synthesised	4.28	278	0.3	30.9 ± 0.9	{1 1 1}
Cubes	N/A	Precipitation	Ce(NO ₃) ₃ , HMT	Synthesised	10.57	248	0.5	-1.9 ± 0.5	{1 1 1}
Needles	N/A	Hydrothermal	Ce(NO ₃) ₃ , NaOH	Synthesised	75.61 x 7.13	290	0.6	31 ± 2	{1 1 1}
Dots	N/A	N/A	N/A	Commercial	3.20	4	0.2	-25 ± 3	{1 1 1}
PVP-CeO ₂	PVP	Precipitation	Ce(NO ₃) ₃ , TMAOH, PVP	Synthesised	3.36	87	0.1	-1.1 ± 0.8	{1 1 1}
PEG-CeO ₂	PEG	Precipitation	Ce(NO ₃) ₃ , TMAOH, PEG	Synthesised	3.67	69	0.4	34 ± 3	{1 1 1}
Dextran-CeO ₂	Dextran	Precipitation	Ce(NO ₃) ₃ , TMAOH, Dextran	Synthesised	1.88	121	0.3	-0.4 ± 0.3	N/A
PBS-CeO ₂ (spheres)	PBS	Precipitation	Ce(NO ₃) ₃ , TMAOH	Synthesised	4.71	1709	0.2	-17.4 ± 0.6	{1 1 1}
PBS-CeO ₂ (cubes)	PBS	Precipitation	Ce(NO ₃) ₃ , HMT	Synthesised	11.98	2088	0.7	-19 ± 2	{1 1 1}

Table 4. 2 provides a description of the CeO₂ NPs used in this thesis. As observed, the average sizes of the CeO₂ NPs are within the nano-scale. The size of the NPs from TEM images ranges between 1.88 nm to 75.61 nm. As already mentioned, the needles break after sonication and it is difficult to determine the real size of the needles in dispersion. Despite the problems the needles generate, the NPs were included in this thesis because they provided a different size and shape of NPs to work with and showed interesting results. The size of the NPs in dispersion from DLS is much higher than the size observed from TEM images, which indicates that the NPs aggregate. The Pdl of the spheres (0.3) is lower than the Pdl of the cubes and the needles (0.5 and 0.6, respectively). These values indicate the size distribution of the cubes and needles aggregates is higher than for the spheres. Washed CeO₂ NPs have a Z-Potential of around 30mV in H₂O. This is the case of spheres and needles in H₂O. Washed cubes in H₂O have a Z-Potential close to 0mV, which indicates there is a synthesis product adsorb on the NP surface. Otherwise, cubes would have a Z-Potential close to 30mV. HMT in water discompose with time to form ammonia and formaldehyde to provide the basic medium necessary for the synthesis of the nanoparticles. The EDX spectrum of the cubes (Appendix 4. 9) shows no presence of nitrogen in the sample. However, despite the fact EDX is a good technique for the qualitative detection of elements, it is not suitable for light elements detection. Anyway, the product adsorbed on the surface of the cubes does not produce a response in the RCV. The interaction between HMT and DOPC was studied to avoid false-positive results. HMT did not show an interaction with DOPC. Experimental details can be found in 7.1. Contrary to the spheres, cubes and needles, the dots are highly dispersed. The Z-Ave of the dots (4.nm) is close to the particle size obtained from TEM (3.20nm) and its polydispersity is low 0.2. The reason behind the high stability of the dots is the coating. Despite being sold as “uncoated”, Z-Pot results show a negative charge of -25mV. In a later communication with the supplier, the supplier of the dots indicated citrate was used for the synthesis of the NPs.

Coated CeO₂ NPs are aggregated as well. The Z-Ave values obtained from DLS are bigger than the diameter size obtained from TEM images. Colloidal stability is expected to increase with the presence of coatings as a result of electrostatic repulsions. In this case, it is important to notice that the DLS measurements of the coated NPs are taken from the washed CeO₂ NPs and not from the as synthesised NPs. To carry out the experiments of 7.5, the NPs are washed using milli-Q water and centrifugation to until obtaining a free coating agent supernatant (In-depth details about the methodology can be found in 7.5). During the washing process, molecules of the coating agent can be washed out from the NP surface which would promote aggregation. Nevertheless, Z-Potential values show the NPs are sill coated. PVP-CeO₂ NPs, PEG-CeO₂ NPs, Dextran-CeO₂ NPs and PBS-CeO₂ NPs have a Z-Potential of -1.1mV, +34mV, -0.4mV and -20mV respectively. DLS results show PVP-CeO₂, PEG-CeO₂ and Dextran-CeO₂ NPs form aggregates of around 70-120nm. The PBS treated (PBS-CeO₂ NPs spheres and cubes) form the biggest aggregates.

CHAPTER 5. HIGH-THROUGHPUT ELECTROCHEMICAL DETECTION OF SUBSTANCES

5.1 Voltammetry and Rapid Cyclic Voltammetry

Voltammetry is an electrochemical technique that measures the current flow as a function of an applied potential and the concentration of a compound. Its great sensitivity allows the determination of low electro-active compound concentrations and distinguishes between different oxidation states.

This project focuses on membrane interaction studies using rapid cyclic voltammetry which is a specific type of voltammetry. It measures the generated current produced by an applied potential. In this way, interactions between a “model” membrane and nanoparticles can be analysed by the examination of their voltammograms [10, 127, 128]

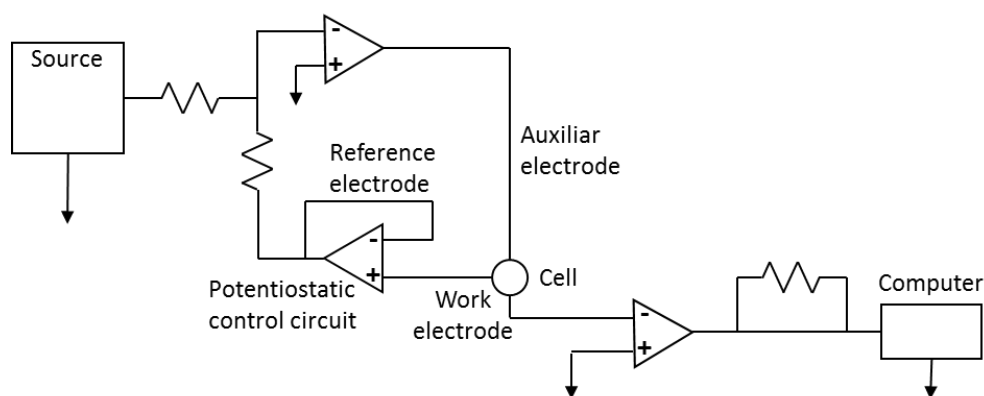
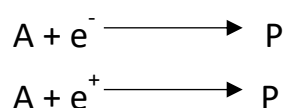


Figure 5. 1: Voltammetry circuit

The flow cell on voltammetry consists of three electrodes in a solution that is formed by the analyte and a background electrolyte. The first electrode is called the microelectrode or working electrode and its potential varies with time. The working electrode used to have a low size in order to decrease its tendency to be polarizable. The second one is the reference electrode, commonly made of mercury or silver, which maintain a constant potential. The last one is the auxiliary electrode. This electrode is used to drive the current from the potential source to the microelectrode. On the other hand, a control circuit adjusts the

potential so that the potential between the microelectrode and the reference electrode are the same as the potential produced by the signal source. The generated current intensity is transformed then in a potential that is registered with time producing a voltammogram.

Electrochemical techniques are known for offering a fast, reproducible and sensitive way to obtain qualitative or quantitative data when an electron flow, which generates a potential answer, is produced. In this way, the activation energy of a reaction can be altered by applying a potential to the electrode which opposes and exceeds the thermodynamic potential and favours one of the reactions [129].



When a semi-redox reaction takes place in function of an applied potential, the reactive species (A) concentration starts to decrease with time while the product concentrations begin to increase. To maintain the necessary superficial concentration over the electrode, a continuous current is needed. The intensity of the current depends on the reactants (A) concentration over the surface of the electrode. This is determined by the transport speed of A from the bulk to the electrified double layer of the electrode. In the meanwhile, the generated product is diffused from the electrode surface to the bulk by a concentration gradient. In this way, the applied potential determines the current [129].

At the same time, the Butler-Volmer equation (eq. 5.1), relates electrical current (j) with the potential (η) produced in an electrode in which anodic and cathodic reaction occurs. It is considered that the potential difference between two charges in the electrical double layer affects the activation energy of both reactions.

$$j = j_0 [e^{(1-\alpha)} - e^{-\alpha f \eta}] \quad \text{eq. 5.1}$$

Where:

- j: electrode current density (A/m²)

- j_0 : exchange current density (A/m^2)
- α : cathodic or anodic charge transfer coefficient, dimensionless
- $f = F/RT$
- F : Faraday constant
- R : universal gas constant
- T : temperature

In addition, electrical current can be related to concentration. Figure 5. 2 displays the variation in current that it is produced when a linear potential is applied.

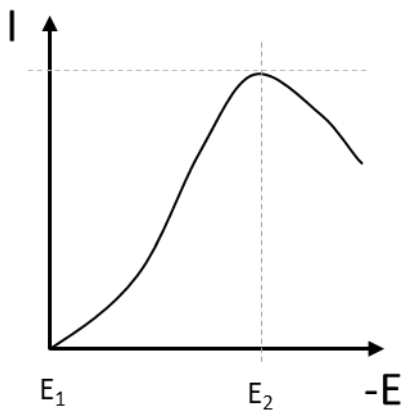


Figure 5. 2: Current variation at an increasing lineal potential.

In this example, the reduction reaction is promoted against the oxidation thanks to a modification of the activation energy. When a potential is applied, an associated current is expected to be obtained. In this way, the current increases up to the high peak current (maximum of the curve) and then it decreases. This behaviour is produced by the concentration of reactants. The potential

favours the reduction reaction and the speed of the reaction increases as much as the potential does. However, with time, reactants transform into products over the electrode surface in such a way the concentration of reactants diminishes and a concentration gradient, placed in the diffusion layer, is generated between the surface of the electrode and the bulk of the solution [130]. In this way, the current declines because the concentration of reactants over the electrode is not enough to maintain the speed of the reaction.

5.1.1 Cyclic voltammetry

Cyclic voltammetry (CV) is characterised by its applied triangular waveform. In rapid cyclic voltammetry (RCV), the potential scan rate is rapid. The potential is applied in cycles that run from E_1 to E_2 and then to E_2 to E_1 . This, produces an associated current with peaks which appears as a voltammogram

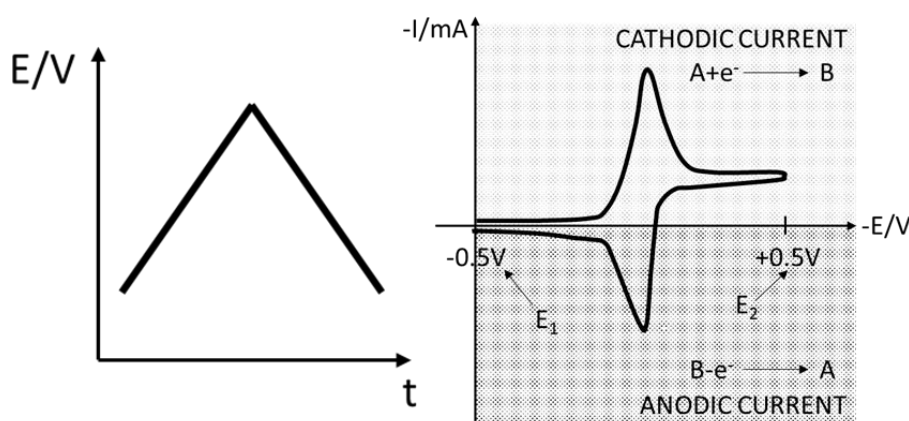


Figure 5. 3: Left graph: cyclical potential variation with time. Right graph: Current variation in function of an applied cyclical potential.

At the same time, that potential becomes more negative, and the cathodic reaction takes place. The current start to increase to the high cathodic peak current (i_{pc}) moment where the concentration of reactive species cannot meet the Nernst equation (eq. 5.2) and the current starts to decrease.

$$E = E^{\circ} - \frac{RT}{nF} \ln(Q) \quad \text{eq. 5.2}$$

Where:

- E: potential of the electrode
- E° : standard potential of the electrode
- R: universal gas constant= $8.31 \text{ J K}^{-1} \text{ mol}^{-1}$
- T: temperature (K)
- n: number of electrons transferred in the reaction
- F: Faraday constant= $96485.33 \text{ C mol}^{-1}$
- Q: reaction quotient

The potential at this point is called cathodic peak potential (E_{pc}). Then, the potential becomes more positive and the inverse reaction occurs. The high

anodic peak current (i_{pa}) belongs to the lowest current point in a voltammogram with a potential (E_{pa}) [130].

The type of obtained graphic varies according to the analyte of study. The position of the voltammogram, peak height and width and curve shape depends on the analyte nature and makes possible to identify and characterize compounds. In addition, the current observed is proportional to the analyte concentration, which enables quantitative experiments to be carried out and limits of detection to be analysed.

$$i_{px} = kC_x \quad \text{eq. 5.3}$$

Where:

- i_{px} = anodic or cathodic peak current
- k = constant
- C_x = analyte concentration

For this reason, it is possible to use voltammetry with quantitative or qualitative purposes to detect active compounds even at very low concentrations (10^{-9} - 10^{-10} M)

This technic can be used with mixtures of reactants too. Each substance has different behaviour in the electrode, so the voltammogram is the sum of the individual components. However, this conduct may not happen when there is some kind of interaction between both analytes.

5.2 The electrified interface

5.2.1 The electric double layer

The electrical double (EDL) layer is formed when an electrolyte solution, which is in contact with a charged surface, gives rise to charge separation. This effect can be caused by [131]:

- The application of an external potential difference
- Adsorption of ions on solid or colloidal particle surfaces.
- The transfer of electrons between a metallic conductor and ions in solution.
- The ionisation of functional groups like: carboxylate, phosphate or amino groups, in micelles, macromolecules or membranes.

Oppositely charged ions are attracted and ions of the same charge are repelled. This effect causes a change in the charge density and produces two charge regions, the surface layer and an oppositely charged ions zone near the surface. In this case, the EDL is produced by the application of an external potential to an electrode immersed in an electrolyte solution.

The structure of the EDL is complex and it is difficult to find a general model which can explain its behaviour in all experimental situations. The behaviour of the EDL depends on the material of the electrode, the type of solvent, the temperature and the different adsorption of ions and molecules [132].

The first approach to the modern concept of EDL was proposed by Helmholtz in 1871. According to his theory, the surface charge of an electrode in an electrolyte solution is neutralised by immobilised counter ions over the electrode surface because of an electrostatic attraction. This theory implies the potential in the interface electrode/solution would linearly fall from the surface of the electrode (Ψ_0) to the bulk as shown in Figure 5. 4a.

Some years later, Gouy and Chapman took into account the random thermal motion of the ions. They suggested that the ions would be dispersed forming a diffuse double layer and that they would not be trapped on the electrode. As a

result, the electric potential would not fall to zero as steeply as in the Helmholtz model Figure 5. 4b.

In 1924 Stern combined the Helmholtz and Gouy-Chapman theories and created the modern concept of EDL. He postulated that both previously mentioned effects took place at the same time. The electrostatically trapped ions would neutralise part of the charge of the electrode (Stern layer) while the rest of the charge would be neutralised by ions generating a diffuse layer out into solution (Figure 5. 4) [133]. This would create two zones where the potential behaves differently. On the one side, a zone where the accumulation of charge in the electrode-electrolyte generates a linear drop of the potential and, on the other side, a zone where the diffuse layer generates an exponential decrease of the potential.

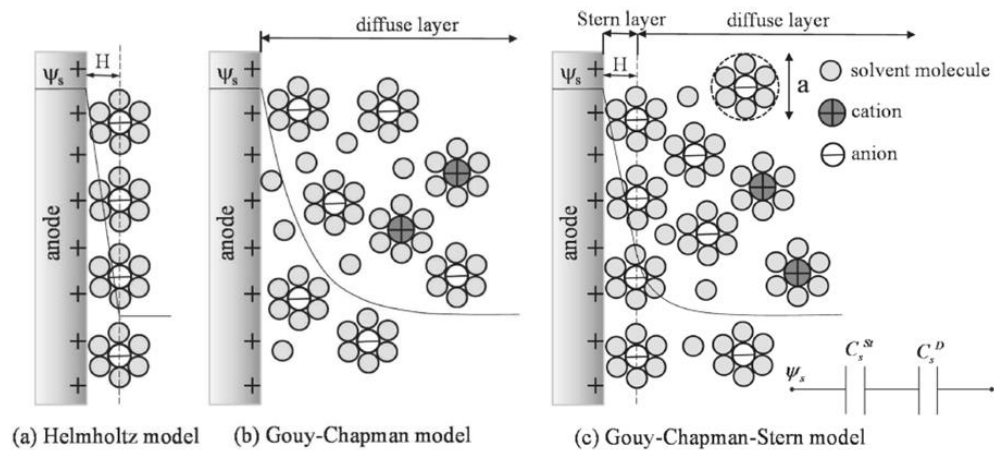


Figure 5. 4: EDL structure showing the arrangement of solvated anions and cations according to: (a) the Helmholtz model. (b) the Gouy-Chapman model. (c) the Gouy-Chapman-Stern model. Copied from [131].

5.2.2 Capacitance and the RC-circuit.

A capacitor, as opposed to a battery, cannot produce new electrons due to a chemical reaction. The capacitance is the ability of a body to accumulate electric charge and it can be defined as the ratio of the charge stored to the voltage applied.

$$C = \frac{Q}{E} = \epsilon_0 \frac{A}{d} \quad \text{eq. 5.4}$$

Where:

- ϵ_0 : vacuum permittivity $\approx 8.854 \cdot 10^{-12}/\text{F}\cdot\text{m}^{-1}$

Equation 5.4 allows the calculation of the stored charge (Q) by isolating the variable (Q) from the equation, where C is the capacitance, Q is the charge and E is the applied voltage. Additionally, capacitance is proportional to the area (A) and inversely proportional to the distance between the two capacitor surfaces (d). A variation on one of them will affect the other. In that way, it is possible to increase the capacitance by increasing the surface area or by decreasing the distance between the surfaces.

In this way, when a potential is applied to an electrode immersed in an electrolyte solution, it is expected that the charge of the surface changes as a function of the potential in order to balance the charge space in the double layer and maintain the electrical neutrality. This means the double layer can behave like a capacitor, serving to store electric charge [134].

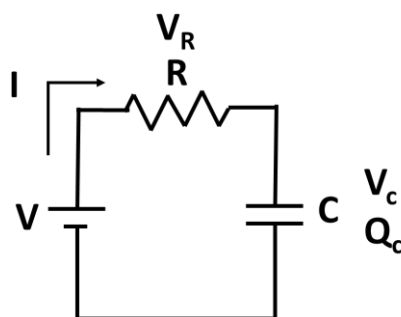


Figure 5. 5: RC-circuit

A resistor/capacitor circuit (RC circuit) is, as the name suggests, an electrical circuit that consists of resistors and capacitors. A simple version of an RC-circuit is shown in Figure 5. 5

Where:

- V: Applied potential
- I: Produced current
- R: resistance
- V_R : potential at the resistor
- C: capacitance
- V_C : Potential at the capacitor
- Q_C : charge of the capacitor

In this situation, when $t= 0s$, a current, able to reach the resistor, is produced due to the applied potential. However, both the charge and the voltage of the capacitor are zero. However, while time passes, $t=\infty$, the current goes through the circuit and reaches the capacitor which starts to charge. In this way, and as mentioned before, the capacitor continues charging until it is fully charged and there is no more current flowing through the circuit or potential at the resistor (Table 5. 1).

Table 5. 1: Potential, charge and current variations in a RC-circuit with time

t=0s	t=∞s
$V_C = 0$	$V_C = V_b$
$Q_C = 0$	$Q_C = C \cdot V_b$
$I = \frac{V_b}{R}$	$I = 0$
$V_R = V_b$	$V_R = 0$

This behaviour can be mathematically described by taking into account the current that dissipates through the resistor and the capacitor with time. In this way, the potential drop of the circuit is:

$$V = V_R + V_C = IR + \frac{Q}{C} \quad (\text{eq. 5.5})$$

In addition, the current can be described as the rate at which the charge is flowing between two points when a difference of potential is applied:

$$V = \frac{dQ}{dt}R + \frac{Q}{c} \quad (\text{eq. 5.6})$$

And re-arranging the equation:

$$\frac{dQ}{dt} = \frac{1}{R} \left(V - \frac{Q}{R} \right); \frac{dQ}{V - \frac{Q}{R}} = \frac{dt}{R} \quad (\text{eq. 5.7})$$

As charge depends on time, the previous equation can be solved by integrating it between the charge at time zero and the charge (Q) at a certain time (t). In this way:

$$\int_0^Q \frac{dQ}{(Q - CV)} = \int_0^t -\frac{dt}{RC}; [\ln(Q - CV)]_0^Q = [\ln(RC)]_0^t \quad (\text{eq. 5.8})$$

$$\ln\left(\frac{Q - CV}{-CV}\right) = \frac{-t}{RC}; \frac{Q - CV}{-CV} = e^{\frac{-t}{RC}} \quad (\text{eq. 5.9})$$

And re-arranging the expression that relates the charge of the capacitor with time (5.7), the following equation is obtained. Where RC is the time constant also known by 'τ'.

$$Q = CV \left(1 - e^{\frac{-t}{RC}} \right) = CV \left(1 - e^{\frac{-t}{\tau}} \right) \quad (\text{eq. 5.10})$$

At this point, the variation of the potential at the capacitor with time can be calculated from combining eq. 5.4 and eq. 5.10. In this way:

$$V_c = \frac{Q(t)}{c} \quad (\text{eq. 5.11})$$

$$\frac{Q}{c} = \frac{CV}{c} \left(1 - e^{-t/\tau} \right) \quad (\text{eq. 5.12})$$

$$V_c = V \left(1 - e^{-t/\tau} \right) \quad (\text{eq. 5.13})$$

5.2.3 *Biological membranes, the double layer and the RC-Circuit*

Phospholipids have a polar head group formed by a phosphate and an amino acid, a glycerol backbone and two apolar fatty acid chains. These singular characteristics permit phospholipids to act as amphipathic substances and thus allow the formation of close structures by the association of polar and apolar sides in aqueous media. Phospholipid polar heads in an aqueous environment tend to associate due to electrostatic interactions produced between the polar heads and the formation of hydrogen bonds with water. In addition, the apolar phospholipid tails tend to aggregate due to the hydrophobic effect. For this reason, and as mentioned before, they can form close structures [135]. However, the structures are not rigid. Phospholipids can change their location by lateral diffusion in the same monolayer or by transversal diffusion (flip-flop) with the opposite one. In this way, they are joined together through cooperative non-polar interactions to form bilayers [136].

Biological membranes are formed by proteins embedded in a phospholipid bilayer. In cells, the membrane is responsible for keeping extra and intracellular media separated and control the exchange of substances between both media. They are, in general, permeable to non-polar substances and impermeable to polar substances. To cross and penetrate apolar part of the membrane, ionic and polar substances must detach their hydration water, a process which is energetically unfavourable for this type of molecules. Nevertheless, the ions exchange between both sides of the membrane is always taking place[136].

The cell is a heterogeneous environment. It is formed from different substances with diverse functional groups, each having different dissociation constants which alter the electric charge at physiological pH. In addition, intra and extracellular media have a different composition what produces concentration gradients.

For these reasons, the lipid bilayer can be described using a resistance-capacitance (RC) circuit model as shown in Figure 5. 6.

As mentioned before, ions are present at different concentrations in the extra and intracellular media. Due to the composition of the extra and intracellular media, both faces of the lipid bilayer are exposed to different substances. This concentration gradient generates a difference of potential known as the membrane potential. In spite of this, the system is electro-neutral. Negatively charged proteins cannot leave the cell and move freely. Negatively and positively charges of the inner and extracellular sides respectively, line up through the membrane to compensate the charge. For this reason, the lipid bilayer behaves as a capacitor storing charge.

Under natural conditions, the ionic channels regulate the passage of ions through the membrane. By doing so, when the passage of ions is allowed, the charge moves from one part of the membrane to the other and generates a current. They are represented in the circuit as the resistances.

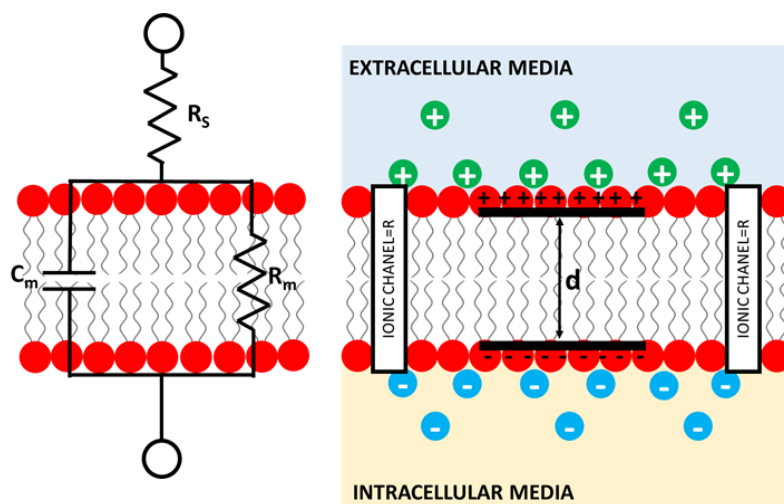


Figure 5. 6:Left graph: RC-circuit in a phospholipid bilayer. Right graph: Equivalent RC-circuit in a cellular membrane

Where:

- C_m : membrane capacitance
- R_m : membrane resistance
- R_s : total resistance of the media (bathing solution and electrodes)

5.3 Adsorption

Adsorption is a superficial phenomenon that happens when an atom, ion or molecule of a gas, liquid or dissolved solid (adsorbate) accumulates at a surface (adsorbent). This process depends on the affinity between adsorbate and adsorbent and it is a consequence of surface charge and other factors. The atoms on the surface of a material (adsorbent) are not completely surrounded by atoms, but they are partially exposed to the surroundings so that they can attract substances (adsorbate). Two types of adsorption can be produced according to the intermolecular forces produced between adsorbate and adsorbent. However, the adsorption phenomena are usually produced by a combination of them.

- Physisorption: The adsorbent is not fixed in a place and it can transfer to another site in the interphase. In this case, the adsorbent is attracted to the adsorbate due to weak Van der Waals forces.
- Chemisorption: A chemical bond is formed between adsorbent and adsorbate. As a consequence, the covalent bonding impedes the adsorbent from moving freely and the adsorbate is linked to the surface.

5.4 Relationship between the electrical interface, capacitance, current phospholipids, adsorption and RCV.

As previously explained in this chapter, the cell membrane can be modelled by an RC-circuit. For this reason, it is possible to model the operation of a cellular membrane using an applied potential and an electrochemical circuit.

Phospholipids behaviour have been studied using electrochemistry techniques for many years [137-139]. Electrochemistry allows the analysis of cell membrane model performance against different substances using RCV. In this way, Nelson et al. [10] created a sensor element able to mimic a phospholipid monolayer using voltammetry.

In general terms, the sensor consists of an Ag/Cl reference electrode, a Pt auxiliary electrode and a mercury coated Pt electrode (Hg/Pt) where phospholipids are deposited. When a potential is applied, it generates a difference in potential between the surface of the electrode and the bulk solution. This change in potential causes ions to be attracted to the surface of the electrode creating an EDL. In consequence, it can be said that the surface of the electrode acts as a capacitor storing charge.

As previously mentioned, the Stern-Helmholtz and Gouy-Chapman model for the EDL states that the EDL is formed by two regions where the force-potential plot has different lope as described followingly. The Stern layer, where the potential drops abruptly and linearly, and an outer layer which is formed by a diffuse layer of ions where the force-potential curve decreases exponentially. In this way, the capacitance in the interface (C_d) electrode/solution can be represented by two capacitors in series:

$$\frac{1}{c_d} = \frac{1}{c_s} + \frac{1}{c_D} \quad (\text{eq 5.14})$$

- C_S : capacitance of the Stern or Compact Layer = $\epsilon\epsilon_0/d$ (eq 5.15)
- C_D : capacitance of the Diffuse layer = $228zc^{1/5}\cosh(19.5zV_i)$ (eq 5.16)

Where:

- ϵ_0 : permittivity of the free space= $8.854 \cdot 10^{-12} \text{ F} \cdot \text{m}^{-1}$
- ϵ : dielectric constant of the medium
- d : interplate spacing
- z : numerical charge of the ion in solution
- c : concentration
- V_i : potential at the interface

In addition, the effect of organics on a dropping mercury electrode (DME) was studied in 1902 by Gouy [140]. He discovered that the interfacial tension of the DME versus an applied potential varied in the presence of organics. In this way, the interfacial tension of the DME in the presence of heptanol was lower than the one obtained with the clean electrode.

Further, capacitance and interfacial tension can be related by double differentiating the interfacial tension versus the applied potential. As a result, two characteristic capacitance peaks for the DME with heptanol were observed while the peaks were not observed on the clean DME [141]. Also, capacitance and current can be related by using eq 5.3. In a similar but not identical way, when phospholipids are deposited on a Hg electrode, they produce a two peaks capacitance-current response.

5.5 The electrochemical sensor device (ESD)

5.5.1 The device

A general scheme about how the electrochemical sensor device works is shown in Figure 5. 7. It comprises mainly of a flow system, a flow cell and a computer. The flow system is formed by a buffer reservoir and a peristaltic pump that provides a continuous flow of buffer through the system. In addition, the buffer is directly connected to an argon gas (Ar(g)) source to eliminate O₂ (g) from solution. Then, the phospholipid or sample can be introduced to the system and reach the electrochemical flow cell or sensing element. The flow cell consists of a microfabricated wafer-based device (WBD) that acts as the sensor element, embedded in a Perspex case that closes it to air. The WBD is connected to a PGSTAT12 potentiostat (Autolab, Metrohm) and to a computer.

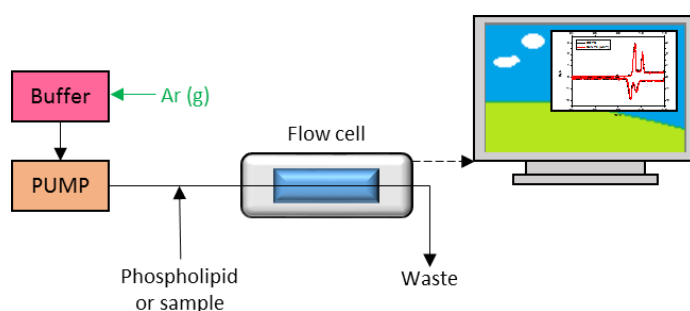


Figure 5. 7: ESD diagram. The ESD device is composed by a buffer reservoir, a pump, a flow cell and a computer

5.5.1.1 The flow cell

The microfabricated electrode consists of a chip with two Pt auxiliary electrodes and eight working electrodes all connected by Si₃N₄ in a silicon wafer. The Ag/Cl reference electrode is located in the Perspex case in such a way that it is perpendicularly oriented to the microfabricated electrode. All the electrodes are connected to the potentiostat so RCV measurements can be taken.

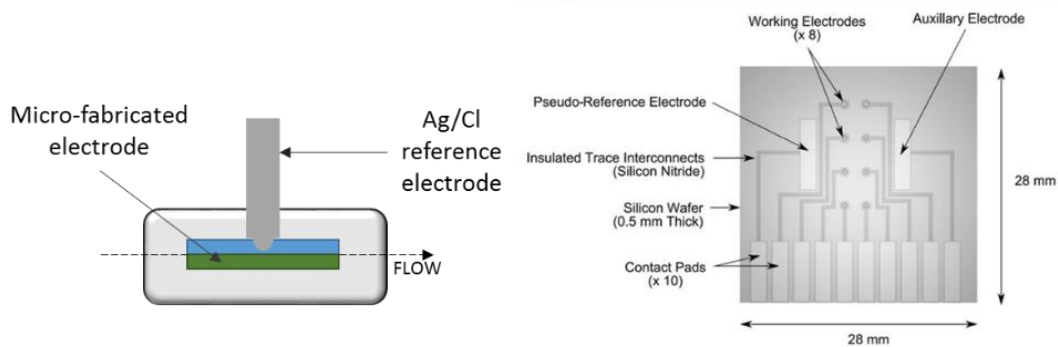


Figure 5. 8: Left image: EDS electrochemical cell with the micro-fabricated electrode and the Ag/Cl reference electrode. Right image: Micro-fabricated electrode with the eight working electrodes and the auxiliary electrodes.

As mentioned before, the working electrodes of the flow cell are Hg coated platinum electrodes (Hg/Pt) where phospholipids can be deposited (Figure 5. 8) [12, 142].

Traditionally, other mercury (Hg) electrodes as hanging mercury drop electrode (HDME), have been used in voltammetry as microelectrodes due to their ability to renew the mercury and create a new and clean surface to work with. For this reason, early versions of the device used an HDME as a working electrode [143]. However, owing to their fragility and the difficulty of an HDME electrode into the cell, it was replaced for a micro-fabricated platinum Hg film electrode. Nelson, A.L. et al. [142, 144] developed the technique to its actual stage.

The usage of a Hg/Pt electrode offers advantages over the HDME electrode. Pt offers a static and small platform to work in and thanks to the significant affinity between Hg and Pt at the Hg/Pt interface [145], it allows strong bonds to be formed. In this way, the amount of Hg is minimised.

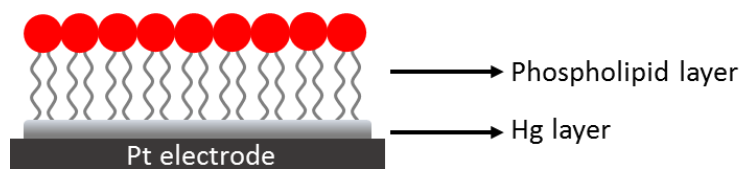


Figure 5. 9: Diagram of the working electrode with the deposited Hg and the phospholipid layer over it.

Hg is a very suitable if not unique metal to use for phospholipid deposition and electrochemistry due to its properties:

1. Hg can be polarised in aqueous solution due to the high hydrogen overpotential thereon so that it can work in a wide range of potentials
2. Hg can be electrodeposited in a well-defined and reproducible geometry. It can be steadily bound to the Pt surface so that the Hg film is stable on the Pt.
3. The Hg apolarity is compatible with the apolar tails of phospholipids (45 en draft cerium).
4. The Hg surface is infinitely smooth, and the Hg is fluid, providing a platform where phospholipids can freely move and re-arrange.

5.5.2 *The ESD and the RCV response. What is it?*

As mentioned before in section 5.4, RCV can be used to model cell membrane behaviour. In this case, it is possible to model half of a lipid bilayer by depositing phospholipids on a Hg/Pt microelectrode by cause of their compatible properties.

Once phospholipids are deposited on the Hg/Pt microelectrode and the potential excursion is applied, the phospholipids act as a dielectric between the charge on the electrode and the charge in solution. In this way, the capacitance decreases. These non-linear changes in capacitance can be registered against an applied potential using RCV to produce voltammograms. These voltammograms have representative phase transition capacitance peaks of each compound [143, 146].

In this way, when a membrane-active substance interacts with the lipid monolayer, the forces within the layer changes. As a result, the capacitance current peaks of the voltammogram decrease. The interaction depends both in the type of phospholipid and substance to be tested. For this reason, this is a unique technique to study single membrane vs compounds interaction from a fundamental point of view.


5.5.3 Uses and limitations

In recent years the ESD has been mainly used to study the effect of membrane disruption and related toxicity. When a toxic/active substance interacts with the phospholipids on the Hg/Pt electrode, suppression or even disappearance of the capacitance-current peak is produced indicating monolayer disruption. Following this principle, the ESD has been used as a biosensor to assess the toxicity of organics [132] or low molecular weight narcotic compounds [147] in water. In addition, recent inter-calibration toxicity results show a good correlation between the capacitance-current peaks suppression, produced when phospholipids are in contact with an active substance, and cell death, produced in cellular culture [11].

In addition, the ESD has been previously used to study the behaviour of nanoparticles when in contact with phospholipids. In this way, Vakurov looked at the interaction of ZnO NPs [127] and [128] TiO₂ NPs with DOPC. Vakurov reported the interaction of NPs was dependant on size. Small size TiO₂ NPs interacted stronger with a DOPC monolayer than the bigger particles. In addition, both ZnO and TiO₂ NPs showed a semiconductor effect when interacting with the DOPC monolayer. Also recently, Nicola William used the ESD to study the interaction of other NPs as Au NPs and Ag NPs. The correspondent results are under review for publication at the moment.

Also, the ESD is not only able to give information in terms of interaction or no interaction (toxicity or not). It is also able to:

- Give an RCV response in less than 5min
- Provide information on how a particular substance interacts with the system.
- Provide quantitative results by relating the degree of interaction with calibration curves
- Distinguish between crystal structures.
- Distinguish between oxidation states.



As mentioned before, the ESD is based on RCV and for this reason, it is subject to the background noise. Electrical equipment and poorly insulated connections can increase the noise on the voltammograms making the testing impossible to carry out. In addition, due to the instrumental error produced by the background noise, there is another error typical to the system under study. When a phospholipid is deposited in the Hg/Pt electrode, the peaks of the produced voltammogram are subjected to small arbitrary changes in current that depend on the medium and type of phospholipid. This changes should be taken into account when testing to avoid false-positive results.

In addition, the ESD is very sensitive, and for this reason, the system must be clean before carrying out any test. Contamination of the system could cause incorrect deposition of the phospholipids or false-positive results.

5.6 Methods.

5.6.1 *The ESD start-up*

RCV is a very sensitive technique and the ESD has proven to be sensitive to compounds at very low concentrations. For example, it is able to detect pyrene at InM concentration. For this reason, a very clean chip surface is necessary for the Hg electro-deposition. Any contaminant could affect the Hg deposition or the correct cell operation. Consequently, the WBD must be cleaned using piranha solution. The WBD is placed into a Pyrex flask. Then, the piranha solution is made in the same flask by slowly pouring 30% H₂O₂ into sulphuric acid (98%) in a ratio of 3:1 (V:V). The reaction is exothermic, long and extremely corrosive. For this reason, the reaction must be prepared in a fume cupboard and it must be left to finish open to the atmosphere overnight before continuing with the cleaning process. The next day, when the piranha solution is cold and no bubbles come out from it, the piranha solution is diluted with copious amounts of water. Then, the piranha solution can be disposed of through the sink under a continuous flow of water. Later, the chip, which remains in the flask, is washed with milli-Q water. Finally, the chip can be taken from the flask and it is rinsed again with milli-Q water and it is dried using compressed air.

Then, the mercury can be deposited following the next procedure:

1. A tiny drop of Hg is placed over each of the Pt electrodes located on the cell chip.
2. The electrochemical cell is closed
3. PBS is allowed to circulate through the cell
4. Hg surface is cleaned by applying potential cycles between -0.4V and -3.0V until RCV profile is obtained (Figure 5. 10a)

5. Then, the potential cycles are switched from -0.4V to -1.2V and the characteristic RCV profile of Hg appears as shown in Figure 5. 10b

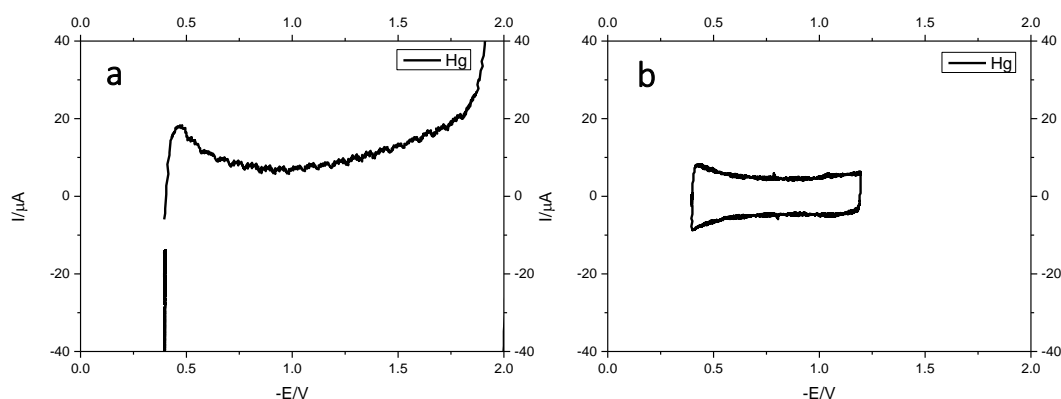


Figure 5. 10: RCV voltammograms of the un-coated Hg/Pt before phospholipid deposition. Left graph: RCV voltammogram recorded at 100Vs^{-1} with a potential excursion from -0.4V to -3.0V. Right graph: RCV voltammogram recorded at 40Vs^{-1} with a potential excursion from -0.4V to -1.2V.

5.6.2 RCV measurements

The following procedure describes, in steps, a general method to test samples using the ESD. This method is used in almost all experiments and any exception from it will be mentioned when appropriate.

1. De-oxygenation of the buffer: The buffer was purged for 30min with Ar(g)
2. Flow: A constant of the buffer is set to 4.67 mL min^{-1} .
3. Cleaning of the electrode: The Hg/Pt electrode is cleaned by a potential excursion from -0.4V to -3.0V at a scan rate of 100Vs^{-1} for 5min. At that negative potentials, the phospholipids are detached from the electrode surface with time. It allows eliminating possible contaminants prior to experiments.
4. Phospholipids deposition: First, 2 mg/mL of the desired phospholipid is dispersed in milli-Q water. Then, the solution is de-oxygenated with Ar(g) for 15min. To deposit the phospholipid, 1mL of the solution is introduced into the system when potential cycles from -0.4V to -3.0V at a scan rate of 100Vs^{-1} are applied. At that moment, the characteristic peaks of the phospholipid appear and the potential set to -0.4V.

5. Acquisition of the RCV phospholipid profile: Each type of phospholipid has its unique RCV profile when deposited over a Hg/Pt electrode. When potential cycles are changed from -0.4V to -1.2V at a scan rate of 40Vs^{-1} , the characteristic phospholipid voltammogram appears.
6. The potential is set to -0.4V and the buffer flow is stopped.
7. Sample testing: All samples are sonicated for 30 min before the test. Then, they are deoxygenated for 5min with Ar(g). Later, 1mL of the phospholipids, at defined concentrations, is introduced in the system without the flow. After that, the flow is switched on again and cycles from -0.4V to -1.2V at a scan rate of 40Vs^{-1} are applied.

CHAPTER 6. ELECTROCHEMICAL BEHAVIOUR OF DIFFERENT LIPIDS. STABILITY OF PHOSPHOLIPIDS ON THE Hg/Pt

Cell membranes are heterogeneous systems which constitute a bilayer composed by lipids and proteins. Also, the composition of the cellular membrane differs according to the function of the cell and the type of organism which the cell belongs to. For example, the composition of the membrane is different for brain cells or muscle cells, and it varies between prokaryotes and eukaryotes.

Also, phospholipids can join together through cooperative weak non-polar interactions [135]. These interactions allow phospholipids to be fluid. They can rotate, move to other parts in the membrane (lateral diffusion) or interchange from one part of the monolayer to another (transversal diffusion) within a lipid bilayer.

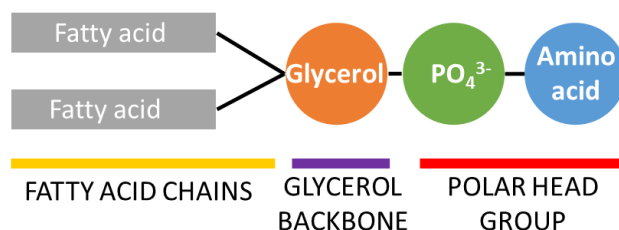


Figure 6. 1: Diagram of a phospholipid

However, the main driving force leading to phospholipid self-assembly is the hydrophobic effect or tendency of non-polar groups to avoid water [148]. Phospholipids are formed from a polar head group, containing an amino acid and a phosphate group, a glycerol backbone and usually two fatty acid chains which are hydrophilic (Figure 6. 1). In this way, hydrophilic tails tend to aggregate together forming closed structures. The preferred amphiphilic supramolecular structure depends mainly on steric factors (Figure 6. 2). However, the environmental conditions also play a vital role as well in the

preferred supramolecular structure phospholipids acquire. Phospholipids tend to aggregate forming the most relaxed structure possible. For example, the modification of the temperature produces changes in the angle between the hydrophobic tails affecting the supramolecular structure. Amphiphiles with one acyl chain tend to form micelles (spherical, ellipsoid or cylindrical) by the association of their apolar tails (HI structures). Phospholipids with two non-parallel apolar tails tend to form hexagonal structures (HII structures) in water. The hydrophilic tails are located facing the exterior of the structure while polar heads are facing in forming a cylindrical core of water [149]. Phospholipids with parallel fatty chains tend to form bilayers, multilamellar liposomes or vesicles (L structures) [150]. However, the supramolecular structure of phospholipids can vary according to environmental conditions as temperature, or ionic strength [149].

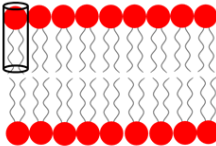
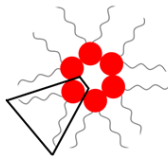
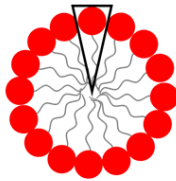
Phospholipid	Preferred supramolecular structure
DOPC, DOPG	Lamellar organisation (L) 
DOPE, DOPA, DOPS	Hexagonal organisation (HII) 
Lysolipids	Micelle organisation (HI) 

Figure 6. 2: Preferred supramolecular structure depending on steric factors.

Other phospholipids physical characteristics can affect phospholipid properties as well. For example, the transition temperature (T_c) between the gel state and the liquid crystalline state of a given phospholipid varies depending on the polar head and on the length of the fatty acid chains of the phospholipid [151]. The longer the hydrophilic tails, the higher the enthalpy of the transition due to the strength of the hydrophilic interactions [152]. In addition, the presence of a double bond in the apolar tails decreases T_c [151].

Also, the pK of the phospholipids varies according to the functional groups on their polar heads. Table 6.1 shows the pK_a values of phospholipids with different polar heads and identical fatty acid chains (Figure 6.3). The data has been collected from reference [153].

Table 6.1: pK value of different phospholipids

Phospholipid	pK_{a1}	pK_{a2}	pK_{a3}
DOPC	1.0	-	-
DOPE	1.7	11.3	-
DOPS	2.6	5.5	11.55
DOPA	3.0	8.0	-
DOPG	3.5	-	-

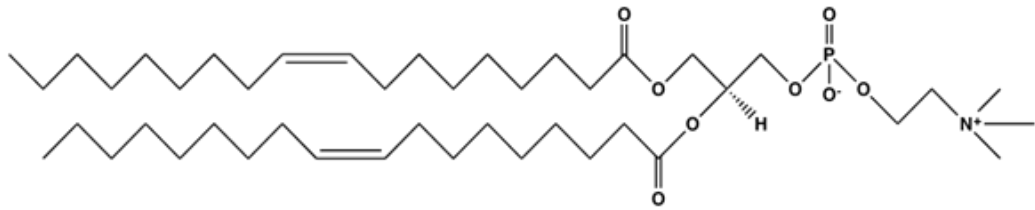
As previously seen, phospholipid physical characteristics affect the macromolecular structure and chemical properties. In addition, the chemical properties of phospholipids are affected by the environment they are subjected to. For this reason, phospholipids behave in a different manner once deposited on a Hg/Pt electrode. As a result, each phospholipid has a distinctive RCV profile (voltammogram) that behaves differently when they are exposed to a particular buffer. The study of the behaviour of different phospholipids on the Hg/Pt electrode is of extreme importance. As already mentioned, cells are heterogeneous systems formed by different phospholipids depending function. Being able to deposit different phospholipids on the Hg/Pt, allows forming more complex model membranes that can better mimic real cellular membranes. In this chapter, the stability of DOPC, DOPE DOPS, DOPG and DOPA in the Hg/Pt electrode using RCV is analysed. These phospholipids were chosen for being representative of different organisms or being specific to a particular type of cell. It is important to notice that mixtures of lipids will not be used in this chapter. This chapter provides all the necessary information for the correct deposition of phospholipids, which are used in followings chapters, and their stability. This information can be used in the future to further explore

the behaviour of mixtures of lipids to create more complex model membranes. Additionally, chapter 6 provides information about the relevance of the phospholipids used in the experiments of this thesis.

In this way, the different phospholipids were deposited on the Hg/Pt electrode and the variations in current versus time were analysed for the different systems to:

1. Assess the stability of the phospholipid monolayers in different media on the Hg/Pt electrode;
2. Evaluate the reference RCV profile of each phospholipid in different media for later RCV studies;
3. Evaluate the errors associated with the phospholipid deposition;

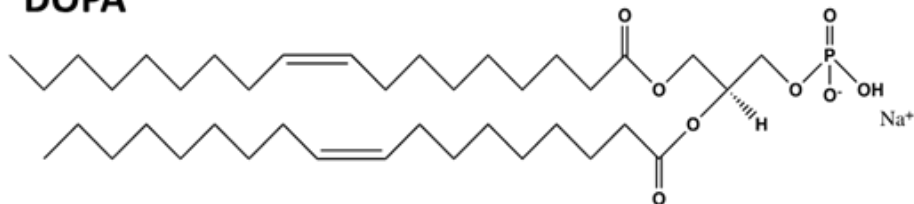
DOPC



DOPE



DOPA



DOPG



DOPS

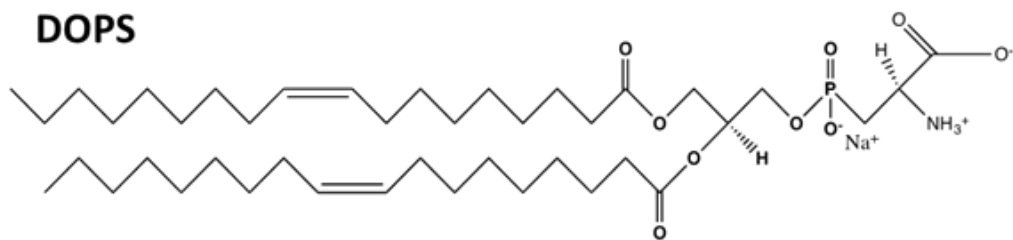


Figure 6. 3: Chemical structure of: (a) 1,2-dioleoyl-*sn*-glycero-3-phosphocholine, (DOPC), (b) 1,2-dioleoyl-*sn*-glycero-3-phosphoethanolamine, (DOPE), (c) 1,2-dioleoyl-*sn*-glycero-3-phosphate (sodium salt), (DOPA), (d) 1,2-dioleoyl-*sn*-glycero-3-phospho-(1'-*rac*-glycerol) (sodium salt), (DOPG), (e) 1,2-dioleoyl-*sn*-glycero-3-phospho-*L*-serine (sodium salt), (DOPS).

6.1 Materials and methods

6.1.1 Materials

Phosphate buffered saline (PBS), pH 7.4 (powder), sodium citrate tribasic dehydrate, 99.5%, potassium chloride, ACS grade, were bought from Sigma Aldrich. Citric acid, analytical reagent grade, was bought from Fisher Scientific. Glycine-HCl buffer, 10mM, pH 2.5 and 3.0 was obtained from Bio-Rad. 1,2-dioleoyl-sn-glycero-3-phosphocholine (DOPC), 1,2-dioleoyl-sn-glycero-3-phosphoethanolamine (DOPE), 1,2-dioleoyl-sn-glycero-3-phospho-L-serine (sodium salt) (DOPS), 1,2-dioleoyl-sn-glycero-3-phosphate (sodium salt) (DOPA) and 1,2-dioleoyl-sn-glycero-3-phospho-(1'-rac-glycerol) (sodium salt) (DOPG) were purchased from Avanti Polar Lipids and Stratech.

6.1.2 Buffer preparation

Phospholipid stability on the Hg/Pt electrode was studied using RCV under different conditions. PBS, Glycine-HCl (GLY) buffer and citric/citrate buffer (CCB) were employed as a solution buffers for the experiments. PBS and GLY buffer were commercially purchased. However, CCB buffer was made in situ by mixing the proper amounts of 0.1M, citric acid monohydrate and 0.1M, sodium citrate tribasic (Table 6. 2)

Table 6. 2: Volume of citric acid and sodium citrate tribasic needed to make a buffer solution of a certain pH

	0.1M citric acid	0.1M sodium citrate tribasic
pH	Volume/mL	Volume/mL
3	82.0	18.0
4	59.0	41.0
5	35.0	65.0
6	11.5	88.5

6.2 DOPC

DOPC is the most abundant phospholipid in eukaryotic cells. It is zwitterionic. Accordingly, it has a negatively charged phosphate group and a positively charged amine group. This unique characteristic gives DOPC extra stability when depositing it on Hg while this property provides free sites for molecules, ions or particles to interact. In addition, the pK_a of DOPC is around 1 [154]. For this reason, the configuration of the polar heads of DOPC should remain neutral when it is exposed to a solution with $pH \geq 3.0$ as observed in [153].

DOPC stability on the Hg/Pt electrode in different pHs and media was assessed using RCV. DOPC deposition was carried out following the specified procedure described in section 5.6.2. In this way, DOPC was exposed to glycine buffer at pH 2.5 and 3.0, citric/citrate buffer at pH 3.0, 4.0, 5.0 and 6.0 and PBS buffer at pH 7.4.

6.2.1 DOPC stability in PBS (pH 7.4)

DOPC in PBS is the most stable system amongst those which have been previously tested. For this reason, DOPC has been used in prior electrochemical studies for both fundamental and applied work. The DOPC voltammogram can be divided into three sections [143, 146] as displayed in Figure 6. 4.

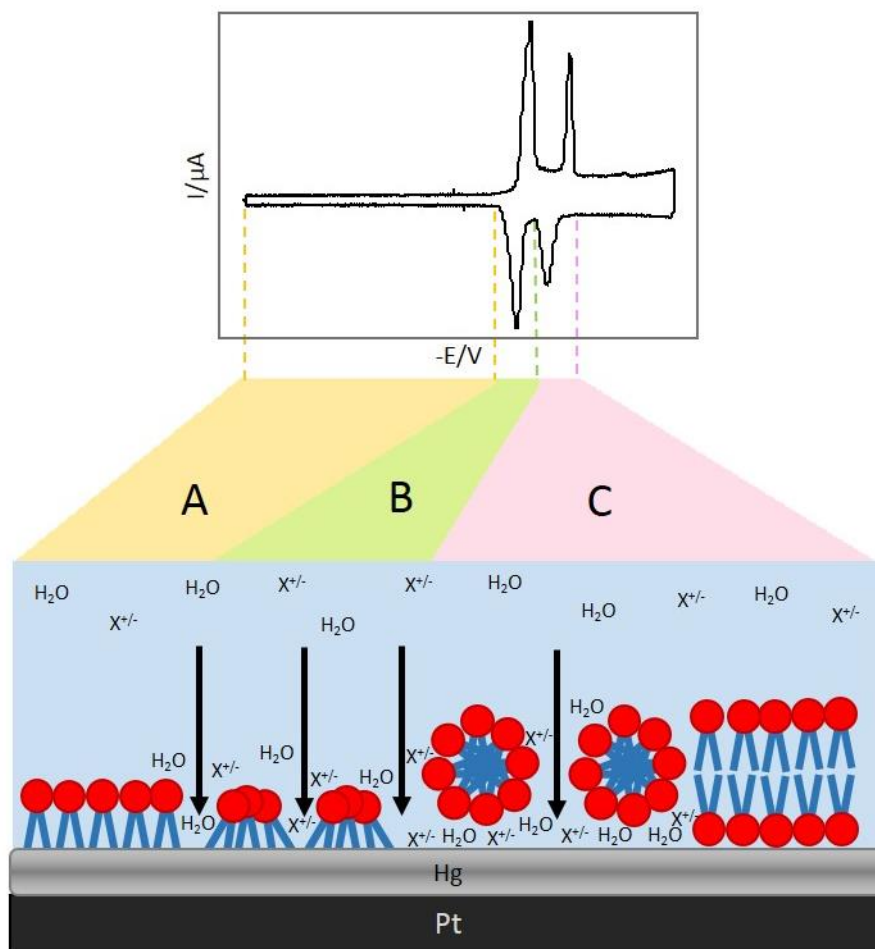


Figure 6. 4: RCV profile of DOPC and related phase of the phospholipids on the Hg/Pt at a certain potential. Zone A: The phospholipids form a mono-layer over the electrode that hampers the passage of ions or water through the membrane. Zone B: Phospholipid polar heads join allowing the passage of ions and water which creates a current. Zone C: correspond to a growth process that ends in a bilayer with patches formation.

Region A of Figure 6. 4, corresponds to a potential domain between -0.40V and -0.90V. Here, the capacitance current remains constant. Phospholipids form a homogeneous layer, and its dielectric structure does not change. As the potential becomes more negative, the first capacitance current peak is initiated. It is located between -0.90V and -0.93V and corresponds to region B of Figure

6. 4. Polar heads of phospholipids dissociate, and the layer begins to be permeable to ions as part of a phospholipid reorientation. The second capacitance current peak occurs in the region -0.96V to -1.00V (region C). It represents a nucleation and growth process, forming patches of the bilayer. On reversal of the potential scan, the two afore-described capacitance current peaks are reversed corresponding to a reversal of the structural reorientations of phospholipid.

Figure 6. 5 shows how the behaviour of the DOPC RCV profile with time, which is a “fingerprint” of DOPC stability on the electrode surface. The current peaks represent two potentially induced phase transitions which are directly related to self-assembly processes holding the DOPC molecules together in a monolayer. If there is a degradation in the stability of the monolayer due in part to its interaction with solution contaminants, the DOPC self-assembly processes will be affected, so causing an alteration in the capacitance peak current profile. As is observed for DOPC in PBS, there is no significant change in the shape of the voltammogram and the conformation of the peaks with time what indicates monolayer stability over the period (Figure 6. 5).

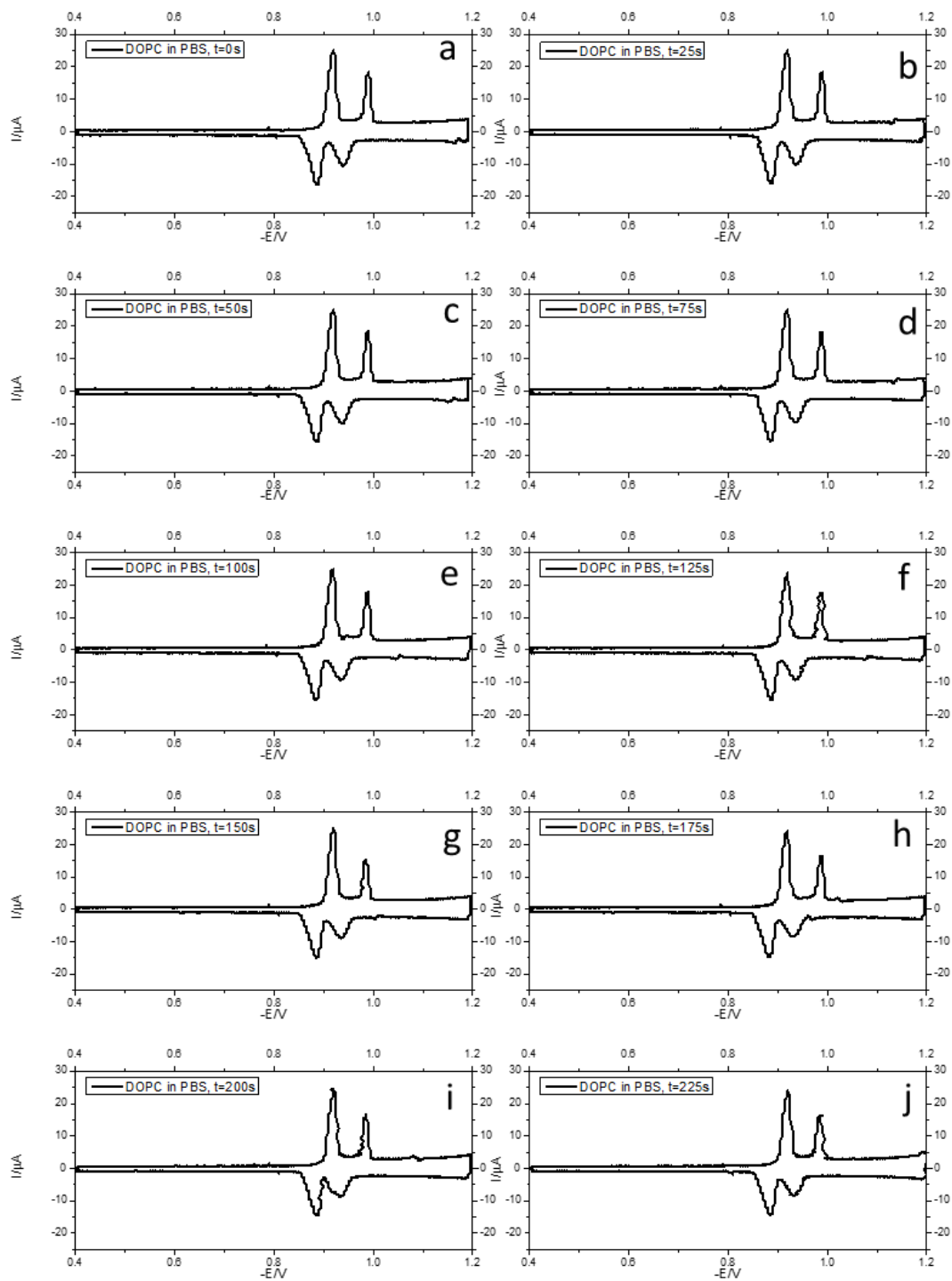


Figure 6. 5: RCV profile of DOPC in PBS (pH 7.4) recorded at 40V s^{-1} using potential cycles from -0.4V to -1.2V at time: (a): $t=0\text{s}$, (b): $t=25\text{s}$, (c): $t=50\text{s}$, (d): $t=75\text{s}$, (e): $t=100\text{s}$, (f): $t=125\text{s}$, (g): $t=150\text{s}$, (h): $t=175\text{s}$, (i): $t=200\text{s}$, and (j) $t=225\text{s}$.

Figure 6. 6 shows the variation of the DOPC current peaks with time for ten different DOPC depositions on the Hg/Pt. As observed, the initial current of the first peak is in between $20\mu\text{A}$ to $25\mu\text{A}$ and the initial current of the second peak is in between $20\mu\text{A}$ and $15\mu\text{A}$. In addition, there is a general tendency of the peaks to decrease with time. However, this reduction is minimal in comparison with the initial current of the peaks. The only observed exception is 'PBS 2' where the second peak current decreases quicker. This behaviour could be caused by an incorrect lipid deposition or a contaminant in the system.

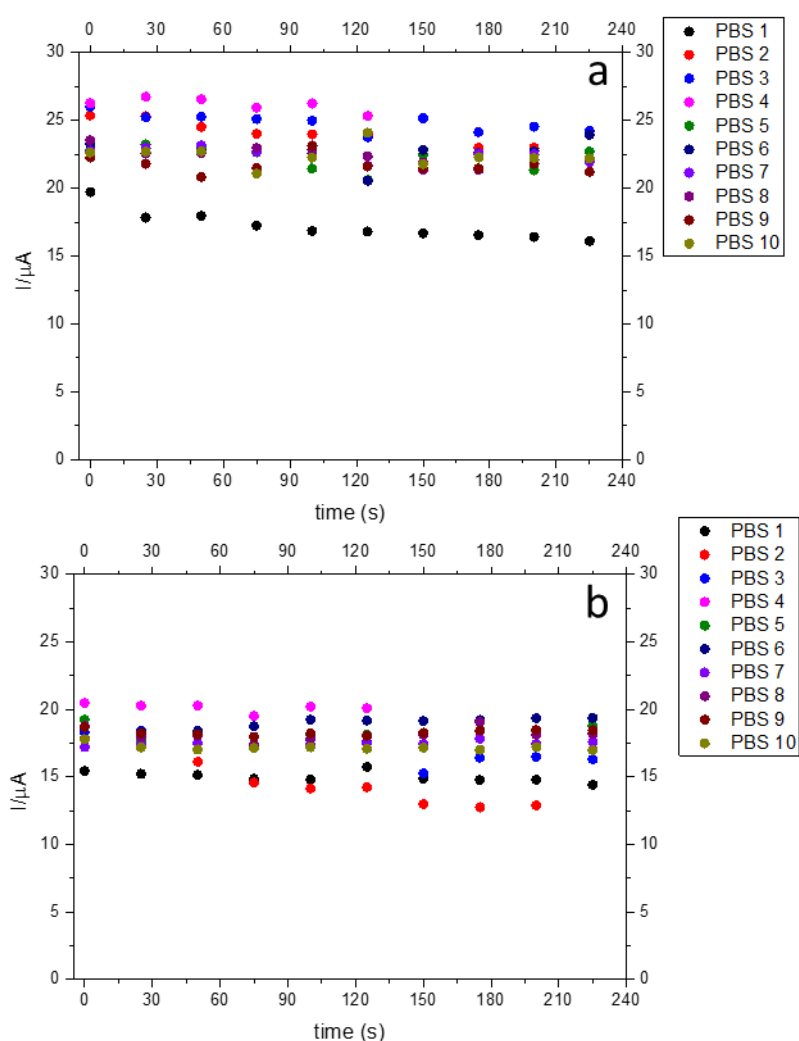


Figure 6. 6: Current variation with time of 10 different DOPC depositions in PBS (pH 7.4) of (a) Peak 1. Black dots: PBS 1, red dots: PBS 2, light blue: PBS 3, pink dots: PBS 4, dark green: PBS 5, dark blue: PBS 6, light purple: PBS 7, dark purple: PBS 8, brown: PBS 9, and light green: PBS 10, (b) Peak 2. Black dots: PBS 1, red dots: PBS 2, light blue: PBS 3, pink dots: PBS 4, dark green: PBS 5, dark blue: PBS 6, light purple: PBS 7, dark purple: PBS 8, brown: PBS 9, and light green: PBS 10

The average peak suppression of the current peaks of DOPC when it is exposed to a PBS buffer flow is displayed in Figure 6. 7. As expected, the current declines with time. Nevertheless, the reduction of the peaks and their associated errors are low and they do not exceed 10%. Nevertheless, a typical RCV test using the ESD does not exceed a time period of 60s so that the stability of DOPC in PBS, in the context of the experiment, is high.

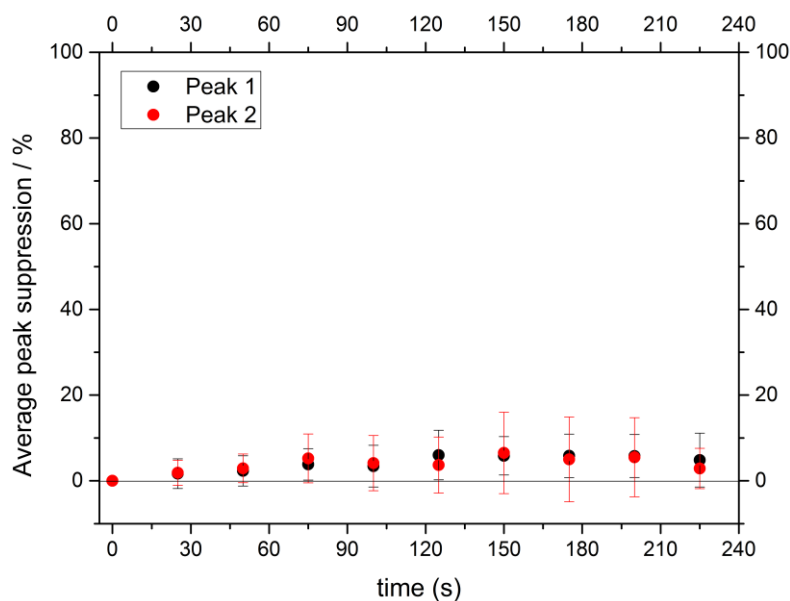


Figure 6. 7: Average peak suppression of the current peaks of the RCV voltammograms with time of DOPC in PBS (pH 7.4). Black dots: Peak 1 of the voltammogram. Red dots: Peak 2 of the voltammogram.

6.2.2 DOPC stability in HCl-Glycine buffer. pH 3.0

DOPC stability on a Hg/Pt under a constant flow of HCl-glycine buffer (pH=3.0) was studied. In this way, the height of the current peaks of the voltammograms with time for 10 different DOPC depositions was analysed.

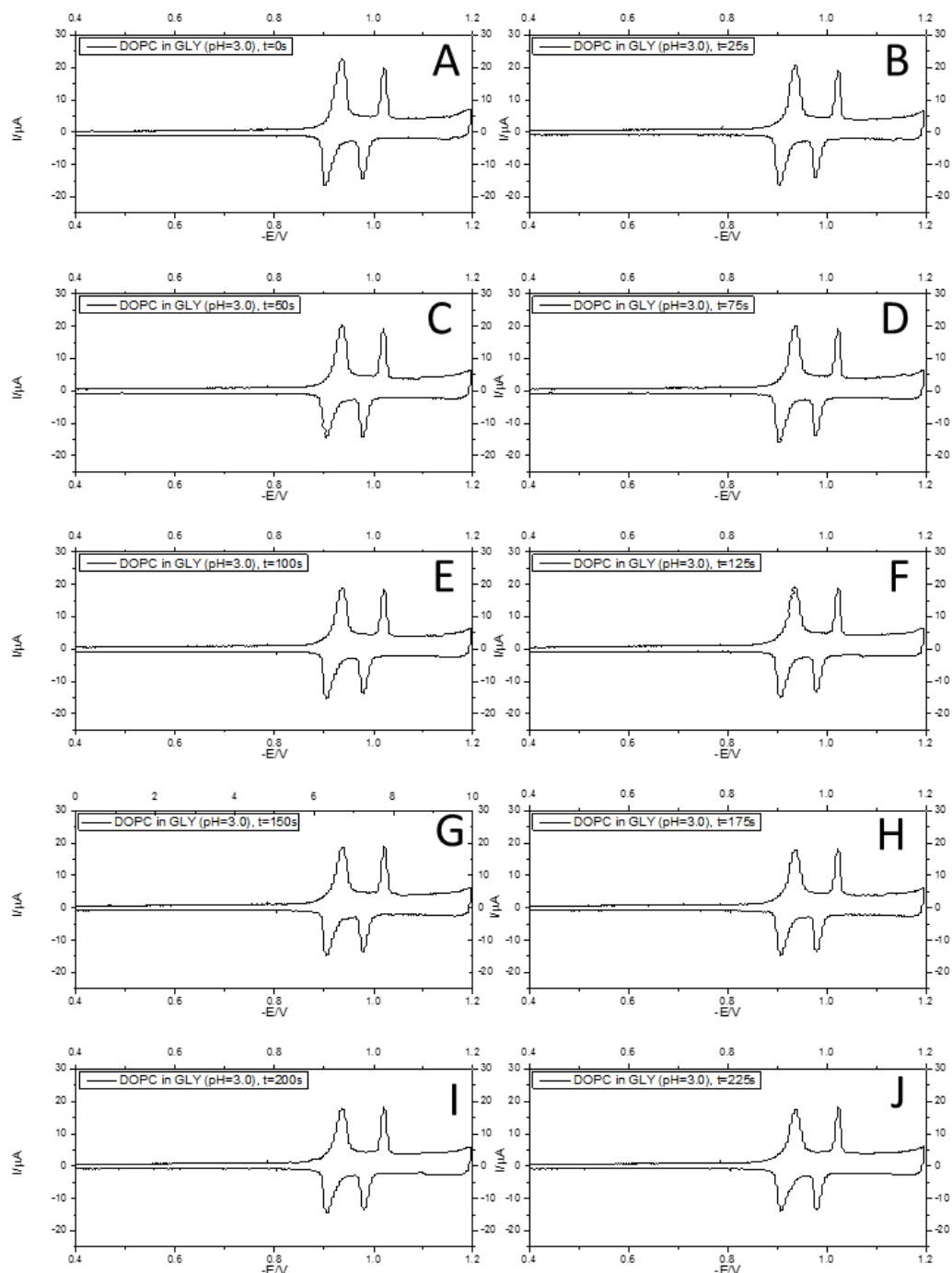


Figure 6. 8: RCV profile of DOPC in GLY (pH 3.0) recorded at 40V s⁻¹ using potential cycles from -0.4V to -1.2V at time: (a): t=0s, (b): t=25s, (c):t=50s, (d): t=75s, (e): t=100s, (f):t=125s, (g): t=150s, (h):t=175s, (i): t=200s, and (j) t=225s.

Figure 6. 8 shows the variation of the RCV profile of DOPC in GLY at pH 3.0 with time. As observed, the two characteristic peaks of DOPC are apparent. Peak 1 is visible at -0.935V and peak 2 is visible at -1.02V . However, the shape of the voltammogram is not precisely the same than the one previously seen in for DOPC in a continuous flow of PBS (Figure 6. 5). In this case, peak 1 is more unstable and subject to variation. However, it declines to approximately to the same current as peak 2 and remains stable.

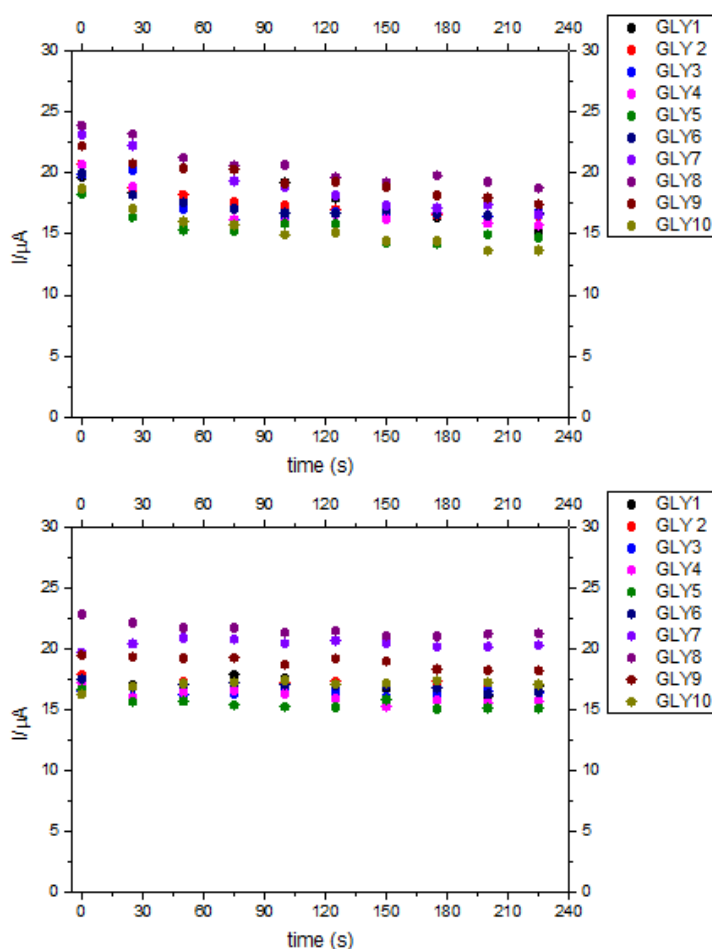


Figure 6. 9: Current variation with time of 10 different DOPC depositions in GLY (pH 3.0) of (a) Peak 1. Black dots: GLY 1, red dots: GLY 2, light blue: GLY 3, pink dots: GLY 4, dark green: GLY 5, dark blue: GLY 6, light purple: GLY 7, dark purple: GLY 8, brown: GLY 9, and light green: GLY 10, (b) Peak 2. Black dots: GLY 1, red dots: GLY 2, light blue: GLY 3, pink dots: GLY 4, dark green: GLY 5, dark blue: GLY 6, light purple: GLY 7, dark purple: GLY 8, brown: GLY 9, and light green: GLY 10

Figure 6. 9 shows the variation of the current of peaks 1 and 2 when DOPC is exposed to GLY (pH 3.0) for ten different depositions. As observed, peak 1

decreases quicker than peak 2 until 30-60s and subsequently, it decreases slower. This change in conformation of peak 1 with time following deposition is more likely due to an adjustment of DOPC coverage rather than solution contamination.

The average peak suppression at different times and their associated errors are displayed in Figure 6. 10. The higher variation in current in comparison to the one obtained for DOPC in PBS (Figure 6. 5) could be indicative of destabilisation or de-attachment of the phospholipid layer from the Hg/Pt. In order to look into the stability of the layer, the current of the homogeneous part of the RCV profile (-0.4V- -0.935V) was analysed. In this way, the current variation of ten DOPC depositions, at -0.6V, was monitored with time (Figure 6. 11).

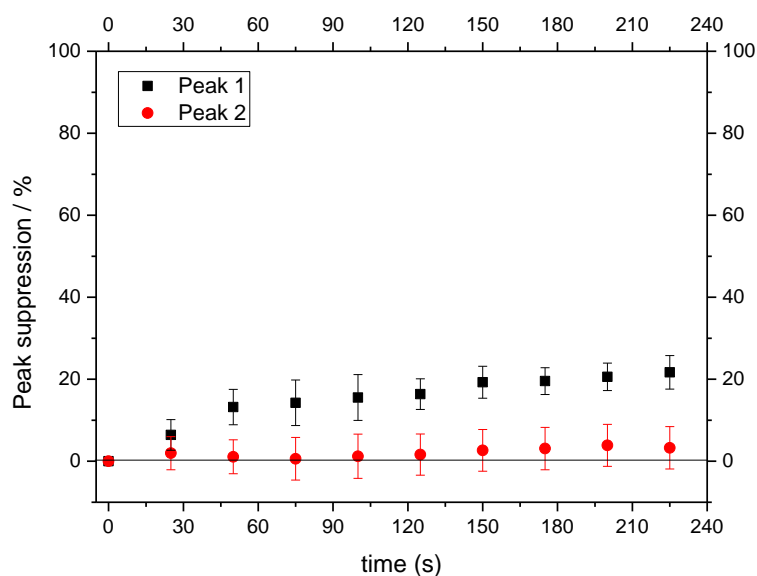


Figure 6. 10: Average peak suppression of the current peaks of the RCV voltammograms with time of DOPC in GLY (pH 3.0). Black dots: Peak 1 of the voltammogram. Red dots: Peak 2 of the voltammogram.

Figure 6. 11 shows how the current decreases in the homogeneous region of the voltammogram with time. Contrary to expectations, DOPC in GLY at pH 3.0 became more stable with time on the Hg/Pt electrode despite the variation of peak 1. A detachment from the electrode would produce an increase in baseline capacitance current, which relates to the dielectric structure on the electrode.

The behaviour of peak 1 could be related to the pK_a of DOPC. At pH regions close to the pK_a value, the negatively charged phosphate group can be protonated in such a way DOPC would become a positively charged molecule. It may be that a small fraction of DOPC molecules is protonated at pH 3.0, sufficient to produce a small change in the voltammogram.

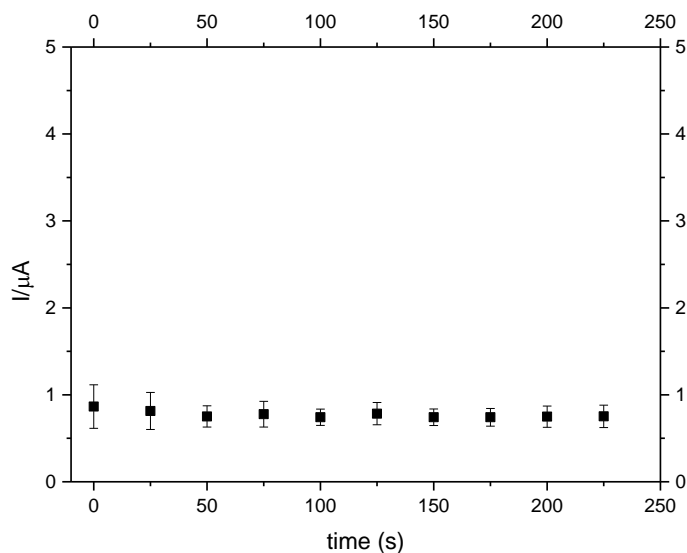


Figure 6. II: Current at $-0.6V$ when DOPC in GLY (pH 3.0) when the RCV profile is recorded at $40Vs^{-1}$ using potential cycles from $-0.4V$ to $-1.2V$.

In order to decrease errors and increase accuracy, the reference RCV profile of DOPC in GLY (pH 3.0) for interaction studies was taken at 50s, where peak 1 was subject to fewer variations.

6.2.3 DOPC stability in citric/citrate buffer

6.2.3.1 Citric/citrate buffer pH 3.0

DOPC stability on a Hg/Pt electrode under a constant flow of tribasic sodium citrate and citric acid buffers (pH=3.0, pH=4.0, pH=5.0 and pH=6.0) was studied. The buffers were prepared following the procedure described in Table 6. 2.

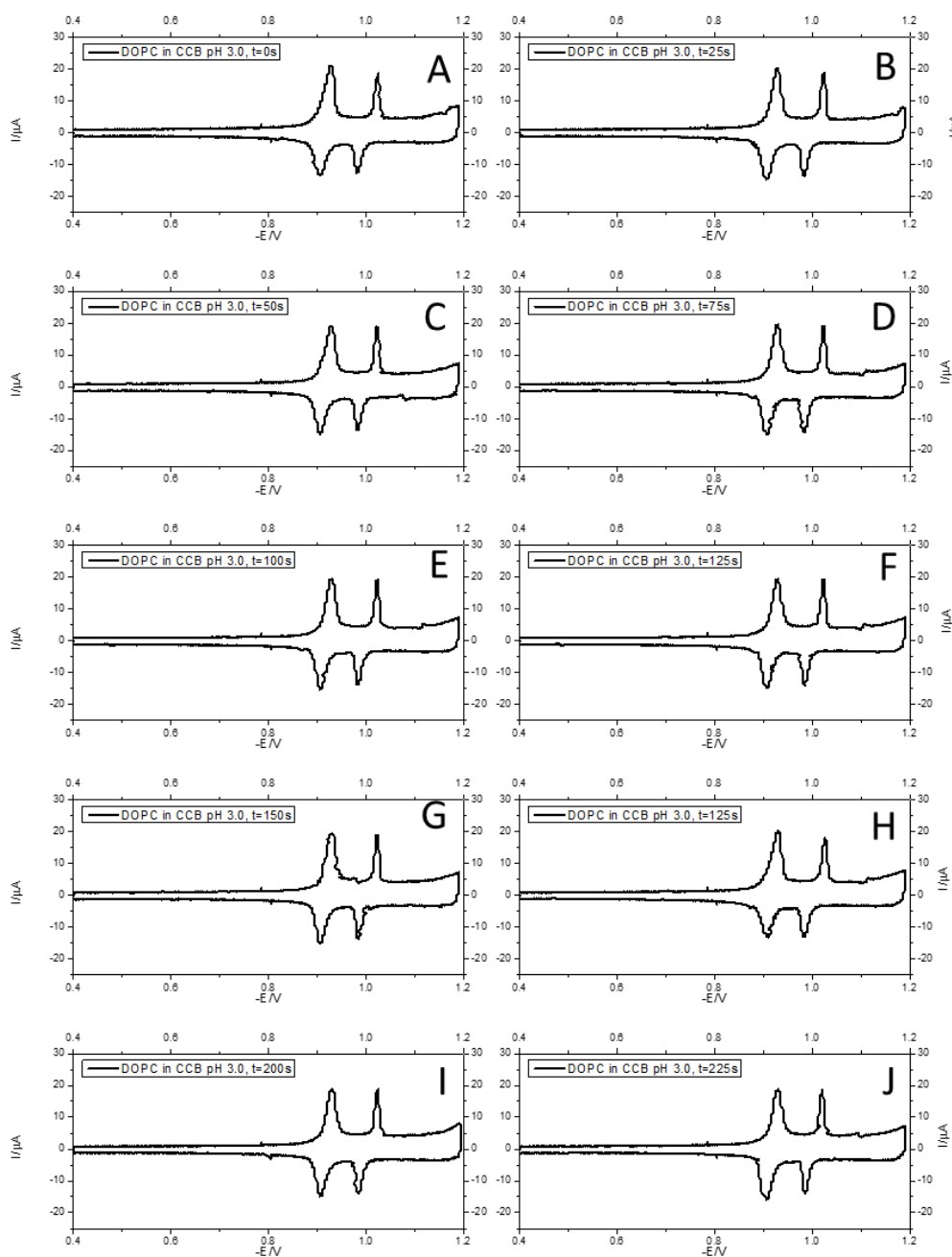


Figure 6. 12: RCV profile of DOPC in CCB (pH 3.0) recorded at 40V s⁻¹ using potential cycles from -0.4V to 1.2V at time: (a): $t=0s$, (b): $t=25s$, (c): $t=50s$, (d): $t=75s$, (e): $t=100s$, (f): $t=125s$, (g): $t=150s$, (h): $t=175s$, (i): $t=200s$, and (j) $t=225s$.

The height of the current peaks of the voltammograms with time for 10 different DOPC depositions was analysed. Figure 6. 12 displays the variation of the RCV profile of DOPC in CCB at pH 3.0. The two characteristic peaks of DOPC: peak 1, at -0.935V, and peak 2, at -1.02V, are evident. The voltammograms are similar to the ones obtained in Figure 6. 8, which indicates DOPC in CCB at pH 3.0 has similar behaviour to that in GLY at pH 3.0.

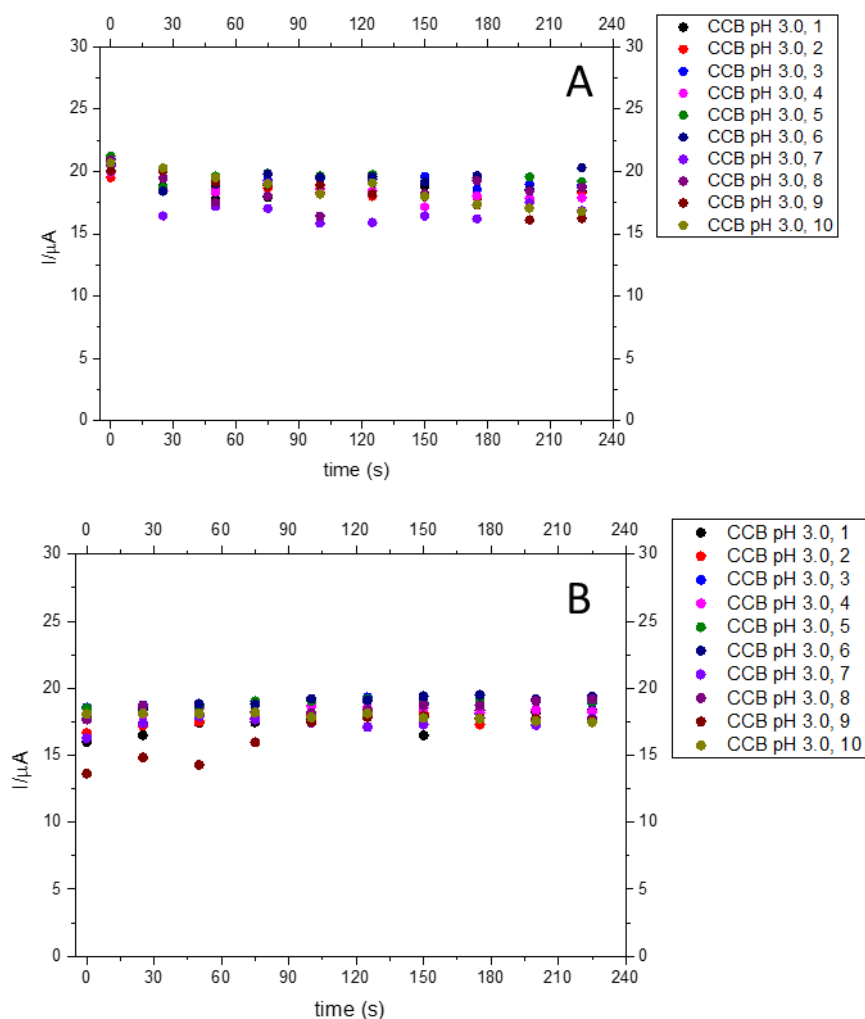


Figure 6. 13: Current variation with time of 10 different DOPC depositions in CCB (pH 3.0) of (a) Peak 1. Black dots: CCB 1, red dots: CCB 2, light blue: CCB 3, pink dots: CCB 4, dark green: CCB 5, dark blue: CCB 6, light purple: CCB 7, dark purple: CCB 8, brown: CCB 9, and light green: CCB 10, (b) Peak 2. Black dots: CCB 1, red dots: CCB 2, light blue: CCB 3, pink dots: CCB 4, dark green: CCB 5, dark blue: CCB 6, light purple: CCB 7, dark purple: CCB 8, brown: CCB 9, and light green: CCB 10.

However, the second peak of the RCV profile (Figure 6. 13B) is more stable than in Figure 6. 9B. In this case, peak 2 tends to increase with time, while peak 1 tends to decrease. This tendency can be clearly observed in Figure 6. 14, which displays the average peak suppression with its associated error in function of

time. Peak 1 decreases approximately by 10% and remains constant while peak 2 increases by approximately 10% at 100s and then remains constant. This is the reason why the reference RCV profile of DOPC in CCB at pH 3.0 for later studies was taken 100s after deposition.

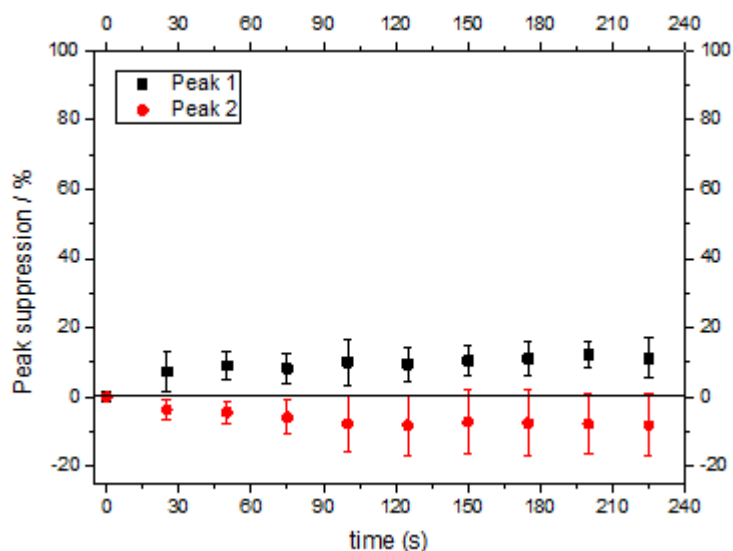


Figure 6. 14: Average peak suppression of the current peaks of the RCV voltammograms with time of DOPC in CCB (pH 3.0). Black dots: Peak 1 of the voltammogram. Red dots: Peak 2 of the voltammogram.

In addition, the baseline current of the voltammogram was monitored as well. Figure 6. 5 shows the current remains constant with time which indicates phospholipids are not being detached from the Hg/Pt. This confirms that before 100s, an adjustment to the coverage of lipids is produced.

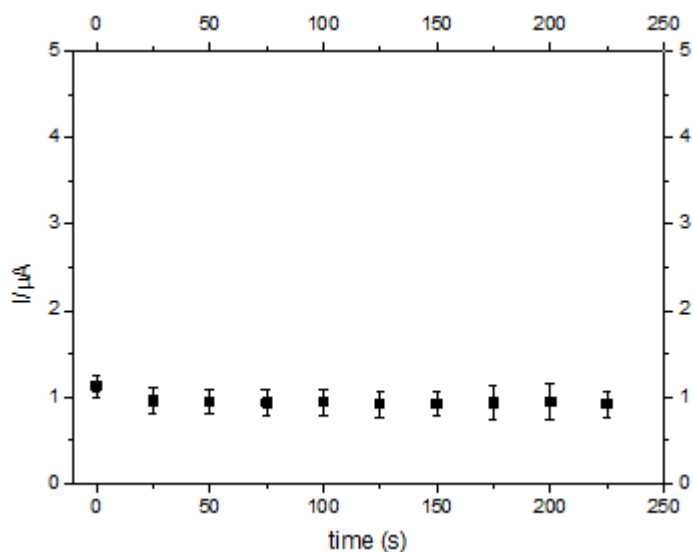


Figure 6. 15: Current at -0.8V when DOPC in CCB (pH 3.0) when the RCV profile is recorded at 40Vs^{-1} using potential cycles from -0.4V to -1.2V.

6.2.3.2 Citric/citrate buffer pH 4.0

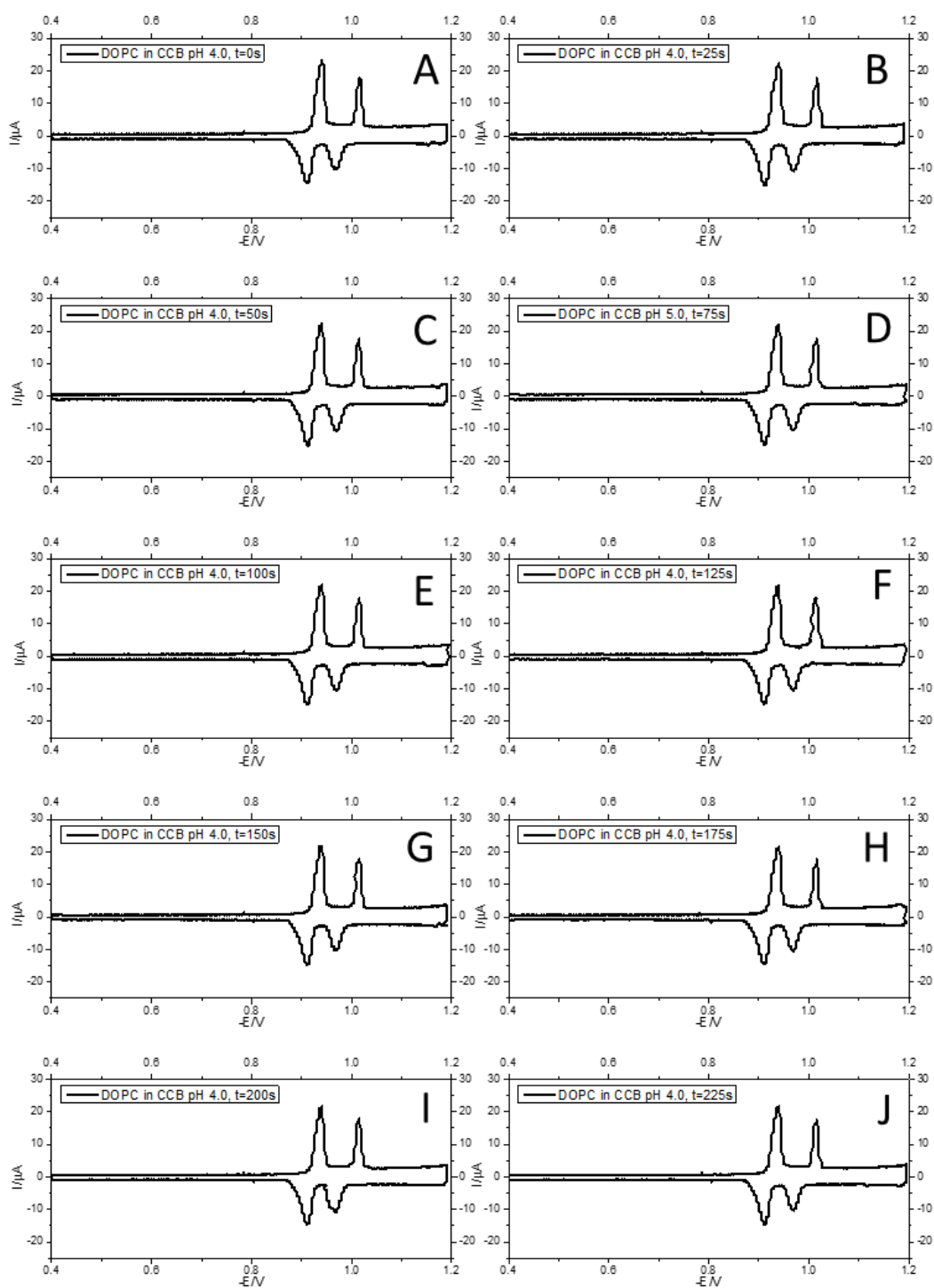


Figure 6.16: RCV profile of DOPC in CCB (pH 4.0) recorded at 40V s⁻¹ using potential cycles from -0.4V to -1.2V at time: (a): $t=0s$, (b): $t=25s$, (c): $t=50s$, (d): $t=75s$, (e): $t=100s$, (f): $t=125s$, (g): $t=150s$, (h): $t=175s$, (i): $t=200s$, and (j) $t=225s$.

Figure 6. 16 shows the variation of the RCV profile of DOPC in CCB at pH 4.0 with time. The voltammogram is similar to the one in Figure 6. 5. The first and second peaks remain stable with time as displayed in Figure 6. 17.

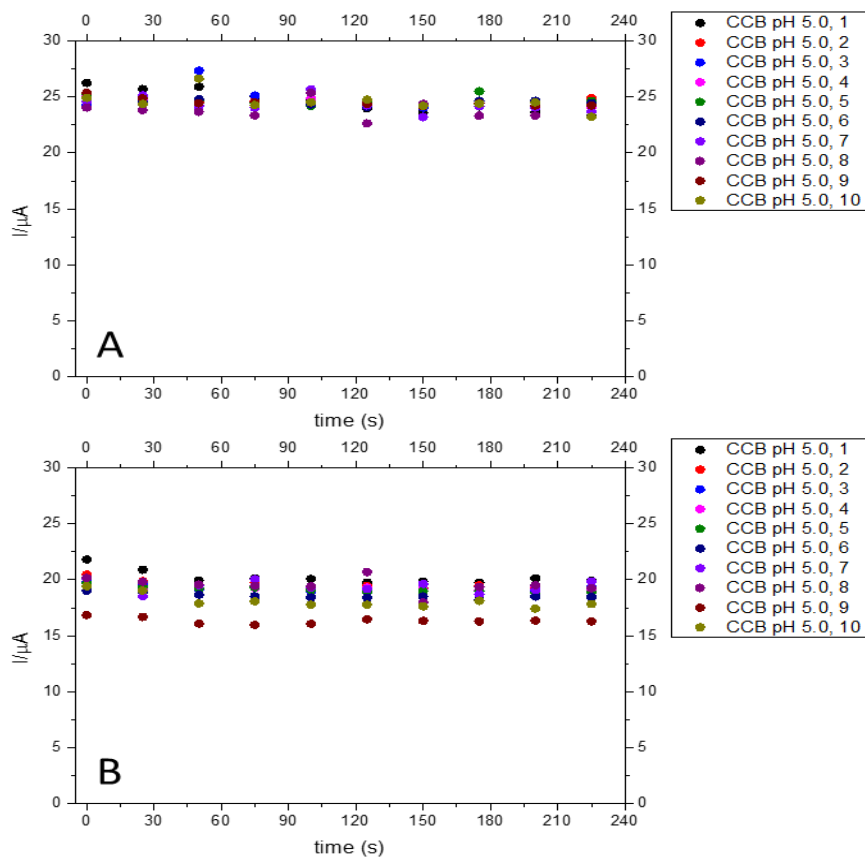


Figure 6. 17: Current variation with time of 10 different DOPC depositions in CCB (pH 4.0) of (a) Peak 1. Black dots: CCB 1, red dots: CCB 2, light blue: CCB 3, pink dots: CCB 4, dark green: CCB 5, dark blue: CCB 6, light purple: CCB 7, dark purple: CCB 8, brown: CCB 9, and light green: CCB 10, (b) Peak 2. Black dots: CCB 1, red dots: CCB 2, light blue: CCB 3, pink dots: CCB 4, dark green: CCB 5, dark blue: CCB 6, light purple: CCB 7, dark purple: CCB 8, brown: CCB 9, and light green: CCB 10.

Figure 6. 18 displays the average current peak suppression of the voltammogram when DOPC is exposed to a continuous flow of CCB at pH 4.0. This produced a decrease in current that remained constant after 75s of the DOPC deposition on the Hg/Pt. For this reason, the voltammogram at 75s after the phospholipid deposition was taken as the reference RCV profile for subsequent studies.

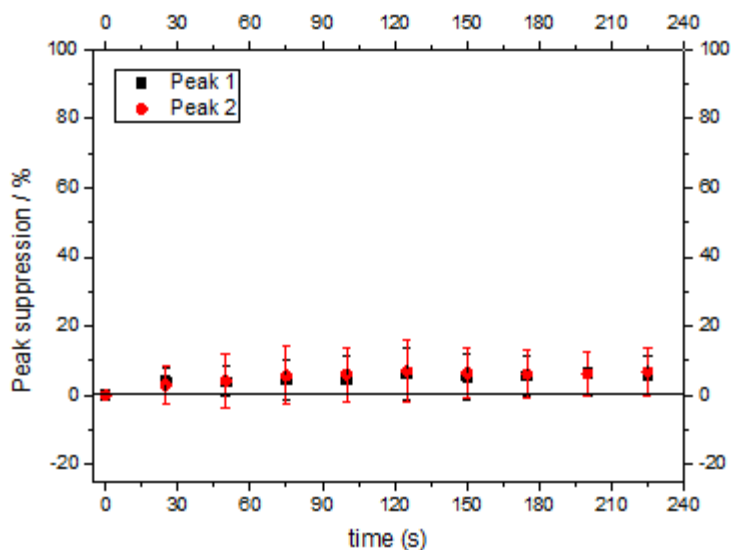


Figure 6. 18: Average peak suppression of the current peaks of the RCV voltammograms with time of DOPC in CCB (pH 4.0). Black dots: Peak 1 of the voltammogram. Red dots: Peak 2 of the voltammogram.

In addition, the baseline current of the voltammogram was monitored. Figure 6. 19 shows that the current remains constant with time which indicates phospholipids are not being detached from the Hg/Pt.

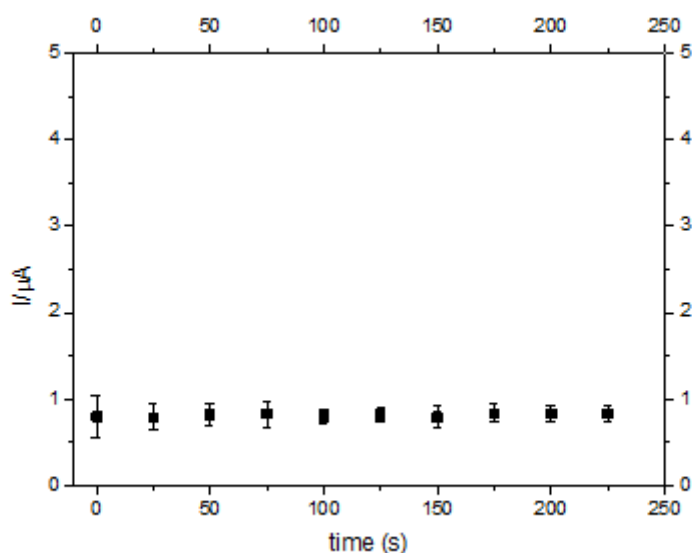


Figure 6. 19: Current at -0.8V when DOPC in CCB (pH 4.0) when the RCV profile is recorded at 40Vs-1 using potential cycles from -0.4V to -1.2V.

6.2.3.3 Citric/citrate buffer pH 5.0

DOPC in CCB at pH 5.0 (the procedure to prepare the buffer is explained in section 6.1.2) shows a similar behaviour to the one previously observed in Figure 6.5 and Figure 6.16. As seen in Figure 6.20, the voltammograms obtained when DOPC is exposed to a continuous flow of CCB at pH 5.0 present the characteristic profile of DOPC.

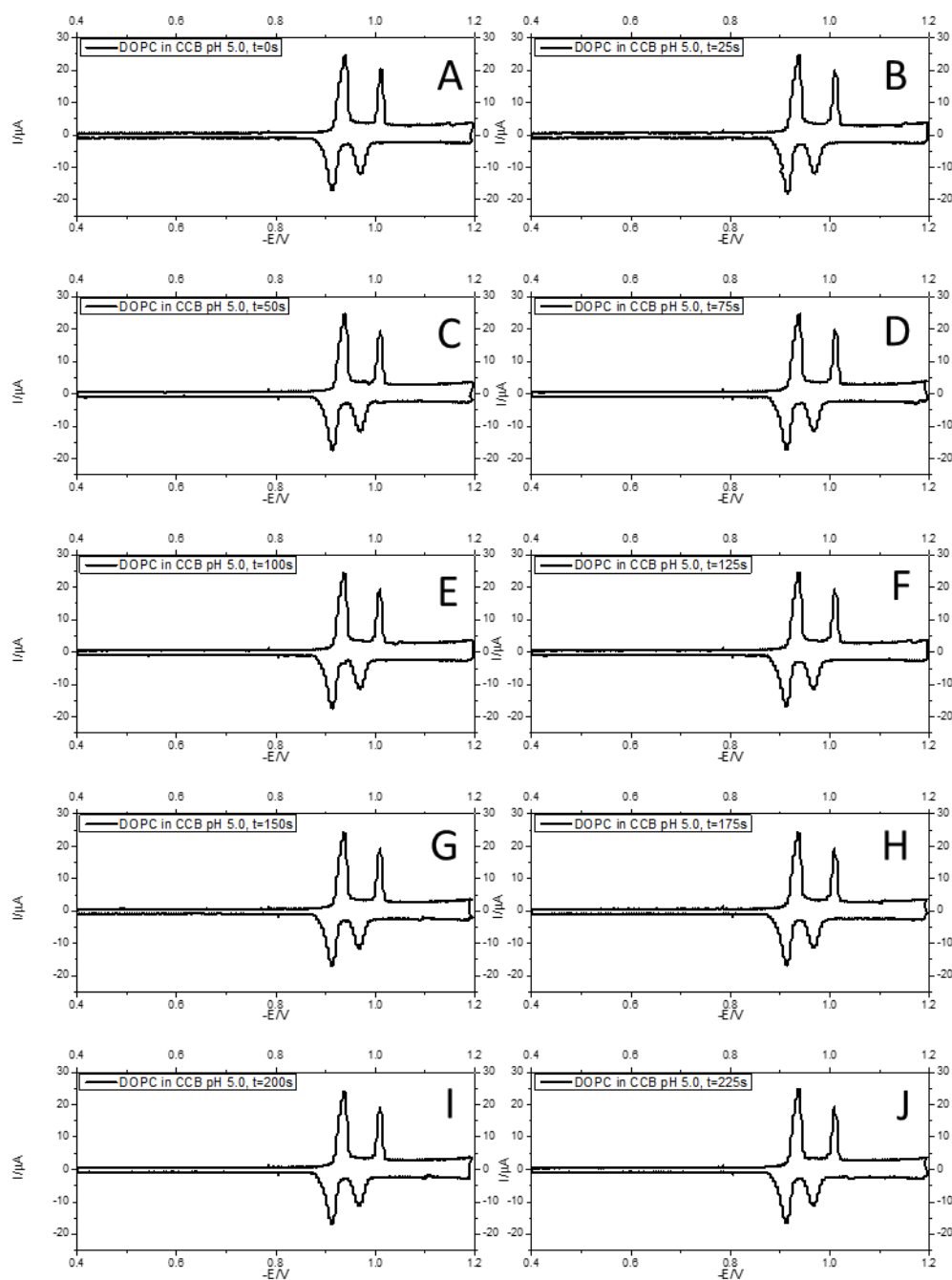


Figure 6.20: RCV profile of DOPC in CCB (pH 5.0) recorded at 40V s⁻¹ using potential cycles from -0.4V to -1.2V at time: (a): t=0s, (b): t=25s, (c):t=50s, (d): t=75s, (e): t=100s, (f):t=125s, (g): t=150s, (h):t=175s, (i): t=200s, and (j) t=225s.

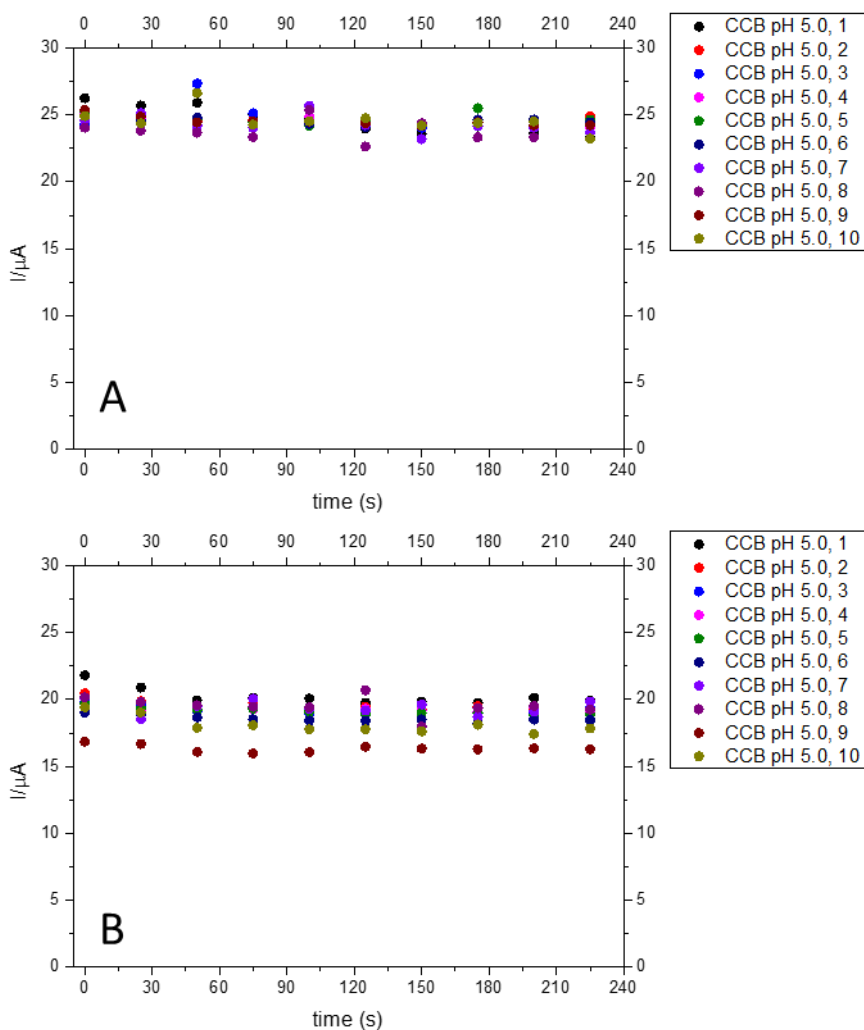


Figure 6. 22: Current variation with time of 10 different DOPC depositions in CCB (pH 5.0) of (a) Peak 1. Black dots: CCB 1, red dots: CCB 2, light blue: CCB 3, pink dots: CCB 4, dark green: CCB 5, dark blue: CCB 6, light purple: CCB 7, dark purple: CCB 8, brown: CCB 9, and light green: CCB 10, (b) Peak 2. Black dots: CCB 1, red dots: CCB 2, light blue: CCB 3, pink dots: CCB 4, dark green: CCB 5, dark blue: CCB 6, light purple: CCB 7, dark purple: CCB 8, brown: CCB 9, and light green: CCB 10.

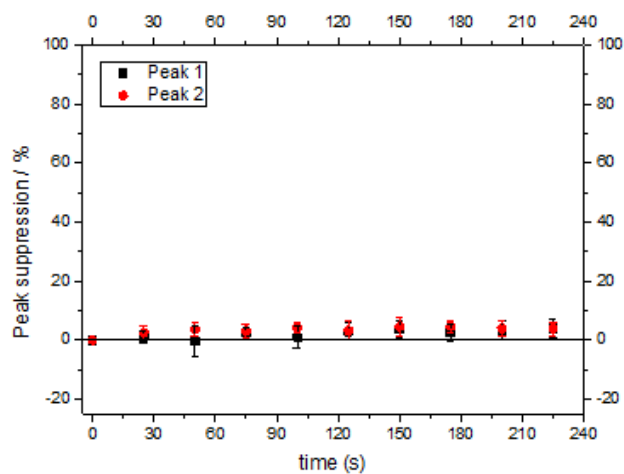


Figure 6. 21: Average peak suppression of the current peaks of the RCV voltammograms with time of DOPC in CCB (pH 5.0). Black dots: Peak 1 of the voltammogram. Red dots: Peak 2 of the voltammogram.

Figure 6. 22 shows the variation of the current peaks of DOPC as a function of time when DOPC is exposed to a continuous flow of CCB pH 5.0. As observed, the current peak remains constant with time. As seen in Figure 6. 22 and confirmed in Figure 6. 21, the current decrease is small, which indicates a high stability of the layer.

In addition, the baseline current of the voltammogram was monitored (Figure 6. 23) and remains constant with time which indicates phospholipids are not being desorbed from the Hg/Pt electrode.

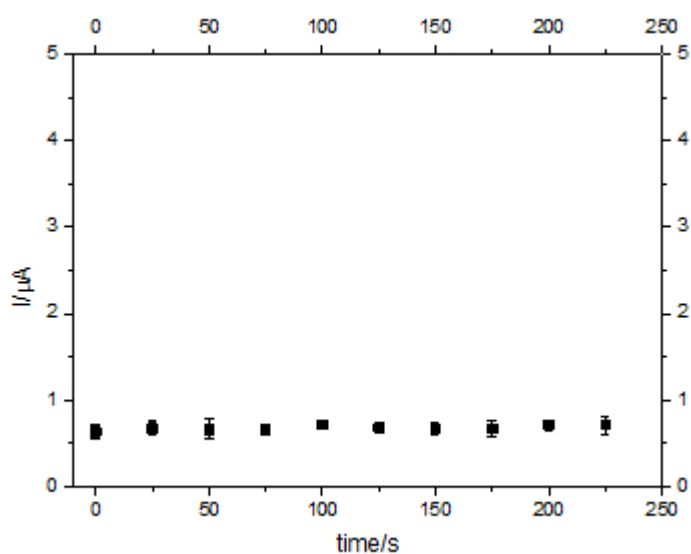


Figure 6. 23: Current at $-0.8V$ when DOPC in CCB (pH 5.0) when the RCV profile is recorded at $40Vs^{-1}$ using potential cycles from $-0.4V$ to $-1.2V$.

6.2.3.4 Citric/citrate buffer pH 6.0

Figure 6. 24 shows how the voltammogram of DOPC in CCB at pH6.0 varies with time. CCB 6.0 was made following the procedure described in 6.1.2. As observed, there are no significant changes in the current with time.

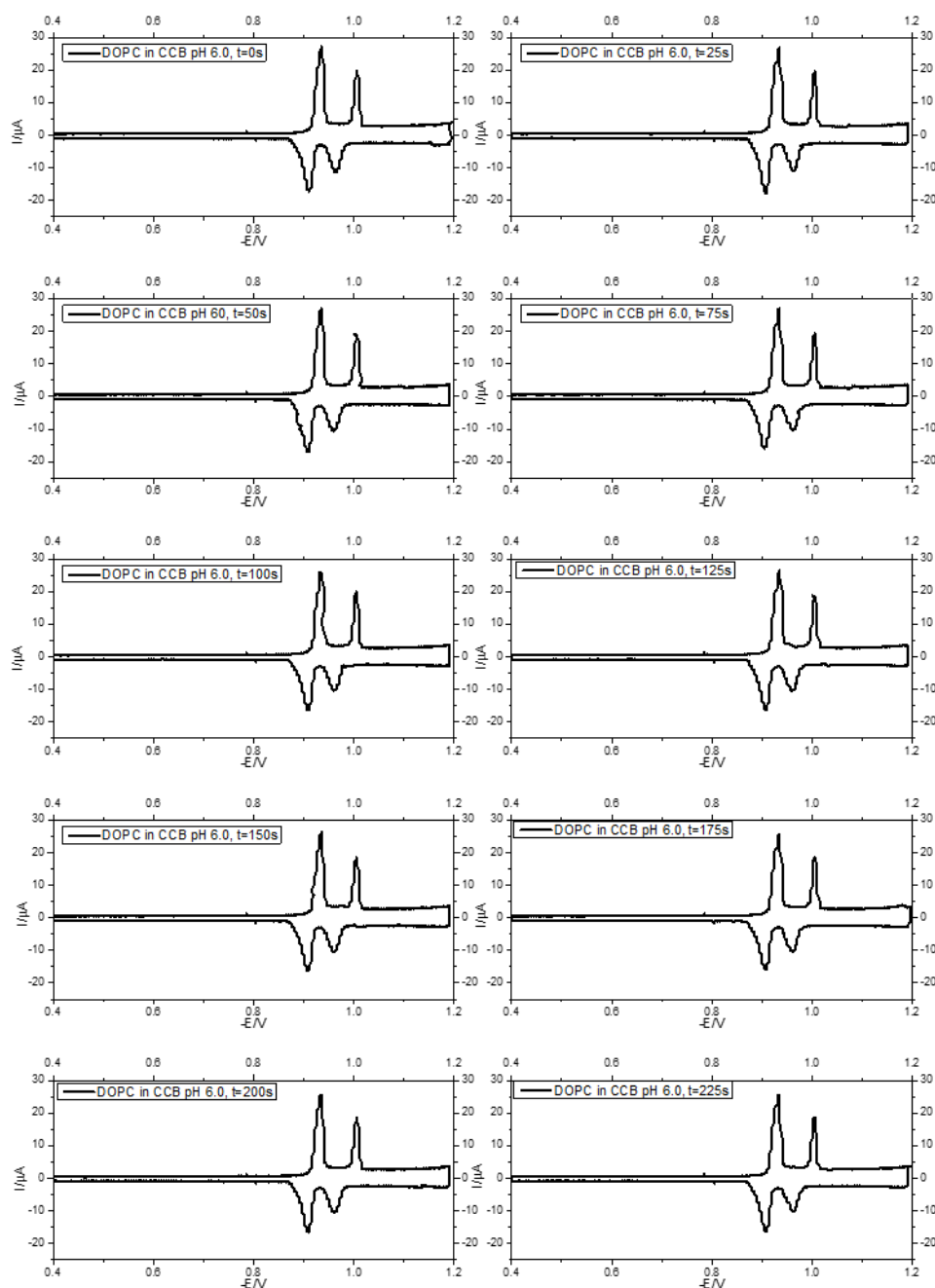


Figure 6. 24: RCV profile of DOPC in CCB (pH 6.0) recorded at 40V s⁻¹ using potential cycles from -0.4V to -1.2V at time: (a): t=0s, (b): t=25s, (c):t=50s, (d): t=75s, (e): t=100s, (f):t=125s, (g): t=150s, (h):t=175s, (i): t=200s, and (j) t=225s.

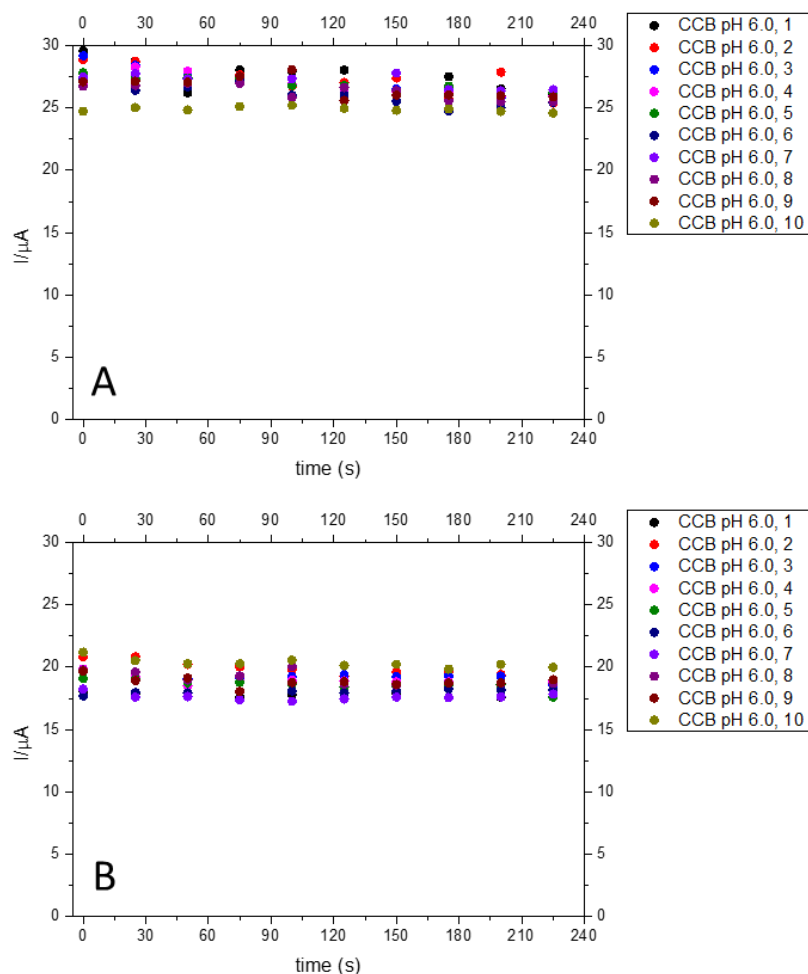


Figure 6. 25: Current variation with time of 10 different DOPC depositions in CCB (pH 6.0) of (a) Peak 1. Black dots: CCB 1, red dots: CCB 2, light blue: CCB 3, pink dots: CCB 4, dark green: CCB 5, dark blue: CCB 6, light purple: CCB 7, dark purple: CCB 8, brown: CCB 9, and light green: CCB 10, (b) Peak 2. Black dots: CCB 1, red dots: CCB 2, light blue: CCB 3, pink dots: CCB 4, dark green: CCB 5, dark blue: CCB 6, light purple: CCB 7, dark purple: CCB 8, brown: CCB 9, and light green: CCB 10.

Figure 6. 25 displays the variation of the first and second current peaks of the voltammograms when DOPC is exposed to a continuous flow of CCB at pH 6.0 versus time for 10 different DOPC depositions.

Figure 6. 27 shows the average peak suppression of the current peaks. As observed, the current remains constant with time. In addition, the baseline of the voltammogram remains constant. For this reason, the reference RCV profile

of DOPC when in contact with a continuous flow of CCB at pH 6.0 was taken immediately after the deposition of the lipid.

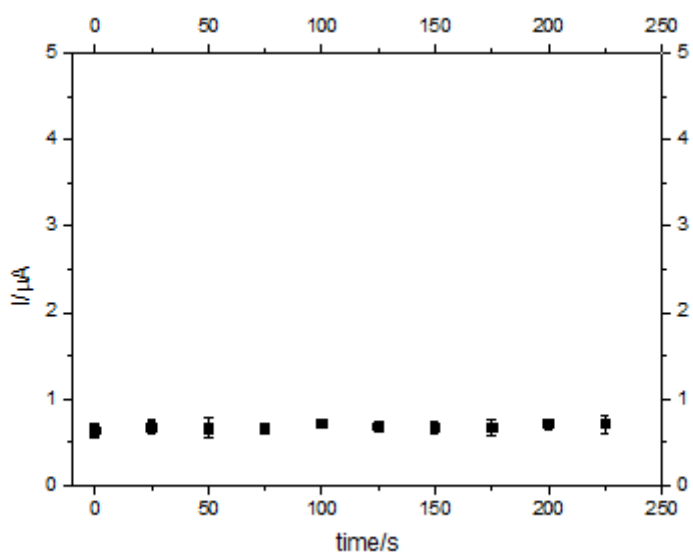


Figure 6. 26: Current at $-0.8V$ when DOPC in CCB (pH 6.0) when the RCV profile is recorded at $40Vs^{-1}$ using potential cycles from $-0.4V$ to $-1.2V$.

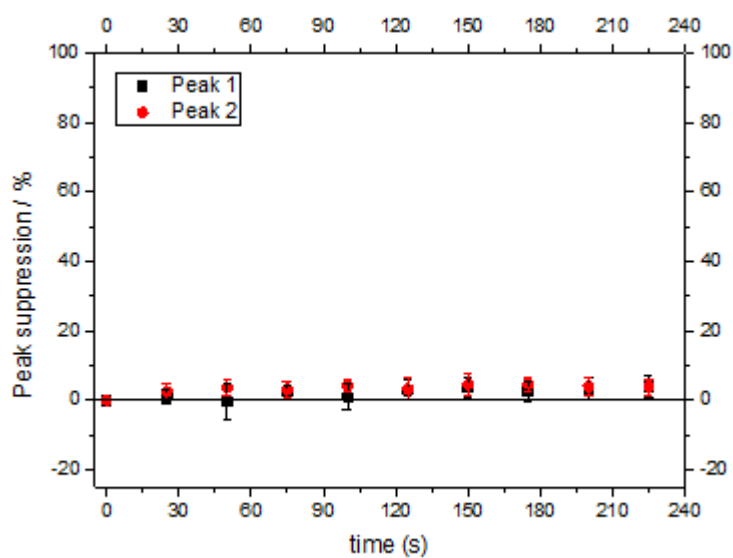


Figure 6. 27: Average peak suppression of the current peaks of the RCV voltammograms with time of DOPC in CCB (pH 6.0). Black dots: Peak 1 of the voltammogram. Red dots: Peak 2 of the voltammogram.

6.3 DOPE

DOPE (1,2-dioleoyl-sn-glycero-3-phosphoethanolamine) like DOPC is zwitterionic. DOPE has two pK_a values: 1.7 and 11.3 (Table 6. 1). For this reason, at physiological conditions, DOPE has both negative and positive charge. The polar head of DOPE is formed by a negatively charged phosphate group and a positively charged amine group.

PE is the second most abundant phospholipid in eukaryotic cells after PC and the most abundant phospholipid in prokaryotic cell membranes. For this reason, most studies involving DOPE also use mixtures of DOPE/DOPC lipids. DOPE usually forms non-lamellar structures (Figure 6. 2). However, in combination with other phospholipids, for example, DOPC, it can retain a lamellar structure. Changes in the DOPE/DOPC ratio affect membrane properties including the lateral pressure, electric field and the dipole potential which could lead to changes to the membrane function including, the arrangement of proteins within the membrane or membrane permeation and binding [155]. The main function of PE is to control the membrane fluidity. It was found, that the PE/PC ratio along with sterols, work in combination to regulate the membrane rigidity. PE, like cholesterol, increased membrane rigidity [156]. Changes in the molar ratio of PE/PC has been related to changes in metabolism and liver diseases [157]

In this section, we will analyse the stability of DOPE on the Hg/Pt electrode, and we will establish the parameters for its correct deposition on the Hg/Pt electrode for future RCV experiments.

DOPE stability under a continuous flow of PBS was studied by depositing DOPE on the Hg/Pt electrode and analysing the current peaks. Figure 6. 28 shows how the RCV profile of DOPE varies with time.

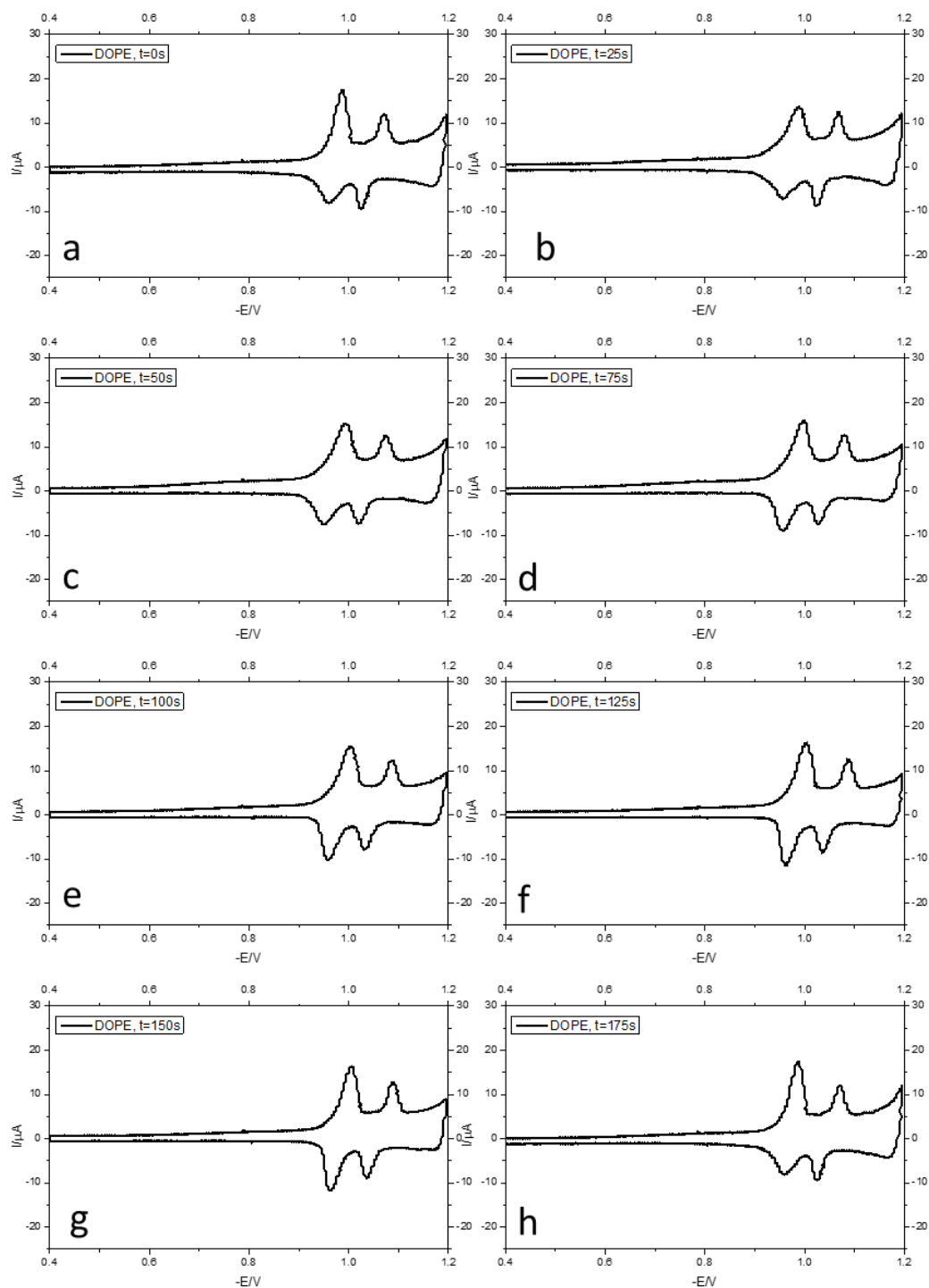


Figure 6. 28: RCV profile of DOPE in PBS (pH 7.4.0) recorded at 40V s⁻¹ using potential cycles from -0.4V to -1.2V at time: (a): t=0s, (b): t=25s, (c):t=50s, (d): t=75s, (e): t=100s, (f):t=125s, (g): t=150s, (h):t=175s, (i): t=200s, and (j) t=225s.

DOPE was deposited by applying cycles from -0.4V to -2.8V. However, the deposition is difficult and it is not sufficiently reproducible. When DOPE is stable, its RCV has two current peaks at -0.99V and -1.07V that vary with time as shown in Figure 6. 28. Figure 6. 29 show the variation of current versus time produced when DOPE is deposited in the Hg/Pt electrode.

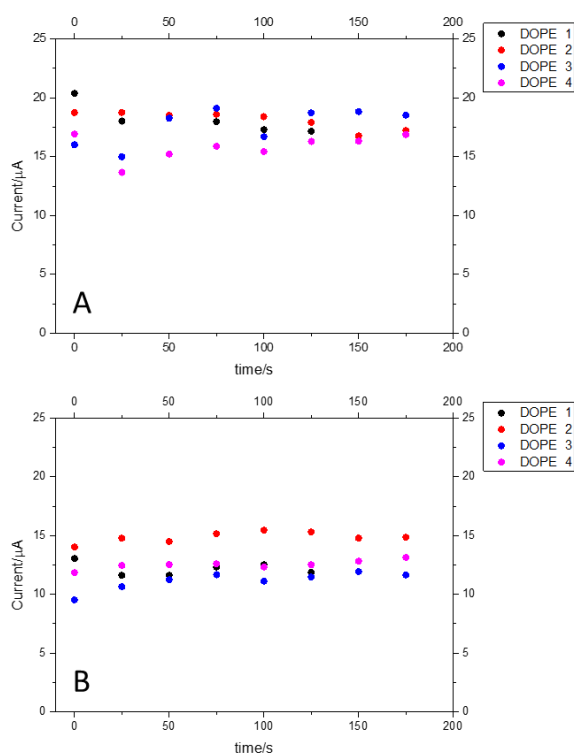


Figure 6. 29: Current variation with time of 4 different DOPE depositions in PBS (pH 7.4) of (a) Peak 1: Black dots: DOPE 1, red dots: DOPE 2, light blue: DOPE 3, pink dots: DOPE 4 and (b) Peak 2. Black dots: DOPE 1, red dots: DOPE 2, light blue: DOPE 3, pink dots: DOPE 4,

As observed in Figure 6. 31, the average peak suppression of the current peaks of DOPE shows that the current of the peaks tend to increase with time which suggests the phospholipid monolayer is becoming more stable with time. This fact is supported by Figure 6. 30, which displays the variation of the baseline current of the phospholipid. For this reason, the reference RCV profile for DOPE was taken after 125s of its deposition.

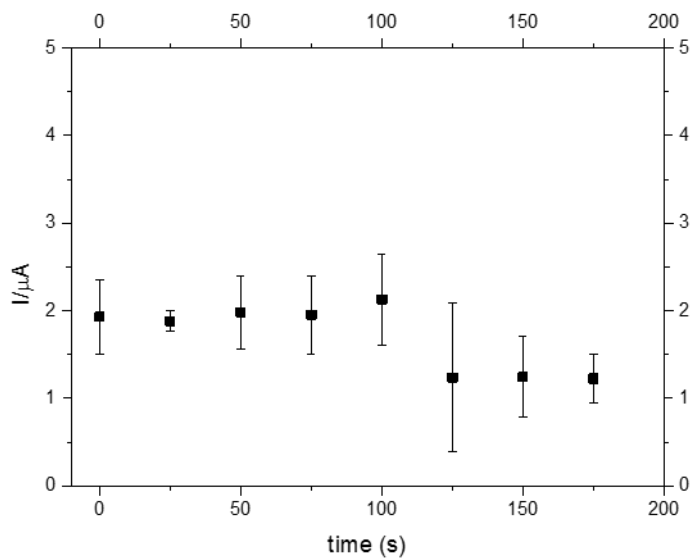


Figure 6.30: Current at $-0.8V$ when DOPE in PBS (pH 7.4) when the RCV profile is recorded at $40Vs^{-1}$ using potential cycles from $-0.4V$ to $-1.2V$.

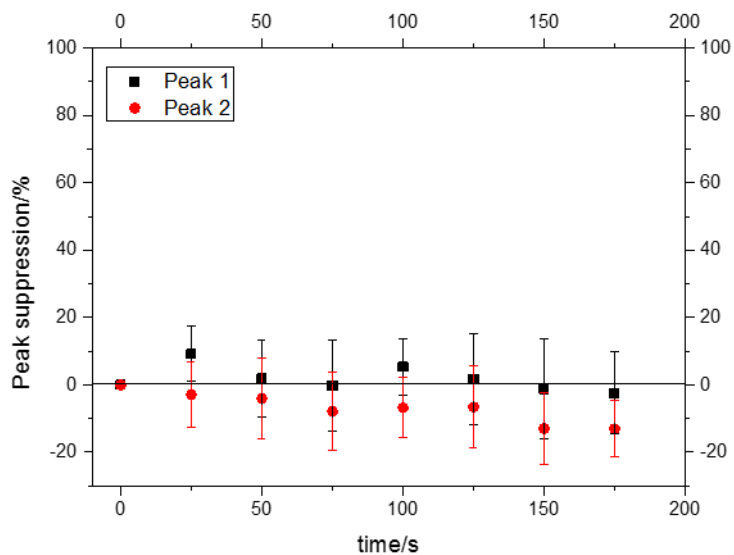


Figure 6.31: Average peak suppression of the current peaks of the RCV voltammograms with time of DOPE in PBS (pH 7.4). Black dots: Peak 1 of the voltammogram. Red dots: Peak 2 of the voltammogram.

6.4 DOPS

DOPS is usually used as a substitute for the naturally occurring PS in the brain. DOPS consists of two fatty chains attached to a glycerol backbone and a polar head formed by a phosphate group and a serine group. Serine contains an amino group and a carboxyl group. DOPS has pK_a values (Table 6. 1) of 2.6, 5.5 and 11.5 thus, DOPS is anionic at physiological pH.

Despite the relatively low abundance of DOPS, it is the commonest negatively charged phospholipid in eukaryotic cells. The role DOPS plays on the cell depends on its location. DOPS can be usually found in the inner leaflet of the cell membrane. However, it can also be present in the outer leaflet of the cell membrane. In addition, DOPS can be present in different organelles. In this way, outer-located DOPS is found to act as a sporadic signal in different processes like in the hemostasis and coagulation of blood [158] and recognition and clearance of apoptotic cells [159, 160]. Outer-located DOPS works as a target for phagocytic cells to engulf apoptotic cells [161]. The role of inner-facing DOPS is less known. Inner-facing DOPS has been found to interact with diverse proteins. However, in general, the selectivity of the proteins towards DOPS is low and they interact with any negatively charged phospholipid [162].

In this section, stability of DOPS on the Hg/Pt electrode is analysed in order to establish the parameters for its correct deposition on the Hg/Pt electrode for future RCV experiments.

DOPS stability on the Hg/Pt electrode was studied by analysing the variation of the current peaks of its voltammogram. When ideally deposited (Figure 6. 32), DOPS voltammogram shows one peak at high current that remains stable with time.

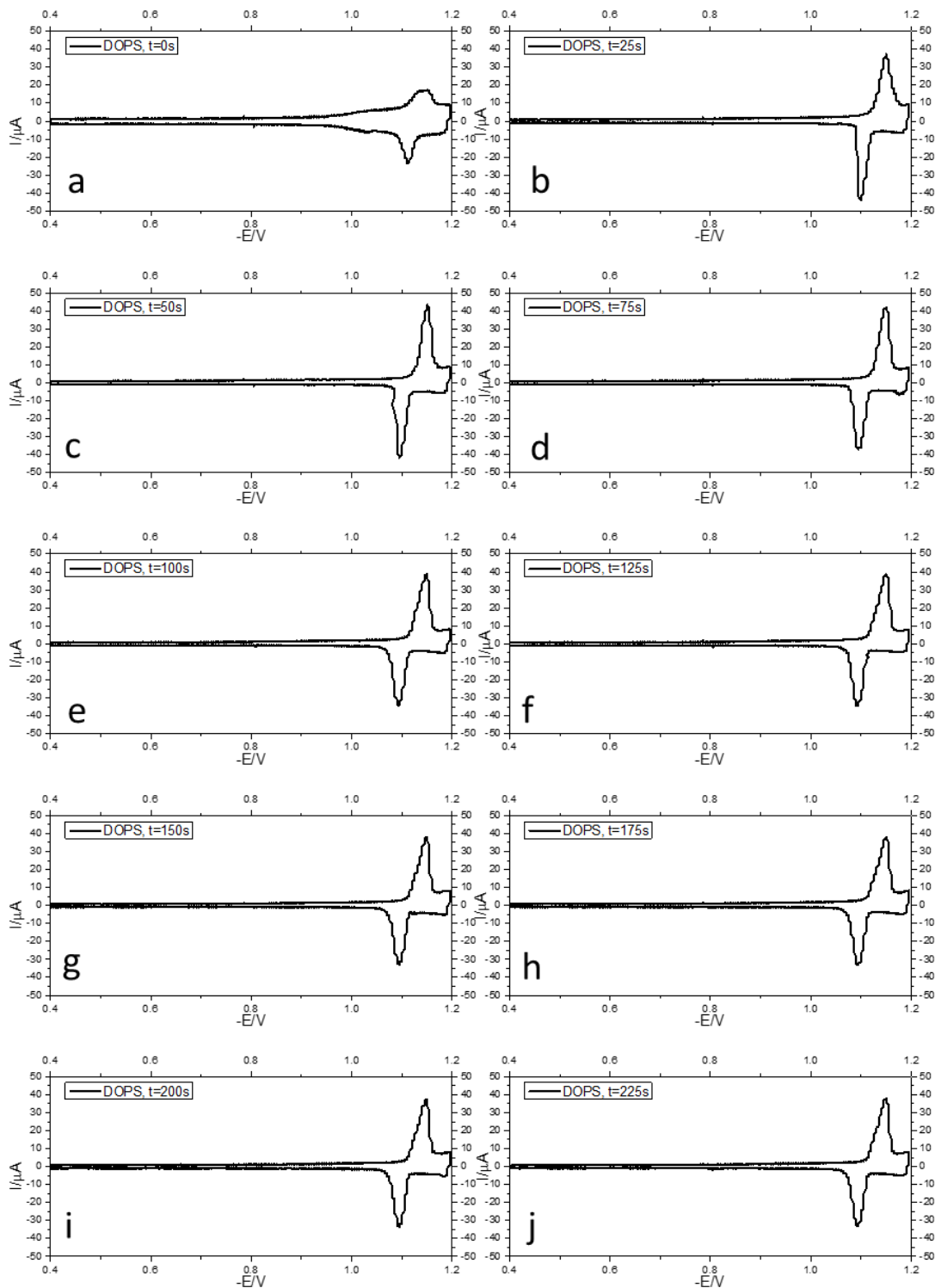


Figure 6. 32: RCV profile of DOPS in PBS (pH 7.4) recorded at $40V s^{-1}$ using potential cycles from $-0.4V$ to $-1.2V$ at time: (a): $t=0s$, (b): $t=25s$, (c): $t=50s$, (d): $t=75s$, (e): $t=100s$, (f): $t=125s$, (g): $t=150s$, (h): $t=175s$, (i): $t=200s$, and (j) $t=225s$.

However, a perfect deposition is hard to obtain, and usually, the voltammogram presents a smaller but constant capacitance-current peak with time (Figure 6.33).

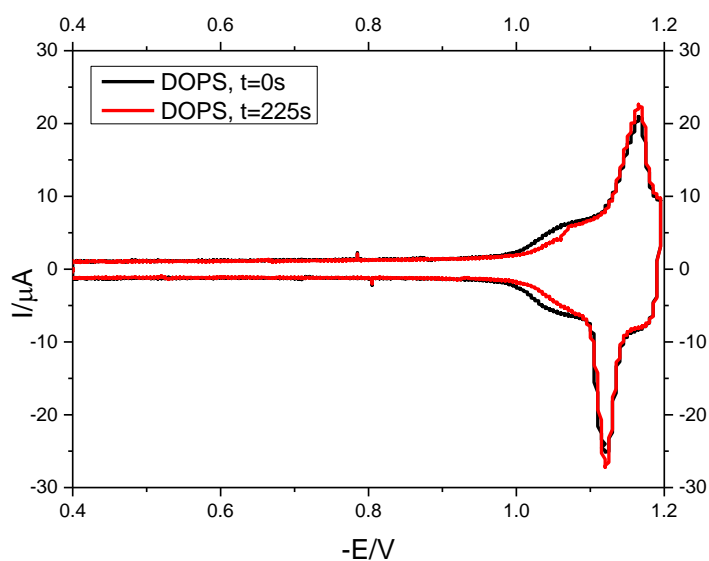


Figure 6.33: RCV profile of DOPS in PBS (pH 7.4) recorded at 40Vs-1 using potential cycles from -0.4V to -1.2V at: Black line: $t=0s$ and red line: $t=225s$.

Figure 6.34 shows the variation of the current of the peak of DOPS. As observed, there is a clear difference between both types of phospholipid depositions. When recently deposited, DOPS exhibits currents from $15\mu A$ to $20\mu A$.

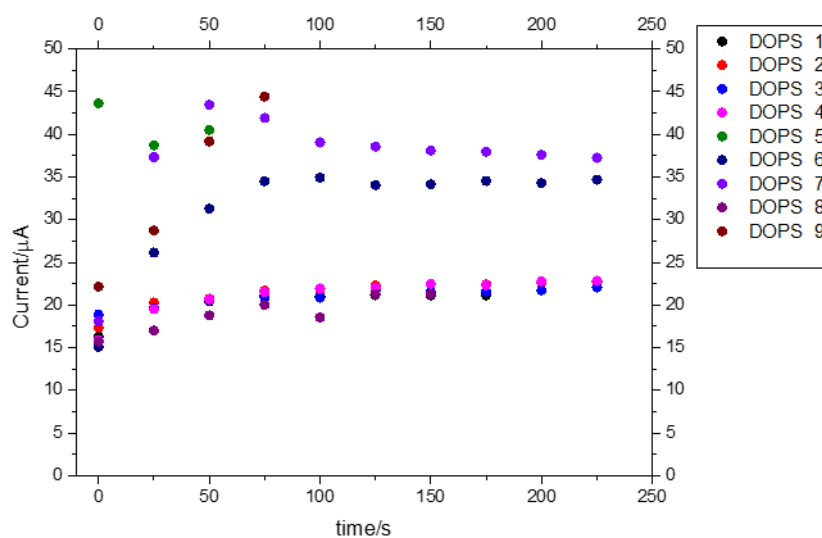


Figure 6.34: Current variation with time of 10 different DOPS depositions in PBS (pH 7.4) of (A) Peak 1. Black dots: DOPS 1, red dots: DOPS 2, light blue: DOPS 3, pink dots: DOPS 4, dark green: DOPS 5, dark blue: DOPS 6, light purple: DOPS 7, dark purple: DOPS 8, brown: DOPS 9.

Nevertheless, when the phospholipid is ideally deposited, the current of the voltammogram peak rapidly increases up to around $40\mu\text{A}$.

The tendency of the baseline to decrease with time in both cases indicates the lipid is getting more stable on the Hg/Pt with time (Figure 6. 35). When DOPS is perfectly deposited, the baseline current is smaller, which indicates the phospholipids are more well-packed on the Hg/Pt electrode.

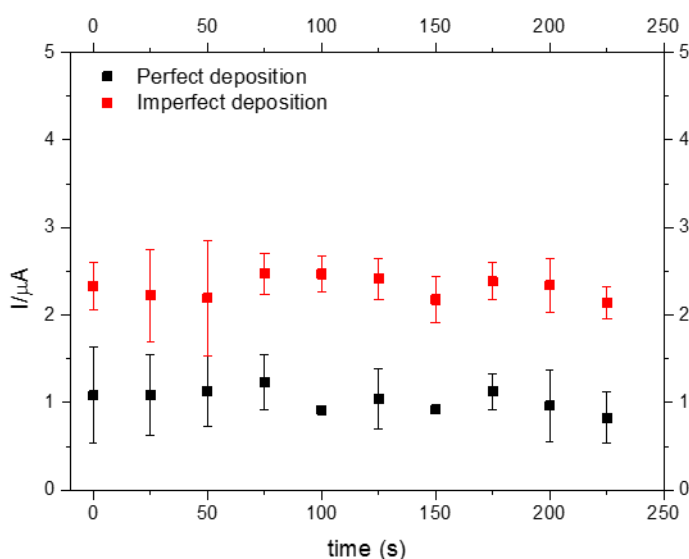



Figure 6. 35: RCV profile current at -0.8V of DOPS in PBS (pH 7.4) when the RCV profile is recorded at 40Vs^{-1} using potential cycles from -0.4V to -1.2V .

DOPS has a negatively charged polar head group that tends to be rejected from the Hg/Pt electrode. For this reason, DOPS tends to be extremely challenging to deposit. When carrying out the experiments, a clear RCV profile response was not common. This behaviour indicates that DOPS is un-stable on the Hg/Pt electrode.

DOPS despite being theoretically unstable on the electrode because of its negative charged polar head, DOPS was observed to be stable on the electrode when correctly deposited. Nevertheless, DOPS requires special conditions for its correct deposition. DOPS is easier to deposit at low temperatures and with a very clean electrode surface. As previously mentioned, DOPS tends to form HII supramolecular structures with polar heads facing inwards and hydrophobic tails facing outwards. If this were the structure DOPS formed when deposited




on the Hg/Pt electrode, the hydrophobic tails could regulate the electrostatic repulsion produced from the electrode, while the affinity between the phospholipid and electrode would increase due to the hydrophobic effect. This theory also implies that DOPS must be forming a closed structure before its deposition on the electrode surface to be stable; thus, the packing on the electrode depends on the concentration of HII structures before deposition. This fact could explain the two RCV profile types, with differences in current height, obtained. A low concentration of HII structures before the phospholipid deposition would produce a high baseline current and low peak current due to the incomplete packing of the phospholipids on the electrode.

6.5 DOPA

DOPA is commonly used as a substitute for the naturally occurring PA in the living cell. PA is the simplest phosphatidic acid. It has two fatty acid chains, a glycerol backbone and a phosphate group with an attached hydroxyl group. Its abundance in living organisms is lower than 1% [163]. However, its presence is vital due to the multiple roles PA can play in the cell. As mentioned before in Table 6. 1, DOPA has two pKa values, 3 and 8, which means the PA polar head can be modified (protonated or deprotonated) at physiological pHs by diverse factors including other phospholipids, environmental pH and proteins.

PA has the rare ability to form intramolecular hydrogen bonds with other phospholipids. This happens in mixtures of PC and PE lipids bilayers with small concentrations of PA. PE, which is a primary amine, thus a good hydrogen bond donor, can promote the deprotonation of PA causing a decrease of the pK_a [164]. Since the composition of cellular membranes is different, the phospholipids ratio determines the functionality. For example, in membranes with a high concentration of PE, the deprotonation of PA by the PE was found to lead to the association of Tas3p protein with PA [165]. In addition, environmental pH conditions, and thus protonation and deprotonation, modulates the attachment of PA to proteins and their activity [166]. In the same way, proteins can promote the deprotonation of PA. For example, proteins with arginine and lysine residues were found to promote the deprotonation of a single charged PA [167].

PA can induce negative curvature in lamellar structures as well. The curvature depends on several factors such as temperature, pH, ionic strength, the concentration of PA in the mixture of lipids and the mixture of lipids itself. As mentioned before, the packaging of phospholipids depends on steric factors. In this way, the size of the polar head is affected by pH and ionic strength [168] which affects PA lamellar structure. PA was found to behave as if it had cylindrical shape under high ionic strengths (150mM NaCl) in pure water which generates a negative curvature in PA rich monolayers [169]. In addition, this



behaviour is enhanced at acidic pH [170] and depends on the concentration of PA in the monolayer [171].

Environmental conditions affect the PA structure and thus its activity. For this reason, PA is involved in many different biological functions which are the main reason for its importance. In this section, DOPA stability on the Hg/Pt electrode is studied. This section will provide information on the methodology to deposit a stable DOPA layer and the information will be used in future RCV studies.

DOPA behaviour on the Hg/Pt electrode was found to be dependent on the switching potential. The following figure shows RCV profiles of DOPA when exposed to potential cycles from -0.4V to -1.2V (Figure 6. 36A) and cycles from -0.4V to -1.4V (Figure 6. 36B). As already mentioned, the peaks of the voltammogram are representative of phase transitions of the phospholipids on the Hg/Pt electrode. When the potential cycle is extended, three additional peaks which correspond to three additional phase transitions appear.

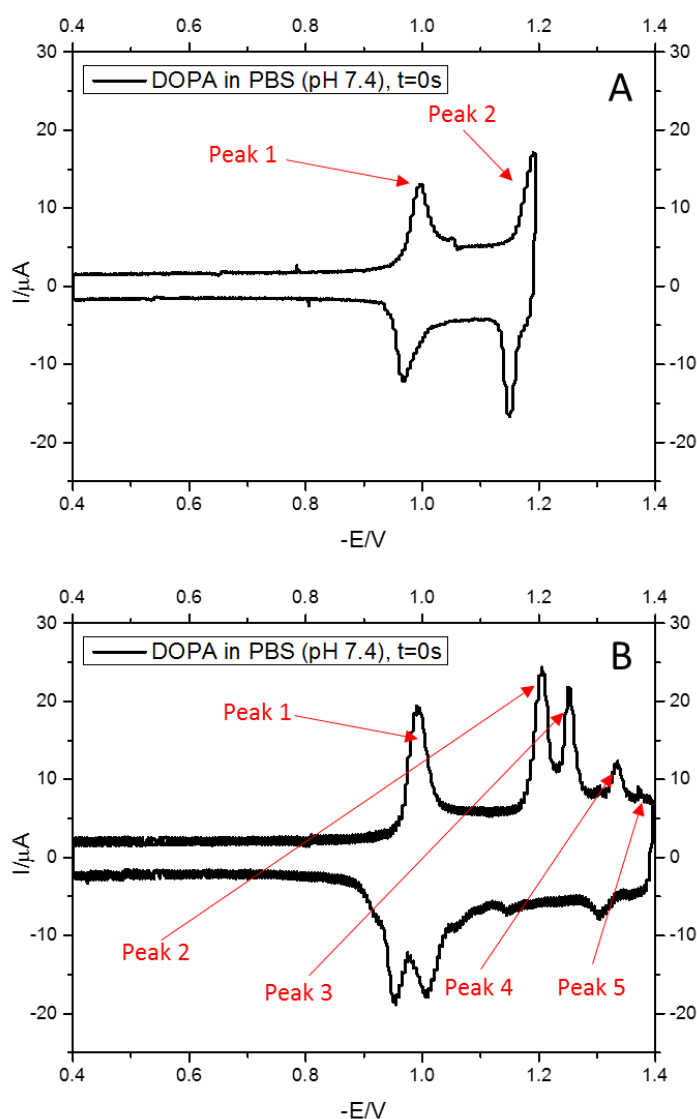



Figure 6. 36: RCV profile of DOPA in PBS (pH 7.4) using potential cycles from: (A): -0.4V to -1.2V recorded at 40V s⁻¹ and (B): -0.4V to -1.4V recorded at 46V s⁻¹



DOPA stability on a Hg/Pt electrode under a constant flow of PBS (pH=7.5) under potential cycles from -0.4V to -1.2V was studied initially as it was the same as the protocol for deposition of other phospholipids. The height of the current peaks of the voltammograms with time for 10 different DOPA depositions was analysed. Figure 6. 37 displays how the RCV voltammogram of DOPA varies under the conditions described above.

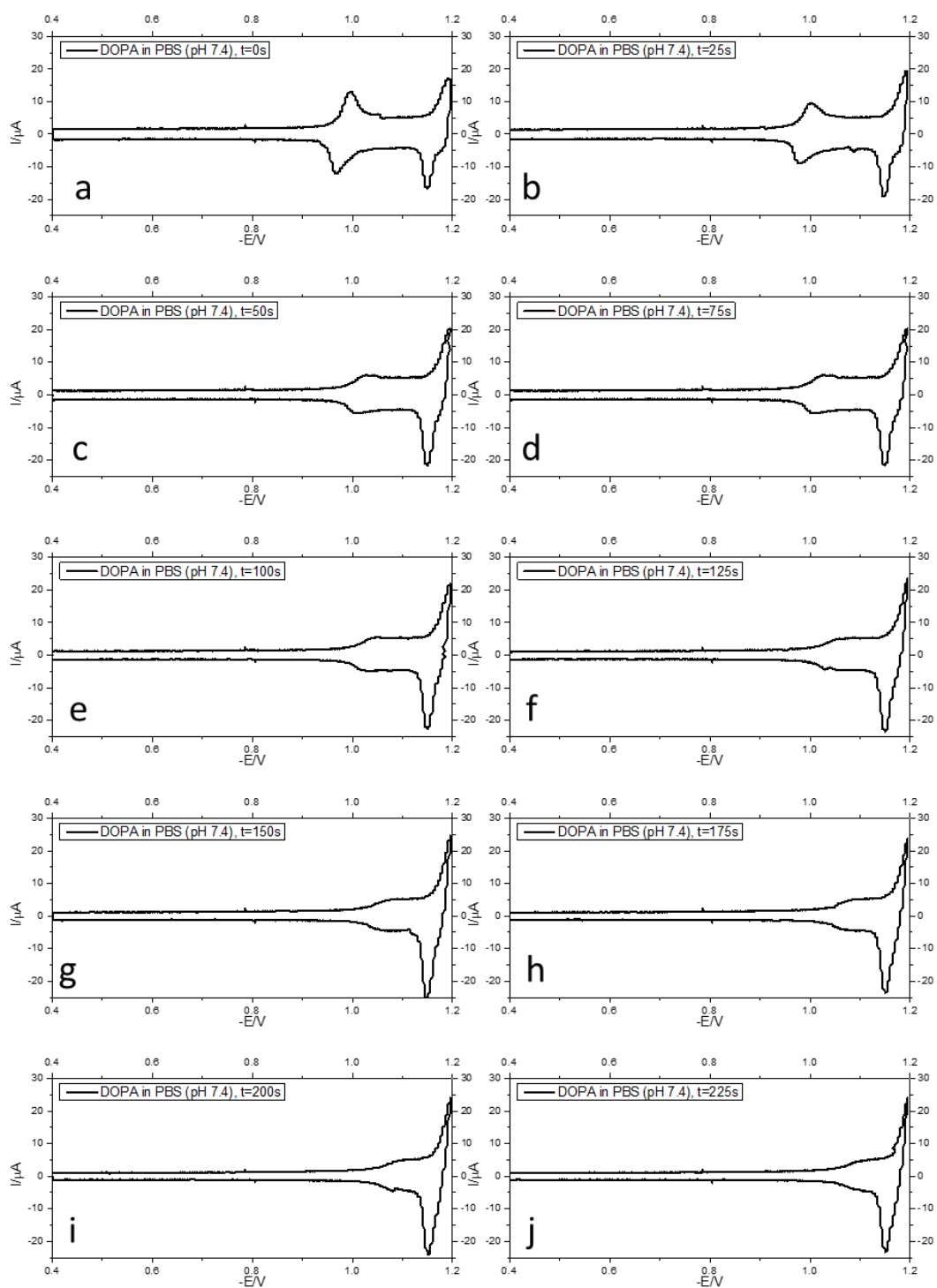


Figure 6. 37: RCV profile of DOPA in PBS (pH 7.4,0) recorded at 40V s⁻¹ using potential cycles from -0.4V to -1.2V at time: (a): t=0s, (b): t=25s, (c):t=50s, (d): t=75s, (e): t=100s, (f):t=125s, (g): t=150s, (h):t=175s, (i): t=200s, and (j) t=225s.

As can be observed, the first peak of DOPA is highly unstable when potential cycles from -1.2V to -1.4V are applied. This fact is confirmed as well by Figure 6. 38, that shows the average peak suppression of the current peaks of the voltammogram versus time. The first peak of the voltammogram is suppressed to approximately 40% of the initial current and then, after 25s, it completely disappears. Nevertheless, the second peak of the RCV voltammogram increases with time while the first peak decreases.

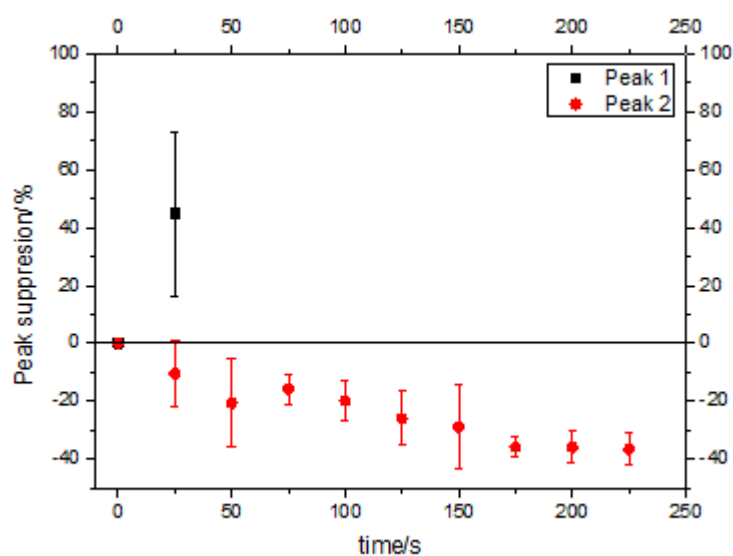


Figure 6. 38: Average peak suppression of the current peaks of the RCV voltammograms with time of DOPA in PBS (pH=7.4). Black dots: Peak 1 of the voltammogram. Red dots: Peak 2 of the voltammogram.

After these experiments, DOPA was deposited on the Hg/Pt electrode in the same manner as previously, but instead, potential cycles from -0.4V to -1.4V were applied. It was observed that:

- The stability of the 1st peak was higher;
- The first peak is recovered when potential cycles were changed from -1.2V to -1.4V;

Figure 6. 39 shows the stability of the DOPA deposited under the conditions described above. In contrast to that previously observed, the first peak remains stable with time.

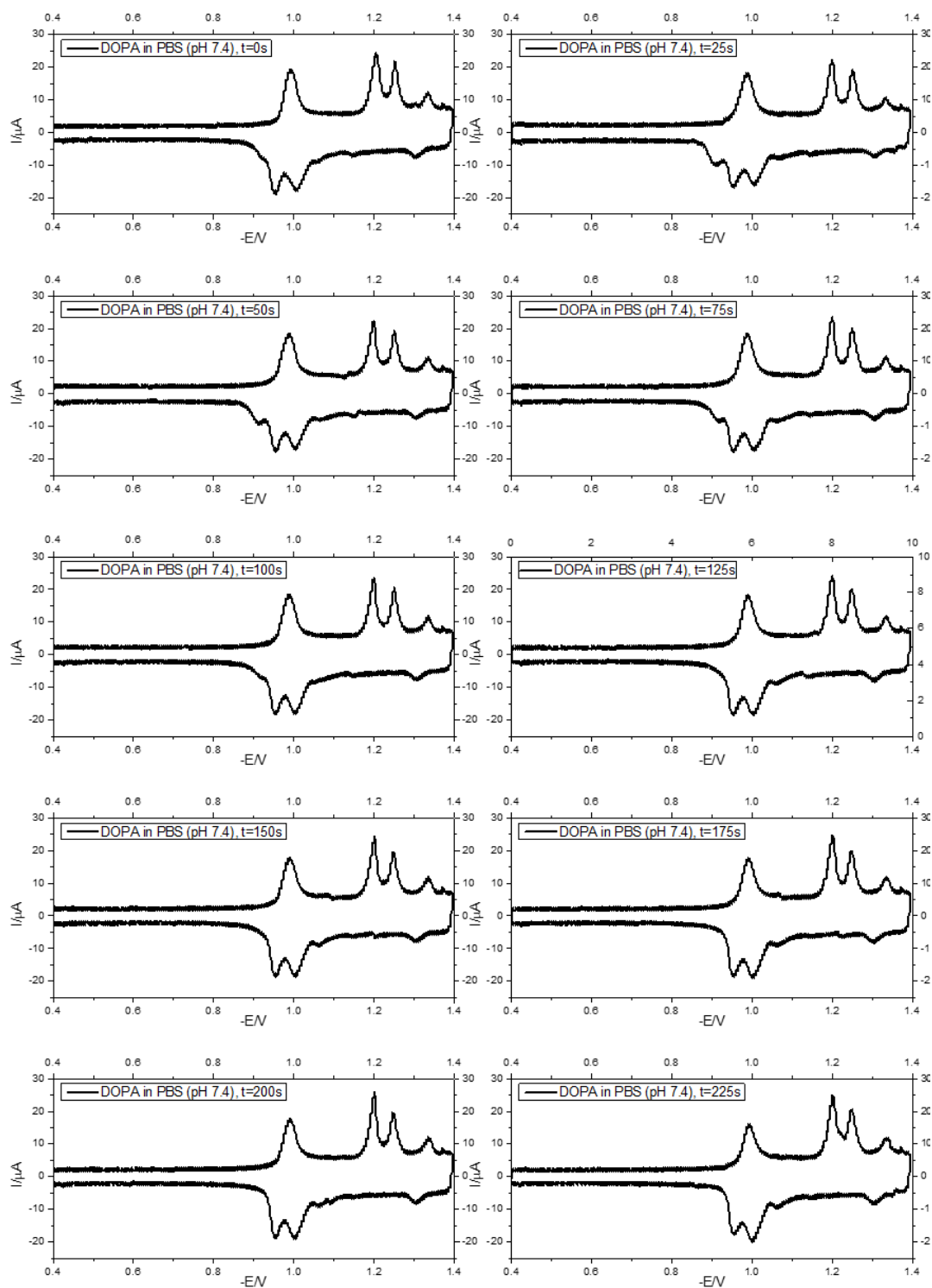


Figure 6. 39: RCV profile of DOPA in PBS (pH 7.4.0) recorded at $40V s^{-1}$ using potential cycles from $-0.4V$ to $-1.4V$ at time: (a): $t=0s$, (b): $t=25s$, (c): $t=50s$, (d): $t=75s$, (e): $t=100s$, (f): $t=125s$, (g): $t=150s$, (h): $t=175s$, (i) $t=200s$, and (j) $t=225s$.

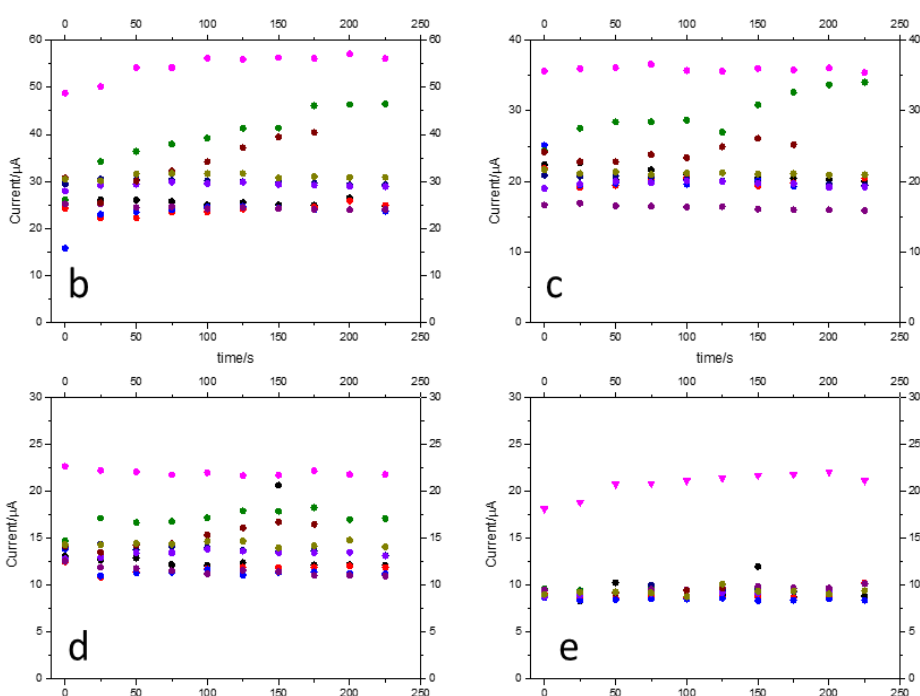
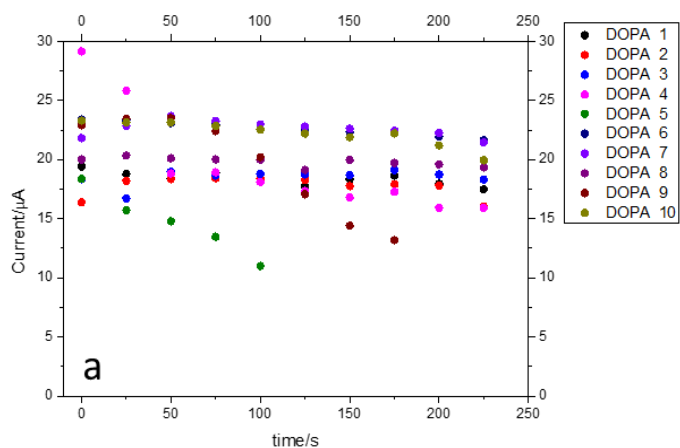


Figure 6. 40: Current variation with time of 10 different DOPA depositions in PBS (pH 7.4) of (a) **Peak 1**: Black dots: DOPA in PBS 1, red dots: DOPA in PBS 2, light blue: DOPA in PBS 3, pink dots: DOPA in PBS 4, dark green: DOPA in PBS 5, dark blue: DOPA in PBS 6, light purple: DOPA in PBS 7, dark purple: DOPA in PBS 8, brown: DOPA in PBS 9, and light green: DOPA in PBS 10, (b) **Peak 2**: Black dots: DOPA in PBS 1, red dots: DOPA in PBS 2, light blue: DOPA in PBS 3, pink dots: DOPA in PBS 4, dark green: DOPA in PBS 5, dark blue: DOPA in PBS 6, light purple: DOPA in PBS 7, dark purple: DOPA in PBS 8, brown: DOPA in PBS 9, and light green: DOPA in PBS 10 (c) **Peak 3**: Black dots: DOPA in PBS 1, red dots: DOPA in PBS 2, light blue: DOPA in PBS 3, pink dots: DOPA in PBS 4, dark green: DOPA in PBS 5, dark blue: DOPA in PBS 6, light purple: DOPA in PBS 7, dark purple: DOPA in PBS 8, brown: DOPA in PBS 9, and light green: DOPA in PBS 10. (d) **Peak 4**: Black dots: DOPA in PBS 1, red dots: DOPA in PBS 2, light blue: DOPA in PBS 3, pink dots: DOPA in PBS 4, dark green: DOPA in PBS 5, dark blue: DOPA in PBS 6, light purple: DOPA in PBS 7, dark purple: DOPA in PBS 8, brown: DOPA in PBS 9, and light green: DOPA in PBS 10 (e) **Peak 5**: Black dots: DOPA in PBS 1, red dots: DOPA in PBS 2, light blue: DOPA in PBS 3, pink dots: DOPA in PBS 4, dark green: DOPA in PBS 5, dark blue: DOPA in PBS 6, light purple: DOPA in PBS 7,

Figure 6. 40 shows the variation of the current of the voltammogram peaks with time for 10 different depositions of DOPA in PBS when cycles from -0.4V to -

1.4V are applied. DOPA 4, DOPA 5 and DOPA 9 displayed an unstable phase transition at around -1V (Peak 1) whereas DOPA 1, 2, 3, 6, 7, 8 and 10 displayed a stable phase transition at -1V.

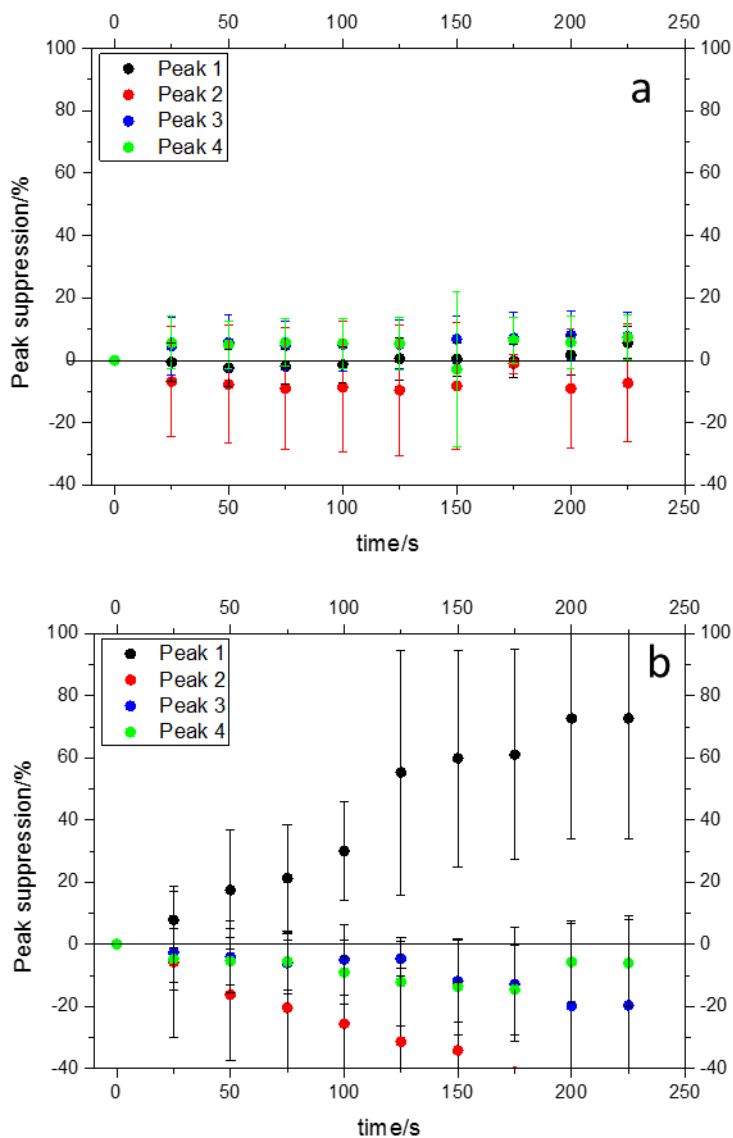


Figure 6. 41: Average peak suppression of the current peaks of the RCV voltammograms with time of DOPA in PBS (pH=7.4) of (a) **Stable Peak 1**: Black dots: Peak 1 of the voltammogram. Red dots: Peak 2 of the voltammogram. Blue dots: Peak 3 of the voltammogram. Green dots: Peak 4 of the voltammogram. (b) **Unstable Peak 1**: Black dots: Peak 1 of the voltammogram. Red dots: Peak 2 of the voltammogram. Blue dots: Peak 3 of the voltammogram. Green dots: Peak 4 of the voltammogram

In general terms, the first peak of the RCV voltammogram of DOPA is more stable when the phospholipid is exposed to potential cycles from -0.4V to -1.4V

than when exposed to cycles from -0.4V to -1.2V. As observed in Figure 6. 41A, all the current peaks of the voltammogram remain constant with time. It is important to notice that the suppression of peak 5 is not displayed in Figure 6. 41. Peak 5 is low in current and, for this reason, it sometimes disappears in the background noise which hampers its characterisation. Figure 6. 41B shows the suppression of the current peaks when peak 1 is unstable. As previously seen, peak 2 along with peaks 3 and 4 increase in current while peak 1 decreases. However, the suppression of the peak is not so abrupt as previously seen in Figure 6. 38, where peak 1 disappeared after 25s. In this case, the height of the peak 1 of DOPA at 25s only reduces to 10% of its initial value.

In this way, it is confirmed that a stable RCV profile of DOPA can be obtained when DOPA is deposited at potential cycles from -0.4V to -1.4V are applied. The reference RCV profile was taken at 25s.

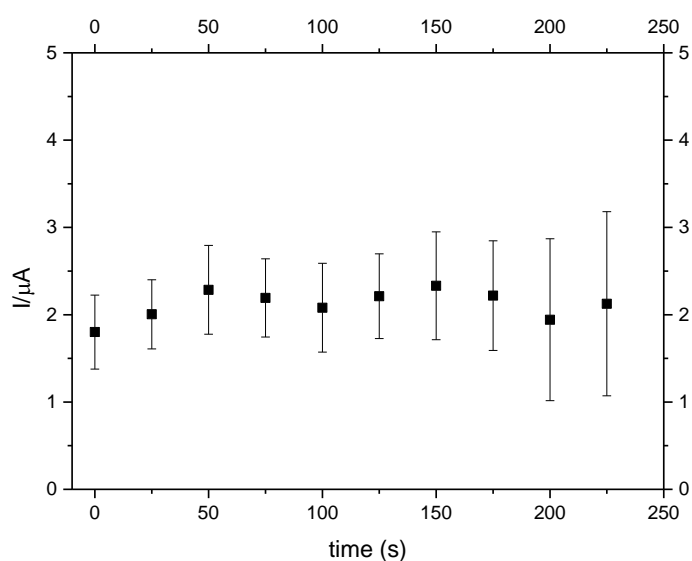


Figure 6. 42: Current at -0.8V when DOPA in PBS (pH 7.4) when the RCV profile is recorded at 40Vs-1 using potential cycles from -0.4V to -1.2V.

Figure 6. 42 shows the variation of the baseline current of the voltammogram. As can be observed, the current remains constant with time. The higher errors can be explained due to the increase in noise when the potential current cycles are increased.

6.6 DOPG

1,2-dioleoyl-*sn*-glycero-3-phospho-(1'-*rac*-glycerol) (sodium salt), also called DOPG, is a phospholipid mostly found in membranes of bacteria and higher plants. DOPG consists of two hydrophilic fatty chains attached to a glycerol backbone which is linked to a phosphate polar head formed by a phosphate attached to a glycerol (Figure 6. 3). The pK_a of DOPG is 3.5 (Table 6. 1). For this reason, DOPG is expected to be negatively charged at pH 7.4 (PBS).

DOPG stability on a Hg/Pt electrode under a constant flow of PBS (pH 7.4) was studied. In this way, the height of the current peaks of the voltammograms as a function of time for 10 different DOPC depositions was analysed.

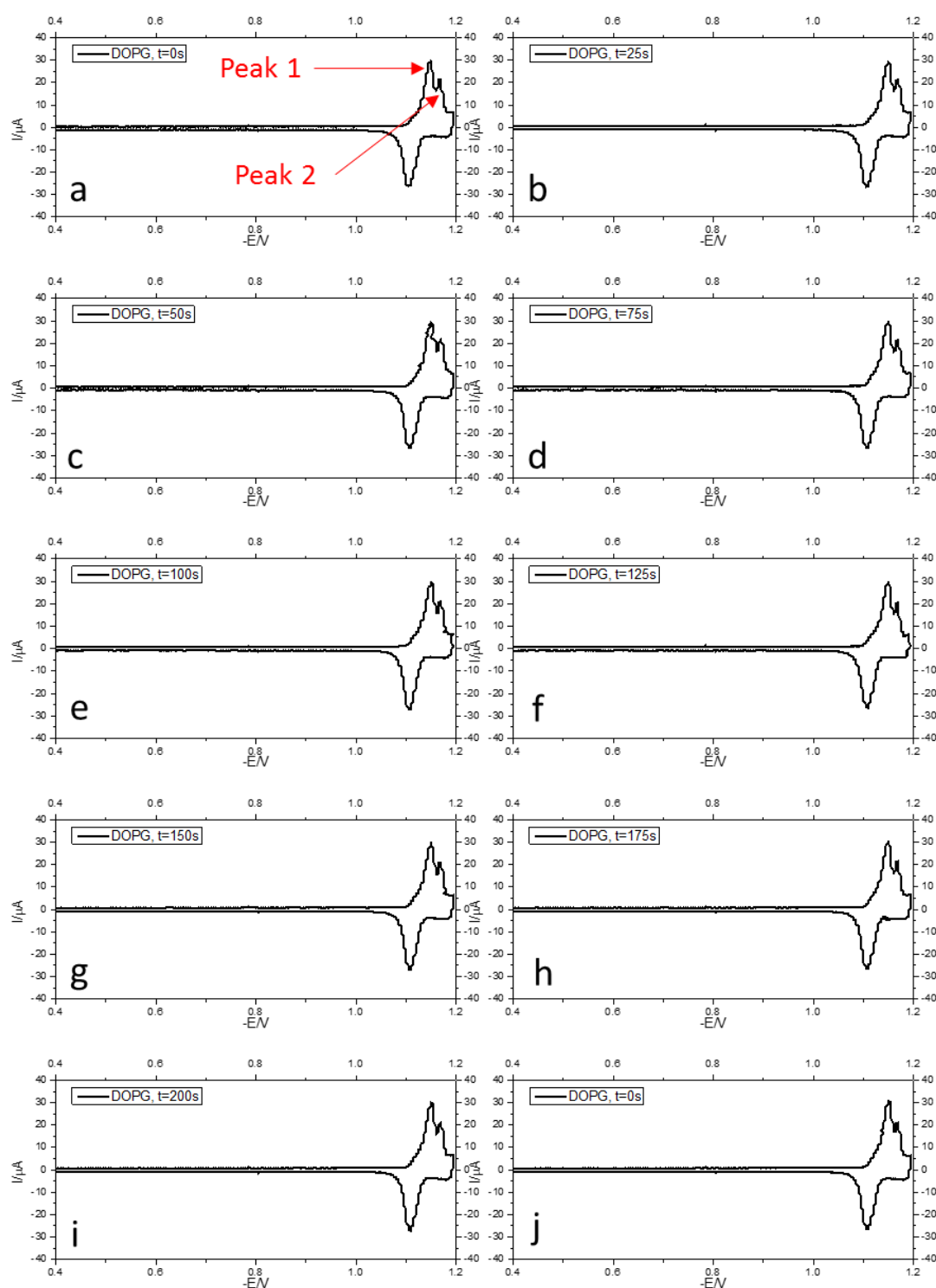


Figure 6. 43: RCV profile of DOPG in PBS (pH 7.4.0) recorded at 40V s⁻¹ using potential cycles from -0.4V to -1.2V at time: (a): t=0s, (b): t=25s, (c):t=50s, (d): t=75s, (e): t=100s, (f):t=125s, (g): t=150s, (h):t=175s, (i): t=200s, and (j) t=225s.

Figure 6. 43 shows how the RCV profile of DOPG under a continuous flow of PBS varies versus time. As can be observed, DOPG has two clear current peaks at -1.15V and -1.17V that remains very stable with time. Peak 2 is low in current and is sometimes hidden by the background. The following figure (Figure 6. 44), shows the variation of current versus time for 10 different depositions of DOPG on the Hg/Pt electrode.

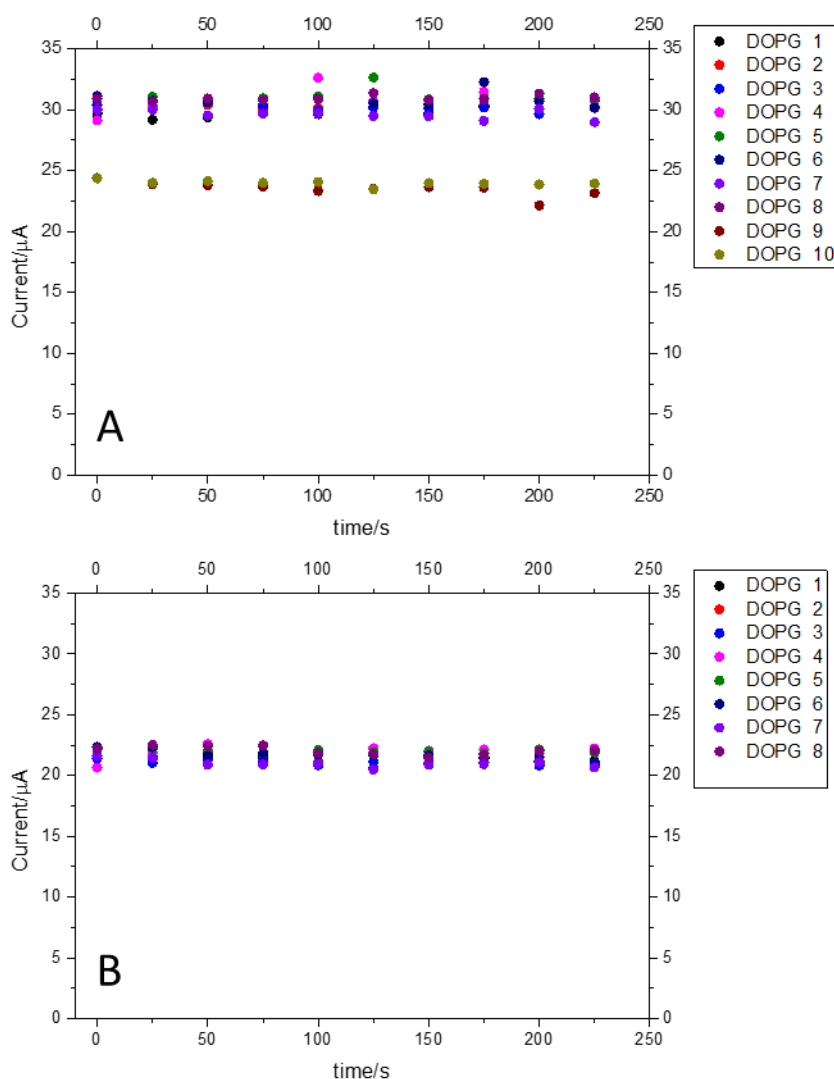


Figure 6. 44: Current variation with time of 10 different DOPG depositions in PBS (pH 7.4) of (A) Peak 1. Black dots: DOPG 1, red dots: DOPG 2, light blue: DOPG 3, pink dots: DOPG 4, dark green: DOPG 5, dark blue: DOPG 6, light purple: DOPG 7, dark purple: DOPG 8, brown: DOPG 9, and light green: DOPG 10, (b) Peak 2. Black dots: DOPG 1, red dots: DOPG 2, light blue: DOPG 3, pink dots: DOPG 4, dark green: DOPG 5, dark blue: DOPG 6, light purple: DOPG 7, dark purple: DOPG 8.

The second peak in depositions 9 and 10 was not visible in the voltammogram. For this reason, they do not appear in Figure 6. 44B.

Figure 6. 45 shows the average peak suppression of the current peaks. As observed, the current remains constant with time. In addition, the baseline of the voltammogram remains constant as well. For this reason, the reference RCV profile of DOPG when in contact with a continuous flow of PBS at pH 7.4 can be taken immediately after the deposition of the lipid.

The stability of the DOPG layer on the Hg/Pt electrode is also confirmed by analysing the baseline current of the voltammograms. As observed, the baseline current is constant with time. In addition, errors are small. The RCV profile was taken straight after its deposition on the electrode.

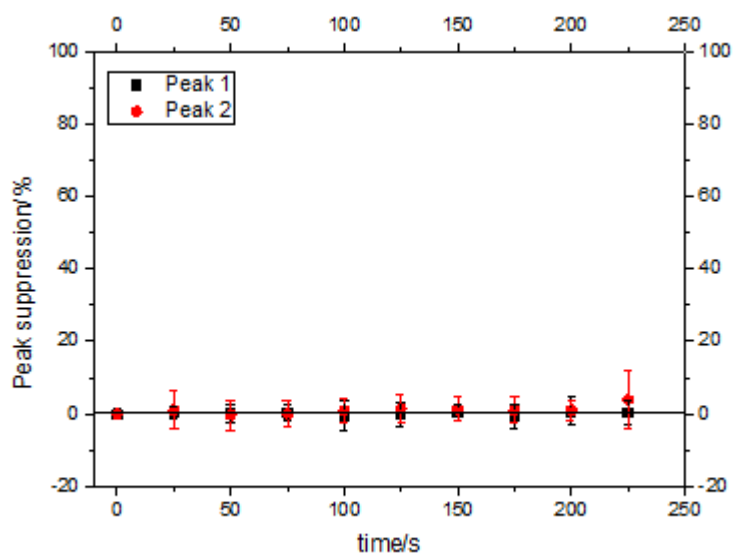


Figure 6. 45: Current at $-0.8V$ when DOPG in PBS (pH 7.4) when the RCV profile is recorded at $40Vs^{-1}$ using potential cycles from $-0.4V$ to $-1.2V$.

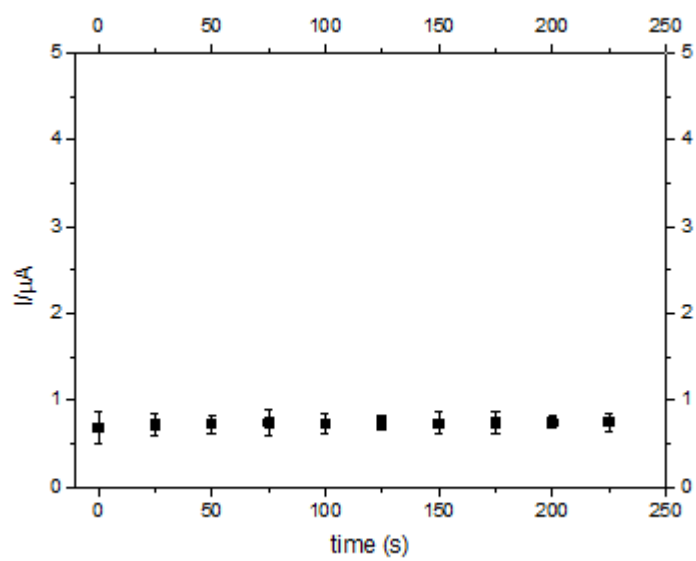


Figure 6. 46: Current at $-0.8V$ when DOPG in PBS (pH 7.4) when the RCV profile is recorded at $40Vs^{-1}$ using potential cycles from $-0.4V$ to $-1.2V$.

6.7 Chapter 6. Summary

DOPE, DOPS, DOPA, DOPG and DOPC were all shown to be stable, to differing extents, when deposited on the Hg/Pt electrode surface under the previously mentioned conditions. Spite of the fact that DOPE can form stable phospholipid monolayers on the Hg/Pt electrode, it is, as well, the most unstable phospholipid used. More than 10 trials were needed to obtain four stable phospholipids to carry out the stability experiments. Most of the time, DOPE did not deposit, which makes difficult working with DOPE. DOPS is also difficult to deposit and, most of the time, it does not deposit at all. Nevertheless, DOPS spite of being negatively charged, thus theoretically unstable in the Hg/Pt electrode, forms stable monolayers in the Hg/Pt electrode and produce two RCV profiles, different in peak size, when correctly deposited. The size of the current peaks is related to how much packaged the electrode is. High current peaks and a small baseline current indicate the phospholipid is perfectly deposited in the electrode. Smaller current peaks and a higher baseline current indicates there are holes in the monolayer and thus DOPS has not completely deposited. It is theorised that DOPS must be forming HII closed structures to reduce the electrostatic repulsion with the electrode before being deposited on the Hg/Pt electrode to obtain a perfect and stable RCV profile. DOPA usually deposited on the Hg/Pt electrode obtaining different RCV profiles when the potential cycles were switched. The RCV profiles were shown to be more stable when applying a cyclic potential between -0.4V to -1.4V than when applying a cyclic potential between -0.4V to -1.2V. The RCV profile of DOPG was very stable and reproducible to obtain. Once, correctly deposited, its stability is high under a continuous flow of PBS. DOPC was chosen as the primary phospholipid type to use in the following experiments. The RCV profile of DOPC is very stable and reproducible to obtain under the flow of buffers with different pH. Additionally, DOPC more affordable than the other phospholipids and it has been well characterised previously (in-depth information about the characterisation of the current peaks of DOPC can be found in 6.2.1).

Table 6. 3 summarises the experimental conditions used in the following experiments, which was created from the data obtained from this chapter. The information helps to correctly deposit the different lipids in order to successfully carry out the experiments of CHAPTER 7.

Table 6. 3: Summary of the time at which the RCV profiles were taken and their associated errors of phospholipids in different media

Phospholipid	Media	pH	Reference RCV profile taken at x(s) after deposition	Current peak error/%			
				1	2	3	4
DOPE	PBS	7.4	125	14	12	N/A	N/A
DOPS			N/A	N/A	N/A	N/A	N/A
DOPA			25	6	17	9	8
DOPG			0	1	N/A	N/A	N/A
			0	1	3	N/A	N/A
DOPC	CCB	6.0	0	1	1	N/A	N/A
		5.0	0	1	1	N/A	N/A
		4.0	25	4	6	N/A	N/A
		3.0	100	6	5	N/A	N/A
	GLY	3.0	50	4	4	N/A	N/A

CHAPTER 7. INTERACTION OF CERIA NANOPARTICLES WITH A MODEL MEMBRANE

In this chapter, I investigate the interaction of CeO₂ NPs with model membranes. This chapter is divided into 4 sections which together, will try to explain the mechanisms through which CeO₂ NPs interact. First of all, there is an introduction to the types of RCV response which can be produced when different substances interact on the phospholipid monolayer. In addition, I examine the interaction reactants produce with the phospholipid monolayer as well as the interaction of the NPs with the uncoated Hg/Pt electrode. Then, I evaluate the role phospholipids play in the interaction of CeO₂ NPs. In this way, the interaction between phospholipids, with different polar heads, and CeO₂ NPs are studied. Later, the effect of the medium in CeO₂ interaction with a DOPC monolayer is analysed. Different buffers with pH from 3 to 7.4 were used to disperse the NPs as well as a buffer for the experiments themselves. The procedure to prepare the buffers is described in 6.2.1. Subsequently, taking into account the results from the previous experiments, I will try to understand what is causing the RCV response. In this section, we will evaluate:

- The response that Ce in solution produces on the voltammogram in the different buffers,
- The amount of dissolved cerium that could be generated from dispersing the NPs in acidic buffers
- The amount of Ce³⁺ on the NP surface

Finally, I study the effect which the NPs coating have on the interaction between coated-CeO₂ NPs and DOPC under a continuous flow of PBS.


7.1 The effects on the voltammogram derived from interactions with phospholipids.

In general terms, six major changes in the voltammogram, indicative of a specific type of interaction, are produced when a DOPC monolayer is exposed to a particular substance. The changes in the voltammogram which can be observed are [172] [173] [128]:

- Suppression of the RCV current peaks: is produced when a substance interacts with the phospholipids and a change of the intermolecular forces is generated. It affects the phospholipid orientation and thus the layer permeability to ions.
- A shift of the current peaks: is produced when a substance induces a change in the dipole moment of the phospholipids arising from the direct interaction between phospholipid polar heads and the substance.
- An increase in the current at negative potentials has been related to the semiconductor effect produced by some substances. In other words, to these types of substances can penetrate the phospholipid membrane and interact directly with the Hg/Pt electrode.

Although these effects can be isolated, it is common to observe a mixture of these during the interaction of a particular substance with phospholipid monolayers using RCV. In the same way, if a mixture of two substances, each with a different effect in the voltammogram, is introduced into the ESD, it will produce a voltammogram which will show the addition of those different types of interaction. For this reason and because RCV is a very sensitive technique, thorough testing of the reactants with the ESD was necessary to avoid false-positive results. Sometimes, reactants can remain on the NP surface even after the cleaning process, which can affect the interaction with the DOCP monolayer.

As a result, 0.01M of $\text{Ce}(\text{NO}_3)_3$, which is the maximum concentration of Ce ion from CeO_2 NPs used in the following experiments, was tested. In addition, 0.5M of HMT and 40mM of TMAOH, which match the maximum



concentration of the reactants used in the synthesis of NPs, were also tested. DOPC and PBS were chosen as the primary phospholipid type and buffer used in the experiments as they together form a stable and reproducible RCV profile. Figure 7. 1 show the interaction of $\text{Ce}(\text{NO}_3)_3$, TMAOH and HMT with DOPC under a continuous flow of PBS. As observed, at the previously mentioned concentrations, TMAOH and HMT do not produce a change of the current peaks of the voltammogram. However, in Figure 7. 1, an apparent suppression and shift of the peaks are seen. In this way, it is concluded that cerium in solution (Ce^{3+}) produces an interaction with the DOPC monolayer under these conditions. Ce^{3+} is probably interacting directly with the polar heads of the phospholipids, which causes a shift of the peaks to more positive and negative potentials.

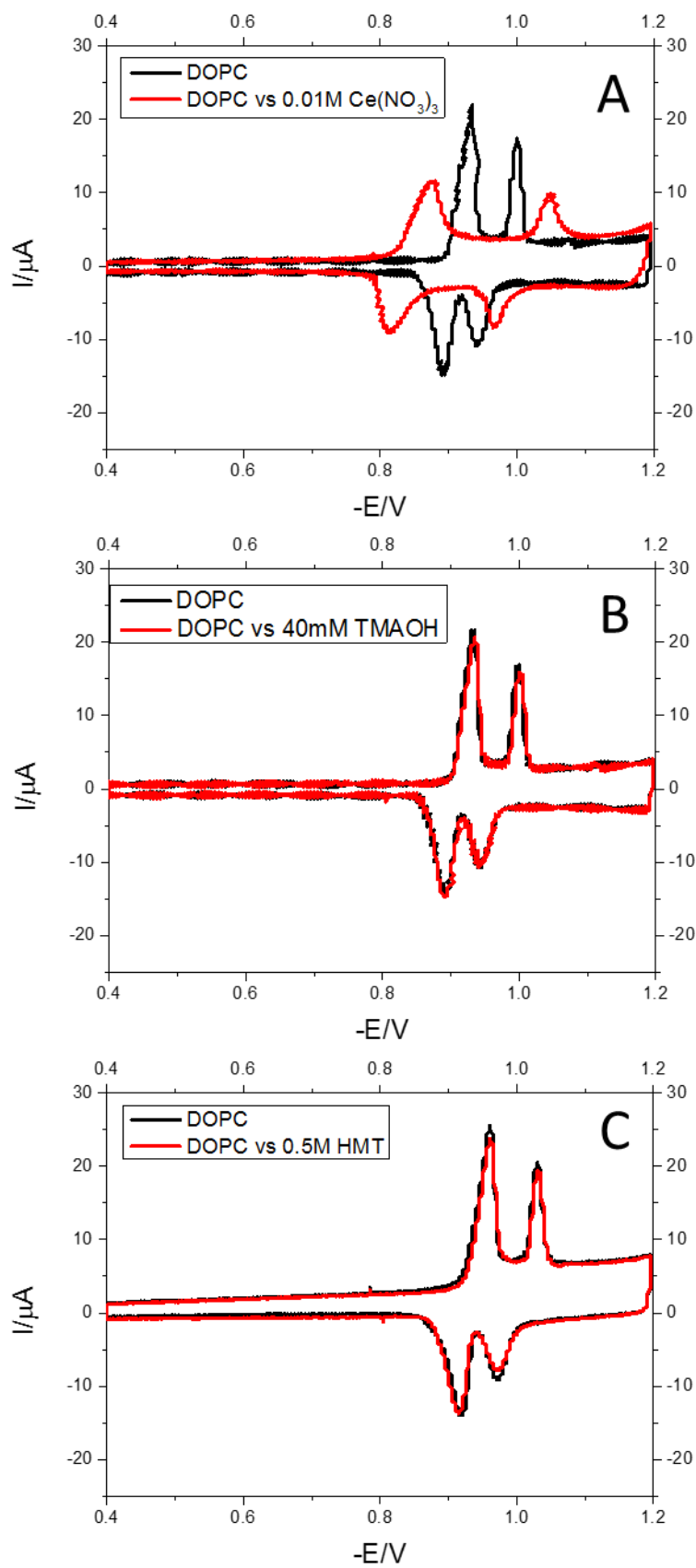


Figure 7.1: RCV voltammograms recorded at 40Vs^{-1} with a potential excursion from -0.4V to -1.20V of DOPC (black lines) under a continuous flow of PBS in the presence of (red lines): A: $0.01\text{M Ce}(\text{NO}_3)_3$, B: 40mM TMAOH and C: 0.5M HMT . RCV voltammograms

In addition, the effect of the NPs with the plain Hg/Pt electrode was studied. The following figure shows the interaction observed when 0.01M of CeO₂ NPs were introduced into the system. As observed in Figure 7. 2, all different morphology CeO₂ NPs at acidic conditions (pH 3.0) show a characteristic increase of the current at negative potentials (red lines of Figure 7. 2). This effect has been previously described for TiO₂ NPs in [128] and has been related to the semiconductor effect.

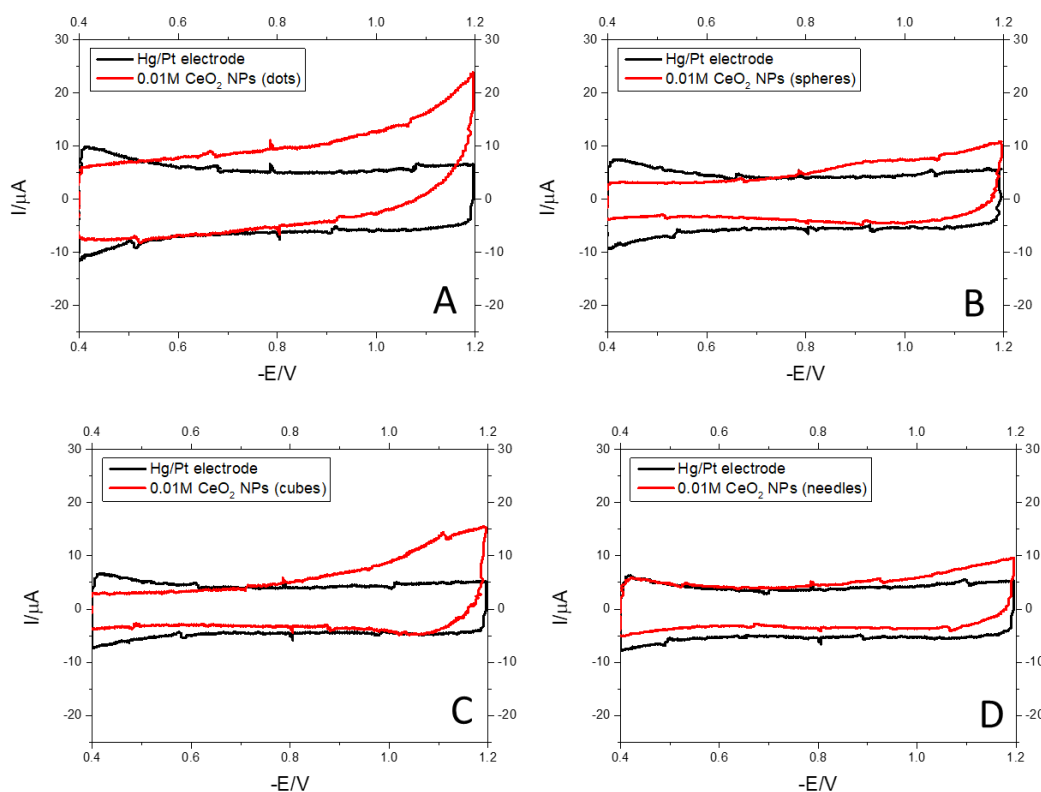


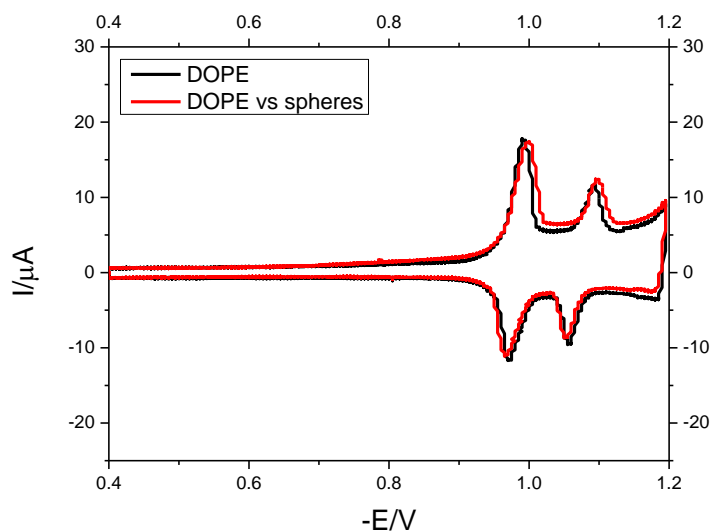
Figure 7. 2: RCV voltammograms recorded at 40Vs⁻¹ with a potential excursion from -0.4V to -1.20V of DOPC (black lines) under a continuous flow of GLY 3.0 in the presence of (red lines): A: 0.01M dots in GLY 3.0, B: 0.01M spheres in GLY 3.0, C: 0.01M cubes in GLY 3.0 and D: 0.01M needles in GLY 3.0.

7.2 Interactions of CeO₂ NPs with model membranes of different lipids

7.2.1 DOPE

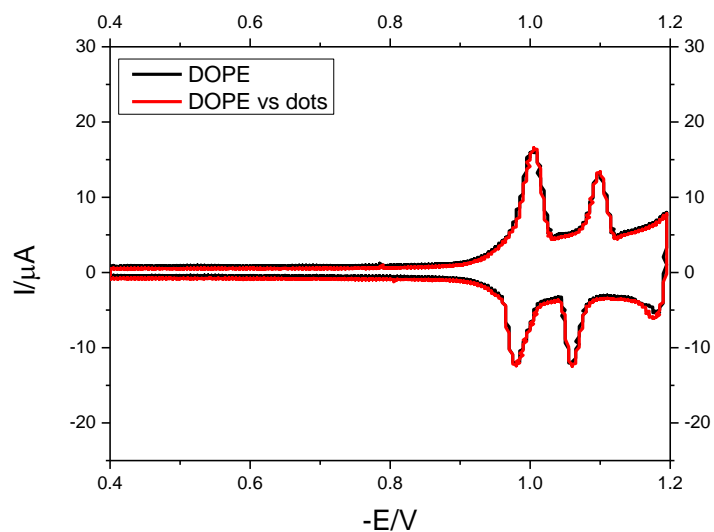
The interaction of two CeO₂ NPs samples with DOPE was studied following the procedure described in 5.6. Here, the correct amount of NPs to obtain 0.01M CeO₂ NPs dispersions was weighted and dispersed in milli-Q water.

The following figures (Figure 7. 3 and Figure 7. 4) show the variation of the voltammogram when DOPE was in contact with the spheres and the commercial sample of CeO₂ NPs. It is important to notice that no interaction between the cubes and DOPE is displayed in this chapter. As already mentioned, DOPE is expensive and difficult to deposit. Stable monolayers were impossible to obtain to carry out the experiments between DOPE and the cubes. Figure 7. 3 and Figure 7. 4 show there is no peak suppression when the spheres and the commercial NPs were in contact with the DOPE monolayer which indicates there is no interaction.



		Average	Error
Peak suppression (%)	Peak 1	1	1
	Peak 2	7	8
ΔE (V) or peak shift	Peak 1	0.002	0.006
	Peak 2	0.003	0.006

Figure 7. 3: RCV voltammogram recorded at 40Vs^{-1} with a potential excursion from -0.4V to -1.2V in a continuous flow of PBS of: black line: DOPE, red line: DOPE vs 0.01M of CeO_2NPs (spheres) **Table:** Average peak suppression (%) and peak shift (V) of the peaks of the voltammograms produced when 0.01M of CeO_2NPs (spheres) are in contact with DOPE

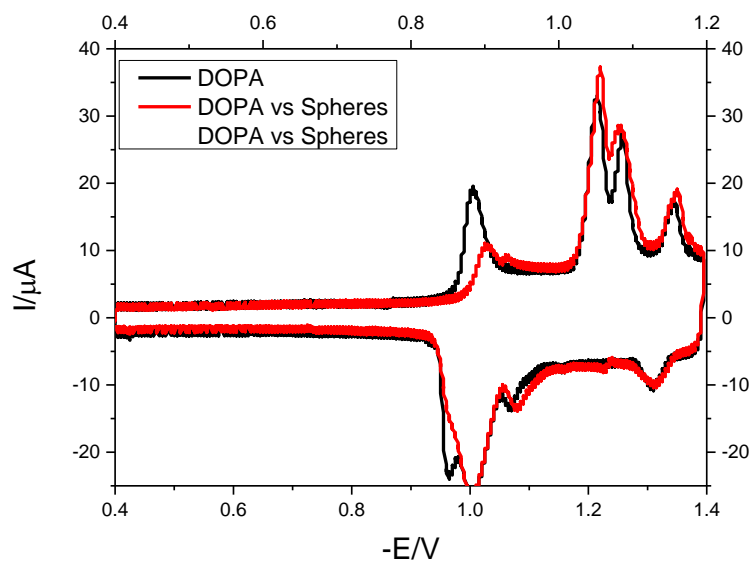


		Average	Error
Peak suppression (%)	Peak 1	-6	4
	Peak 2	-6	1
ΔE (V) or peak shift	Peak 1	0.005	0.004
	Peak 2	0.007	0.007

Figure 7. 4: RCV voltammogram recorded at 40Vs^{-1} with a potential excursion from -0.4V to -1.2V in a continuous flow of PBS of: black line: DOPE, red line: DOPE vs 0.01M of commercial CeO_2NPs (dots) **Table:** Average peak suppression (%) and peak shift (V) of the peaks of the voltammograms produced when 0.01M of commercial CeO_2NPs (dots) are in contact with DOPE

7.2.2 DOPA

The interaction of three different CeO₂ NPs samples with DOPA was studied following the procedure described in 5.6. The DOPA was deposited by applying a potential excursion from -0.4V to -1.4V following Table 6. 3. (The correct amount of NPs to obtain 0.01M dispersions was weighted and dispersed in milli-Q water.

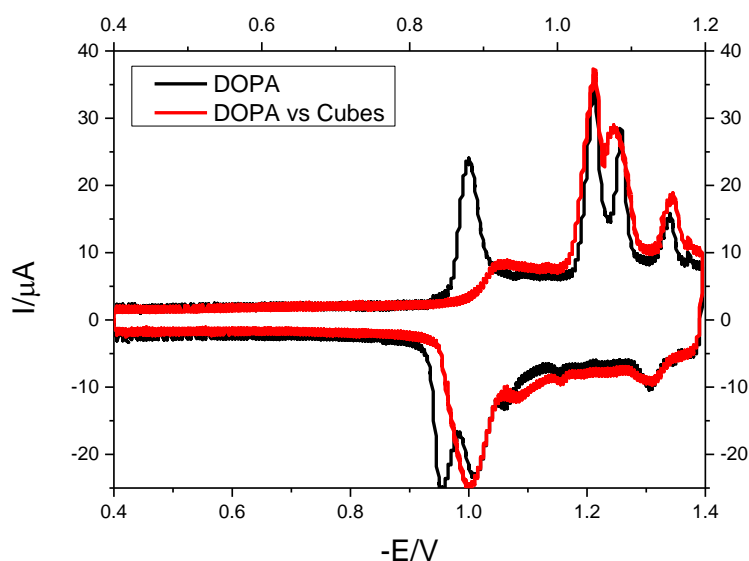


		Average	Error
Peak suppression (%)	Peak 1	69	18
	Peak 2	-14	17
	Peak 3	-8	10
	Peak 4	-39	24
ΔE (V) or peak shift	Peak 1	0.022	0.008
	Peak 2	0.005	0.005
	Peak 3	0.00	0.02
	Peak 4	0.003	0.003

Figure 7. 5: **Graph:** RCV voltammogram recorded at 46Vs^{-1} with a potential excursion from -0.4V to -1.4V in a continuous flow of PBS of: black line: DOPA, red line: DOPA vs 0.01M of CeO₂ NPs synthesised using TMAOH (spheres) **Table:** Average peak suppression (%) and peak shift (V) of the peaks of the voltammograms produced when 0.01M of CeO₂ NPs synthesised with TMAOH (spheres) are in contact with DOPA

Figure 7. 5 shows the interaction produced when 0.01M of CeO₂ NPs (spheres) interact with DOPA. The first peak disappears while the others increase. The significant error in the first peak suppression is produced by a combination of random and systematic errors. When a substance interacts with the phospholipid layer, the interaction does not always happen with the same

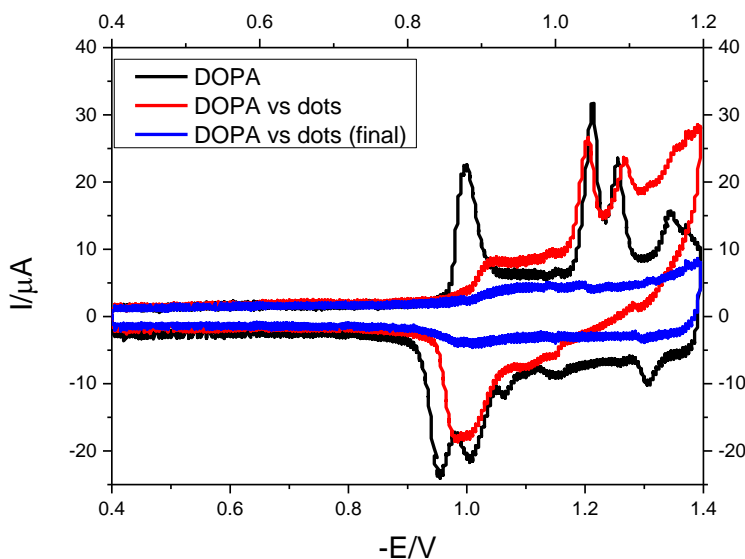
speed, which causes variations in the peaks suppression. Also, as shown in chapter 6.5, the first peak of the DOPA voltammogram is subject to significant variation in the current. The tendency of the first peak to decrease and the others to increase is a general phenomenon. In addition, there is no significant shift in the peaks. The first peak moves slightly to more negative potential values. The extent of the shift is not large enough to be considered an effect of interaction. A shift indicative of interaction occurs more abruptly.



		Average	Error
Peak suppression (%)	Peak 1	81	19
	Peak 2	-15	20
	Peak 3	-3	19
	Peak 4	-40	20
ΔE (V) or peak shift	Peak 1	0.03	0.01
	Peak 2	0.007	0.006
	Peak 3	0.00	0.02
	Peak 4	0.003	0.003

Figure 7. 6: **Graph:** RCV voltammogram recorded at 46Vs^{-1} with a potential excursion from -0.4V to -1.4V in a continuous flow of PBS of: black line: DOPA, red line: DOPA vs 0.01M of CeO_2 NPs synthesised using HMT(cubes) **Table:** Average peak suppression (%) and peak shift (V) of the peaks of the voltammograms produced when 0.01M of CeO_2 NPs synthesised with HMT (cubes) are in contact with DOPA

As observed in Figure 7. 6, the interaction of 0.01M CeO_2 NPs (cubes) with DOPA is similar to the interaction exhibited in the previous figure (Figure 7. 5). There is a complete suppression of the first peak while the other peaks increase in current. In addition, there is no significant peak shift.



		Average	Error
Peak suppression (%)	Peak 1	98	2
	Peak 2	22	12
	Peak 3	5	11
	Peak 4	N/A	N/A
ΔE (V) or peak shift	Peak 1	0.05	0.02
	Peak 2	0.001	0.003
	Peak 3	0.02	0.02
	Peak 4	N/A	N/A

Figure 7. 7: **Graph:** RCV voltammogram recorded at 46Vs^{-1} with a potential excursion from -0.4V to -1.4V in a continuous flow of PBS of: black line: DOPA, red line: DOPA vs 0.01M of commercial CeO_2 NPs (dots), blue line: DOPA vs 0.01M commercial CeO_2 NPs . **Table:** Average peak suppression (%) and peak shift (V) of the peaks of the voltammograms produced when 0.01M of commercial CeO_2 NPs (dots) are in contact with DOPA

Figure 7. 7 (red line) shows the interaction observed when 0.01M of commercial CeO_2 NPs (dots) are in contact with DOPA (black line shows the response in the absence of the NPs). Here, the interaction of the NPs with the phospholipid monolayer is different from the interactions described above. There is a complete suppression of the first peak, a light suppression of the second peak and a third peak which remains constant. In addition, there is a general increase in current from -1.3V to -1.4V which hampers visualisation of the fourth peak. This last effect has been previously reported in ref. [128], who observed a similar effect for TiO_2 was observed from NPs in contact with DOPC monolayers. The marked increase in current corresponds to a semiconductor effect. The NPs pass

through the lipid layer and directly interact with the Hg electrode. The blue line of Figure 7. 7 shows the final voltammogram ($t=2\text{min}$) produced by the interaction of DOPA with CeO_2 NPs (dots). As observed, there is a total disappearance of the peaks indicating the disruption of the monolayer.

As described above, there are two different behaviours of the voltammogram when CeO_2 NPs interact with DOPA. The decrease of the first peak and increase in the other peaks have previously been seen in chapter 6.5 when an unstable phase of DOPA was formed. This behaviour suggests that other factors as, for example, flow, could be altering the already rather unstable first peak. To demonstrate this theory, milli-Q water was tested against DOPA. The results (Figure 7. 8) confirmed that the increase in flow, induced when injecting the sample into the system, could produce the disappearance of the first peak.

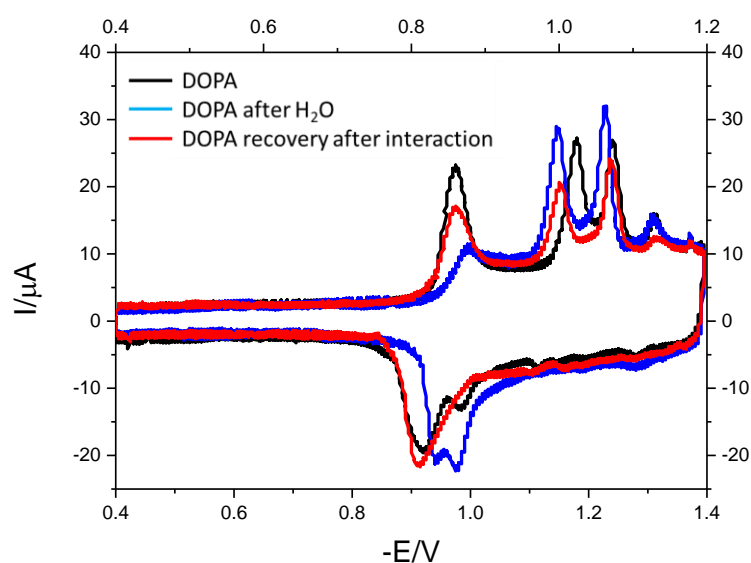


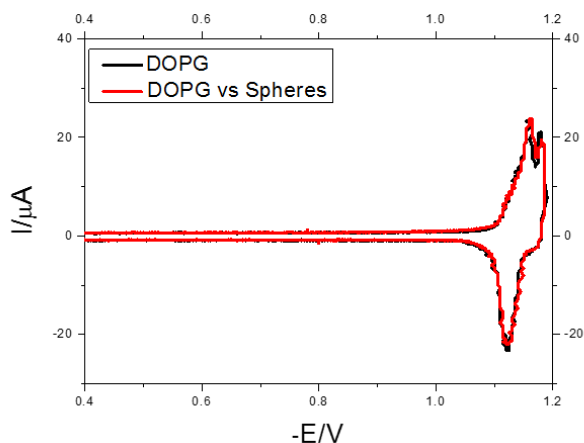
Figure 7. 8: RCV voltammogram recorded at 46Vs^{-1} with a potential excursion from -0.4V to -1.4V in a continuous flow of PBS of: black line: DOPA, blue line: interaction of DOPA with milli-Q water, red line: DOPA recovery after the interaction.

Thus, it can be concluded that is more likely that the nanoceria cubes and spheres do not cause any interaction with the DOPA layer. However, a clear interaction (a semiconductor effect) is produced when the commercial sample of CeO_2 NPs is in contact with DOPA. The difference between these samples is the agglomerate size and the Z-Potential. The characterisation of the NPs can

be found in CHAPTER 4. The dots sample is highly dispersed and has a negative Z-Potential (-25mV). Despite being uncoated, the supplier of the commercial CeO₂ NPs reported citrate was used in the synthesis of the NPs. The high colloidal stability of the NPs and the Z-Potential indicates that citrate is coating the NPs and that this affects the interaction with the DOPC.

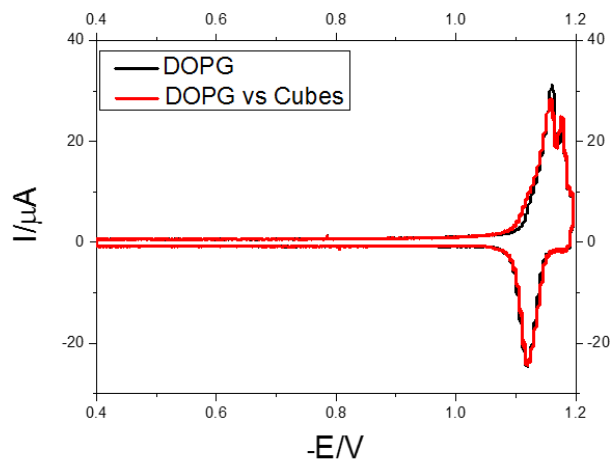
7.2.3 DOPG

The interaction between three CeO₂ NPs dispersions (0.01M) and DOPG under a continuous flow of PBS was studied following the procedure described in 5.6. As observed in Figure 7. 9, Figure 7. 10 and Figure 7. 11 there is no peak suppression nor peak shift which indicates no interaction.



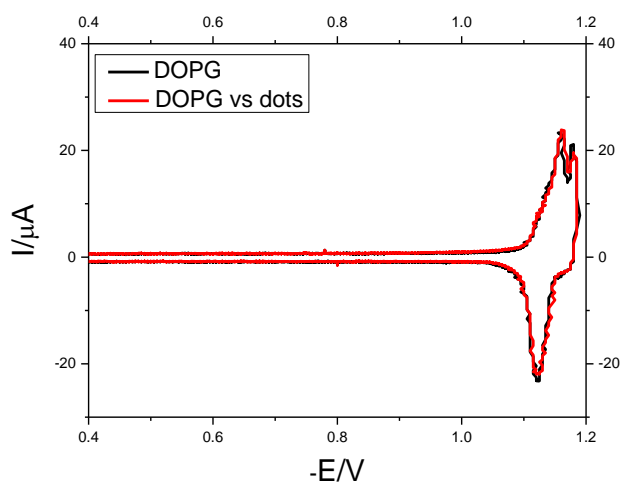
		Average	Error
Peak suppression (%)	Peak 1	-1	1
$ \Delta E $ (V) or peak shift	Peak 1	0.002	0.003

Figure 7. 9: **Graph:** RCV voltammogram recorded at 40Vs^{-1} with a potential excursion from -0.4V to -1.2V in a continuous flow of PBS of: black line: DOPG, red line: DOPG in contact with 0.01M of CeO₂ NPs synthesised using TMAOH (spheres) **Table:** Average peak suppression (%) and peak shift (V) of the peaks of the voltammograms produced when 0.01M of CeO₂ NPs synthesised with TMAOH (spheres) are in contact with DOPC



		Average	Error
Peak suppression (%)	Peak 1	6	4
$ \Delta E $ (V) or peak shift	Peak 1	0.000	0.001

Figure 7. 11: **Graph:** RCV voltammogram recorded at 40Vs^{-1} with a potential excursion from -0.4V to -1.2V in a continuous flow of PBS of: black line: DOPG, red line: DOPG in contact with 0.01M of CeO_2 NPs synthesised using HMT (cubes) **Table:** Average peak suppression (%) and peak shift (V) of the peaks of the voltammograms produced when 0.01M of CeO_2 NPs synthesised with HMT (cubes) are in contact with DOPC

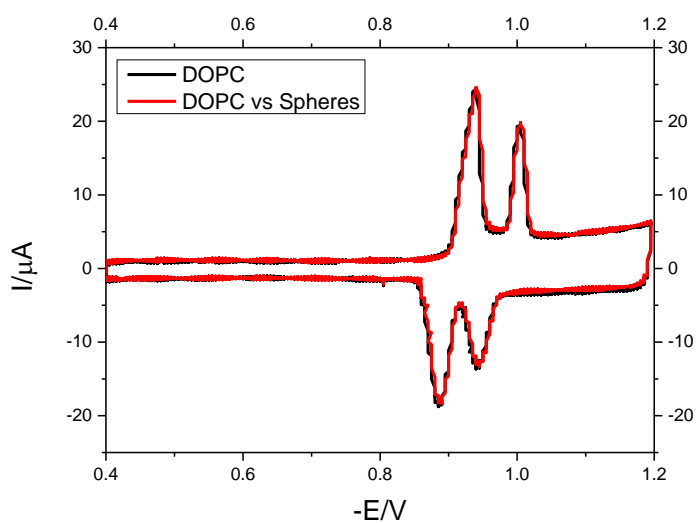


		Average	Error
Peak suppression (%)	Peak 1	0	4
$ \Delta E $ (V) or peak shift	Peak 1	0.003	0.001

Figure 7. 10: **Graph:** RCV voltammogram recorded at 40Vs^{-1} with a potential excursion from -0.4V to -1.2V in a continuous flow of PBS of: black line: DOPG, red line: DOPG in contact with 0.01M of CeO_2 NPs synthesised using HMT (cubes) **Table:** Average peak suppression (%) and peak shift (V) of the peaks of the voltammograms produced when 0.01M of CeO_2 NPs synthesised with HMT (cubes) are in contact with DOPC

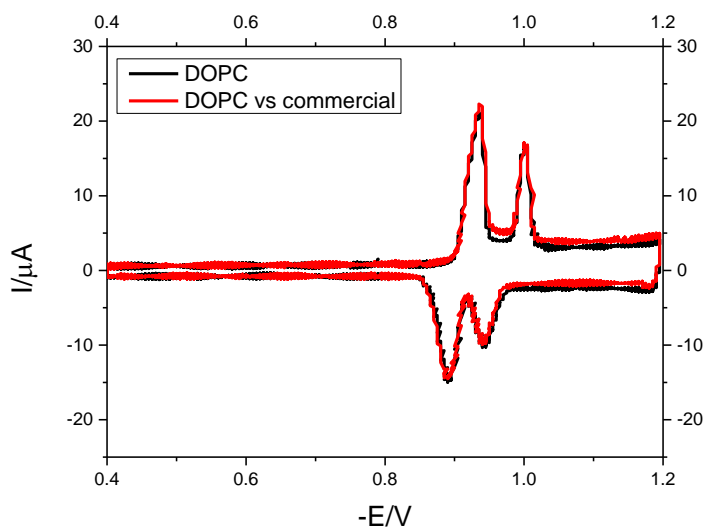
7.2.4 DOPC

The interaction of three CeO₂ NPs samples with DOPC was studied following the procedure described in 5.6. In this way, the correct amount of NPs to get 0.01M nanoceria dispersions was weighted and dispersed in milli-Q water. As observed in the following figures, there is no peak suppression nor peak shift which indicate no interaction of the NPs with the monolayer of DOPC.



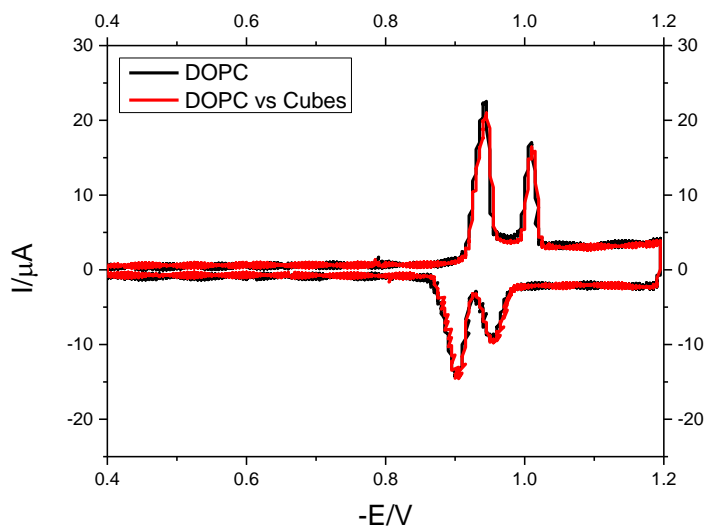
		Average	Error
Peak suppression (%)	Peak 1	-2	3
	Peak 2	-2	2
ΔE (V) or peak shift	Peak 1	0.003	0.003
	Peak 2	0.002	0.003

Figure 7. 12: **Graph:** RCV voltammogram recorded at 40Vs^{-1} with a potential excursion from -0.4V to -1.2V in a continuous flow of PBS of: black line: DOPC, red line: DOPC vs 0.01M of CeO₂ NPs synthesised using TMAOH (spheres) **Table:** Average peak suppression (%) and peak shift (V) of the peaks of the voltammograms produced when 0.01M of CeO₂ NPs synthesised with TMAOH (spheres) are in contact with DOPC



		Average	Error
Peak suppression (%)	Peak 1	-2	11
	Peak 2	-1	5
ΔE (V) or peak shift	Peak 1	0.000	0.003
	Peak 2	0.003	0.003

Figure 7. 13: RCV voltammogram recorded at 40Vs^{-1} with a potential excursion from -0.4V to -1.2V in a continuous flow of PBS of: black line: DOPC, red line: DOPC vs 0.01M of CeO_2 NPs synthesised using HMT (cubes) **Table:** Average peak suppression (%) and peak shift (V) of the peaks of the voltammograms produced when 0.01M of CeO_2 NPs synthesised with HMT (cubes) are in contact with DOPC



		Average	Error
Peak suppression (%)	Peak 1	5	4
	Peak 2	6	3
ΔE (V) or peak shift	Peak 1	0.003	0.003
	Peak 2	0.002	0.003

Figure 7. 14: RCV voltammogram recorded at 40Vs^{-1} with a potential excursion from -0.4V to -1.2V in a continuous flow of PBS of: black line: DOPC, red line: DOPC vs 0.01M of CeO_2 NPs synthesised using HMT (cubes) **Table:** Average peak suppression (%) and peak shift (V) of the peaks of the voltammograms produced when 0.01M of CeO_2 NPs synthesised with HMT (cubes) are in contact with DOPC

7.2.5 Summary and discussion

Almost all the different morphology CeO₂ NPs showed no interaction when introduced into the ESD under a continuous flow of PBS. This implies that ceria NPs are inert in almost all scenarios under these circumstances.

Only the highly dispersed, commercially sourced ceria dots were observed to interact with DOPA under these conditions. In this case, an increase of current at negative potentials, similar to the interaction that semiconductor materials produce with the Hg/Pt electrode is observed. DOPA has a small polar head which could allow a highly dispersed sample to go through the monolayer of phospholipids and interact directly with the electrode. Additionally, the dots were small and had a negative Z-Potential indicating that a coating, probably citrate, was increasing the colloidal stability of the sample. An increase of colloidal stability enhances the interaction because it increases the active surface area to volume ratio.

7.3 Interactions of CeO₂ NPs with DOPC. Effect of pH and dispersant medium

DOPC was proved to be the most stable and reliable phospholipid to work with in the previous experiments. For this reason, DOPC was used to study the interaction between three synthesised CeO₂ NPs and the aforementioned phospholipid under different buffer types. In this way, the effect of the dispersant medium on the NPs interaction with the model membrane was studied.

The correct amount of NPs to prepare a series of dispersions of 0.01M, 0.006M, 0.002M and 0.0004M was weighted and dispersed in the correct volume of buffer. The buffer solutions, which were used in the experiments, were HCl-Glycine buffer at pH 3.0, citric acid/sodium citrate tribasic at pH 3.0- pH 6.0 and PBS at pH 7.4. The preparation of the buffer solutions is explained in 6.1.2.

The analysis of the interaction of the NPs using the ESD was carried out following the procedure described in 5.6.

7.3.1 Interaction of CeO_2 NPs with DOPC under a flow of HCl-Glycine buffer at pH 3.0 (GLY 3.0).

7.3.1.1 Different concentration of spheres in GLY 3.0

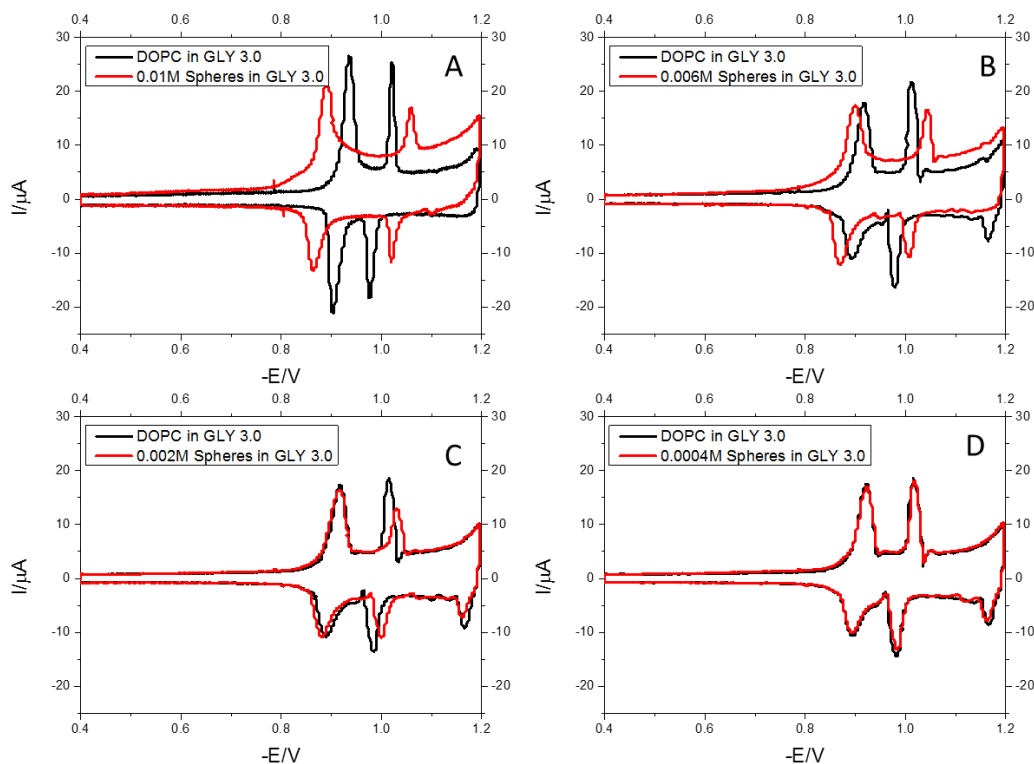


Figure 7. 15: RCV voltammograms recorded at 40Vs^{-1} with a potential excursion from -0.4V to -1.20V of DOPC (black lines) under a continuous flow of GLY 3.0 in the presence of (red lines): A: 0.01M of CeO_2 NPs (spheres) in GLY 3.0, B: 0.006M of CeO_2 NPs (spheres) in GLY 3.0, C: 0.002M of CeO_2 NPs (spheres) in GLY 3.0, D: 0.0004M of CeO_2 NPs (spheres) in GLY 3.0.

As observed in Figure 7. 15, there is an apparent peak suppression, which varies with concentration when CeO_2 NPs (spheres) interact with the DOPC monolayer in GLY 3.0. Figure 7. 15A and B displays the interaction observed when the DOPC monolayer is exposed to 0.01M and 0.006M respectively of CeO_2 NPs (spheres). As observed, there is suppression and shift of both RCV peaks. Peak 1 shifts to more positive potentials, while peak 2 shifts to more negative potentials. This behaviour is similar to the one previously observed in Figure 7. 1A, which showed the interaction of soluble $\text{Ce}(\text{NO}_3)_3$ with DOPC. Thus, it is concluded that, under these conditions (i.e. pH 3.0), Ce^{3+} may play a role in the interaction of the spheres with the phospholipid monolayer. In

addition, both the suppression and the shift of the peaks are dependants on concentration, being stronger for the higher concentration sample. While in Figure 7. 15A there is a suppression of both peaks, in Figure 7. 15B, there is only a significant suppression of peak 2. This tendency is also observed in Figure 7. 15C, where there is only suppression of peak 2 and no shift of the peaks. Figure 7. 15D does not show suppression nor shift of the current peaks, which indicates, no interaction with the DOPC monolayer. This behavioural trend can also be observed graphically as a function of concentration in Figure 7. 16.

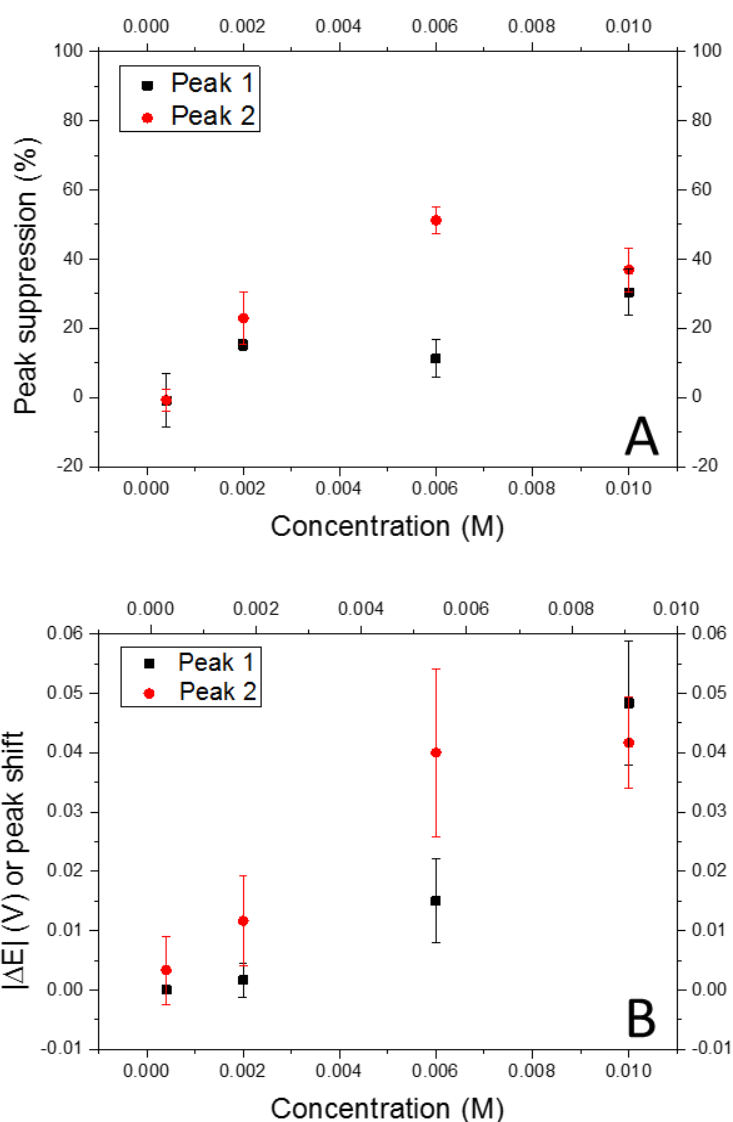



Figure 7. 16: Behaviour of the Peak 1 (black dots) and Peak 2 (red dots) of the voltammograms obtained from the ESD when a varying concentration of CeO₂ NPs (spheres) in GLY 3.0 interact with DOPC under a continuous flow of GLY 3.0. A: Graph showing the suppression, in percentage (%), of the peaks. B: Graph showing the shift (V), in potential, of the peaks.



In addition, a semiconductor effect, similar to the one observed for the interaction of the CeO₂ NPs with the plain Hg/Pt electrode [128] is observed at negative potentials in both Figure 7. 2A and B. This behaviour suggests the NPs are penetrating the membrane and are adsorbing directly on the Hg/Pt electrode.

7.3.1.2 Different concentration of cubes in GLY 3.0

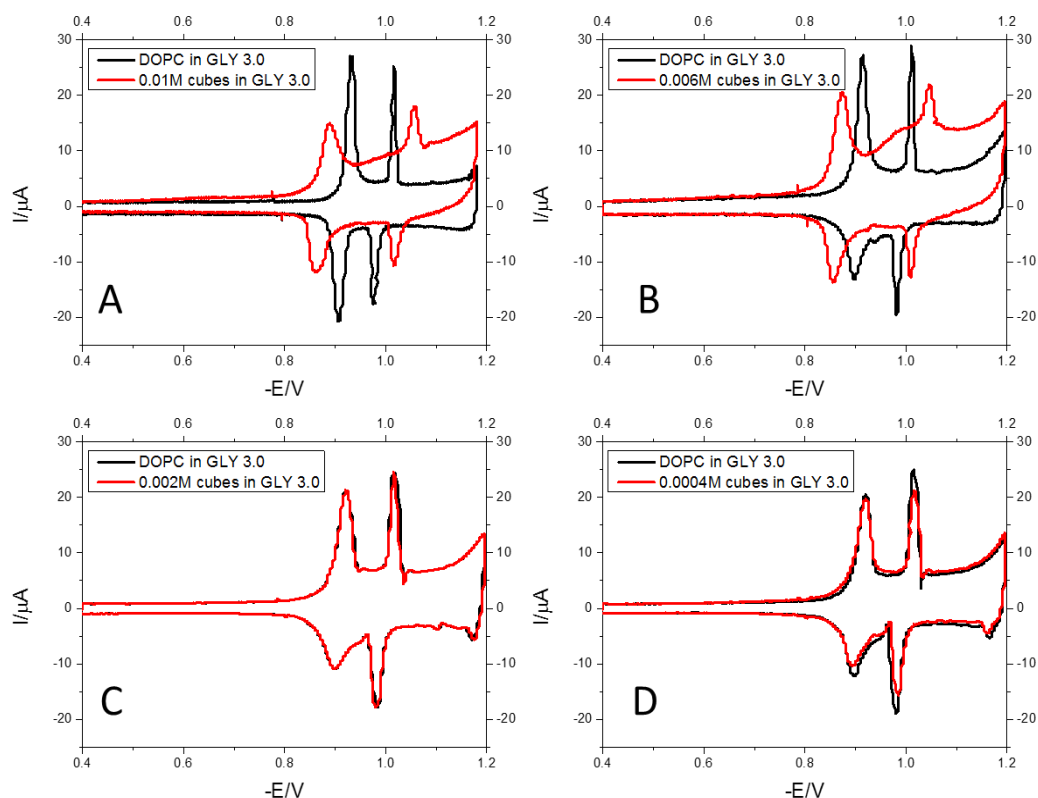


Figure 7.17: RCV voltammograms recorded at 40Vs^{-1} with a potential excursion from -0.4V to -1.20V of DOPC (black lines) under a continuous flow of GLY 3.0 in the presence of (red lines): A: 0.01M of CeO_2 NPs (cubes) in GLY 3.0, B: 0.006M of CeO_2 NPs (cubes) in GLY 3.0, C: 0.002M of CeO_2 NPs (cubes) in GLY 3.0, D: 0.0004M of CeO_2 NPs (cubes) in GLY 3.0.

Figure 7.17 shows how the DOPC voltammogram changes when different concentrations of CeO_2 NPs (cubes) interact with the phospholipid monolayer. A suppression and shift of the peaks with increasing concentration relationship were observed. Figure 7.17A and B both show a suppression and shift of the current peaks both to more negative and more positive potentials, while in Figure 7.17C and D there is no significant variation of the current peaks which indicates little interaction. The shift of the peaks shows similar behaviour to the one previously observed in Figure 7.1A, which illustrates the interaction of $\text{Ce}(\text{NO}_3)_3$ with DOPC. It is concluded that Ce^{3+} plays a role in the interaction of the CeO_2 NPs (cubes) with the phospholipid monolayer. This behaviour is graphically illustrated in Figure 7.18, where the average suppression and shift of the RCV peaks is plotted as a function of concentration.

In addition, a semiconductor effect, similar to the one observed for the interaction of CeO₂ NPs with the plain Hg/Pt electrode (Figure 7. 2) is observed at negative potentials in Figure 7. 17A and B

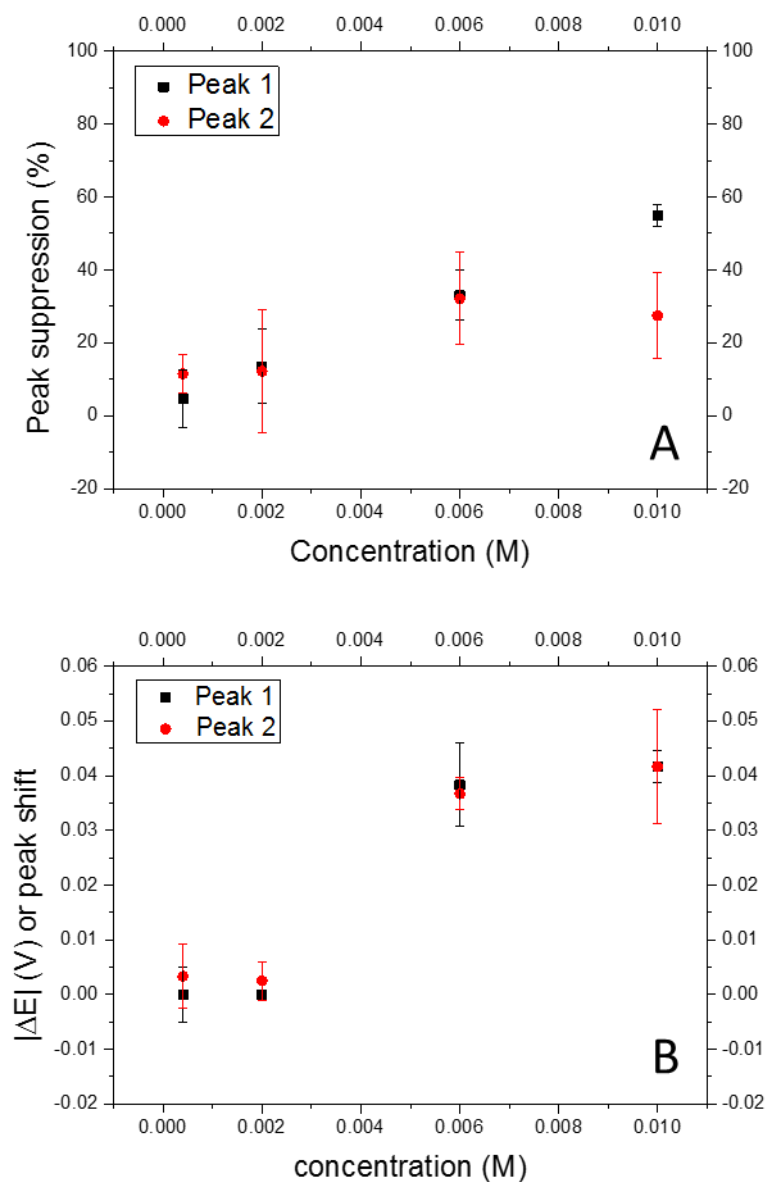


Figure 7. 18: Behaviour of the Peak 1 (black dots) and Peak 2 (red dots) of the voltammograms obtained from the ESD when a varying concentration of CeO₂ NPs (cubes) in GLY 3.0 interact with DOPC under a continuous flow of GLY 3.0. A: Graph showing the suppression, in percent age (%), of the peaks. B: Graph showing the shift (V), in potential, of the peaks.

7.3.1.3 Different concentrations of ceria needles in GLY 3.0

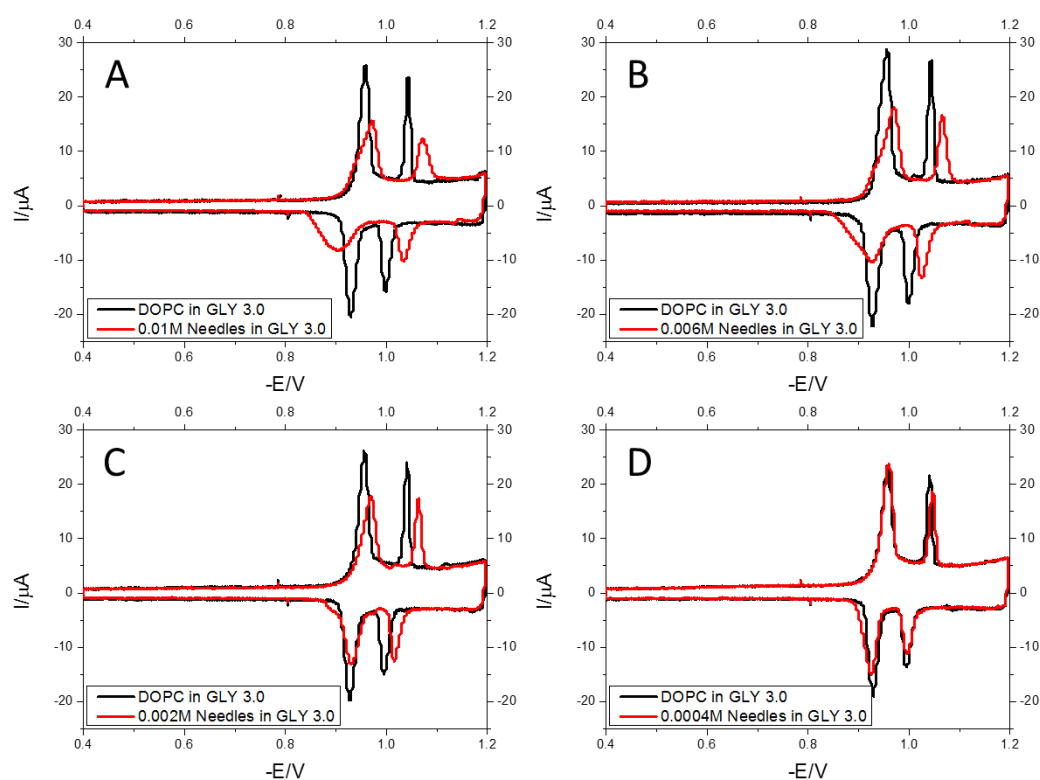


Figure 7.19: RCV voltammograms recorded at 40Vs^{-1} with a potential excursion from -0.4V to -1.2V of DOPC (black lines) under a continuous flow of GLY 3.0 in the presence of (red lines): A: 0.01M of CeO_2 NPs (needles) in GLY 3.0, B: 0.006M of CeO_2 NPs (needles) in GLY 3.0, C: 0.002M of CeO_2 NPs (needles) in GLY 3.0, D: 0.0004M of CeO_2 NPs (needles) in GLY 3.0.

Figure 7.19 shows the interaction of CeO_2 NPs (needles) produced when they were introduced into the ESD. As can be observed, the effect of the needles in the voltammogram is not totally the same as previously seen for spheres and cubes (Figure 7.15 and Figure 7.17 respectively) under the same conditions. There is a clear suppression of the RCV peaks with concentration and a small shift of the peaks to more negative potentials. This behaviour is more clearly seen in Figure 7.20, which shows the average peak suppression and peak shift of the samples as a function of concentration.

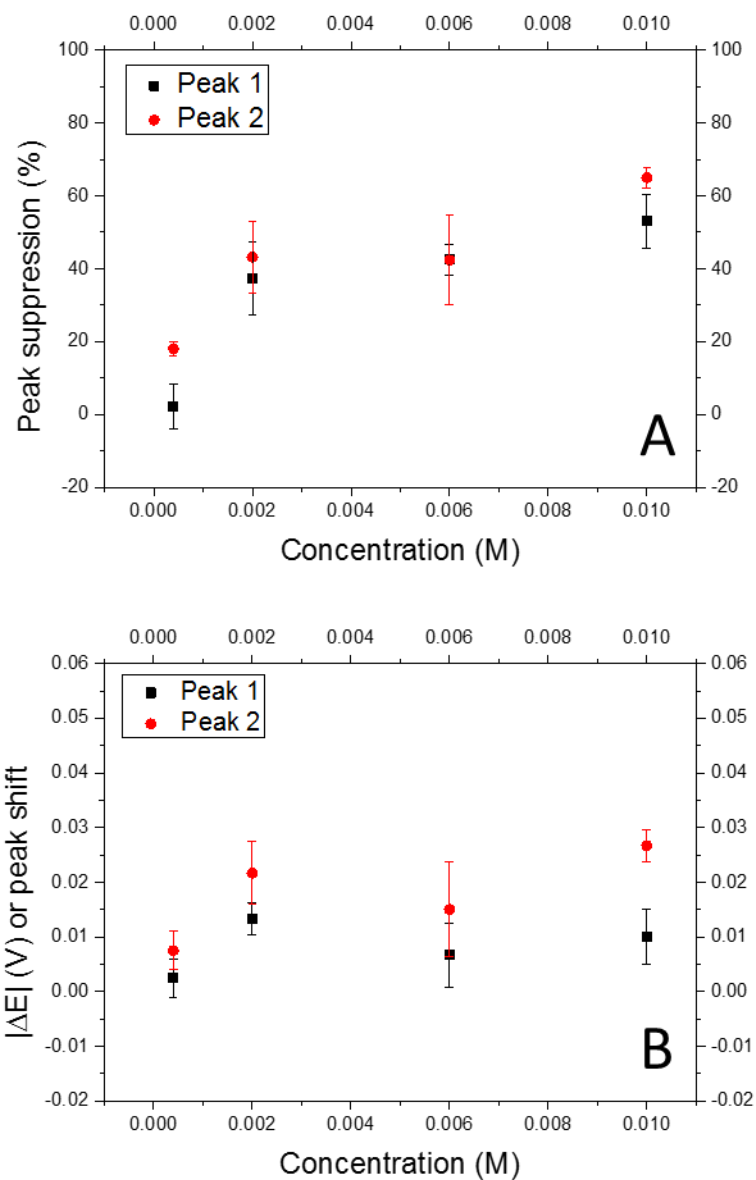


Figure 7. 20: Behaviour of the Peak 1 (black dots) and Peak 2 (red dots) of the voltammograms obtained from the ESD when a varying concentration of CeO₂ NPs (cubes) in GLY 3.0 interact with DOPC under a continuous flow of GLY 3.0. A: Graph showing the suppression, in percentage (%), of the peaks. B: Graph showing the shift (V), in potential, of the peaks.

7.3.2 Interaction of CeO_2 NPs with DOPC under a flow of citric/citrate buffer at pH 3.0 (CCB 3.0)

7.3.2.1 Different concentration of ceria spheres in CCB 3.0

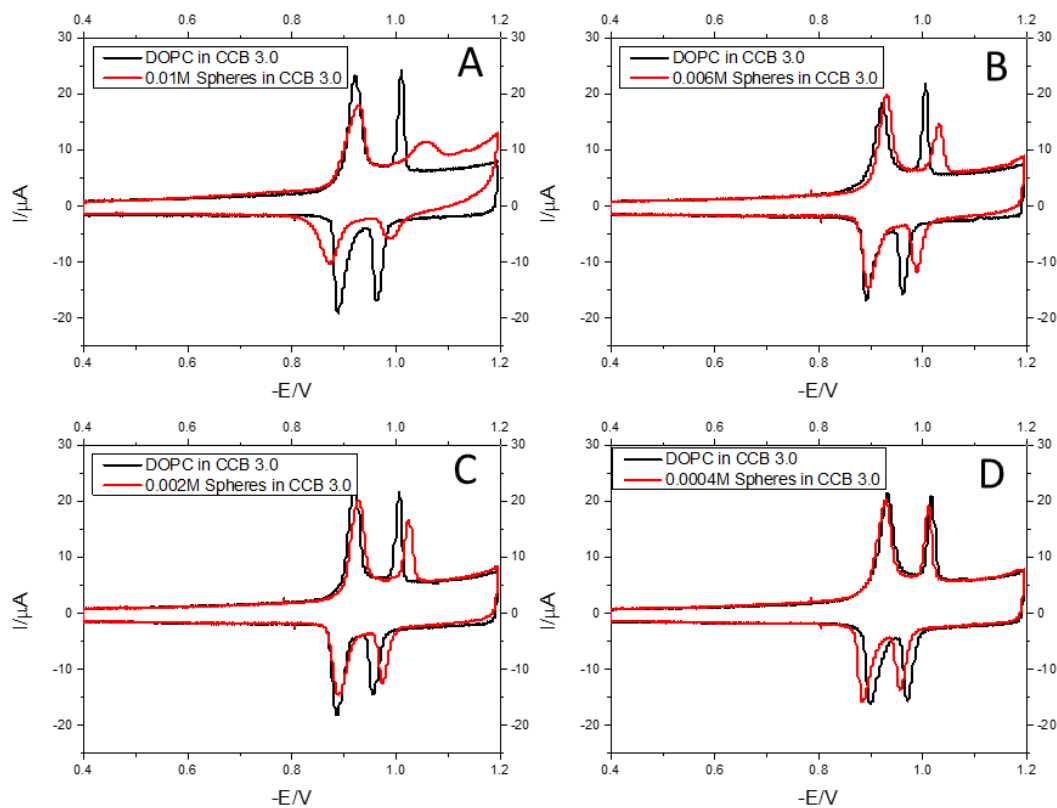


Figure 7. 2l: RCV voltammograms recorded at 40Vs^{-1} with a potential excursion from -0.4V to -1.20V of DOPC (black lines) under a continuous flow of CCB 3.0 in the presence of (red lines): A: 0.01M of CeO_2 NPs (spheres) in CCB 3.0, B: 0.006M of CeO_2 NPs (spheres) in CCB 3.0, C: 0.002M of CeO_2 NPs (spheres) in CCB 3.0, D: 0.0004M of CeO_2 NPs (spheres) in CCB 3.0.

Figure 7. 2l shows the interaction of CeO_2 NPs (spheres) with DOPC for different concentrations under a continuous flow of CCB 3.0. Suppression of both peaks and a shift of the second peak, which is dependent on concentration, can be observed. Figure 7. 22 shows the trend of this behaviour graphically. At high concentrations, there is a bigger suppression of the second peak relative to the first one. At lower concentrations, there is no distinct interaction between the NPs and the phospholipid membrane.

Again, a semiconductor effect, similar to the one observed in Figure 7. 2 is evident when 0.01M of CeO_2 NPs (cubes) interact with DOPC. At these high concentrations, the CeO_2 NPs appear to be penetrating the lipid monolayer.

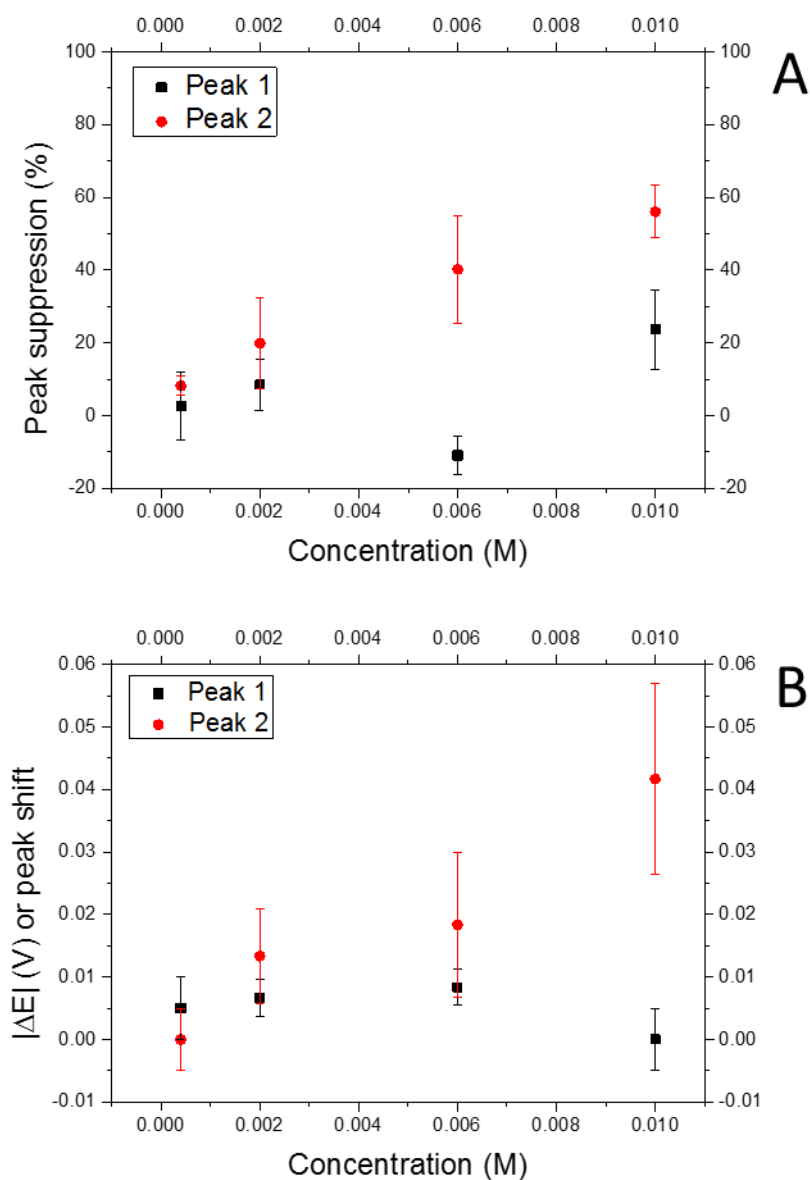


Figure 7. 22: Behaviour of the Peak 1 (black dots) and Peak 2 (red dots) of the voltammograms obtained from the ESD when a varying concentration of CeO_2 NPs (spheres) in CCB 3.0 interact with DOPC under a continuous flow of CCB 3.0. A: Graph showing the suppression, in percentage (%), of the peaks. B: Graph showing the shift (V), in potential, of the peaks.

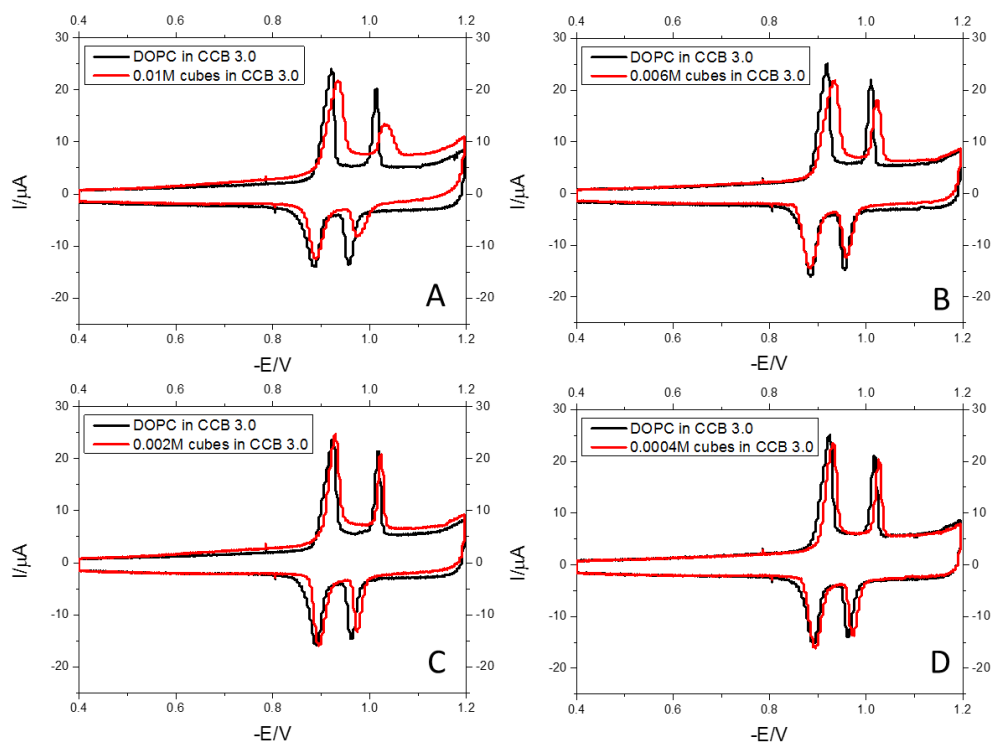


Figure 7. 23: RCV voltammograms recorded at 40Vs^{-1} at a cycling potential that ranges from -0.4V to -1.20V of DOPC (black lines) under a continuous flow of CCB 3.0 in the presence of (red lines): A: 0.01M of CeO_2 NPs (cubes) in CCB 3.0, B: 0.006M of CeO_2 NPs (cubes) in CCB 3.0, C: 0.002M of CeO_2 NPs (cubes) in CCB 3.0, D: 0.0004M of CeO_2 NPs (cubes) in CCB 3.0.

Figure 7. 23 shows the interaction of CeO_2 NPs (cubes) with DOPC for different concentrations under a continuous flow of CCB 3.0. Suppression of both peaks and a shift of the second peak can be observed, which is dependant on concentration. Figure 7. 24 shows the trend of this behaviour graphically. At high concentrations, there is a bigger suppression of the second peak relative to the first one. At lower concentrations, there is no distinct interaction between the NPs and the phospholipids membranes.

Again, a semiconductor effect, similar to the one observed in (Figure 7. 2) can be evident when 0.01M of CeO_2 NPs (cubes) interact with DOPC. At high concentrations, the CeO_2 NPs appear to be penetrating the monolayer.

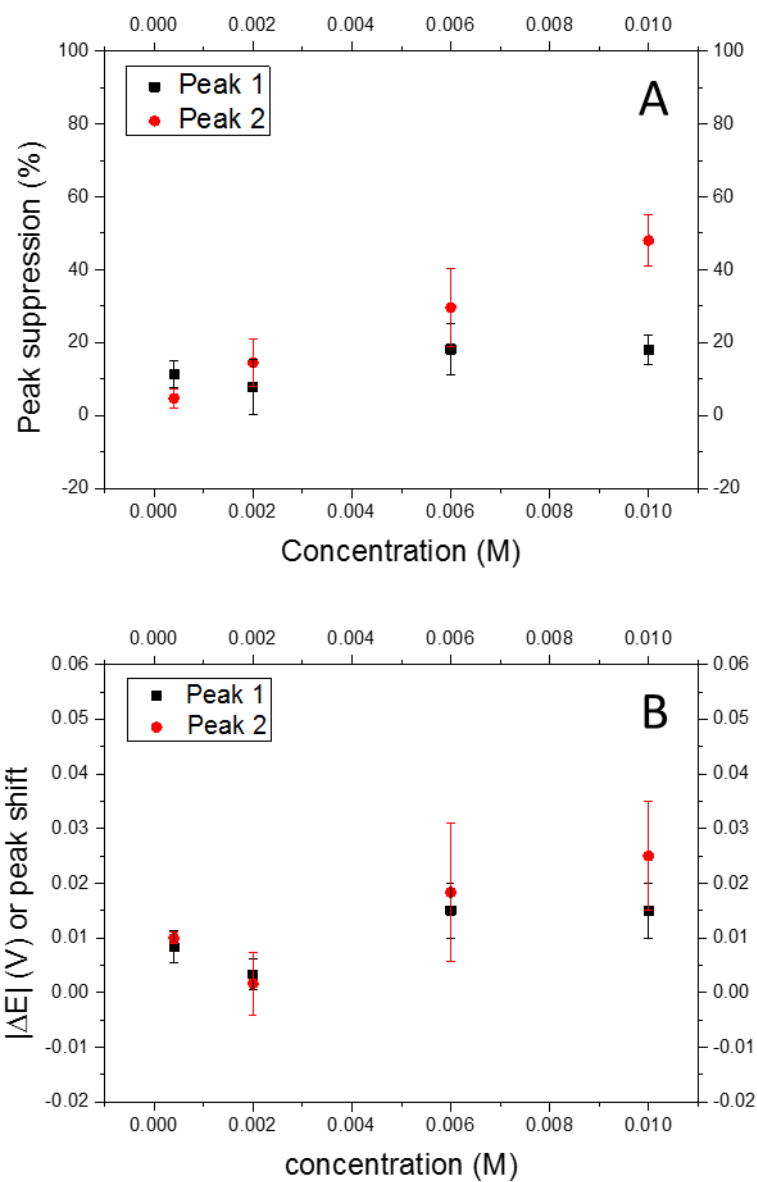


Figure 7. 24: Behaviour of the Peak 1 (black dots) and Peak 2 (red dots) of the voltammograms obtained from the ESD when a varying concentration of CeO₂ NPs (cubes) in CCB 3.0 interact with DOPC under a continuous flow of CCB 3.0. A: Graph showing the suppression, in percentage (%), of the peaks. B: Graph showing the shift (V), in potential, of the peaks.

7.3.2.3 Different concentration of ceria needles in CCB 3.0

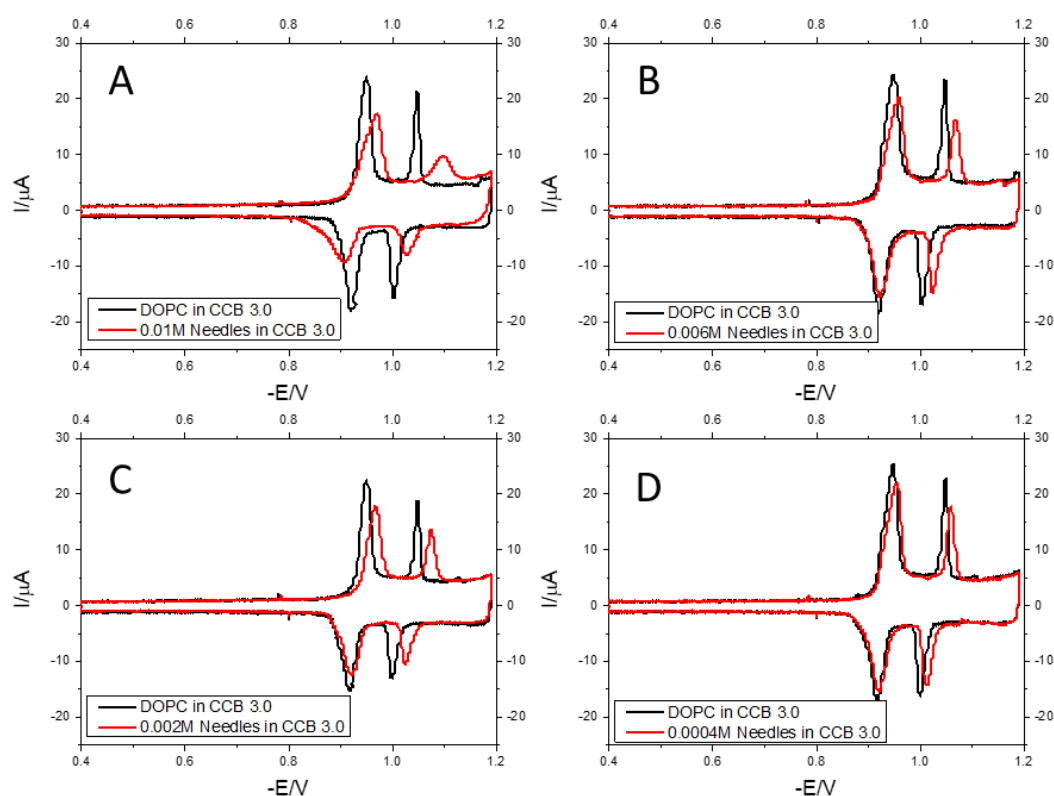


Figure 7. 25: RCV voltammograms recorded at 40Vs^{-1} at a cycling potential that ranges from -0.4V to -1.20V of DOPC (black lines) under a continuous flow of CCB 3.0 in the presence of (red lines): A: 0.01M of CeO_2 NPs (needles) in CCB 3.0, B: 0.006M of CeO_2 NPs (needles) in CCB 3.0, C: 0.002M of CeO_2 NPs (needles) in CCB 3.0, D: 0.0004M of CeO_2 NPs (needles) in CCB 3.0.

Figure 7. 25 shows the interaction of different concentration of CeO_2 NPs (needles) with DOPC under a continuous flow of CCB 3.0. The same effect than the previously observed with spheres (Figure 7. 21) and cubes (Figure 7. 23) is observed in this case. When 0.01M CeO_2 NPs interact with DOPC under these conditions (Figure 7. 25A), a suppression and shift of both peaks to more negative potentials, more pronounced in the second peak, are evident. Approximately the same peak suppression is obtained when 0.006M of NPs are introduced into the system. However, in this case, there is no substantial shift in the peaks of the voltammogram. This behaviour is summarised in Figure 7. 26. In addition, contrary to the previous behaviour, a semiconductor effect is not observed in this case.

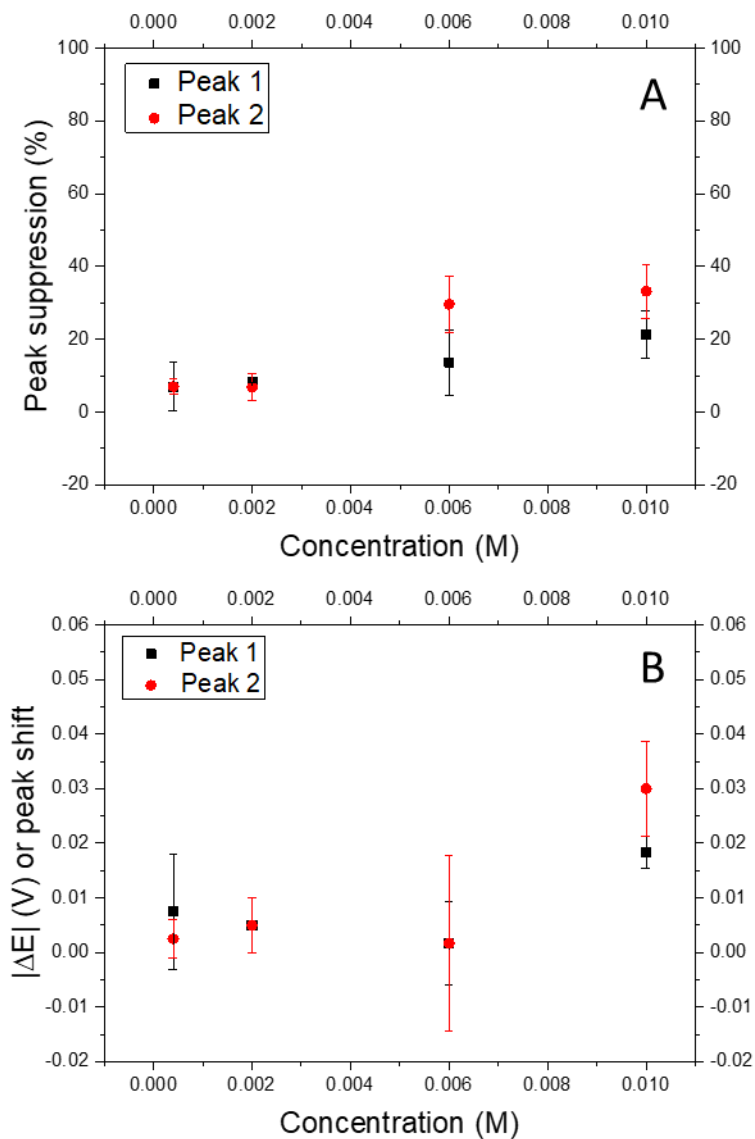


Figure 7. 26: Behaviour of the Peak 1 (black dots) and Peak 2 (red dots) of the voltammograms obtained from the ESD when a varying concentration of CeO₂ NPs (broken needles) in CCB 3.0 interact with DOPC under a continuous flow of CCB 3.0. A: Graph showing the suppression, in percentage (%), of the peaks. B: Graph showing the shift (V), in potential, of the peaks.

7.3.3 Interaction of CeO₂ NPs with DOPC under a flow of citric/citrate buffer at pH 4.0 (CCB 4.0)

7.3.3.1 Different concentration of ceria spheres in CCB 4.0

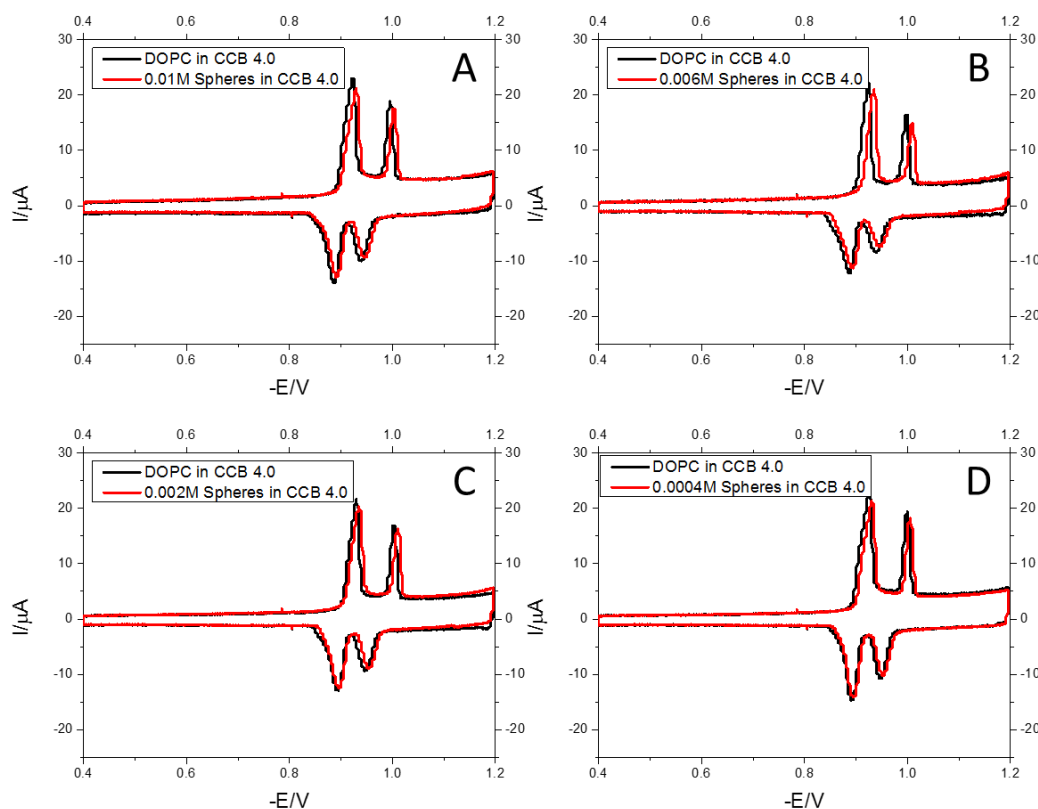


Figure 7. 27: : RCV voltammograms recorded at 40Vs^{-1} with a potential excursion from -0.4V to -1.20V of DOPC (black lines) under a continuous flow of CCB 4.0 in the presence of (red lines): A: 0.01M of CeO₂ NPs (spheres) in CCB 4.0, B: 0.006M of CeO₂ NPs (spheres) in CCB 4.0, C: 0.002M of CeO₂ NPs (spheres) in CCB 4.0, D: 0.0004M of CeO₂ NPs (spheres) in CCB 4.0.

Figure 7. 27 displays the voltammograms obtained when different concentrations of CeO₂ NPs (spheres) in CCB 4.0 interact with a monolayer of DOPC in CCB 4.0. As observed, there is no significant suppression nor shift of the peaks at any the concentration. Figure 7. 28 summarises the behaviour of the peaks graphically.

When 0.01M of CeO₂ NPs are introduced into the system, a light suppression and shift of the peaks are produced. However, this change is not large enough to be considered the effect of a NPs phospholipid interaction.

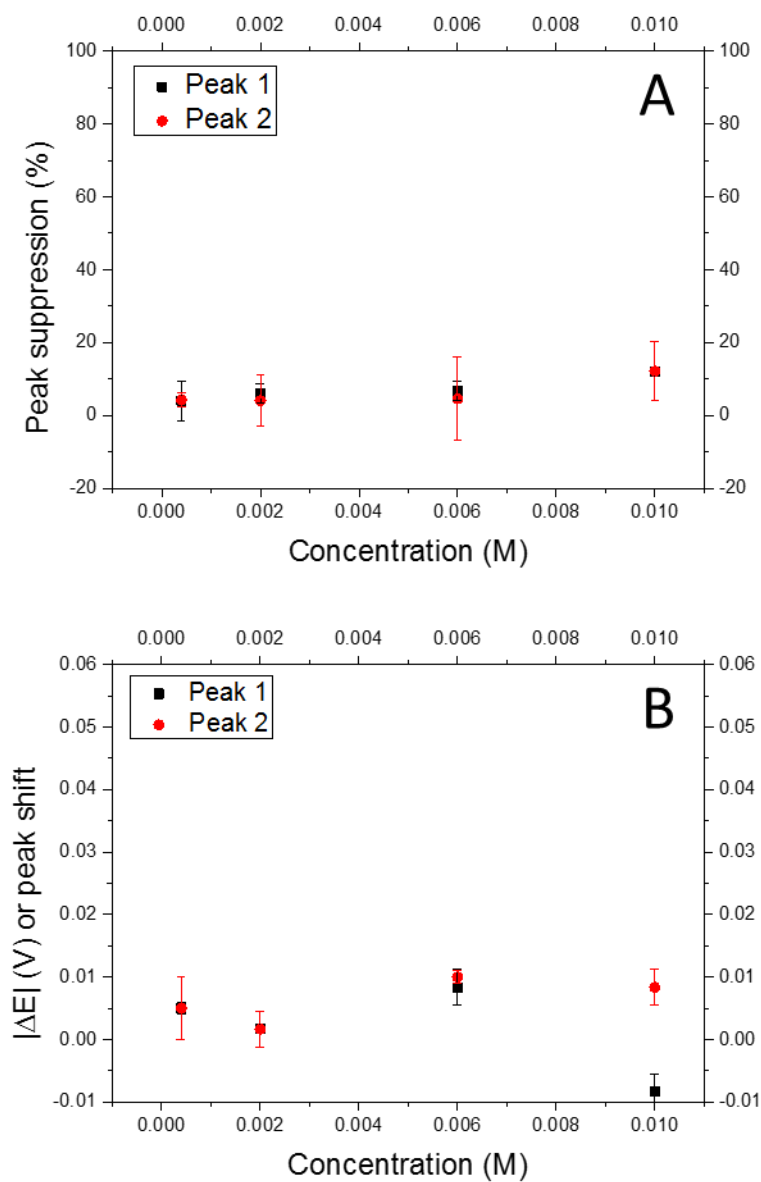


Figure 7. 28: Behaviour of the Peak 1 (black dots) and Peak 2 (red dots) of the voltammograms obtained from the ESD when a varying concentration of CeO₂ NPs (spheres) in CCB 4.0 interact with DOPC under a continuous flow of CCB 4.0. **A:** Graph showing the suppression, in percentage (%), of the peaks. **B:** Graph showing the shift (V), in potential, of the peaks.

7.3.3.2 Different concentration of ceria cubes in CCB 4.0

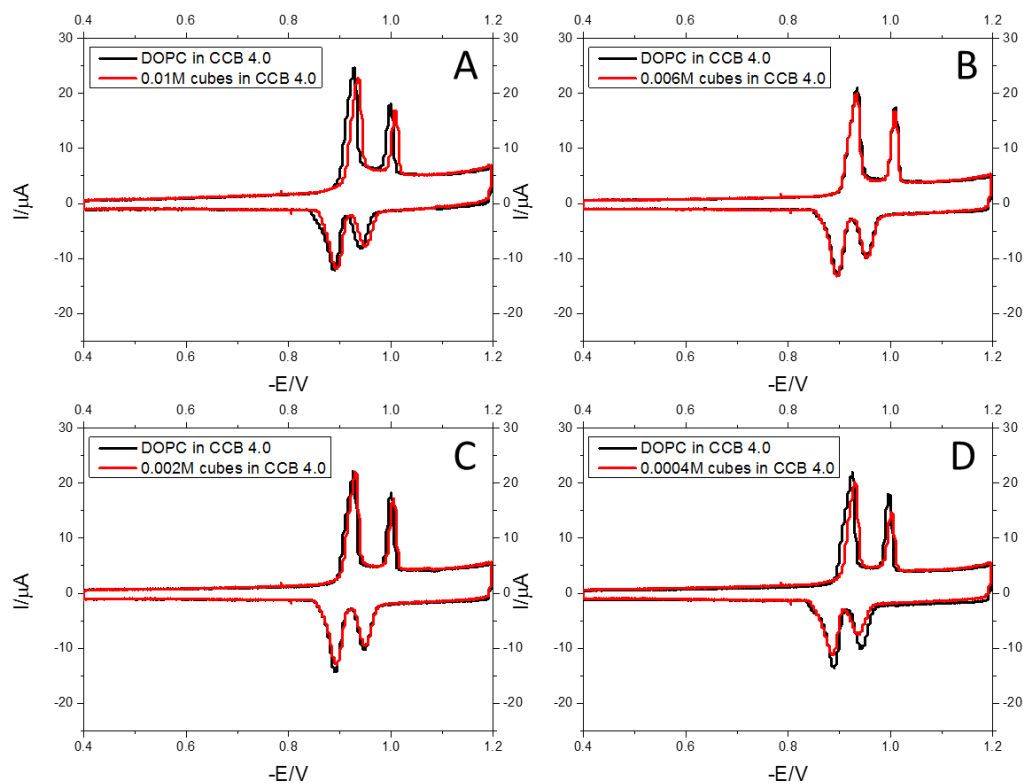


Figure 7. 29: RCV voltammograms recorded at 40Vs^{-1} with a potential excursion from -0.4V to -1.20V of DOPC (black lines) under a continuous flow of CCB 4.0 in the presence of (red lines): A: 0.01M of CeO_2 NPs (cubes) in CCB 4.0, B: 0.006M of CeO_2 NPs (cubes) in CCB 4.0, C: 0.002M of CeO_2 NPs (cubes) in CCB 4.0, D: 0.0004M of CeO_2 NPs (cubes) in CCB 4.0.

Figure 7. 29 shows the variation of the voltammograms when CeO_2 NPs (cubes) interact with a monolayer of DOPC in CCB 4.0. This is summarised graphically in Figure 7. 30. As observed, there is no significant variation of the current peaks and there is no observed interaction between the NPs and the DOPC monolayer.

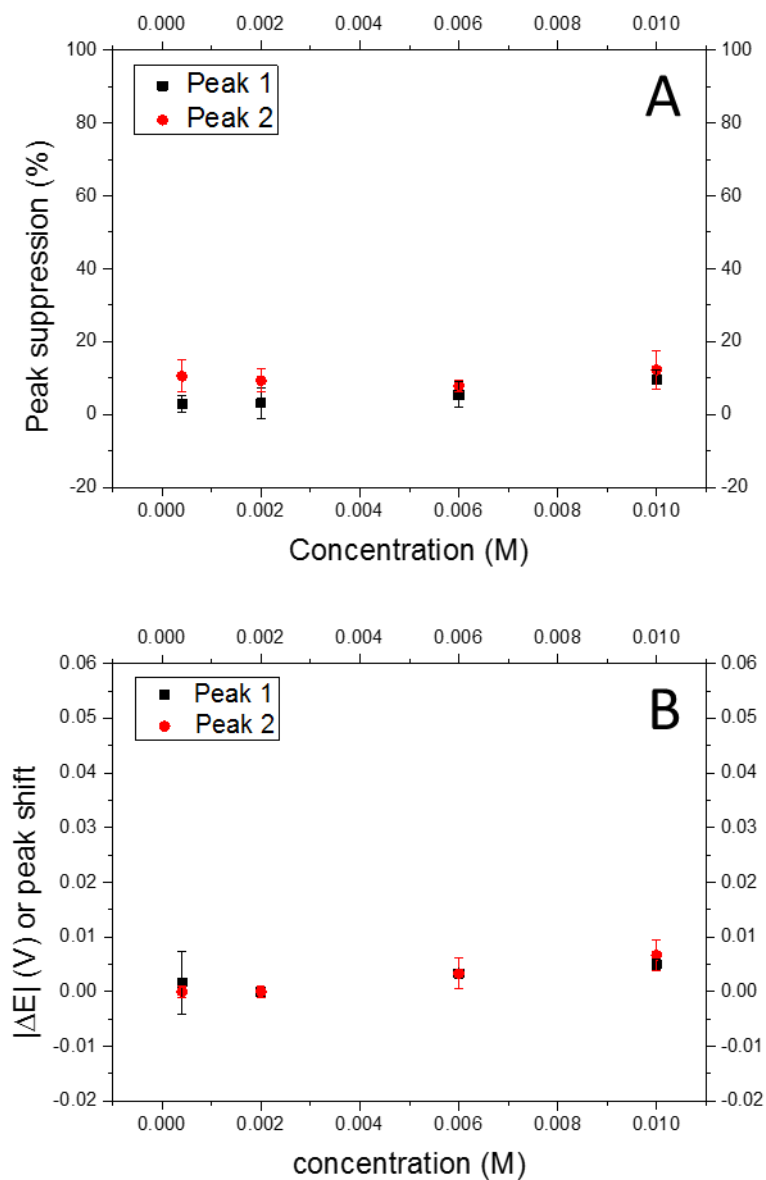


Figure 7. 30: Behaviour of the Peak 1 (black dots) and Peak 2 (red dots) of the voltammograms obtained from the ESD when a varying concentration of CeO₂ NPs (cubes) in CCB 4.0 interact with DOPC under a continuous flow of CCB 4.0. A: Graph showing the suppression, in percentage (%), of the peaks. B: Graph showing the shift (V), in potential, of the peaks.

7.3.3.3 Different concentration of ceria needles in CCB 4.0

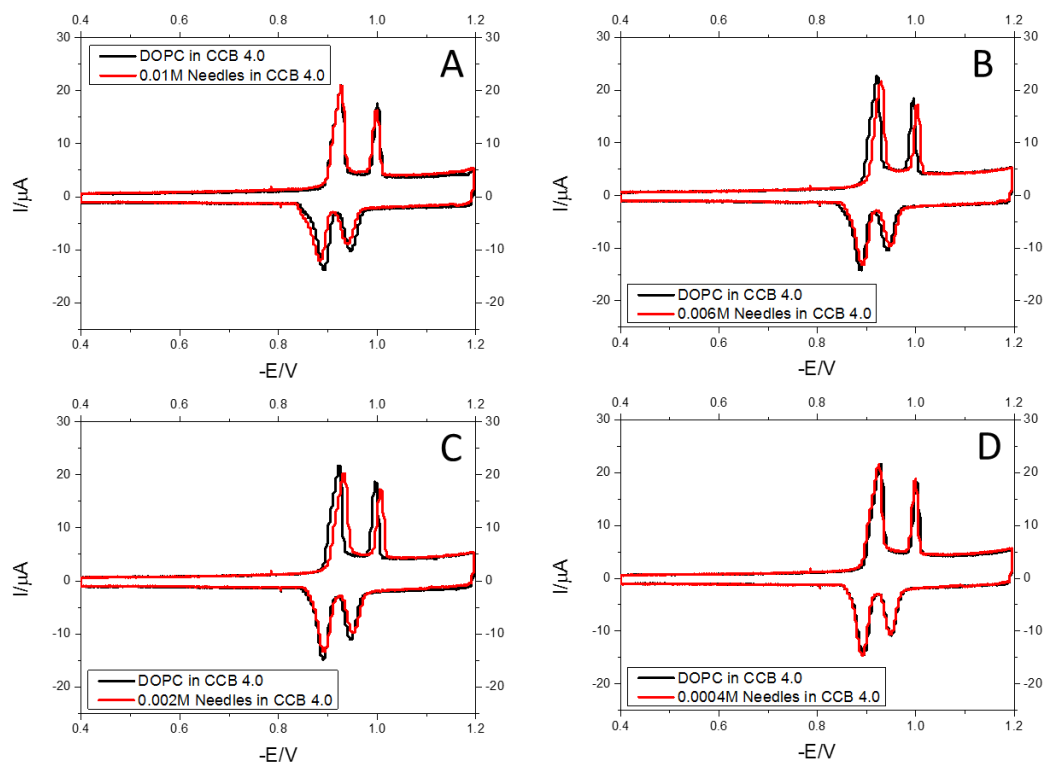


Figure 7. 31: RCV voltammograms recorded at 40Vs^{-1} with a potential excursion from -0.4V to -1.20V of DOPC (black lines) under a continuous flow of CCB 4.0 in the presence of (red lines): A: 0.01M of CeO_2 NPs (needles) in CCB 4.0, B: 0.006M of CeO_2 NPs (needles) in CCB 4.0, C: 0.002M of CeO_2 NPs (needles) in CCB 4.0, D: 0.0004M of CeO_2 NPs (needles) in CCB 4.0.

As observed in Figure 7. 31 and summarised Figure 7. 32, there is no significant peak suppression nor peak shift when CeO_2 NPs with different concentrations interact with a monolayer of DOPC under a continuous flow of CCB 4.0.

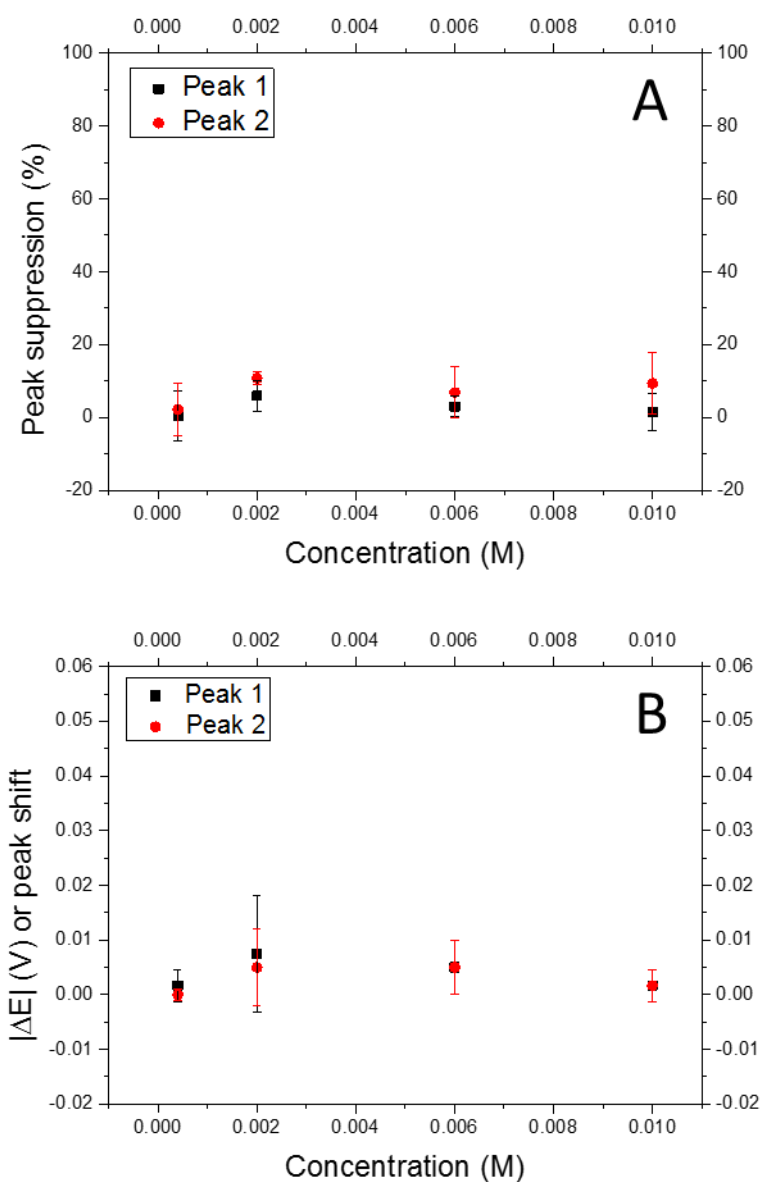


Figure 7. 32: Behaviour of the Peak 1 (black dots) and Peak 2 (red dots) of the voltammograms obtained from the ESD when a varying concentration of CeO₂ NPs (needles) in CCB 4.0 interact with DOPC under a continuous flow of CCB 4.0. A: Graph showing the suppression, in percentage (%), of the peaks. B: Graph showing the shift (V), in potential, of the peaks.

7.3.4 Interaction of CeO_2 NPs with DOPC under a flow of citric/citrate buffer at pH 5.0 (CCB 5.0)

7.3.4.1 Different concentrations of ceria spheres in CCB 5.0

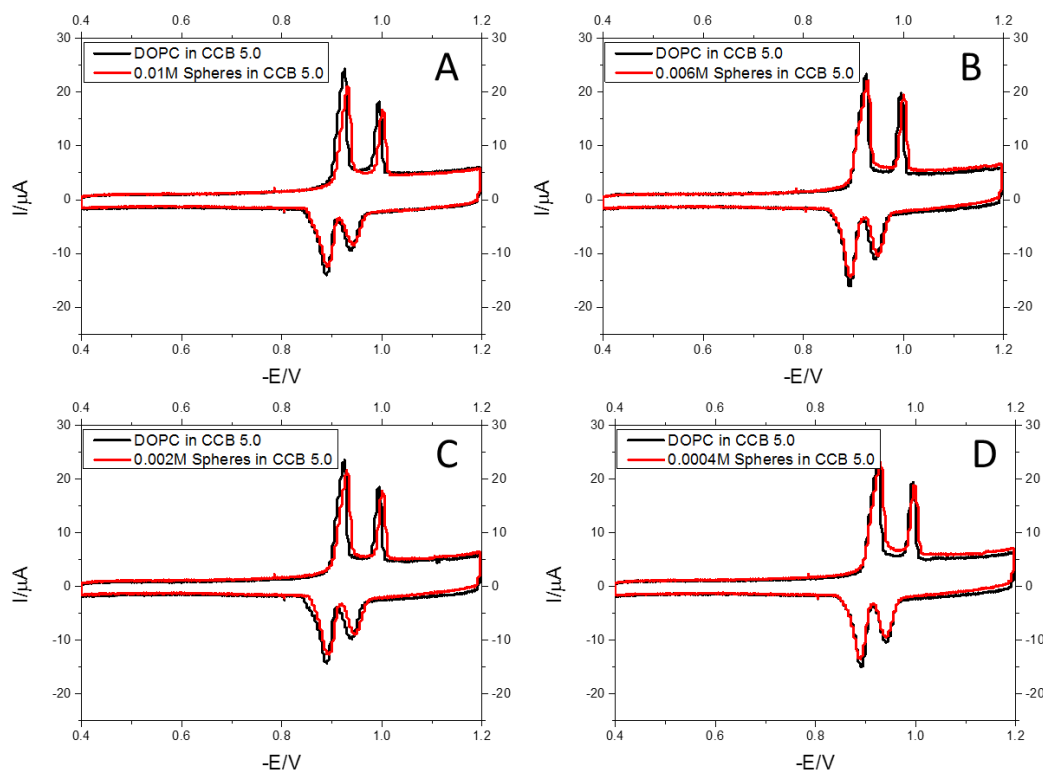


Figure 7.33: RCV voltammograms recorded at 40Vs^{-1} with a potential excursion from -0.4V to -1.20V of DOPC (black lines) under a continuous flow of CCB 5.0 in the presence of (red lines): A: 0.01M of CeO_2 NPs (spheres) in CCB 5.0, B: 0.006M of CeO_2 NPs (spheres) in CCB 5.0, C: 0.002M of CeO_2 NPs (spheres) in CCB 5.0, D: 0.0004M of CeO_2 NPs (spheres) in CCB 5.0.

Figure 7.33 displays the voltammograms which are obtained when CeO_2 NPs (spheres) at different concentration, interact with a monolayer of DOPC in CCB 5.0. As observed in Figure 7.33 and Figure 7.34, there is no significant peak suppression nor peak shift for any of the samples. This behaviour indicates that CeO_2 NPs, under these conditions, do not interact with the phospholipid monolayer.

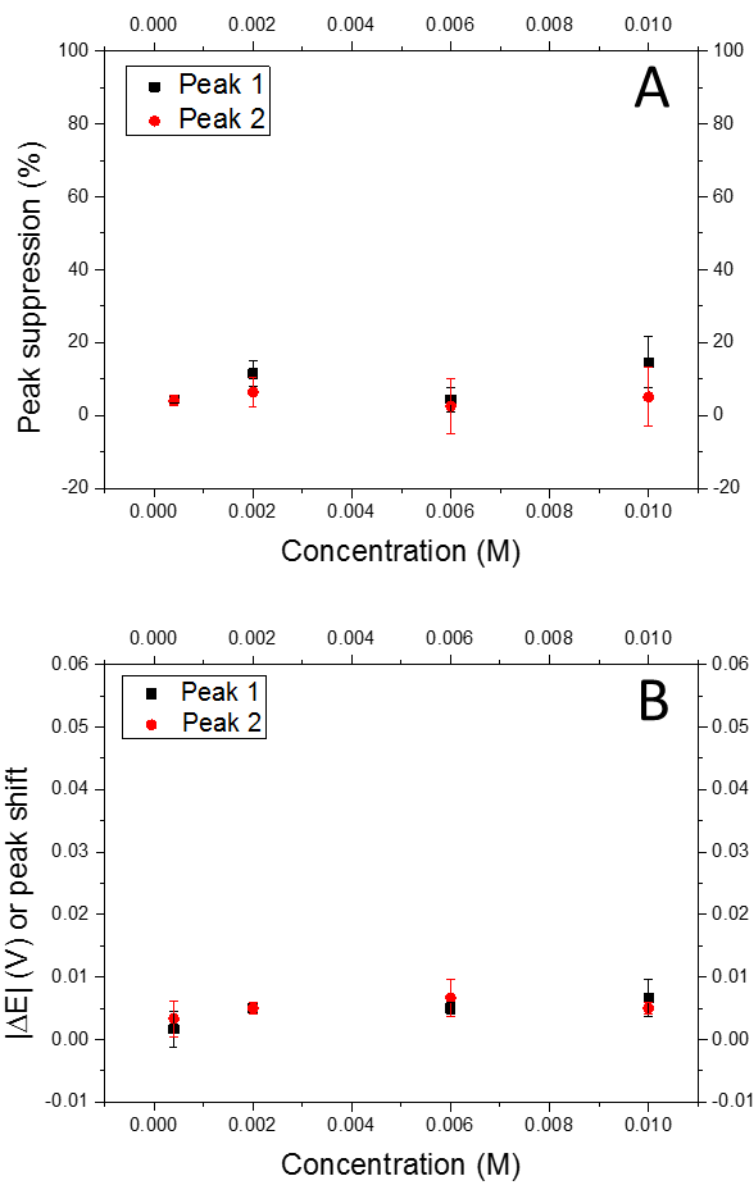


Figure 7.34: Behaviour of the Peak 1 (black dots) and Peak 2 (red dots) of the voltammograms obtained from the ESD when a varying concentration of CeO₂ NPs (spheres) in CCB5.0 interact with DOPC under a continuous flow of CCB5.0. A: Graph showing the suppression, in percentage (%), of the peaks. B: Graph showing the shift (V), in potential, of the peaks.

7.3.4.2 Different concentrations of ceria cubes in CCB 5.0

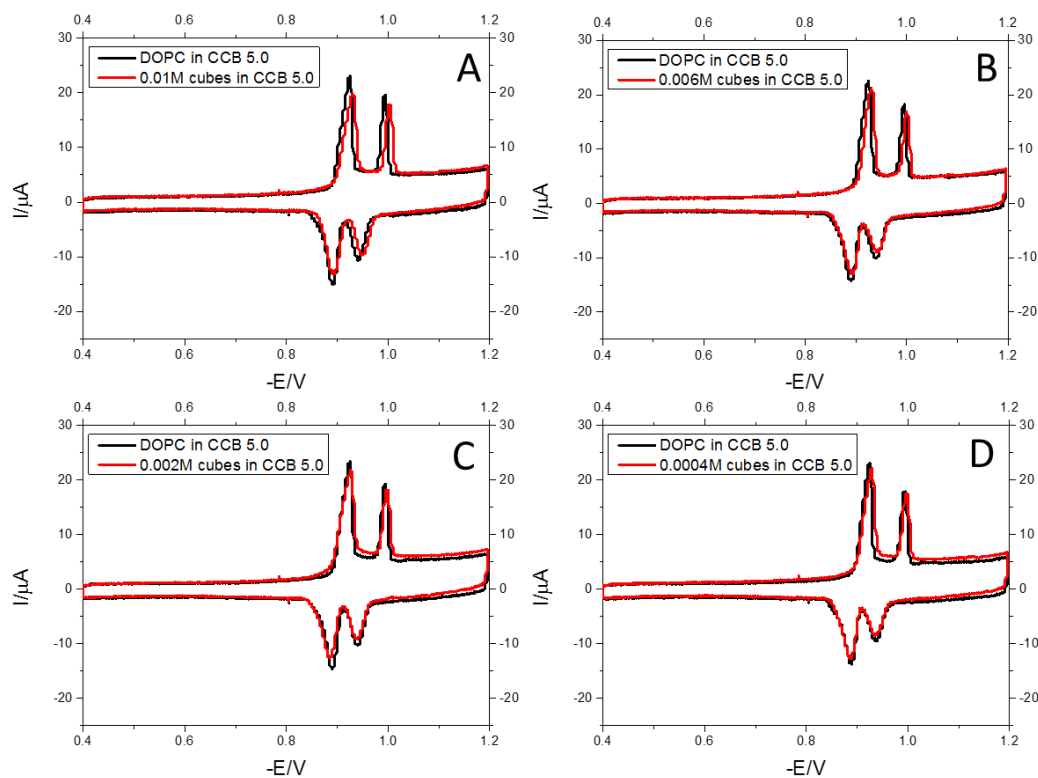


Figure 7. 35: RCV voltammograms recorded at $40\text{V}\text{s}^{-1}$ with a potential excursion from -0.4V to -1.20V of DOPC (black lines) under a continuous flow of CCB 5.0 in the presence of (red lines): A: 0.01M of CeO_2 NPs (cubes) in CCB 5.0, B: 0.006M of CeO_2 NPs (cubes) in CCB 5.0, C: 0.002M of CeO_2 NPs (cubes) in CCB 5.0, D: 0.0004M of CeO_2 NPs (cubes) in CCB 5.0.

Figure 7. 35 shows the voltammograms produced when CeO_2 NPs (cubes) at different concentrations, interact with DOPC in CCB 5.0. As observed graphically in Figure 7. 36, there is no peak suppression nor peak shift at any NP. This behaviour indicates that, under these conditions, CeO_2 NPs (cubes) do not interact with DOPC.

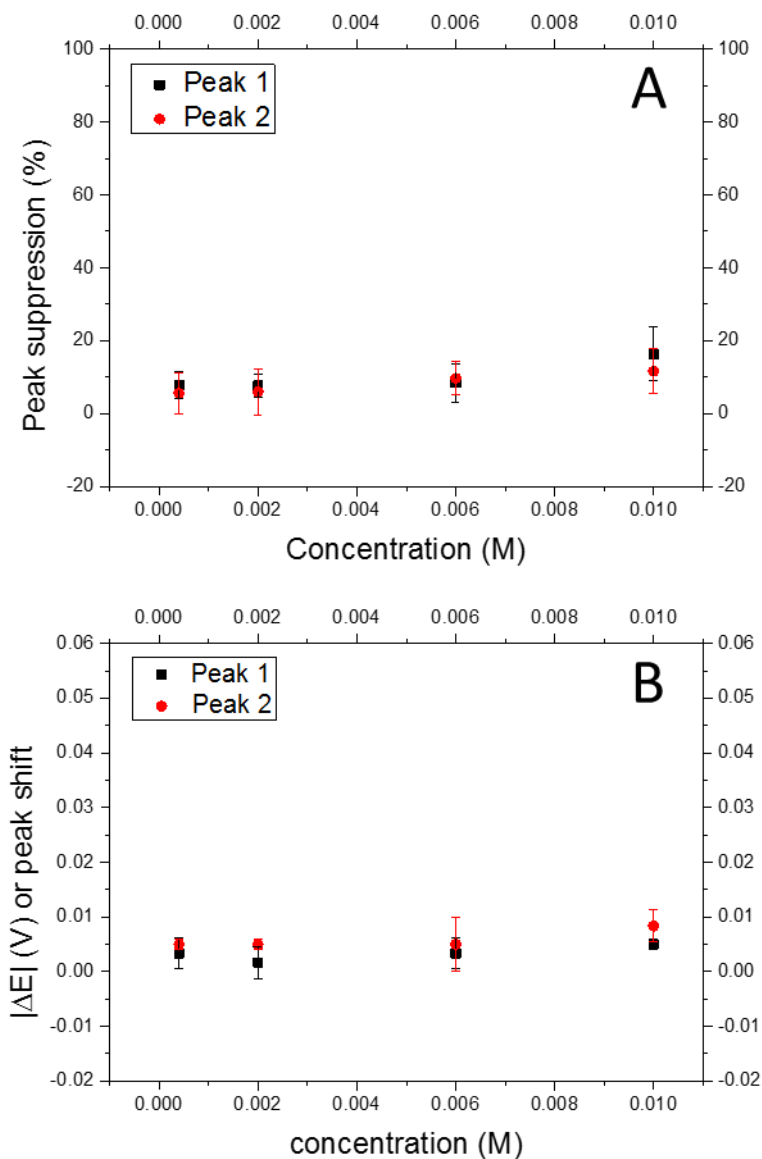


Figure 7. 36: Behaviour of the Peak 1 (black dots) and Peak 2 (red dots) of the voltammograms obtained from the ESD when a varying concentration of CeO₂ NPs (cubes) in CCB5.0 interact with DOPC under a continuous flow of CCB5.0. A: Graph showing the suppression, in percentage (%), of the peaks. B: Graph showing the shift (V), in potential, of the peaks.

7.3.4.3 Different concentration ceria needles in CCB 5.0

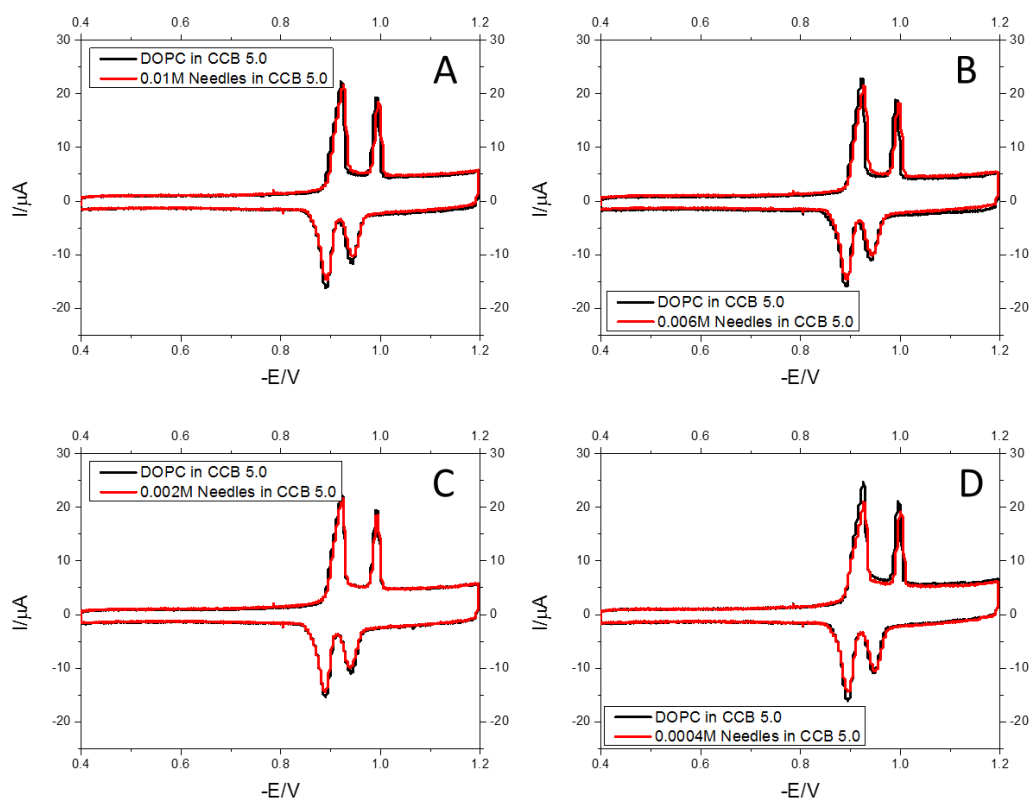


Figure 7.37: RCV voltammograms recorded at 40Vs^{-1} with a potential excursion from -0.4V to -1.20V of DOPC (black lines) under a continuous flow of CCB 5.0 in the presence of (red lines): A: 0.01M of CeO_2 NPs (needles) in CCB 5.0, B: 0.006M of CeO_2 NPs (needles) in CCB 5.0, C: 0.002M of CeO_2 NPs (needles) in CCB 5.0, D: 0.0004M of CeO_2 NPs (needles) in CCB 5.0.

As observed in Figure 7.37 and Figure 7.38, there is no peak shift nor peak suppression when a DOPC monolayer is exposed to different concentrations of CeO_2 NPs (needles).

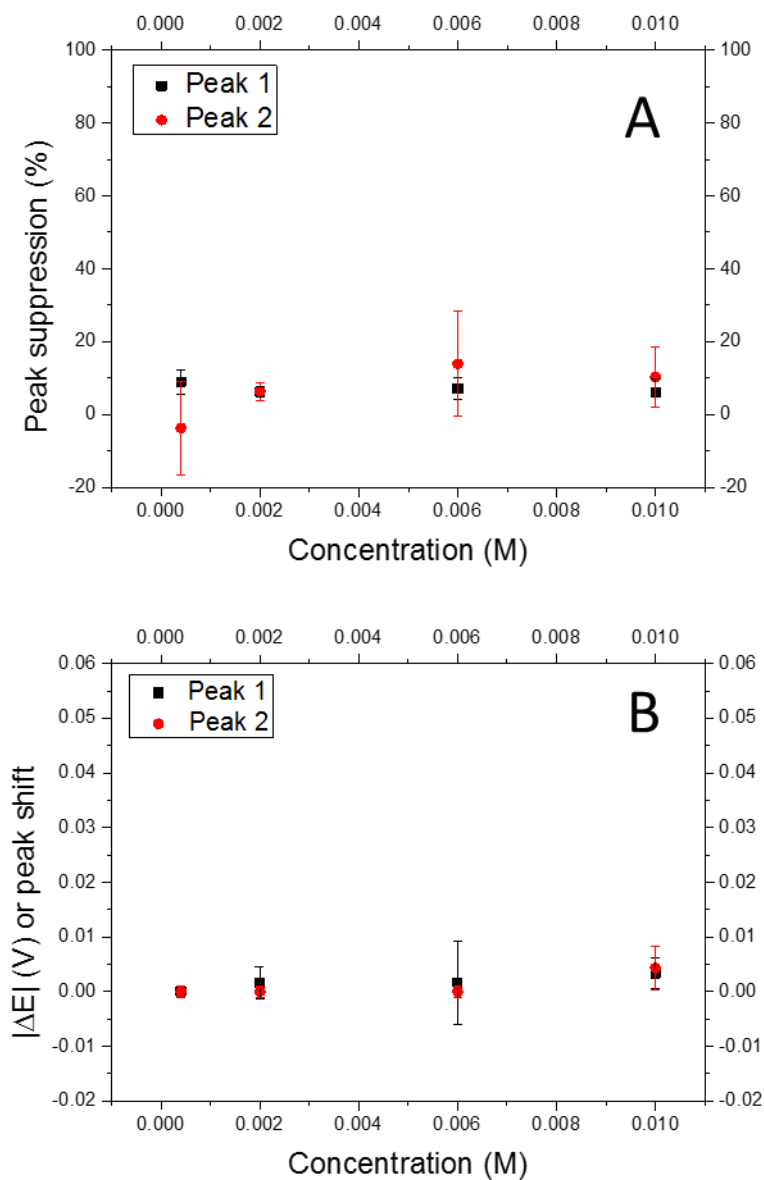


Figure 7. 38: Behaviour of the Peak 1 (black dots) and Peak 2 (red dots) of the voltammograms obtained from the ESD when a varying concentration of CeO₂ NPs (needles) in CCB5.0 interact with DOPC under a continuous flow of CCB5.0. A: Graph showing the suppression, in percentage (%), of the peaks. B: Graph showing the shift (V), in potential, of the peaks.

7.3.5 Interaction of CeO_2 NPs with DOPC under a flow of citric/citrate buffer at pH 6.0 (CCB 6.0)

7.3.5.1 Different concentration of ceria spheres in CCB 6.0

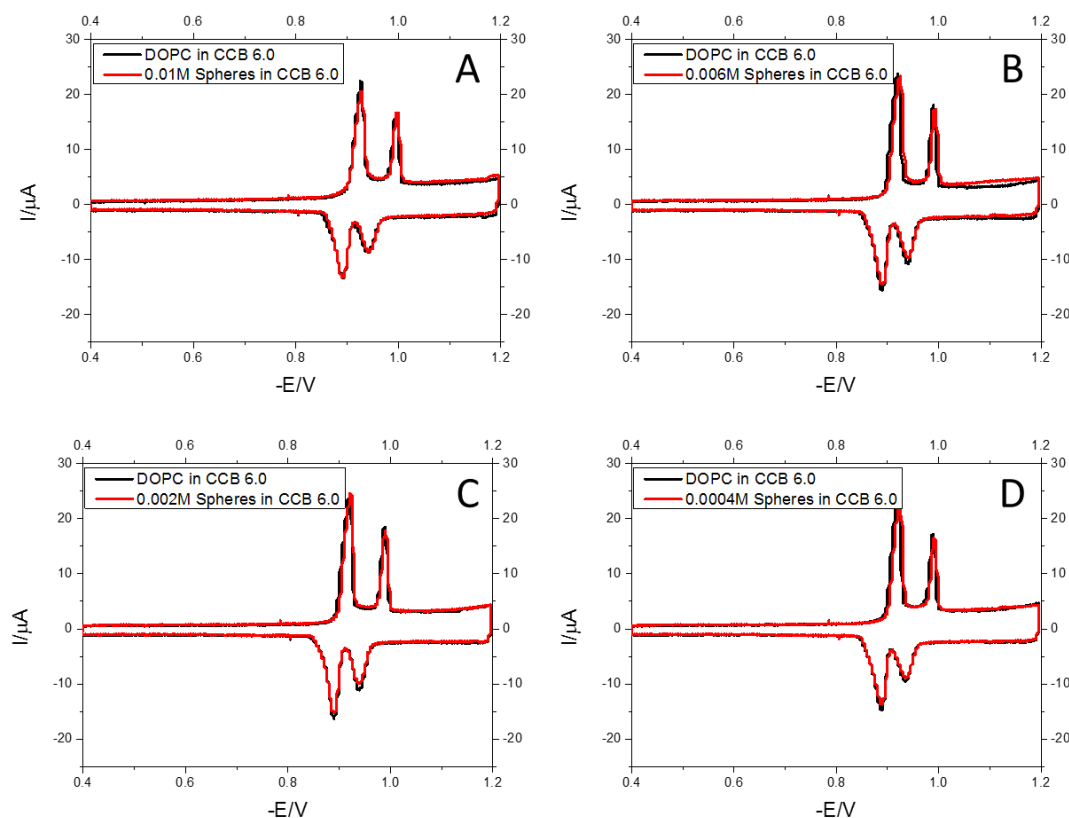


Figure 7. 39: RCV voltammograms recorded at 40Vs^{-1} with a potential excursion from -0.4V to -1.20V of DOPC (black lines) under a continuous flow of CCB 6.0 in the presence of (red lines): A: 0.01M of CeO_2 NPs (spheres) in CCB 6.0, B: 0.006M of CeO_2 NPs (spheres) in CCB 6.0, C: 0.002M of CeO_2 NPs (spheres) in CCB 6.0, D: 0.0004M of CeO_2 NPs (spheres) in CCB 6.0.

Figure 7. 39 shows the interaction produced when the DOPC monolayer is exposed to different concentration of CeO_2 NPs (spheres) dispersion in GLY 3.0. As observed in Figure 7. 40, there is no peak suppression nor peak shift, which indicates that under these conditions, the NPs do not interact with the phospholipid monolayer.

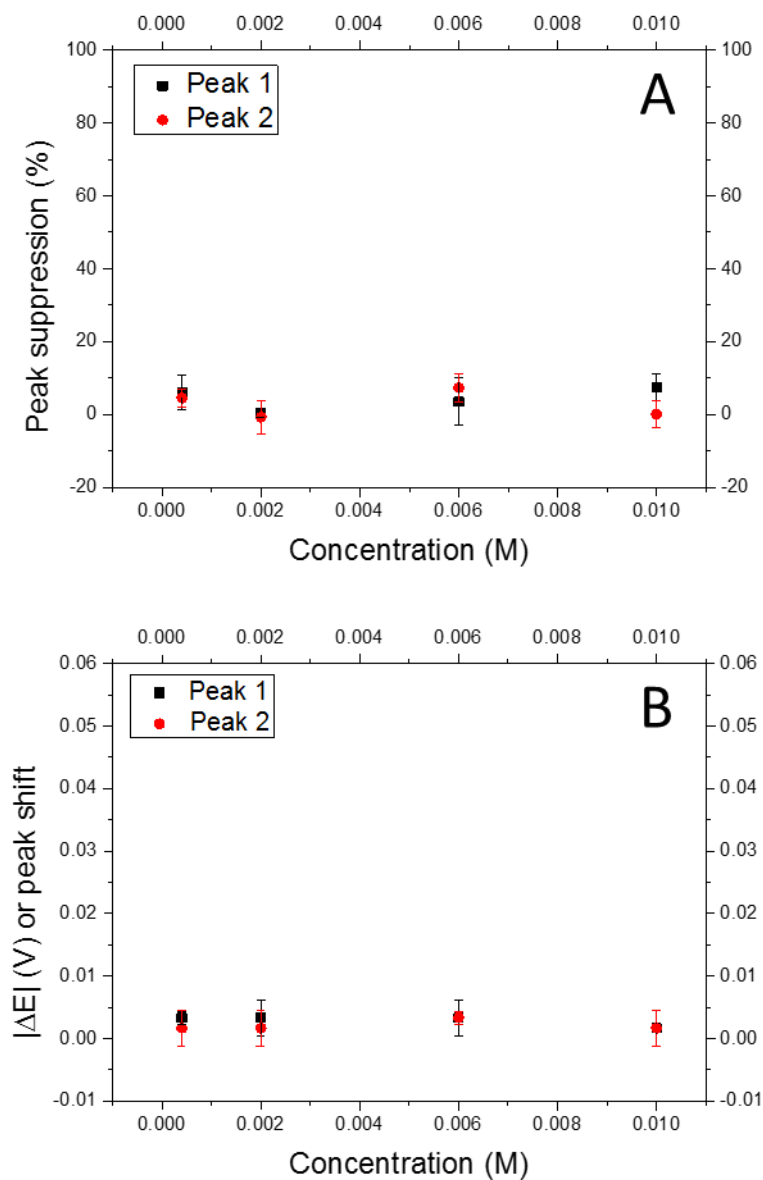


Figure 7. 40: Behaviour of the Peak 1 (black dots) and Peak 2 (red dots) of the voltammograms obtained from the ESD when a varying concentration of CeO₂ NPs (spheres) in CCB 6.0 interact with DOPC under a continuous flow of CCB 6.0. A: Graph showing the suppression, in percentage (%), of the peaks. B: Graph showing the shift (V), in potential, of the peaks.

7.3.5.2 Different concentration of ceria cubes in CCB 6.0

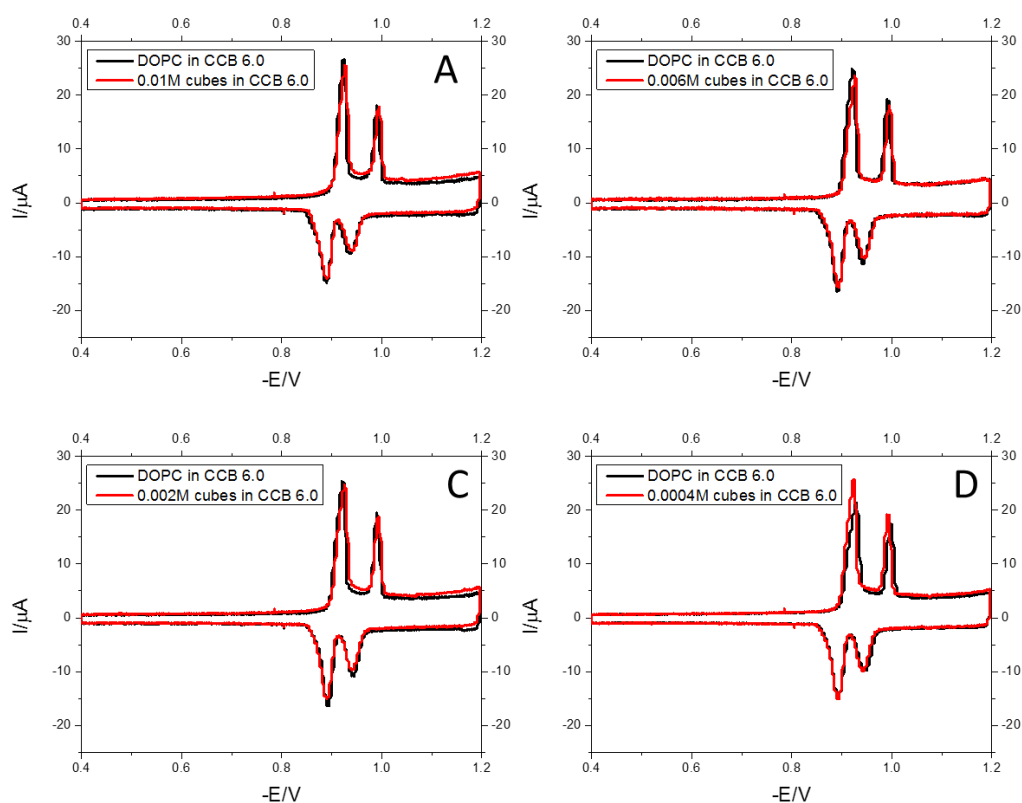


Figure 7. 41: RCV voltammograms recorded at 40Vs^{-1} with a potential excursion from -0.4V to -1.20V of DOPC (black lines) under a continuous flow of CCB 6.0 in the presence of (red lines): A: 0.01M of CeO_2 NPs (cubes) in CCB 6.0, B: 0.006M of CeO_2 NPs (cubes) in CCB 6.0, C: 0.002M of CeO_2 NPs (cubes) in CCB 6.0, D: 0.0004M of CeO_2 NPs (cubes) in CCB 6.0.

Figure 7. 41 displays the behaviour of the voltammogram when dispersions of CeO_2 NPs (cubes) with different concentration are introduced into the ESD and are in contact with DOPC in a continuous flow of CCB 6.0. As summarised in Figure 7. 42, there is no suppression nor shift of the peaks, which indicates the NPs (cubes) do not interact with the phospholipid monolayer under these conditions.

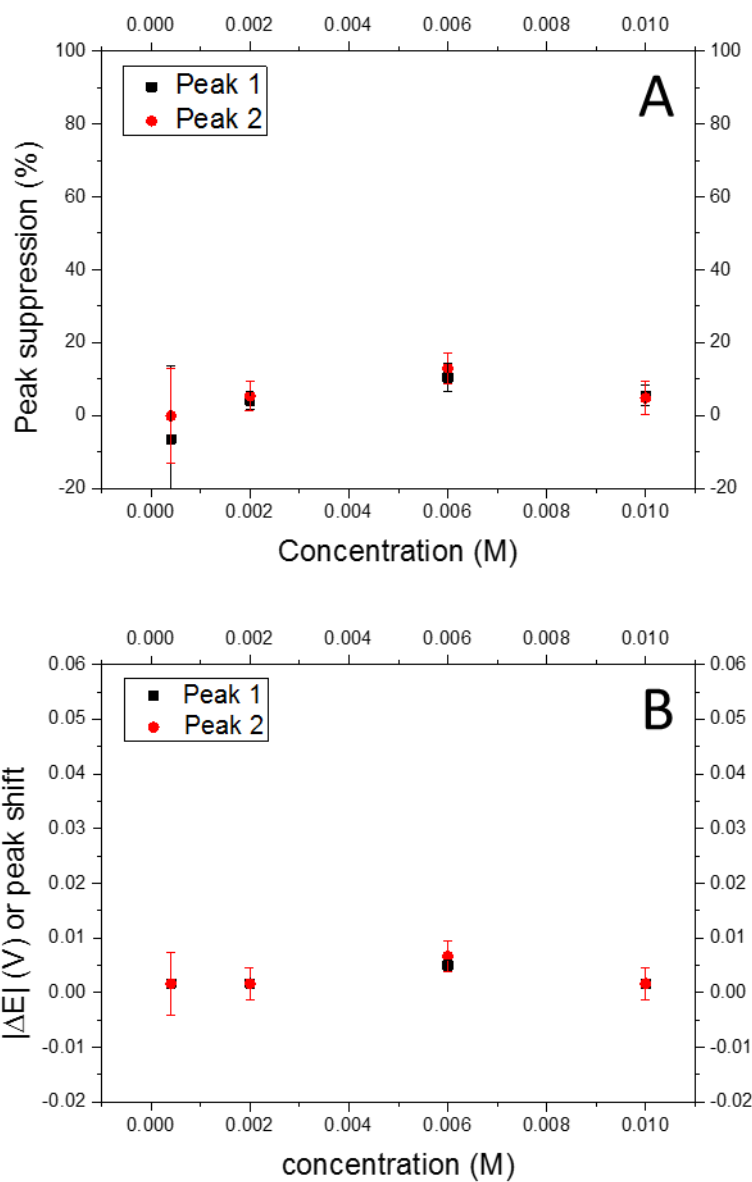


Figure 7. 42: Behaviour of the Peak 1 (black dots) and Peak 2 (red dots) of the voltammograms obtained from the ESD when a varying concentration of CeO₂ NPs (cubes) in CCB 6.0 interact with DOPC under a continuous flow of CCB 6.0. A: Graph showing the suppression, in percentage (%), of the peaks. B: Graph showing the shift (V), in potential, of the peaks.

7.3.5.3 Different concentrations of ceria needles in CCB 6.0

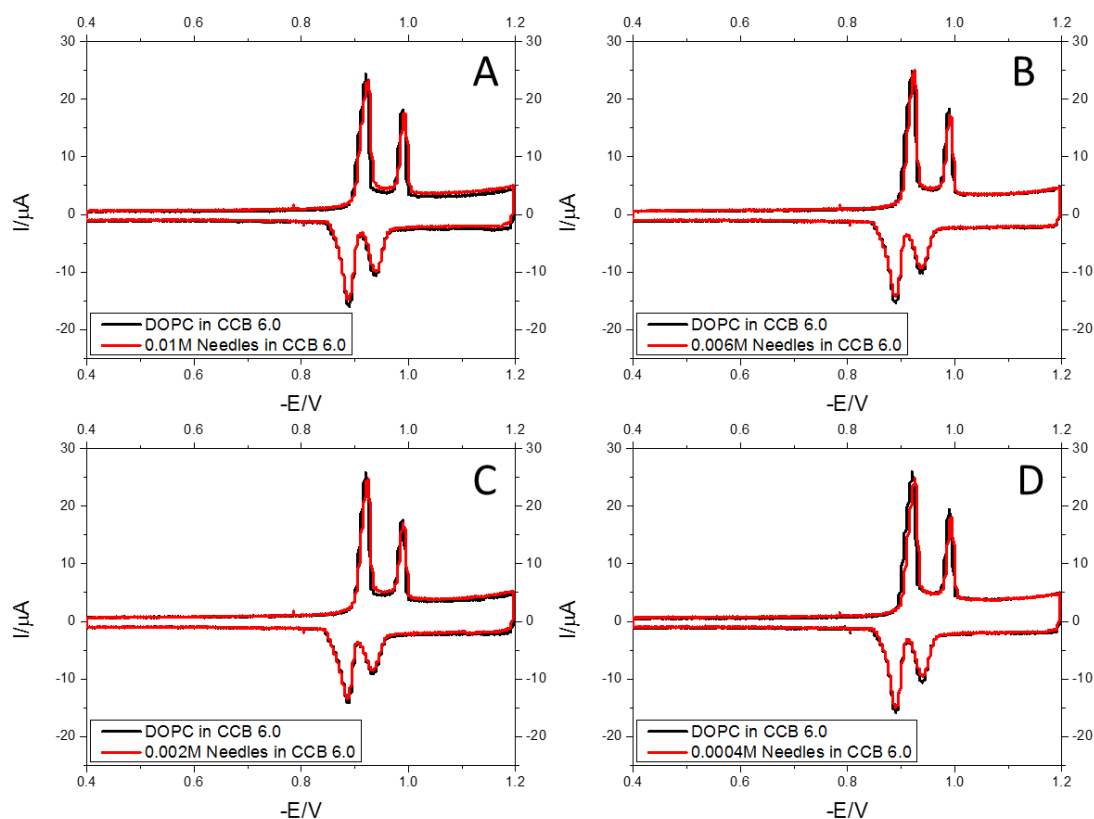


Figure 7. 43: RCV voltammograms recorded at 40Vs^{-1} with a potential excursion from -0.4V to -1.20V of DOPC (black lines) under a continuous flow of CCB 6.0 in the presence of (red lines): A: 0.01M of CeO_2 NPs (needles) in CCB 6.0, B: 0.006M of CeO_2 NPs (needles) in CCB 5.0, C: 0.002M of CeO_2 NPs (needles) in CCB 6.0, D: 0.0004M of CeO_2 NPs (needles) in CCB 6.0.

Figure 7. 43 shows the voltammograms produced when CeO_2 NPs (needles) at different concentrations, interact with DOPC in CCB 6.0. As summarised in Figure 7. 44, there is no peak suppression nor peak shift no matter what the concentration of the NPs. This behaviour indicates that, under these conditions, CeO_2 NPs (needles) do not interact with DOPC.

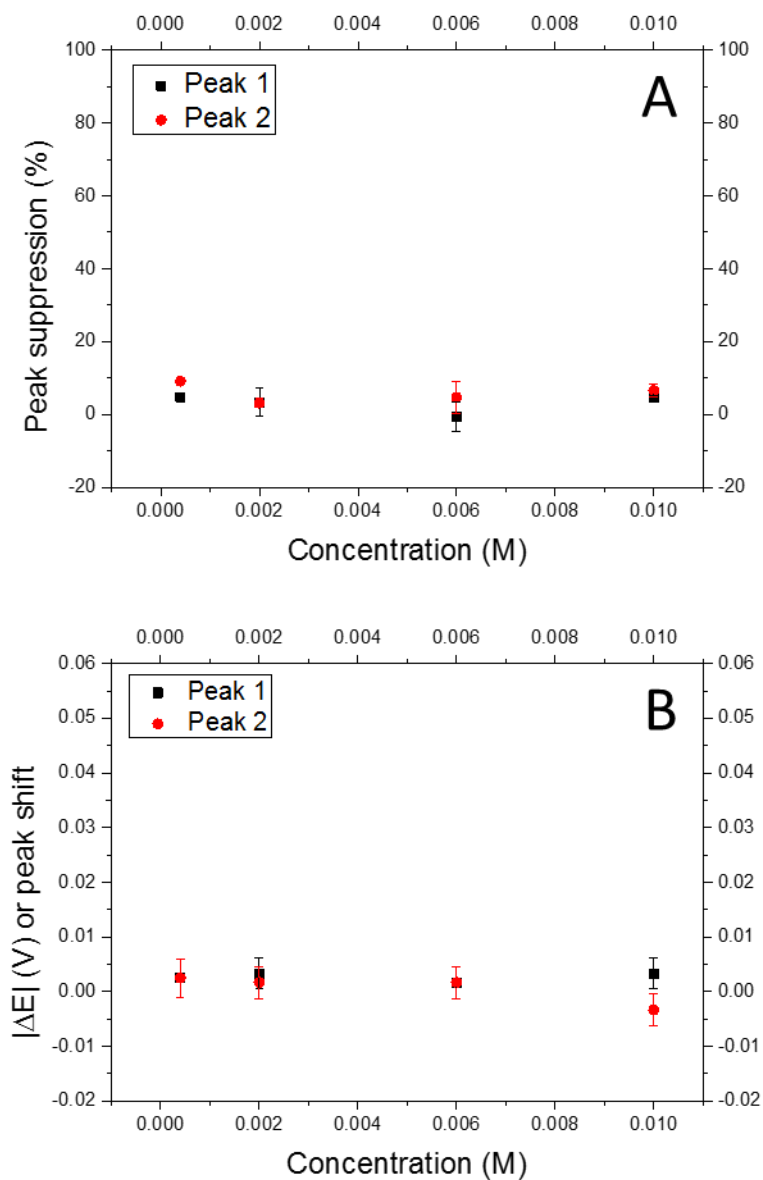


Figure 7. 44: Behaviour of the Peak 1 (black dots) and Peak 2 (red dots) of the voltammograms obtained from the ESD when a varying concentration of CeO₂ NPs (needles) in CCB 6.0 interact with DOPC under a continuous flow of CCB 6.0. A: Graph showing the suppression, in percentage (%), of the peaks. B: Graph showing the shift (V), in potential, of the peaks.

7.3.6 Summary and discussion

As observed in Table 7. 1, a clear relationship between the NP-phospholipid interaction and pH can be observed. CeO₂ NPs in acidic buffers show a clear interaction with the DOPC monolayer while for NPs in environments with pH values > 3 do not show any interaction.

Table 7. 1: Summary table of the interaction between different CeO₂ NPs and a DOPC monolayer under the influence of different buffers

NPs/Buffers	GLY 3.0	CCB 3.0	CCB 4.0	CCB 5.0	CCB 6.0	PBS
SPHERES	YES	YES	NO	NO	NO	NO
CUBES	YES	YES	NO	NO	NO	NO
NEEDLES	YES	YES	NO	NO	NO	NO

In addition, three major effects in the voltammogram, dependant on the pH and type of buffer could be noticed:

- **Suppression and shift of the current peaks of the voltammogram to more negative and positive potentials (spread of the peaks)** when the dispersion buffer was **GLY 3.0**. A spread of the peaks has been observed when the spheres, cubes and dots interacted with DOPC under a continuous flow of DOPC. This effect has been previously observed for Ce(NO₃)₃ with DOPC in PBS (Figure 7. 1A) and correspond to the binding of Ce³⁺ with the phosphate groups of the phospholipid monolayer. Nevertheless, this effect is not observed for CeO₂ NPs in contact with DOPC under a continuous flow of PBS. The effect of PBS will be further analysed in section 7.5.4.
- **Suppression of both current peaks and shift of the second peak** to more negative potentials when the buffer GLY 3.0 was used. This effect is produced in the case of the ceria needles. Note, despite having an initial well-defined size and shape, when sonicating the needles break forming pieces of different sizes and shapes which could affect the interaction produced.

- **Suppression of the second current peak and shift** to more negative potentials when the buffer used was **CCB 3.0**. This effect is observed for CeO₂ NPs spheres, cubes and needles.
- **Increase of the current in the voltammogram at -1.2V** when CeO₂ NPs interact with DOPC under a continuous flow of GLY 3.0 and CCB 3.0 buffers. CeO₂ is a known semiconductor material and it is assumed CeO₂ NPs penetrate the membrane and interact directly with the Hg/Pt electrode. This effect has been described in [127, 128]. However, such an effect is not observed for the needles under the same conditions. As already mentioned, the needles break into pieces of different size. It is more difficult for large particles to penetrate the monolayer of phospholipids.

CeO₂ NPs show a different interaction behaviour with the phospholipid monolayer depending on the buffer they are dispersed in. The dispersant medium can change the surface characteristics of the NP in such a way it affects interaction. For this reason, it can be concluded the dispersion medium can affect the NP-phospholipid interaction. The following section (7.4) will study further how these changes affect the interaction of the CeO₂ NPs with DOPC in different buffers. Additionally, the NP size and shape affect the interaction with the monolayer. Small particles as the spheres or the cubes, produced a semiconductor effect on the voltammograms. Nevertheless, bigger needles did not produce the same effect. The semiconductor effect was previously described in 7.2.5 for commercial CeO₂ NPs.

As already mentioned, the interaction between NPs and DOPC has been previously studied in the past [127, 128, 173]. The type of interaction showed to be particular to the type of NP. Nevertheless, some effects were common to NPs with similar characteristics and properties. This is the case of the effect observed for the semiconductor TiO₂ NPs and ZnO NPs. Despite producing a different interaction when in contact with DOPC in the ESD, SiO₂ and ZnO both showed a semiconductor effect [128]. This is the case also for CeO₂ NPs. Cerium is one

of the lanthanide elements but has dual properties. Cerium properties changes depending on its oxidation state. In this way, Ce^{3+} behaves as a lanthanide while Ce^{4+} behaves more like a IVB group elements (TiO_2) [55]. Additionally, some trends in behaviour about the interaction of NPs with model membranes were found. The degree of interaction showed to be dependant on size, aggregation and concentration of the NPs. In this way, smaller nanoparticles with higher active surface area to volume ratio interacted stronger than bigger nanoparticles [128]. This behaviour has been also observed by Nicola Williams with Au NPs. Nicola observed small size Au NPs interacted stronger than high size NPs. Her work is in review for publication at the moment. The effect of aggregation was observed by the first time with ZnO NPs [127]. Freshly sonicated ZnO NPs interacted stronger than the ZnO NPs aged for 30 min. Additionally, the degree of interaction is dependant on concentration. The more concentrated the sample is, the higher the degree of interaction.

7.4 The cerium response in the RCV measurements

As previously discussed, the ceria spheres and the cubes in GLY at pH 3.0 showed an interaction with the DOPC monolayer, which was similar to the interaction of Ce^{3+} with the DOPC monolayer. Also, CeO_2 NPs (spheres, cubes and needles) in CCB 3.0 showed an effect on the phospholipid monolayer. Two different sources of Ce^{3+} are proposed to explain the Ce^{3+} signal on the voltammograms of Figure 7. 15 and Figure 7. 17. Ce^{3+} formed from the reduction of Ce^{4+} to Ce^{3+} on the nanoparticle surface and free $\text{Ce}^{3+}(\text{aq})$ formed from the dissolution of the NPs.

There are a number of different reports in the literature that could provide evidence for both theories. On the one hand, there are those who report that cerium nanoparticles, despite being a relatively insoluble material, dissolve under acidic conditions [114, 174, 175], alternatively, there are those who report Ce^{3+} on the NP surface is the main driver for the NP activity [102].

7.4.1 The effect of the buffer in Ce^{3+} interaction

However, first, the effect of the medium on the interaction between cerium ions and DOPC was studied. DOPC was exposed to different concentrations of soluble $Ce(NO_3)_3$ in different media. The buffers which were used matched the buffers used in 6.1.2.

7.4.1.1 $Ce(NO_3)_3$ in GLY 3.0

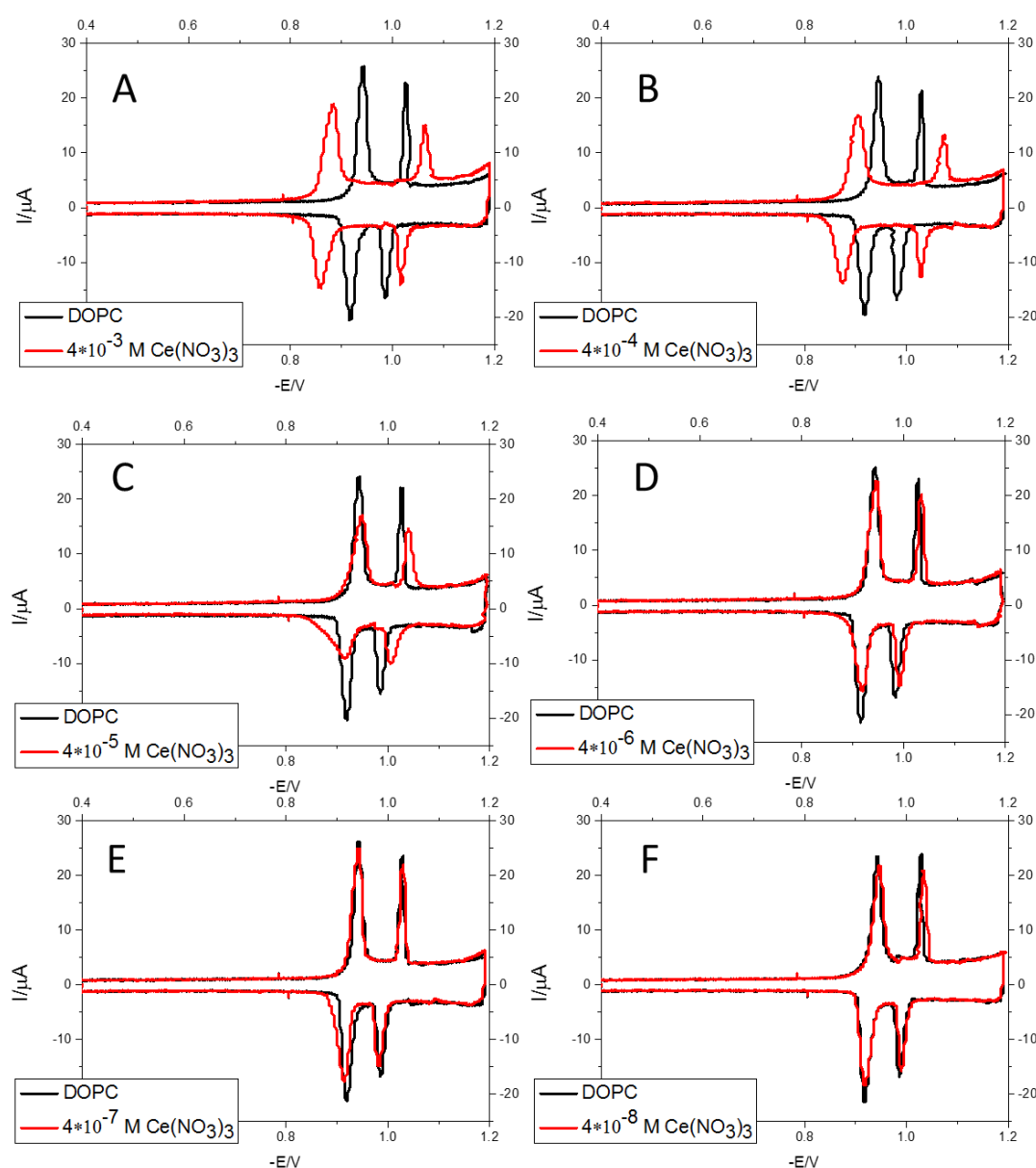


Figure 7. 45: RCV voltammograms recorded at 40V s^{-1} with a potential excursion from -0.4V to -1.20V of DOPC (black lines) under a continuous flow of GLY 3.0 in the presence of (red lines): A: $3.95 \cdot 10^{-3}$, B: $3.95 \cdot 10^{-4}$, C: $3.95 \cdot 10^{-5}$, D: $3.95 \cdot 10^{-6}$, E: $3.95 \cdot 10^{-7}$, F: $3.95 \cdot 10^{-8}$

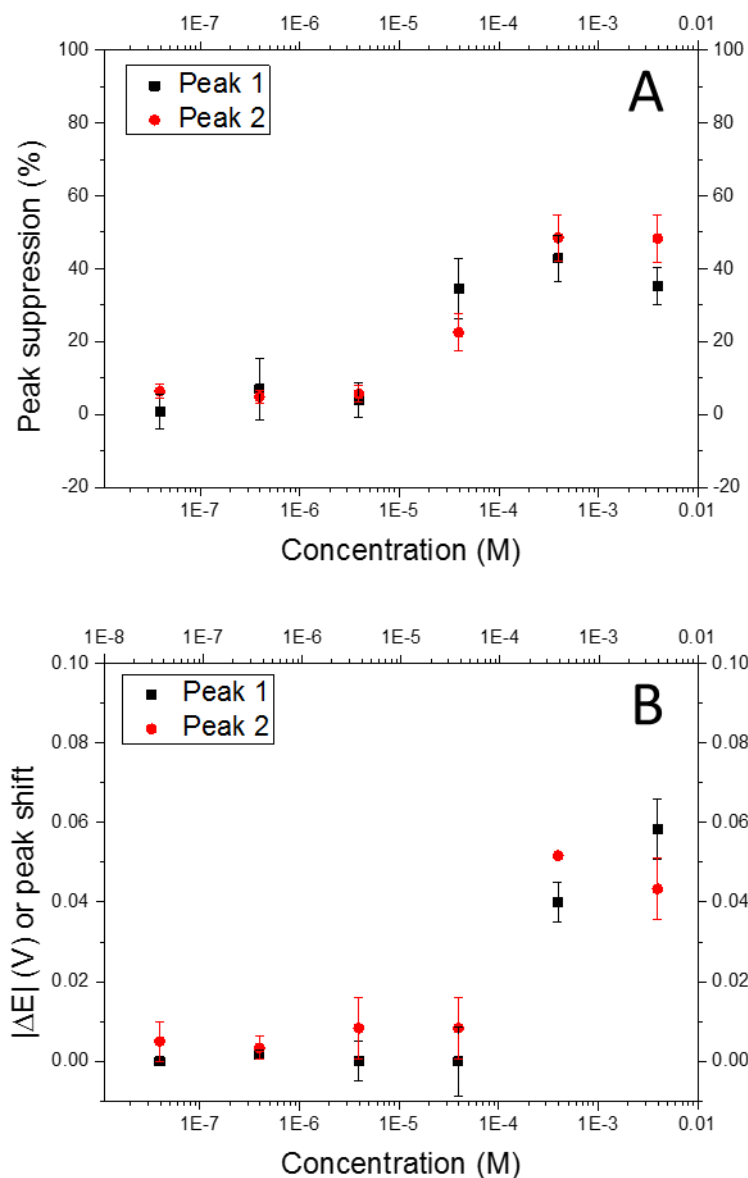


Figure 7. 46: Behaviour of the Peak 1 (black dots) and Peak 2 (red dots) of the voltammograms obtained from the ESD when a varying concentration of $\text{Ce}(\text{NO}_3)_3$ in GLY 3.0 interact with DOPC under a continuous flow of GLY 3.0. A: Graph showing the suppression, in percentage (%), of the peaks. B: Graph showing the shift (V), in potential, of the peaks.

Figure 7. 45 shows the behaviour of the voltammogram when DOPC is exposed to an increasing concentration of $\text{Ce}(\text{NO}_3)_3$ (i.e. Ce^{3+} (aq)). As observed, there is an effect of concentration on the interaction of Ce^{3+} with the phospholipid monolayer. This effect is very similar to the one previously observed in Figure 7. 15A and Figure 7. 17A, which correspond to the interaction of the CeO_2 NPs (spheres and cubes) with the DOPC monolayer under a constant flow of GLY

3.0 buffer. This behaviour is summarised in Figure 7. 46, where the average suppression and shift of the peaks is displayed for the different measurements. The limit of detection (LOD), understood as the minimum significant concentration of the analyte able to produce a change in the voltammogram, of $\text{Ce}(\text{NO}_3)_3$ in GLY 3.0 was found to be $3.95 \cdot 10^{-5} \text{M}$.

7.4.1.2 $\text{Ce}(\text{NO}_3)_3$ in CCB at different pH values

A similar experiment to the previous one, but using CCB was carried out to analyse the effect of the buffer on the Ce^{3+} interaction with a monolayer of DOPC. Figure 7. 47 shows the interaction of $\text{Ce}(\text{NO}_3)_3$ and DOPC under a continuous flow of CCB 3.0. This interaction is very similar to the behaviour of the voltammograms in Figure 7. 21A and Figure 7. 23A , which suggests that the medium affects cerium activity in phospholipid monolayers.

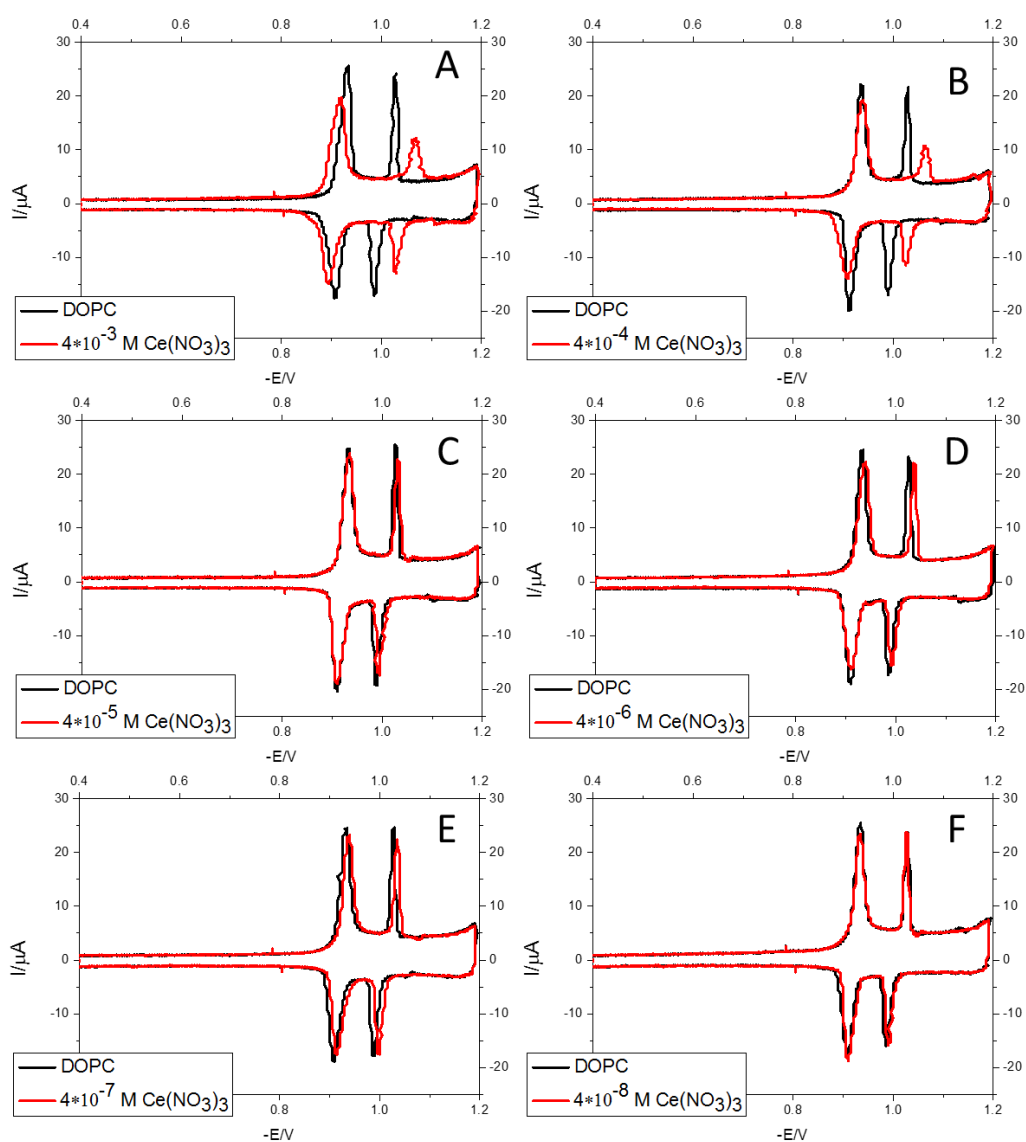


Figure 7. 47: RCV voltammograms recorded at 40Vs^{-1} with a potential excursion from -0.4V to -1.20V of DOPC (black lines) under a continuous flow of CCB 3.0 in the presence of (red lines): A: $3.95\cdot 10^{-3}$, B: $3.95\cdot 10^{-4}$, C: $3.95\cdot 10^{-5}$, D: $3.95\cdot 10^{-6}$, E: $3.95\cdot 10^{-7}$, F: $3.95\cdot 10^{-8}$

Figure 7. 48 summarises the variation of the peak suppression (A) and peak shift (B) in the voltammogram in figure Figure 7. 47 as a function of concentration. The limit of detection of $\text{Ce}(\text{NO}_3)_3$ in CCB 3.0 was found to be $3.97 \cdot 10^{-4} \text{M}$.

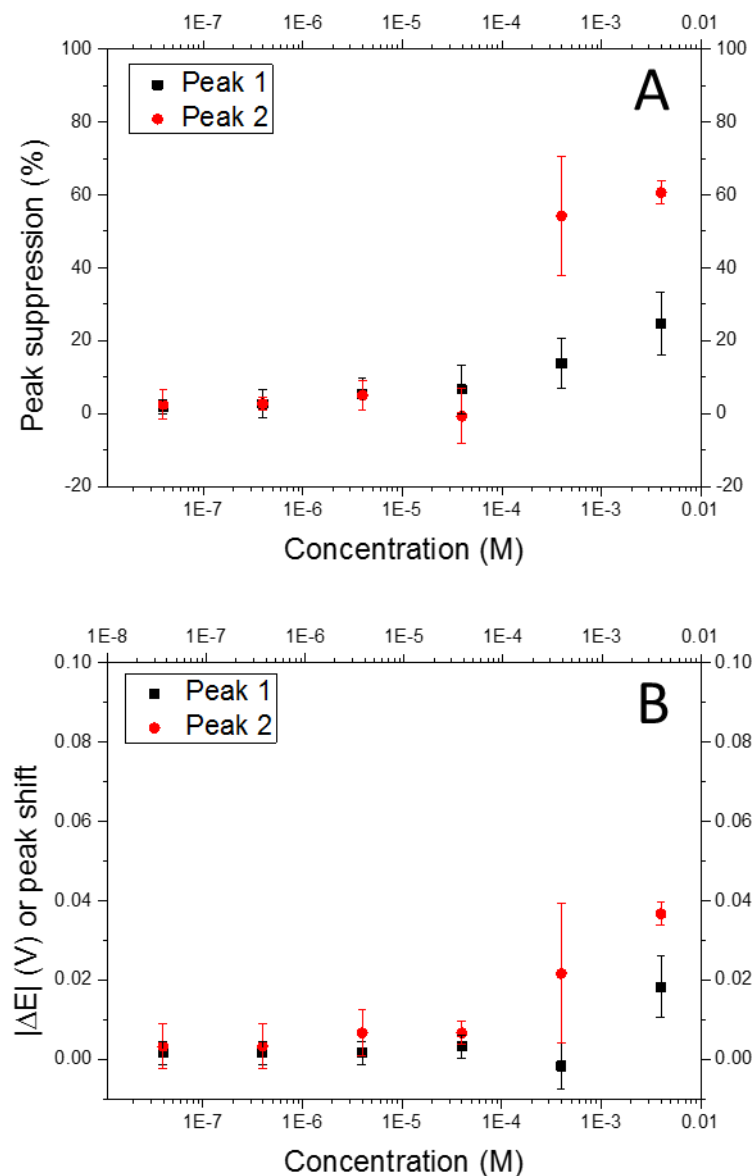


Figure 7. 48: Behaviour of the Peak 1 (black dots) and Peak 2 (red dots) of the voltammograms obtained from the ESD when a varying concentration of $\text{Ce}(\text{NO}_3)_3$ in CCB 3.0 interact with DOPC under a continuous flow of CCB 3.0. A: Graph showing the suppression, in percentage (%), of the peaks. B: Graph showing the shift (V), in potential, of the peaks.

Figure 7. 49 show the variation of the peaks of the voltammogram when an increasing concentration of $\text{Ce}(\text{NO}_3)_3$ interacts with DOPC in a flow of CCB 4.0, CCB 5.0 and CCB 6.0. As observed, there is no significant suppression nor shift

of the peaks of the voltammogram, which indicates no interaction. DOPC shows different behaviour when exposed to $\text{Ce}(\text{NO}_3)_3$ in the same buffer at lower pH, which indicates that the buffer is affecting $\text{Ce}(\text{NO}_3)_3$ interaction.

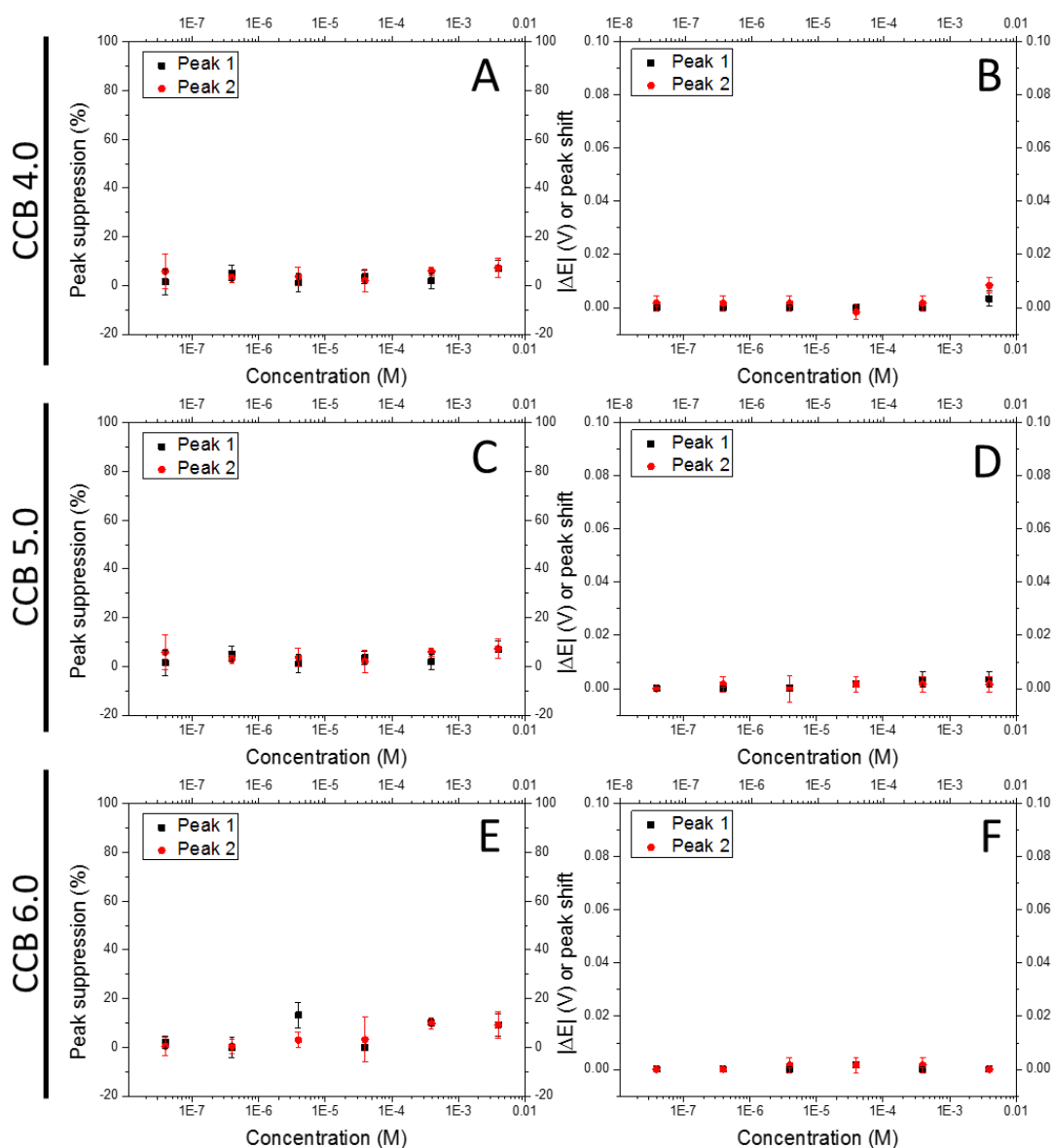


Figure 7.49: Behaviour of the Peak 1 (black dots) and Peak 2 (red dots) of the voltammograms obtained from the ESD when a varying concentration of $\text{Ce}(\text{NO}_3)_3$ interact with DOPC under a continuous flow of different buffers: A: peak suppression versus concentration of $\text{Ce}(\text{NO}_3)_3$ under a continuous flow of CCB 4.0, B: peak shift versus concentration of $\text{Ce}(\text{NO}_3)_3$ under a continuous flow of CCB 4.0, C: peak suppression versus concentration of $\text{Ce}(\text{NO}_3)_3$ under a continuous flow of CCB 5.0, D: peak shift versus concentration of $\text{Ce}(\text{NO}_3)_3$ under a continuous flow of CCB 5.0, E: peak suppression versus concentration of $\text{Ce}(\text{NO}_3)_3$ under a continuous flow of CCB 6.0, and F: peak shift versus concentration of $\text{Ce}(\text{NO}_3)_3$ under a continuous flow of CCB 6.0.

7.4.1.3 $\text{Ce}(\text{NO}_3)_3$ in PBS (pH7.4)

Figure 7. 50 displays how the peaks of the voltammogram vary when different concentrations of $\text{Ce}(\text{NO}_3)_3$ were introduced into the ESD under a continuous flow of PBS and with DOPC as the primary phospholipid. The LOD of $\text{Ce}(\text{NO}_3)_3$ under these conditions was found to be 0.01M.

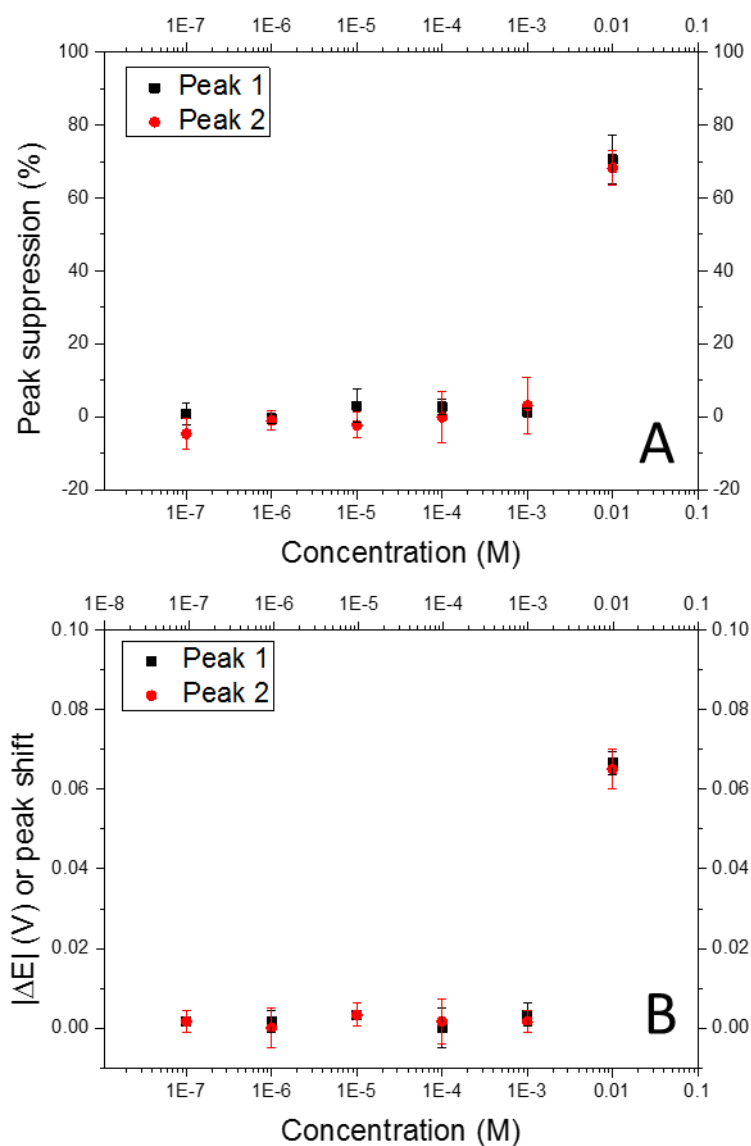


Figure 7. 50: Behaviour of the Peak 1 (black dots) and Peak 2 (red dots) of the voltammograms obtained from the ESD when a varying concentration of $\text{Ce}(\text{NO}_3)_3$ in PBS (pH 7.4) interact with DOPC under a continuous flow of CCB 3.0. A: Graph showing the suppression, in percentage (%), of the peaks. B: Graph showing the shift (V), in potential, of the peaks.

Figure 7. 51 previously observed in Figure 7. 1 shows the behaviour of Ce^{3+} in PBS on the phospholipid monolayer in contact with DOPC.

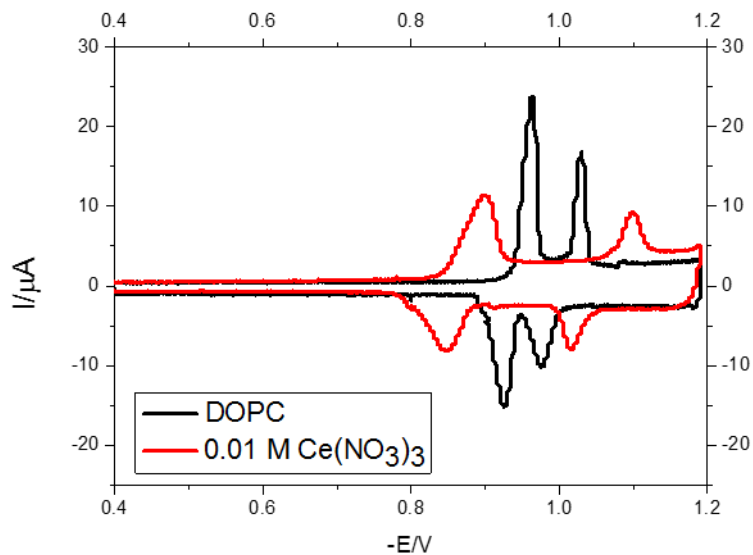


Figure 7. 51: RCV voltammogram recorded at 40Vs^{-1} potential excursion from -0.4V to -1.20V of DOPC (black lines) under a continuous flow of PBS in the presence of (red line) $0.01\text{M Ce}(\text{NO}_3)_3$.

7.4.1.4 Summary and discussion

In summary, it can be concluded that:

-The medium affects the interaction of $\text{Ce}(\text{NO}_3)_3$ with DOPC:

- Ce^{3+} in contact with DOPC under a continuous flow of PBS produces a similar effect to the one previously observed with Ce^{3+} and DOPC under a continuous flow of GLY 3.0. In addition, the RCV response is more sensitive for the CeO_2 NPs dispersions in GLY 3.0 than in PBS.
- Ce^{3+} in contact with DOPC under a continuous flow of GLY 3.0 produces a characteristic separation of the current peaks and a suppression of the current peaks which varies with concentration.
- Ce^{3+} in contact with DOPC under a continuous flow of CCB 3.0 produces a suppression and shift of the peaks, which is more noticeable in the second peak.
- Ce^{3+} in contact with DOPC under a continuous flow of CCB 4.0, CCB 5.0 or CCB 6.0 do not produce any variation in the voltammograms.

As observed in this section (7.4.1), media affect the interaction of Ce^{3+} in solution with the DOPC monolayer. Cerium forms complexes with the different buffers that hamper or promote its interaction with the phospholipid monolayer. The formation of these complexes generates a different response on the ESD when DOPC is exposed to $\text{Ce}(\text{NO}_3)_3$.

$\text{Ce}(\text{NO}_3)_3$ only shows an interaction with the DOPC monolayer under a continuous flow of PBS at high concentrations. The characteristic separation of the peaks that Ce^{3+} ions produce in the voltammogram arises from the direct interaction between the phosphate groups of the phospholipid and Ce^{3+} . A shift of the current peaks of the voltammogram implies a change of the dipole moment of the phospholipids. There are many examples in the literature of the synthesis of laboratory-scale CePO_4 using different phosphorus-containing compounds (acids and salts) and cerium salts [176, 177], which is a clear indication of the compatibility between Ce^{3+} and PO_4^{3-} . In addition, it is known

that PO_4^{3-} can coat the CeO_2 NP surface by directly interacting with Ce^{3+} [113], which could hamper the interaction of the NPs with the phospholipid monolayer. The interaction between $\text{Ce}(\text{NO}_3)_3$ and DOPC in PBS is produced an excess of Ce^{3+} ions (aq) in solution.

Ce^{3+} in GLY 3.0 in contact with DOPC generates a similar response to the one observed for Ce^{3+} in PBS. A suppression and shift of the peaks to more positive and negative potentials. This effect in the voltammogram has been related to the direct interaction Ce^{3+} - PO_4^{3-} and for this reason, it is concluded $\text{Ce}(\text{NO}_3)_3$ in GLY acts in the same manner once in contact with DOPC under these conditions.

$\text{Ce}(\text{NO}_3)_3$ shows different behaviour when in contact with the DOPC monolayer depending on the pH of the used buffer. In this way, $\text{Ce}(\text{NO}_3)_3$ in CCB 3.0 interacts with the phospholipid monolayer while in CCB 4.0, CCB 5.0 and CCB 6.0 $\text{Ce}(\text{NO}_3)_3$ does not show any interaction.

According to [178] the pK_a values of citric acid are 3.1, 4.7 and 6.4. At pHs close to the pK_a value (CCB 3.0) there is about the same concentration of the acid ($[\text{H}_3\text{A}]$) and its conjugate base ($[\text{H}_2\text{A}^-]$). Nevertheless, at pH 4, the equilibrium moves towards the formation of H_2A^- , which could form complexes with Ce^{3+} . At pH 3.0, even there would be a noticeable concentration of the H_2A^- , there would be still enough Ce^{3+} in solution to interact with the phospholipid monolayer. At higher pHs, 5.0 and 6.0, the formation of HA^{2-} and A^{3-} is favoured. In these cases, citrate would act as a moderator of the interaction.

7.4.2 Evaluating the presence of Ce(III) in solution. ICP-MS results

The amount of dissolved cerium from CeO₂ NPs spheres in GLY 3.0, CCB 3.0, CCB 4.0, CCB 5.0, CCB 6.0 and PBS 7.4 and CeO₂ NPs cubes in GLY 3.0, CCB 3.0, CCB 4.0, CCB 5.0, CCB 6.0 and PBS 7.4 was analysed using ICP-MS. Here, the correct amount of CeO₂ NPs (spheres and cubes) to create 0.01M NPs dispersions were weighed and sonicated in the desired buffer for 30min (GLY 3.0, CCB 3.0, CCB 4.0, CCB 5.0, CCB 6.0 and PBS 7.4). The NPs were then centrifuged for 30min at 16.873G and the supernatant separated from the NPs. This supernatant was then passed through a Vivacon ultrafiltration spin column equipped with a Hydrosart cellulose membrane of 2 kDa molecular weight cut-off (nominally a 1.5nm pore size) in order to eliminate any remaining undissolved NPs in suspension. This centrifugation-ultrafiltration procedure was employed to reduce the amount of NPs in suspension [179], which could give false-positive results in ICP-MS. Finally, following a dilution of 100 times (0.1mL of the supernatant were diluted in 10mL of the desired buffer), the concentration of cerium ($\mu\text{g L}^{-1}$) in the supernatant was measured using ICP-MS in Full Quant. mode to identify the amount of dissolved cerium from the ceria NPs. A cerium ICP-MS standard (cerium elemental in 2% HNO₃ (1000 $\mu\text{g/mL}$) from SPEX CertiPrep) was used to create calibration curves for each of the different media.

Table 7. 2: Table showing data obtained from ICP-MS experiments

SAMPLE	MEDIUM	pH	Ce _{dissolved} (%)	[Ce] _{dissolved} (mol· L ⁻¹)
SPHERES	GLY	3.0	0.03	3E-06
		3.0	0.27	3E-05
	CCB	4.0	0.06	6E-06
		5.0	0.17	2E-05
		6.0	0.09	9E-06
	PBS	7.4	0.01	1E-06
	CUBES	GLY	3.0	0.03
3.0			0.05	5E-06
CCB		4.0	0.11	1E-05
		5.0	0.04	4E-06
		6.0	0.06	6E-06
PBS		7.4	0.02	2E-06

Table 7. 1 shows the data obtained from the ICP-MS experiments and the amount of cerium (mol/L) which is obtained from a sample containing 0.01M of CeO₂ NPs.

Figure 7. 52 shows two graphs which correspond to the average percentage of dissolved cerium in different buffers produced by the different NPs. As observed, in both cases, the amount of dissolved cerium was found to be smaller than 0.27%. In general, the spheres dissolve slightly more than the cubes. In addition, for spheres, the higher concentration of cerium in solution was found in CCB 3.0, CCB 5.0 and CCB 6.0. However, all these values are relatively small. Despite the nano-spheres being bigger (4.28nm) than the pore size of the cellulose membrane (1.5nm). The real size of the CeO₂ NPs (spheres) ranges between 1nm to 10nm. A little fraction of the NPs in dispersion could pass through the cellulose membrane producing a false-positive ICP-MS result for the nano-spheres, which explains the bigger errors produced in ICP-MS. In addition, in all cases, the amount of ionic Ce from ICP-MS results are within the error of one another measurement so the dissolution of the CeO₂ NPs, if produced, could be considered trace.

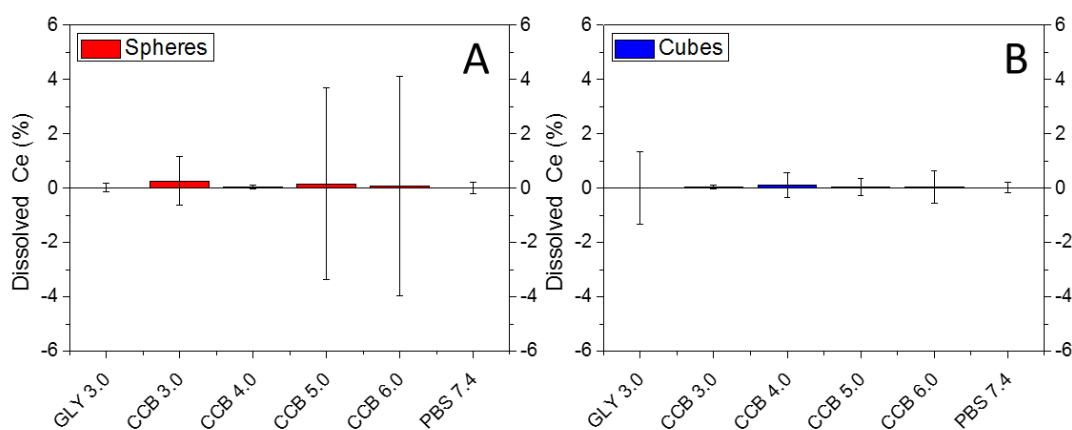


Figure 7. 52: Average percentage of dissolved cerium from dispersions of the metal in different matrixes (GLY 3.0, CCB 3.0, CCB 4.0, CCB 5.0, CCB 6.0, PBS 7.4) of: CeO₂ NPs (spheres) and B: CeO₂ NPs (cubes)

Both CeO₂ NPs spheres and cubes produce an interaction with DOPC under a continuous flow of GLY 3.0 and CCB 3.0. Figure 7. 53 A and B show the variation of the current peaks with time for different concentrations of Ce(NO₃)₃ in GLY 3.0 and CCB 3.0, respectively. The blue and orange lines represent the average

amount of dissolved cerium and their associated error produced when 0.01M of CeO₂ NPs (spheres and cubes) are dispersed in GLY 3.0 or CCB 3.0 buffers. As observed, in both cases, the average amount of dissolved cerium is below the LOD of Ce(NO₃)₃ in the ESD under their respective conditions. Nevertheless, taking into account the uncertainty of the measurement, the concentration of dissolved cerium could be above the LOD of Ce(NO₃)₃ for the cubes in GLY 3.0 (Figure 7. 53A, Blue line) or really close to it for the spheres in GLY 3.0 and CCB 3.0 (Figure 7. 53A and B, orange lines). However, the cubes in GLY, show an uncertainty far from the LOD (Figure 7. 53B, blue line). Considering the results, the evidence suggests that the Ce³⁺ is mainly on the NPs surface.

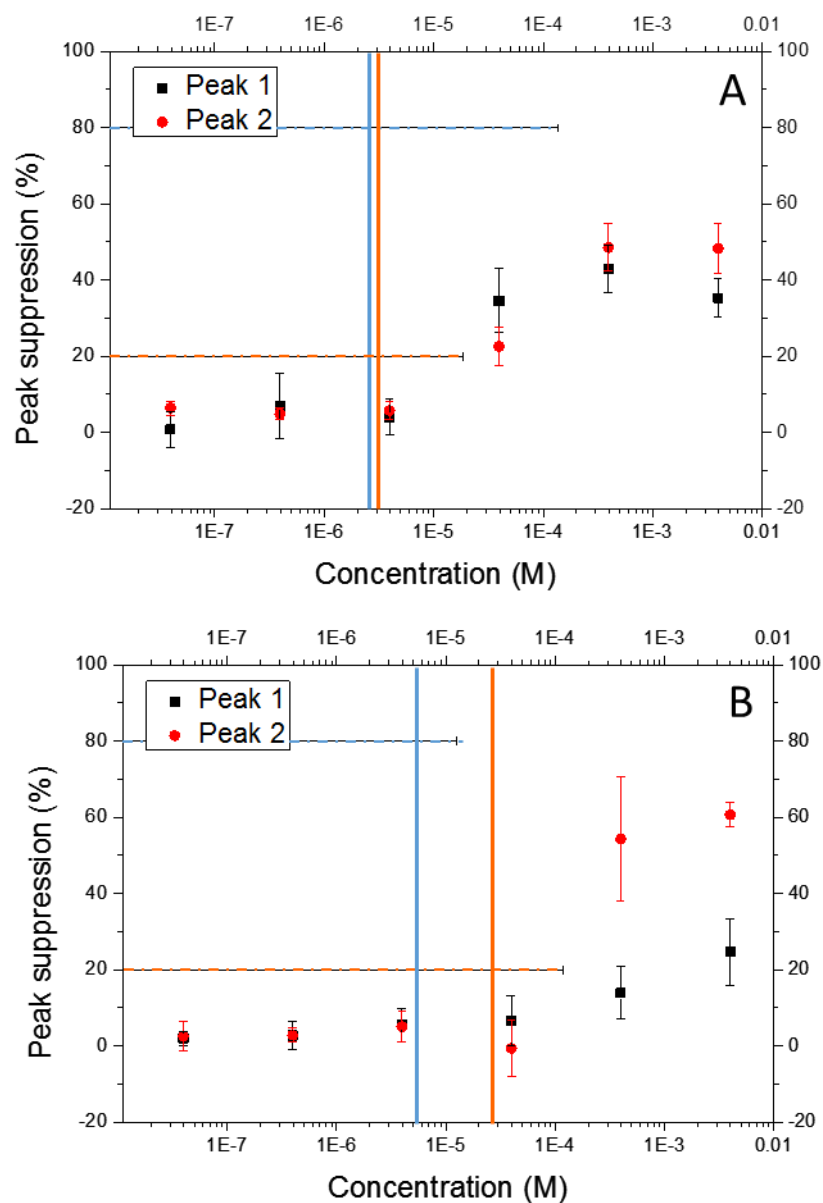


Figure 7. 53: **A:** Suppression of the peak 1 (black dots) and peak 2 (red dots) of the voltammogram when different concentrations of $Ce(NO_3)_3$ (M) interact with DOPC under a constant flow of GLY 3.0. Orange lines: average cerium in solution from ICP-MS experiments (continuous line) and its associated error (dashed line) produced from 0.01M of CeO_2 NPs (spheres). Blue lines: average cerium in solution from ICP-MS experiments (continuous line) and its associated error (dashed line) produced from 0.01M of CeO_2 NPs (Cubes). **B:** Suppression of the peak 1 (black dots) and peak 2 (red dots) of the voltammogram when different concentrations of $Ce(NO_3)_3$ (M) interact with DOPC under a constant flow of CCB 3.0. Orange lines: average cerium in solution from ICP-MS experiments (continuous line) and its associated error (dashed line) produced from 0.01M of CeO_2 NPs (spheres). Blue lines: average cerium in solution from ICP-MS experiments (continuous line) and its associated error (dashed line) produced from 0.01M of CeO_2 NPs (Cubes).

7.4.3 Evaluating the presence of Ce(III) in the particle surface.

EELS results

The analyses of the surface chemical composition of the samples were made using electron energy loss spectroscopy (EELS) [105]. This technique allows to distinguish in between the oxidations states of an element [180, 181]. The peaks of the spectra are related with the 4f self-electron occupancy and they correspond to the spin-orbit splitting of $3d_{3/2} \rightarrow 4f_{5/2}$ (M₄) and $3d_{5/2} \rightarrow 4f_{7/2}$ (M₅) [182, 183].

EELS spectra were obtained using an FEI Titan Themis 300 equipped with a Gatan Quantum ER energy filter and Gatan OneView 4K CMOS digital camera. The M₄/M₅ edges were recorded in an area of the sample. The Ce³⁺ and Ce⁴⁺ ratio on the particle surface was calculated by comparing the area under the peaks of the spectra of the reference materials with the sample. Commercial cerium (IV) oxide nanoparticles and cerium (III) phosphate were used as reference materials for the studies. Due to their small size, it is not necessary special sample preparation. A drop of the sample (in CCB 3.0, GLY 3.0 or PBS) was cast over a holey carbon film-cooper grid, 300 mesh (Agar Scientific) and was let to dry.

In this way, CeO₂ NPs (spheres) were dispersed in GLY 3.0, CCB 3.0 and PBS 7.4. EELS spectra, from different five areas, were taken to study the Ce³⁺/Ce⁴⁺ ratio in different media. The Ce³⁺/Ce⁴⁺ ratio was found to be 0.03 ± 0.02 in PBS, 0.02 ± 0.01 in CCB 3.0 and 0.11 ± 0.08 in GLY 3.0. Spheres in PBS and CCB 3.0 do not have Ce³⁺ on their surface. However, spheres in GLY 3.0 present a relevant amount of Ce³⁺ on the NPs surface. Nevertheless, the uncertainty for the value is big. Figure 7. 54 displays the EELS spectra of the spheres in different media. Black and red lines of the graphs correspond to the reference materials. Ce (III) and Ce (IV) respectably. Figure 7. 54 A shows the EELS spectra of the spheres in PBS and CCB 3.0. As it can be observed, their peaks correspond to the characteristic peaks for Ce(IV). The EELS spectra of the spheres in GLY 3.0

can be observed in Figure 7. 54B. A slight shift to the left, indicative of the presence of Ce^{3+} is produced.

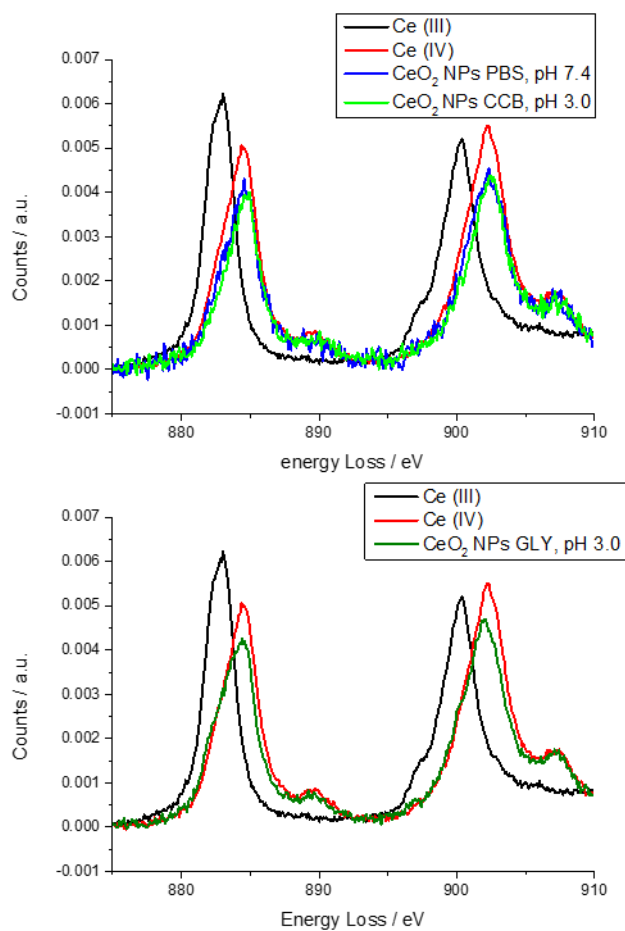


Figure 7. 54: EELS spectra of: Black line: Ce(IV) reference material, red line: Ce(III) reference material, blue line: spheres in PBS (pH 7.4), light green line: spheres in CCB at pH 3.0, dark green line: spheres in glycine pH 3.0

7.5 The effect of coating in the interaction of CeO₂ NPs with model membranes

To study the effect of an NP coating on CeO₂ NP interactions with the DOPC monolayer, the NPs were coated with different substances, and the interaction with DOPC analysed using the ESD. PBS was used as a buffer for the experiments because earlier, it had been proven that CeO₂ NPs do not interact with the phospholipid monolayer under these conditions. The NPs were separated from the coating agent in solution before testing the NPs in the ESD. In this way, the RCV response is produced by the coatings agent on the NPs surface. To eliminate the coating agent from dispersion, centrifugation was used. The NPs were centrifuged and re-dispersed in milli-Q water. At each step of the cleaning process, the remaining supernatant was tested in the ESD to control de amount of coating agent in dispersion.

The NPs were centrifuged for 30min and then the particles were separated from the supernatant, which was tested with the ESD. Later, the nanoparticles were redispersed in milli-Q water and the process was repeated again until the supernatant did not show an interaction in the ESD. The supernatant obtained directly from the synthesis of the NPs were called supernatant 0, the supernatant obtained after the second centrifugation was called 'supernatant 1' and so on. Once the supernatant did not show any interaction with the DOPC monolayer, the NPs dispersion was then tested.

7.5.1 PVP-coated NPs

40-PVP was used to coat the CeO₂ NPs dispersions. The synthesis method and characterisation of the NPs can be found in 3.2.2.4.1 and 4.3.1, respectively.

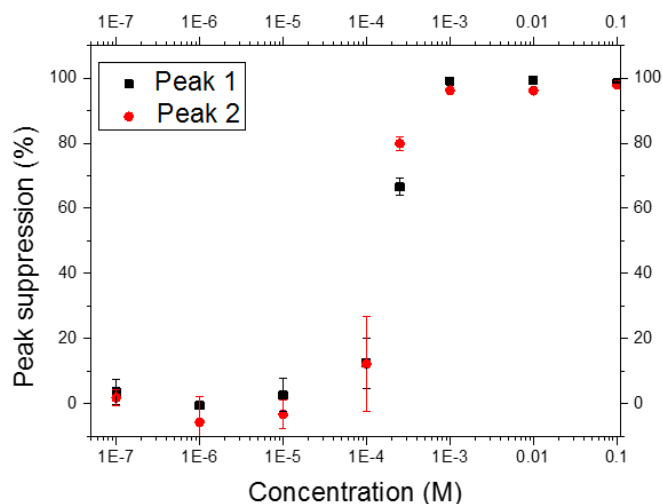


Figure 7. 55: Average suppression of the peak 1 (black dots) and peak 2 (red dots) versus concentration of 40-PVP of the voltammograms produced when DOPC interacts with 40-PVP

Figure 7. 55 shows the average suppression of the RCV current peaks versus concentration of 40-PVP produced when 40-PVP interacts with the DOPC monolayer. The LOD for 40-PVP was found to be $1 \cdot 10^{-4}$ M. The interaction that $2.5 \cdot 10^{-4}$ M and $1 \cdot 10^{-3}$ M of 40-PVP produce on the monolayer of DOPC is shown in Figure 7. 56.

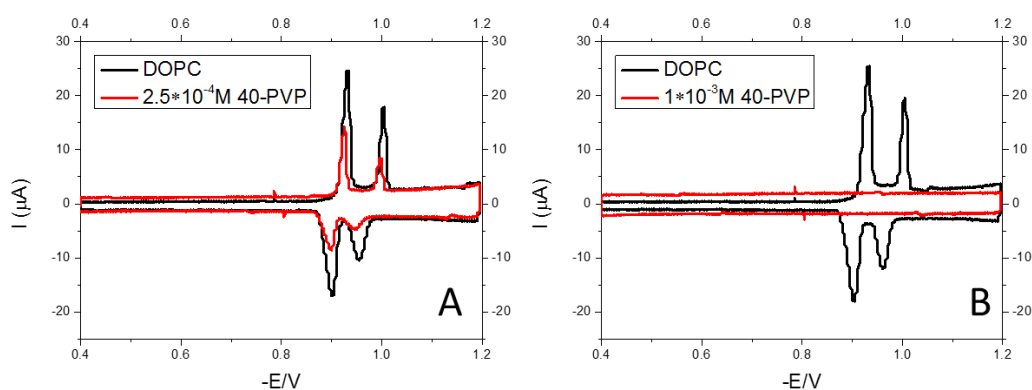


Figure 7. 56: RCV voltammograms recorded at 40Vs^{-1} at a cycling potential that ranges from -0.4V to -1.20V of DOPC (black lines) under a continuous flow of PBS in the presence of (red lines): A: $2.5 \cdot 10^{-4}\text{M}$ 40-PVP and B: $1 \cdot 10^{-3}\text{M}$

The characteristic RCV profile of PVP can be observed in Figure 7. 56A. It produces a suppression of both peaks, slightly more significant in the second peak than the first one, which varies with concentration. High concentrations of 40-PVP produce the total disruption of the phospholipid monolayer (Figure 7. 56B). The speed of the disruption of the phospholipid monolayer depends on concentration.

Figure 7. 57 displays the RCV profiles obtained when the supernatants from the synthesis of 40-PVP CeO₂ NPs were tested. As observed, the supernatant 2 (after three washing steps) produces a total disruption of the monolayer while the supernatant 3 (after 4 washing steps) does not. This behaviour indicates that there is no more free PVP in solution after four washing steps.

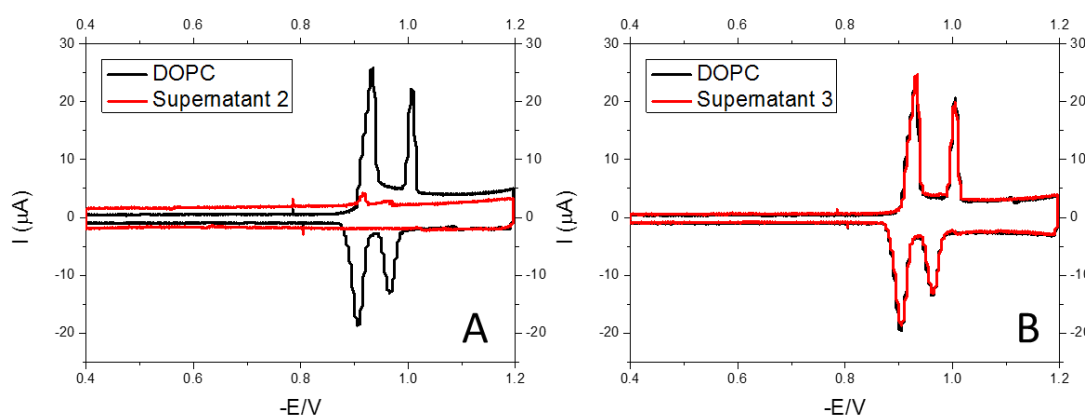


Figure 7. 57: RCV voltammograms recorded at 40Vs^{-1} at a cycling potential that ranges from -0.4V to -1.20V of DOPC (black lines) under a continuous flow of PBS in the presence of (red lines): A: Supernatant 2 and B: supernatant 3.

Subsequently, the NP sample following three washing steps was sonicated again and tested against DOPC using the ESD. Figure 7. 58 shows the interaction is similar to the one previously seen for PVP (Figure 7. 56). It is important to remember that CeO₂ NPs in PBS do not interact with DOPC and hence it can be concluded that PVP on the particle surface is the cause of the interaction with DOPC.

Next, the sample where supernatant 3 came from was sonicated again and tested against DOPC using the ESD. Figure 7. 58 shows the interaction the

sample showed in the ESD. As observed, the interaction is similar to the one previously seen for PVP (Figure 7. 56A). It is important to remember that CeO₂ NPs do not interact with DOPC in PBS. For this reason, it can be concluded that PVP on the particle surface is the cause of the interaction.

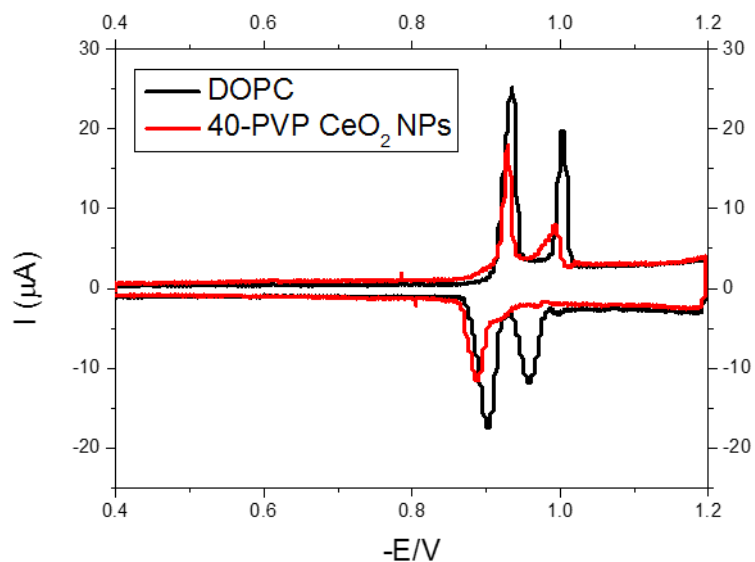


Figure 7. 58: RCV voltammogram recorded at 40Vs^{-1} at a cycling potential that ranges from -0.4V to -1.20V of DOPC (black line) under a continuous flow of PBS in the presence of (red line) 40 PVP CeO₂ NPs

7.5.2 PEG-coated NPs

PEG-CeO₂ coated NPs were synthesised following the procedure described in 3.2.2.4.3. Then, the NPs were characterised (4.3.2), and the sample was found to be formed by little spheres with around 3.67nm in size.

The experiment was carried out following the same procedure than described above. In this way, the supernatant from the cleaning process was tested in the ESD first showing no interaction. Figure 7. 60 A display the RCV profile obtained when the supernatant from the synthesis is tested in the ESD. An in-depth experiment looking at the interaction of PEG with the DOPC monolayer showed no interaction no matter the concentration (Figure 7. 60B).

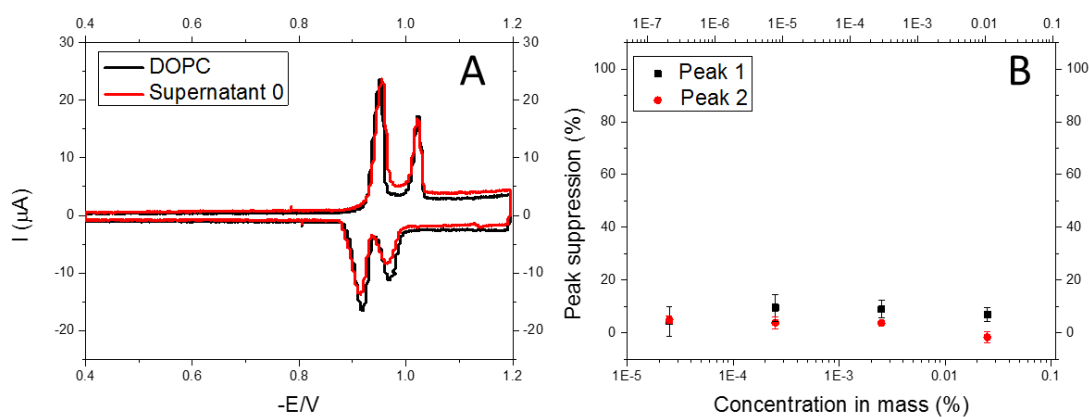


Figure 7. 60: RCV voltammograms recorded at 40Vs^{-1} at a cycling potential that ranges from -0.4V to -1.20V of DOPC (black line) under a continuous flow of PBS in the presence of the supernatant 0 from the synthesis of PEG-coated CeO₂ NPs. B: Graph showing peak suppression versus concentration of PEG.

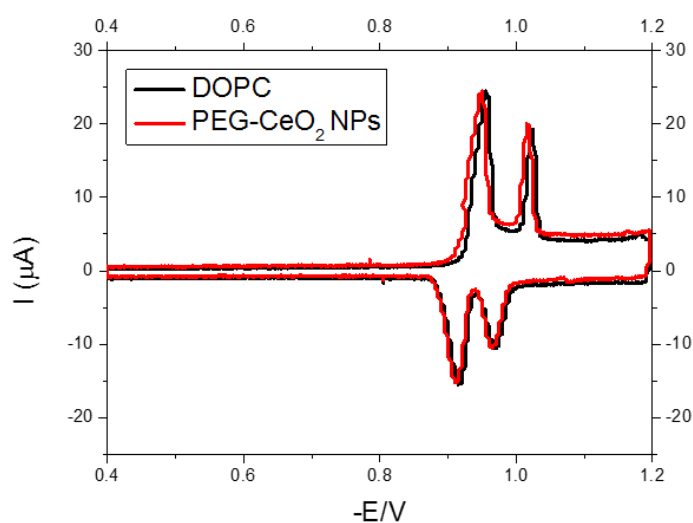



Figure 7. 59: RCV voltammograms recorded at 40Vs^{-1} at a cycling potential that ranges from -0.4V to -1.20V of DOPC (black line) under a continuous flow of PBS in the presence of PEG-CeO₂ NPs



Finally, DOPC was exposed to PEG-CeO₂ NPs and the generated voltammogram is displayed in Figure 7. 59. As observed, there is no interaction of the coated NPs with the phospholipid monolayer.

7.5.3 Dextran-coated NPs

The following figure shows the interaction dextran produces on a DOPC monolayer under a continuous flow of PBS (Figure 7. 61 A) and the effect concentration has on the interaction of dextran with the monolayer (Figure 7. 61B). As observed, dextran only produces an interaction with the DOPC monolayer at high concentrations. The LOD of dextran in the ESD is 1.6%.

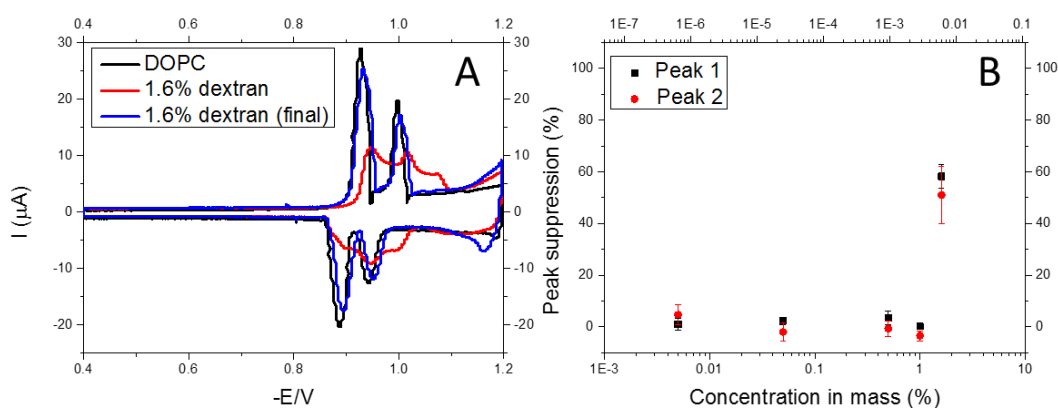


Figure 7. 61: RCV voltammograms recorded at 40Vs^{-1} at a cycling potential that ranges from -0.4V to -1.20V of DOPC (black line) under a continuous flow of PBS in the presence of 1.6% dextran at 5s (red line) and 1.6% dextran at 1.5min. B: Graph showing peak suppression versus concentration of dextran.

Following the same procedure previously described in this chapter, the supernatant from the synthesis of dextran-coated CeO_2 NPs were tested against DOPC using the ESD. Figure 7. 62A shows the interaction of the first supernatant and the DOPC monolayer under a continuous flow of PBS. As observed, there is nor suppression nor shift of the peaks, which indicates there is no free dextran in solution. The pellet from the synthesis was redispersed and tested in the ESD. Dextran coated CeO_2 NPs were found to produce an interaction which can be observed in Figure 7. 62B. The behaviour of the voltammogram at negative potentials is similar to the previously observed in Figure 7. 61A, which indicates dextran on the particle surface is causing the interaction.

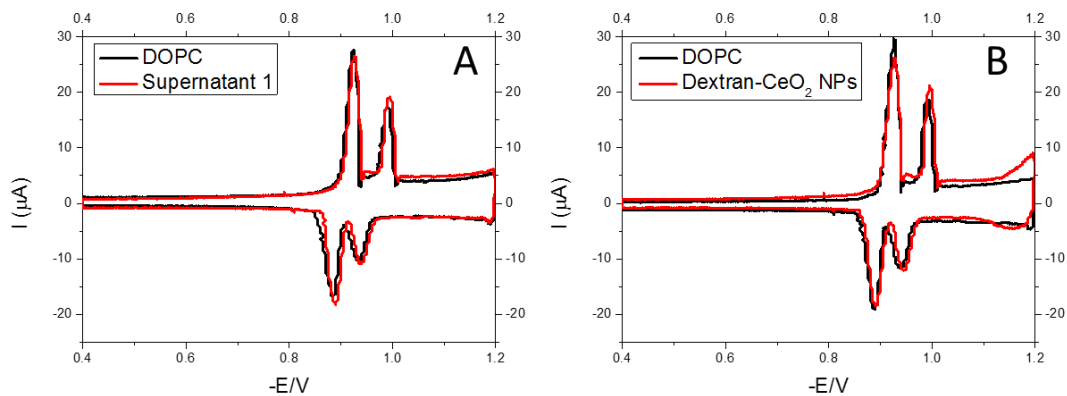


Figure 7.62: A: RCV voltammograms recorded at 40Vs^{-1} at a cycling potential that ranges from -0.4V to -1.20V of DOPC (black lines) under a continuous flow of PBS in the presence of (red lines): A: the supernatant 1 and B: dextran- CeO_2 NPs.

7.5.4 PBS-coated NPs in acidic pH.

Phosphate groups are known for interacting relatively easy with Ce^{3+} . For this reason, PBS in contact with CeO_2 NPs could be coating the NPs once they were introduced into the system. In order to study the effect of the PBS coating on the interaction of the CeO_2 NPs in the ESD, two CeO_2 NPs types (cubes and rods) were deliberately coated with PBS. The procedure followed to coat the NPs is described in section 3.2.2.4.4.

Dispersions containing 0.01M CeO_2 NPs in PBS (PBS- CeO_2 NPs) were centrifuged to separate the particulate material from the supernatant to eliminate the free PBS. Then the NPs were redispersed in GLY 3.0 and CCB 3.0. (maintaining a concentration of 0.01M). Finally, DOPC was exposed to the PBS- CeO_2 NPs in GLY 3.0 and CCB 3.0, with a continuous flow of GLY 3.0 and CCB 3.0, respectively.

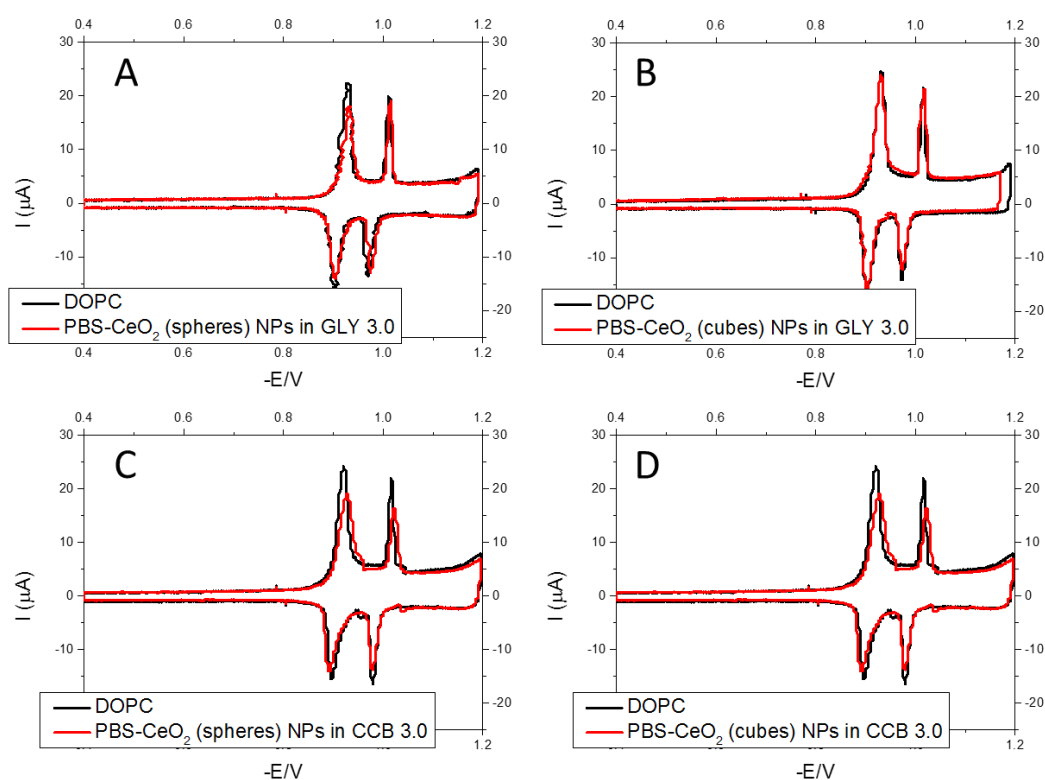



Figure 7.63: RCV voltammograms recorded at 40V s^{-1} at a cycling potential that ranges from -0.4V to -1.20V of DOPC (black line) in the presence of (red line): A: PBS- CeO_2 (spheres) in GLY 3.0, B: PBS- CeO_2 (cubes) in GLY 3.0, C: PBS- CeO_2 (spheres) in CCB 3.0 and D: PBS- CeO_2 (cubes) in CCB 3.0.



As previously observed in Figure 7. 15 and Figure 7. 17, CeO₂ NPs in GLY 3.0 and CCB 3.0 produced an interaction with the DOPC monolayer. However, under the same conditions, PBS-CeO₂ NPs did not show a significant interaction with the monolayer. These findings suggest that PBS can coat the NPs and hamper their interaction by probably preventing the NPs to dissolve or blocking the Ce³⁺ of the particle surface.

7.5.5 Summary and discussion

Table 7. 3: Summary of the findings of 8.5. Table showing 'YES or NO' interaction of coated-CeO₂ NPs and free coating agents with a monolayer of DOPC.

Coated-CeO ₂ NPs	40-PVP CeO ₂ NPs	PEG-CeO ₂ NPs	Dextran-CeO ₂ NPs	PBS-CeO ₂ NPs
Interaction with DOPC	YES	NO	YES	NO
Coating agents	40-PVP	PEG	Dextran	PBS
Interaction with DOPC	YES	NO	YES	NO

Amongst other factors, NP membrane activity is closely related to particle size and surface characteristics. Due to the small size of NPs, they have a big surface area to volume ratio and, for this reason, the surface of the NPs plays a key role in how the particle interacts with the membrane. In this section, it is demonstrated that the surface plays a critical role in the interaction of the NP with the DOPC monolayer.

Table 7. 1 shows a summary of the findings of section 7.5. Free PVP and dextran showed an interaction with the DOPC monolayer while PEG and PBS did not. Likewise, PVP- and dextran-coated NPs showed an interaction while PEG- and PBS-coated NPs did not show an interaction.

In this way it can be concluded that a coating affects the NP activity as it modifies the surface of the particle. Un-coated CeO₂ NPs did not show any interaction with DOPC under a continuous flow of PBS, because PBS coats the surface of the NPs. However, PVP-CeO₂ NPs and dextran-CeO₂ NPs interacted with the DOPC monolayer under the same conditions as PBS-CeO₂ NPs and showed an interaction similar to PVP and dextran, respectively. Hence it is not primarily the effect of the NP, but the effect of the coating agent that appears in the voltammogram. If the coating agent interacts with the DOPC monolayer, the coated NP will probably interact with the DOPC monolayer as well.

7.6 Conclusions of Chapter 7

In summary, it can be concluded that:

Table 7. 4: Table showing the type of interaction and its cause when CeO₂ NPs interact with different phospholipids under a continuous flow of PBS

MATRIX	SAMPLE	PHOSPHOLIPID	TYPE OF INTERACTION	CAUSE OF THE INTERACTION
SPHERES		DOPE	No effect	<ul style="list-style-type: none"> • Ce⁴⁺ on the particle surface do not produce an interaction with the phospholipids monolayers
		DOPG		
		DOPC		
		DOPA		
CUBES		DOPE	N/A	<ul style="list-style-type: none"> • PBS coats the NPs surface and prevents the interaction between the NPs and the phospholipid monolayers
		DOPG	No effect	
		DOPC		
		DOPA		
PBS		DOPE	No effect	
		DOPG		
		DOPC		
DOTS		DOPA	Semiconductor effect	<ul style="list-style-type: none"> • CeO₂ NPs pass through the monolayer and interact with the Hg/Pt electrode • Highly dispersed sample • Citrate could promote the interaction with DOPA • Other synthesis products could promote the interaction with DOPA

- **CeO₂ NPs (dots) show selectivity towards DOPA.** They only interact with DOPA under a continuous flow of PBS. DOPA, contrary to other lipids, has a small polar head group which could facilitate the penetration of a highly dispersed CeO₂ sample through the DOPA. DOPA has a hydroxyl group which facilitates the interaction due to steric factors. In addition, the CeO₂ dots are probably coated with citrate and have a pH of 8.0. Citrate can increase the colloidal stability of the NPs and enhance their interaction with DOPA.

- The semiconductor effect causes the observed interaction. In this case, the NPs are penetrating through the membrane and interacting directly with the Hg/Pt electrode.

Table 7. 5: Table showing the effect and the cause of the effect CeO₂ NPs have on the RCV voltammogram when they interact with a DOPC monolayer under different buffers

SAMPLE	MATRIX	EFFECT ON THE RCV VOLTAMMOGRAM	CAUSE OF THE EFFECT
Suppression of the peaks			
SPHERES CUBES	GLY 3.0	Shift of the peaks to more negative and positive potentials	• Ce ³⁺ on the NP surface binds to the phospholipid molar heads
		Semiconductor effect	• CeO ₂ NPs pass through the monolayer and interact with the Hg/Pt electrode
	CCB 3.0	Suppression of the peaks, bigger in intensity in the second peak than in the first one	• Citrate coats the NPs surface and affects the interaction of the CeO ₂ NPs with the monolayer
		Shift of the peak 2 to negative potentials	
		Semiconductor effect	• CeO ₂ NPs pass through the monolayer and interact with the Hg/Pt electrode NPs interacting with the Hg/Pt electrode
	CCB 4.0 CCB 5.0 CCB 6.0	No effect	• Citrate coats the CeO ₂ NPs surface and hampers the NPs to interact with the phospholipid monolayer.
	PBS	No effect	• PBS coats the surface of the CeO ₂ NPs and hampers the NPs to interaction with the phospholipid monolayer.
NEEDLES	GLY 3.0	Suppression of the peaks with the same intensity	• Ce ³⁺ on the NP surface binds to the phospholipid molar heads
		Light shift of both peaks to negative potentials	
	CCB 3.0		• Citrate coats the NPs surface and affects the interaction of the CeO ₂ NPs with the monolayer
	CCB 4.0 CCB 5.0 CCB 6.0	No effect	• Citrate coats the CeO ₂ NPs surface and hampers the NPs interaction with the phospholipid monolayer.
	PBS	No effect	• PBS coats the surface of the CeO ₂ NPs and hampers the NPs interaction with the phospholipid monolayer.

- CeO₂ NPs interact with DOPC in acidic conditions when GLY 3.0 and CCB 3.0 are used as buffers, no matter what the shape or size of the NPs (Table 7. 5).
 - There are two effects which produce the observed interaction of ceria spheres, cubes and needles with the phospholipid

monolayer of DOPC. There is an effect, which is caused by Ce^{3+} from the particle surface, and there is also a semiconductor effect. The NPs interact directly with the Hg/Pt electrode.

- Needles in GLY 3.0 showed a lower effect than the spheres and the cubes under the same conditions. This effect might be related to the size of the NPs. CeO_2 needles are bigger in length than the other NPs, which could hamper the interaction between the phospholipids polar heads and the NPs.

Table 7. 6: Table showing the effect and cause of the effect produced when Ce^{3+} interact with the phospholipid monolayer in different buffers.

Sample	Buffer	TYPE OF INTERACTION	CAUSE OF THE INTERACTION
		Suppression of the peaks	
	GLY 3.0	Shift of the peaks to more negative and positive potentials	• Ce^{3+} binds to the phosphate group of the phospholipid polar heads
		Suppression of the peaks	
$Ce(NO_3)_3$	CCB 3.0	Shift of the peaks to negative potentials, bigger in the second peak than in the first one	• Formation of complexes with citrate
	CCB 4.0		• Formation of complexes with citrate
	CCB 5.0	No effect	
	CCB 6.0		
			Suppression of the peaks
	PBS 7.4	Shift of the peaks to more negative and positive potentials	• Ce^{3+} binds to the phosphate group of the phospholipid polar heads

- **The dispersion media affects the interaction of $Ce(NO_3)_3$ with a model monolayer of DOPC** (Table 7. 6). A different RCV response is obtained when Ce^{3+} from nitrate interacts with DOPC under a continuous flow of GLY (pH 3.0), CCB (pH 3.0, 4.0, 5.0 and 6.0) and PBS. Ionic Ce^{3+} (aq) produces a characteristic spread and suppression of the current peaks of the RCV voltammogram when DOPC is exposed to $Ce(NO_3)_3$ under a continuous flow of GLY 3.0. A different effect is observed when $Ce(NO_3)_3$ interacts with DOPC in CCB 3.0. In addition, this effect is dependant on pH. An interaction is not observed for $Ce(NO_3)_3$ when exposed to DOPC under a continuous flow of CCB 4.0,

CCB 5.0 or CCB 6.0. This evidence suggests that citrate is able to form complexes with Ce^{3+} and modulate the interaction.

- **Ce^{3+} on the particle surface is related to the activity of CeO_2 NPs.** As mentioned before, the effect produced when CeO_2 NPs interact with the DOPC monolayer at acidic pH is produced by the effect of Ce^{3+} . ICP-MS and EELS results indicate the interaction is produced by the Ce^{3+} sites on the CeO_2 NPs surface.
- **Coatings affect NP activity by changing the surface characteristics and changing the way they interact with their surroundings.** If a membrane-active coating agent functionalises an NP, the interaction with the phospholipid monolayer will be produced by the coating agent and not the NP.

The activity of CeO_2 NPs depends on the size and its surface chemistry.

Un-coated CeO_2 NPs, in general, do not strongly interact with the DOPC but they can penetrate the monolayer at acidic pH. However, any compound able to alter or change the chemistry or the surface will change its activity. In addition, a semiconductor effect is observed for the smaller particles (spheres and cubes) at acidic pH while a semiconductor effect was not observed for the needles (bigger in size) under the same conditions. This behaviour could explain why there are so many contradictory reports regarding the activity of CeO_2 NPs.

Figure 7. 64 shows a diagram that summarises the CeO_2 NPs interaction with DOPC in different buffers observed in this thesis. Spheres, cubes and needles CeO_2 NPs in GLY 3.0 remain uncoated and, in contact with DOPC, directly interact with the phosphate group of the phospholipids through Ce^{3+} on the NP surface. Spheres, cubes and needles NPs in citrate are coated by the citrate and the effect observed in the RCV depends on pH (CCB 3.0, CCB 4.0, CCB 5.0 and CCB 6.0) Citrate at pH 3.0 produce a decrease of the second peak in the RCV response, while at higher pH there is no RCV response. Also, a semiconductor effect is observed in spheres and cubes in GLY 3.0 and CCB 3.0. CeO_2 NPs (spheres, cubes and needs) in PBS do not show an interaction when in contact

with DOPC. PBS forms a coating on the CeO₂ NPs surface which hampers the interaction with the DOPC monolayer.

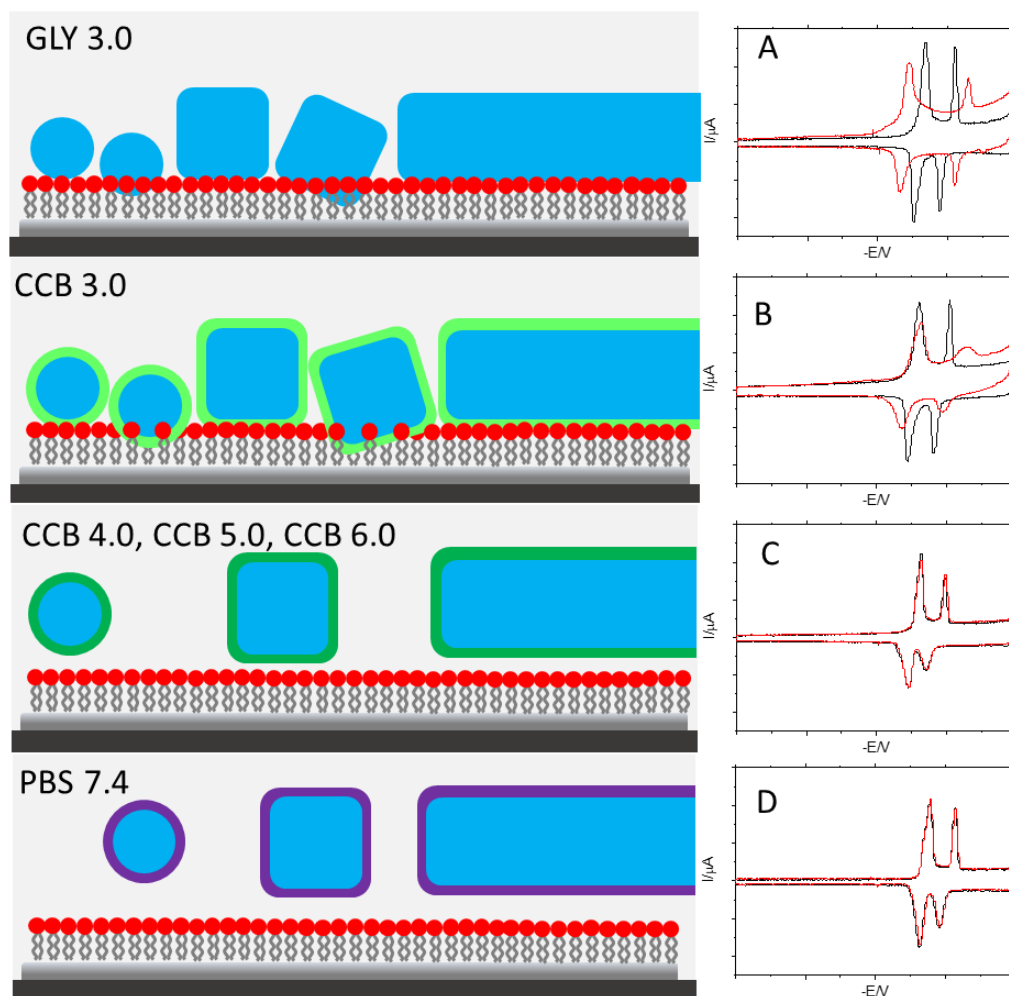


Figure 7. 64: The left image shows how CeO₂ spheres, cubes and needles NPs interact with a DOPC monolayer in the Hg/Pt electrode in different buffers (GLY 3.0, CCB 3.0, CCB 4.0, CCB 5.0, CCB 6.0 and PBS 7.4). The light green colour surrounding the NPs represent a citrate coating in CCB 3.0, the dark green colour surrounding the NPs represent a citrate coating in CCB 4.0, CCB 5.0 and CCB 6.0 and the purple colour surrounding the NPs represent a phosphate coating. The right graphs show the RCV response the CeO₂ NPs generate in different buffers. The black line of the RCV voltammograms indicate the RCV of DOPC. The red line of the RCV voltammograms indicate the interaction with the CeO₂ NPs (spheres, cubes and needles) when in contact with DOPC under a continuous flow of: A: GLY 3.0, B: CCB 3.0, C: CCB 4.0, CCB 5.0 and CCB 6.0, and D: PBS 7.4.

Figure 7. 66 and Figure 7. 65 summarises the interaction observed between coated CeO₂ NPs and a monolayer of DOPC. PVP-CeO₂ NPs and Dextran-CeO₂ NPs produce an interaction with DOPC under a continuous flow of PBS while no interaction is observed for PEG-CeO₂ NPs under the same conditions. Additionally, Figure 7. 65 shows how PBS hamper the interaction of the CeO₂ NPs with DOPC in acidic conditions. Synthesised naked CeO₂ NPs produce an interaction under the same acidic conditions (Figure 7. 64 A and B).

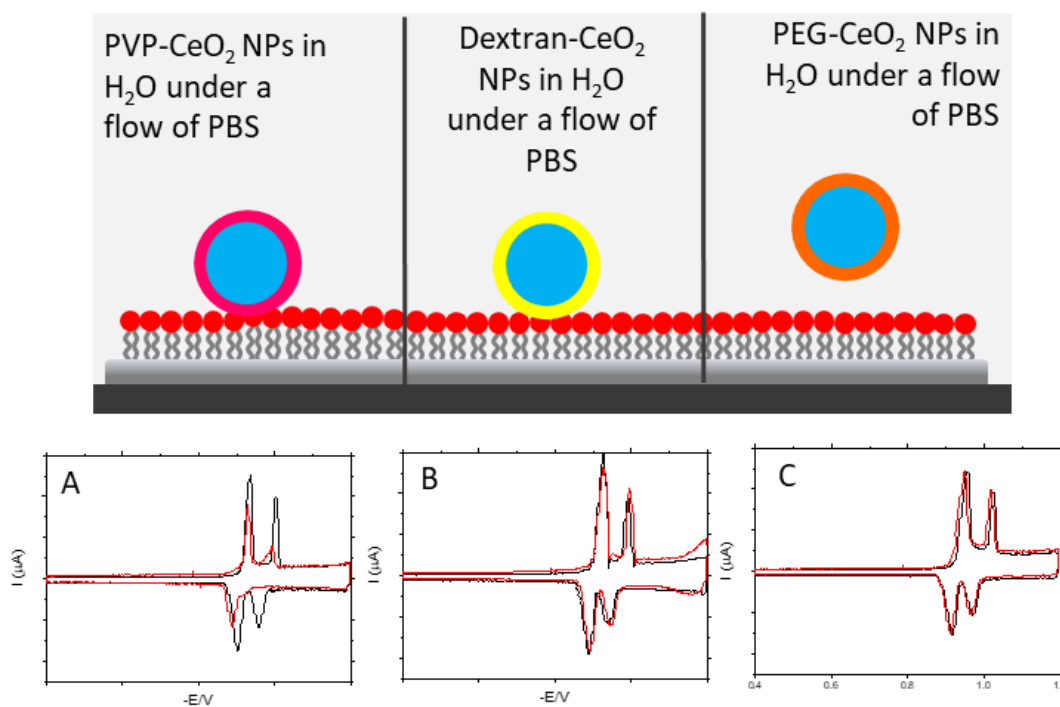


Figure 7.66: The top image shows the interaction of coated CeO_2 NPs (blue spheres) with a monolayer of DOPC under a continuous flow of PBS. The pink colour surrounding the NPs represents the PVP coating. The yellow colour surrounding the NPs represent the dextran coating. The orange colour surrounding the NPs represent the PEG coating. The bottom graphs are the RCV profiles that coated CeO_2 NPs produce when in contact with a DOPC monolayer. The black lines are the RCV profile of the monolayer of DOPC. The red lines are the RCV response which is produced when DOPC interacts with: A: PVP- CeO_2 NPs, B: Dextran- CeO_2 NPs and C: PEG- CeO_2 NPs

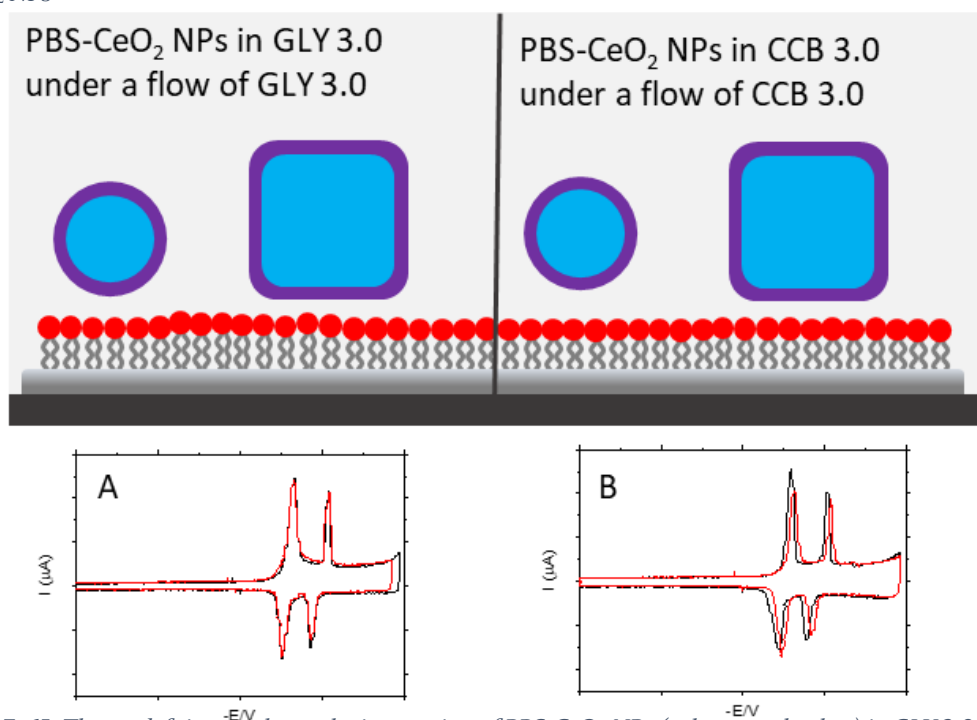


Figure 7.65: The top left image shows the interaction of PBS- CeO_2 NPs (spheres and cubes) in GLY 3.0 with a monolayer of DOPC under a continuous flow of GLY 3.0. The top right image shows the interaction of PBS- CeO_2 NPs (spheres and cubes) in CCB 3.0 with a monolayer of DOPC under a continuous flow of CCB 3.0. The purple colour surrounding the NPs represents the PBS coating the NPs. The bottom graphs are the RCV profiles that coated CeO_2 NPs produce when in contact with a DOPC monolayer. The black lines are the RCV profile of the monolayer of DOPC. The red lines are the RCV response which is produced when DOPC interacts with: PBS- CeO_2 NPs (spheres and needles) in: A: GLY 3.0 under a continuous flow of GLY 3.0 and B: CCB 3.0 under a continuous flow of CCB 3.0.

CHAPTER 8. CONCLUSIONS AND FUTURE WORK


The interaction of CeO₂ NPs with phospholipid monolayers is principally governed by the characteristics of the NPs surface and the size. The conditions of the medium, as for example, pH or dispersant can affect the interaction of the NPs with phospholipids. As already mentioned, the formation of oxygen free sites; thus Ce³⁺, is favoured at acidic pH for CeO₂ NPs.

ICP-MS results show there is no significant amount of dissolved CeO₂ NPs in the form of Ce³⁺ ions when dispersed in CCB, GLY and PBS for 30min. In addition, all measurements are within the error of one another and, for this reason, the amount of dissolved cerium could be considered trace (2·10⁻⁵M to 9·10⁻⁶M). However, the dissolution of CeO₂ NPs could be produced in samples dispersed for more extended periods, which could produce an enhancement of the effects observed in the RCVs. However, this would not contribute to the observations in this particular case, although the effect could be analysed in future work. EELS results show there is no significant amount of Ce³⁺ in the CeO₂ NPs (spheres) when dispersed in CCB or PBS. Nevertheless, the amount of Ce³⁺ in the CeO₂ NPs when the NPs were dispersed in GLY was found to be 11% of the total cerium atoms in the NP. For a particle of 3nm in diameter, the approximate amount of cerium atoms on the NP surface was estimated to be 30%. A third of the cerium atoms on the NPs would be Ce³⁺ if the defects were located on the NPs surface. The intensity of the EELS spectrum depends on the volume of the sample. In this case, the sample was very small (4.28nm). In addition, to prevent the formation of Ce³⁺ sites on the NPs surface, the EELS spectra were collected over different areas; thus they were taken using low magnitudes and low dose rates. Under these conditions, it is possible the Ce³⁺ signal, which was produced by the NPs, was not big enough to be detected by the EELS detector. This is the case of the CeO₂ NPs in CCB 3.0 and PBS 3.0. Nevertheless, RCV results show a clear Ce³⁺ response, similar to the interaction between Ce(NO₃)₃ with DOPC in acidic media, when the NPs interact with DOPC under the same conditions. This effect indicates that Ce³⁺ sites were

created in the NP surface from the synthesis, or that the contact of the NPs with the media promoted the creation of Ce^{3+} sites on the NPs surface.

Un-coated CeO_2 NPs (spheres, cubes and needles) interacted with DOPC at acidic pH (CCB 3.0 and GLY 3.0) and showed an interaction proper to Ce^{3+} on the NP surface. The interaction observed when the CeO_2 NPs (spheres and cubes) are dispersed in GLY 3.0 is facilitated by the binding of the Ce^{3+} sites of the NP surface to the phosphate group of the phospholipid layer. The interaction observed when the CeO_2 NPs (spheres and cubes) are dispersed in CCB 3.0 are produced by the effect of citrate. DOPC exposed to the same concentration of $\text{Ce}(\text{NO}_3)_3$ at different pHs gives a different response depending on the pH. While there is an observable reduction of the peaks at pH 3.0, there is no interaction at pH 4.0, 5.0 or 6.0. This effect is produced by the complexation of Ce^{3+} by citrate, which impedes the interaction at solution pH above 3.0. Similar behaviour was observed for the needles in the same buffers. Needles in CCB 3.0 manifest an effect produced by the Ce^{3+} on the particle surface and citrate. Needles in GLY 3.0 showed a reduced effect of the Ce^{3+} in GLY 3.0 (Figure 7. 45C). Needles break with sonication; for this reason, it is impossible to know the real size of the needles when carrying out the RCV screening. Breakage of the needles would create highly reactive fresh surfaces. Nevertheless, the needles are probably much bigger in length than cubes and spheres when they are introduced into the ESD, so their surface area to volume ratio is smaller than for spheres or cubes. In addition, all CeO_2 NPs show a semiconductor effect on the naked Hg/Pt electrode at pH 3.0. However, all NPs but needles showed such an effect when DOPC was deposited on the Hg/Pt electrode. The behaviour of the needles indicates that size and shape is important for NPs to go through the monolayer and interact with the Hg/Pt electrode. The ability of NPs to go through the monolayer increases as size decreases.

Un-coated CeO_2 NPs did not produce any interaction with DOPC, DOPA, DOPG and DOPE under a continuous flow of PBS. In this case, phosphate from the PBS coats the NPs surface preventing the NP interaction with the




phospholipids layer. It was found that DOPC under a flow of PBS only showed an interaction when exposed to $\text{Ce}(\text{NO}_3)_3$ at high concentrations, in other words, to an excess of Ce^{3+} ions. In addition, PBS was found to decrease the interaction of CeO_2 NPs at acidic buffers. PBS-treated CeO_2 NPs in CCB 3.0 and GLY 3.0 did not show an interaction with DOPC when un-coated CeO_2 NPs under the same conditions did. The behaviour of CeO_2 NPs in other neutral pH buffers which do not contain phosphate, as for example HEPES, could be a subject to study in future work. In addition, RCV tests could be done in future work using mixtures of lipids to increase the stability and complexity of the monolayer sensor element in order to better mimic biological conditions.

The effect of coated- CeO_2 NPs produced in DOPC under a continuous flow of PBS showed the interaction was produced by the coating agent rather than the CeO_2 NPs itself. It is important to notice that un-coated CeO_2 NPs under the same conditions did not show an interaction with the phospholipid layer. Membrane active coating agents (PVP or dextran), in other words, substances which interact with the phospholipid monolayer, produced their characteristic interaction when coating the CeO_2 NPs. PEG, which did not produce an interaction with the phospholipid monolayer, did not produce an interaction when coating the CeO_2 NPs. These findings suggest that the behaviour of CeO_2 NPs can be modified by changing the CeO_2 NPs surface chemistry and could explain the disparate reports regarding the activity of CeO_2 NPs and related toxicity. (Table 8. 1) shows a summary of the key findings of different literature reports which studied the effect of coated CeO_2 NPs in various toxicity studies. As observed, there is a good correlation between the results of this work and the literature. PEG and phosphate produced a protective effect, while PVP and dextran produced a damaging effect.

Table 8. 1: A literature review of papers which show the effect coated-CeO₂ NPs have on biological activity

Shape	Size/nm	Coating	Effect	Cause of the effect	Observations	Reference
Spheres	3-5	dextran	Damaging	Growth inhibition + ROS generation		[184]
Spheres	5-12	PVP	Damaging	ROS generation		[185]
Spheres	5	Un-coated	Damaging	Membrane damage		
Spheres	N/A	PO ₄ ²⁻	Protective	Growth stimulation	Catalase activity +ROS reduction	[102]
Spheres	8-10	dextran	Damaging	Antibacterial effect		[186]
Spheres	3-4	PEG	Protective	OS reduction		[187]

Even though this thesis answers many questions regarding the activity of CeO₂ NPs, it also opens the door to questions yet to be explored. The stability of DOPA, DOPS, DOPG, DOPE and DOPC was analysed in this thesis in order to create a guide for their correct deposition. This information can be used in the future to create more complex model membranes composed by mixtures of lipids and proteins. This could help to create a more advance biosensor which could be used in toxicity tests and which would help to better understand the operation of cellular membranes. The formation of Ce³⁺ on the particle surface is a subject that also requires further exploration. Information obtained from the literature and results in this thesis indicates the Ce³⁺/Ce⁴⁺ ratio is related to the environment. In this way, the formation of Ce³⁺ can be promoted by the presence of a high electron beam, high vacuums or acidic pHs. Additionally, [110] showed CeO₂ NPs can undergo changes in the oxidation state while in dispersion in a certain medium. For this reason, the analysis of the Ce³⁺/Ce⁴⁺ ratio should be done with NPs in dispersion. Techniques as Cryo-TEM or



XANES allow distinguishing between the oxidation states of the same element in a liquid dispersion. These experiments could be complemented with dissolution rate experiments in order to understand the dissolution mechanisms behind CeO₂ NPs in different media. Finally, the effect of coating should be explored further. As demonstrated in this thesis, the coating can play a vital role in CeO₂ NPs activity because it changes the NPs surface characteristics. This could affect biodistribution and activity and can explain why there are so many contradictory reports about CeO₂ NPs. Usually, when NPs are synthesised, coatings are used to improve the colloidal stability of the dispersion. Toxicity test evaluates the effect of the NPs but usually neglect the effect of the coating. For this reason, the effect of the coating agent should be taken into account when carrying out a toxicity test. The ESD could be used to study the effect of the NPs and the coating agent. The results could be later compared with toxicity test in cell culture media.

BIBLIOGRAPHY

1. Colombari, P., *The use of metal nanoparticles to produce yellow, red and iridescent colour, from bronze age to present times in lustre pottery and glass: Solid state chemistry, spectroscopy and nanostructure*. Journal of Nano Research, 2009. **8**: p. 109.
2. Sciau, P., E.a., *Double nanoparticle layer in a 12th century lustreware decoration: accident or technological mastery?* Journal of Nano Research, 2009. **8**.
3. Henglein, A., *Photo-Degradation and Fluorescence of Colloidal-Cadmium Sulfide in Aqueous Solution*. Berichte der Bunsengesellschaft für physikalische Chemie, 1982. **86**(4): p. 301-305.
4. Birrenbach, G. and P.P. Speiser, *Polymerized micelles and their use as adjuvants in immunology*. J. Pharm. Sci., 1976. **65**(12): p. 1763-6.
5. W. Lin, Y.H., X. Zhou et al., *Toxicity Of Cerium Oxide Nanoparticles in Human Lung Cancer Cells*. 2006. **25**(6): p. 451-457.
6. Donaldson, K., et al., *Combustion-derived nanoparticles: a review of their toxicology following inhalation exposure*. Part Fibre Toxicol, 2005. **2**: p. 10.
7. Gupta, R. and H. Xie, *Nanoparticles in Daily Life: Applications, Toxicity and Regulations*. J Environ Pathol Toxicol Oncol, 2018. **37**(3): p. 209-230.
8. Calderón-Garcidueñas, L., et al., *Combustion-derived nanoparticles, the neuroenteric system, cervical vagus, hyperphosphorylated alpha synuclein and tau in young Mexico City residents*. Environmental Research, 2017. **159**: p. 186-201.
9. Guerra, F.D., M.F. Attia, and D.C. Whitehead, *Nanotechnology for Environmental Remediation: Materials and Applications*. 2018. **23**(7).
10. Coldrick, Z., et al., *High throughput systems for screening biomembrane interactions on fabricated mercury film electrodes*. Journal of Applied Electrochemistry, 2011. **41**(8): p. 939-949.
11. Owen, J., et al., *High-throughput electrochemical sensing platform for screening nanomaterial–biomembrane interactions*. Review of Scientific Instruments, 2020. **91**(2): p. 025002.
12. Nelson, A., N. Auffret, and J. Borlakoglu, *Interaction of hydrophobic organic compounds with mercury adsorbed dioleoylphosphatidylcholine monolayers*. Biochimica et Biophysica Acta (BBA) - Biomembranes, 1990. **1021**(2): p. 205-216.
13. Tiwari, J.N., R.N. Tiwari, and K.S. Kim, *Zero-dimensional, one-dimensional, two-dimensional and three-dimensional nanostructured materials for advanced electrochemical energy devices*. Progress in Materials Science, 2012. **57**(4): p. 724-803.
14. Buffle, J., et al., *A Generalized Description of Aquatic Colloidal Interactions: The Three-colloidal Component Approach*. Environmental Science & Technology, 1998. **32**(19): p. 2887-2899.

15. McCarthy, J.F. and L.D. McKay, *Colloid Transport in the Subsurface: Past, Present, and Future Challenges*. *Vadose Zone Journal*, 2004. **3**(2): p. 326-337.
16. Griffin, S., et al., *Natural Nanoparticles: A Particular Matter Inspired by Nature*. *Antioxidants* (Basel), 2017. **7**(1).
17. Oliveira, M.L.S., et al., *Nanoparticles from construction wastes: A problem to health and the environment*. *Journal of Cleaner Production*, 2019. **219**: p. 236-243.
18. Bandala, E.R. and M. Berli, *Engineered nanomaterials (ENMs) and their role at the nexus of Food, Energy, and Water*. *Materials Science for Energy Technologies*, 2019. **2**(1): p. 29-40.
19. Koczkur, K.M., et al., *Polyvinylpyrrolidone (PVP) in nanoparticle synthesis*. *Dalton Transactions*, 2015. **44**(41): p. 17883-17905.
20. Pelaz, B., et al., *Surface Functionalization of Nanoparticles with Polyethylene Glycol: Effects on Protein Adsorption and Cellular Uptake*. *ACS Nano*, 2015. **9**(7): p. 6996-7008.
21. Lv, L., et al., *PVP-coated gold nanoparticles for the selective determination of ochratoxin A via quenching fluorescence of the free aptamer*. *Food Chemistry*, 2018. **249**: p. 45-50.
22. Wang, H., et al., *Mechanisms of PVP in the preparation of silver nanoparticles*. *Materials Chemistry and Physics*, 2005. **94**(2): p. 449-453.
23. Sarkar, A., T. Mukherjee, and S. Kapoor, *PVP-Stabilized Copper Nanoparticles: A Reusable Catalyst for "Click" Reaction between Terminal Alkynes and Azides in Nonaqueous Solvents*. *The Journal of Physical Chemistry C*, 2008. **112**(9): p. 3334-3340.
24. Park, S.K., K.D. Kim, and H.T. Kim, *Preparation of silica nanoparticles: determination of the optimal synthesis conditions for small and uniform particles*. *Colloids and Surfaces A: Physicochemical and Engineering Aspects*, 2002. **197**(1): p. 7-17.
25. Veronese, F.M. and A. Mero, *The Impact of PEGylation on Biological Therapies*. *BioDrugs*, 2008. **22**(5): p. 315-329.
26. Suk, J.S., et al., *PEGylation as a strategy for improving nanoparticle-based drug and gene delivery*. *Adv Drug Deliv Rev*, 2016. **99**(Pt A): p. 28-51.
27. Shinohara, S., et al., *The Role of Citric Acid in the Stabilization of Nanoparticles and Colloidal Particles in the Environment: Measurement of Surface Forces between Hafnium Oxide Surfaces in the Presence of Citric Acid*. *Langmuir*, 2018. **34**(8): p. 2595-2605.
28. Ojea-Jiménez, I., et al., *Citrate-Coated Gold Nanoparticles As Smart Scavengers for Mercury(II) Removal from Polluted Waters*. *ACS Nano*, 2012. **6**(3): p. 2253-2260.
29. Bastús, N.G., et al., *Synthesis of Highly Monodisperse Citrate-Stabilized Silver Nanoparticles of up to 200 nm: Kinetic Control and Catalytic Properties*. *Chemistry of Materials*, 2014. **26**(9): p. 2836-2846.
30. Saraswathy, A., et al., *Citrate coated iron oxide nanoparticles with enhanced relaxivity for in vivo magnetic resonance imaging of liver fibrosis*. *Colloids and Surfaces B: Biointerfaces*, 2014. **117**: p. 216-224.

31. Christian, P., et al., *Nanoparticles: structure, properties, preparation and behaviour in environmental media*. Ecotoxicology, 2008. **17**(5): p. 326-343.
32. Loza, K., et al., *The dissolution and biological effects of silver nanoparticles in biological media*. Journal of Materials Chemistry B, 2014. **2**(12): p. 1634-1643.
33. Long, Y.-M., et al., *Surface ligand controls silver ion release of nanosilver and its antibacterial activity against Escherichia coli*. International journal of nanomedicine, 2017. **12**: p. 3193-3206.
34. Sung, J.H., et al., *Lung Function Changes in Sprague-Dawley Rats After Prolonged Inhalation Exposure to Silver Nanoparticles*. Inhalation Toxicology, 2008. **20**(6): p. 567-574.
35. Brill, R.H. and N.D. Cahill, *A RED OPAQUE GLASS FROM SARDIS AND SOME THOUGHTS ON RED OPACUES IN GENERAL*. Journal of Glass Studies, 1988. **30**: p. 16-27.
36. Stark, W.J., et al., *Industrial applications of nanoparticles*. Chemical Society Reviews, 2015. **44**(16): p. 5793-5805.
37. Fan, J., et al., *Dye-sensitized solar cells based on TiO₂ nanoparticles/nanobelts double-layered film with improved photovoltaic performance*. Applied Surface Science, 2014. **319**: p. 75-82.
38. Jia, C.-J. and F. Schüth, *Colloidal metal nanoparticles as a component of designed catalyst*. Physical Chemistry Chemical Physics, 2011. **13**(7): p. 2457-2487.
39. Molnár, Á., A. Sárkány, and M. Varga, *Hydrogenation of carbon-carbon multiple bonds: chemo-, regio- and stereo-selectivity*. Journal of Molecular Catalysis A: Chemical, 2001. **173**(1): p. 185-221.
40. Herzing, A.A., et al., *Identification of Active Gold Nanoclusters on Iron Oxide Supports for CO Oxidation*. Science, 2008. **321**(5894): p. 1331-1335.
41. Li, Y., E. Boone, and M.A. El-Sayed, *Size Effects of PVP-Pd Nanoparticles on the Catalytic Suzuki Reactions in Aqueous Solution*. Langmuir, 2002. **18**(12): p. 4921-4925.
42. Luo, X., et al., *Application of Nanoparticles in Electrochemical Sensors and Biosensors*. Electroanalysis, 2006. **18**(4): p. 319-326.
43. Jia, J., et al., *A Method to Construct a Third-Generation Horseradish Peroxidase Biosensor: Self-Assembling Gold Nanoparticles to Three-Dimensional Sol-Gel Network*. Analytical Chemistry, 2002. **74**(9): p. 2217-2223.
44. Luo, X.-L., et al., *Electrochemically deposited chitosan hydrogel for horseradish peroxidase immobilization through gold nanoparticles self-assembly*. Biosensors and Bioelectronics, 2005. **21**(1): p. 190-196.
45. Crumbliss, A.L., et al., *Colloidal gold as a biocompatible immobilization matrix suitable for the fabrication of enzyme electrodes by electrodeposition*. Biotechnology and Bioengineering, 1992. **40**(4): p. 483-490.
46. Raj, C.R., T. Okajima, and T. Ohsaka, *Gold nanoparticle arrays for the voltammetric sensing of dopamine*. Journal of Electroanalytical Chemistry, 2003. **543**(2): p. 127-133.

47. Wang, L. and E. Wang, *Direct electron transfer between cytochrome c and a gold nanoparticles modified electrode*. *Electrochemistry Communications*, 2004. **6**(1): p. 49-54.
48. Xiao, Y., et al., "*Plugging into Enzymes*": *Nanowiring of Redox Enzymes by a Gold Nanoparticle*. *Science*, 2003. **299**(5614): p. 1877-1881.
49. Dequaire, M., C. Degrand, and B. Limoges, *An Electrochemical Metalloimmunoassay Based on a Colloidal Gold Label*. *Analytical Chemistry*, 2000. **72**(22): p. 5521-5528.
50. Wang, J., G. Liu, and A. Merkoçi, *Electrochemical Coding Technology for Simultaneous Detection of Multiple DNA Targets*. *Journal of the American Chemical Society*, 2003. **125**(11): p. 3214-3215.
51. Patra, J.K., et al., *Nano based drug delivery systems: recent developments and future prospects*. *Journal of Nanobiotechnology*, 2018. **16**(1): p. 71.
52. Zou, L., et al., *Current Approaches of Photothermal Therapy in Treating Cancer Metastasis with Nanotherapeutics*. *Theranostics*, 2016. **6**(6): p. 762-772.
53. Sztandera, K., M. Gorzkiewicz, and B. Klajnert-Maculewicz, *Gold Nanoparticles in Cancer Treatment*. *Molecular Pharmaceutics*, 2019. **16**(1): p. 1-23.
54. Wang, L., C. Hu, and L. Shao, *The antimicrobial activity of nanoparticles: present situation and prospects for the future*. *Int J Nanomedicine*, 2017. **12**: p. 1227-1249.
55. Johansson, B., et al., *Cerium; Crystal Structure and Position in The Periodic Table*. *Scientific Reports*, 2014. **4**: p. 6398.
56. Carnall, W.T. and P.R. Fields, *Lanthanide and Actinide Absorption Spectra in Solution*, in *Lanthanide/Actinide Chemistry*. 1967, AMERICAN CHEMICAL SOCIETY. p. 86-101.
57. Syamchand, S.S. and G. Sony, *Europium enabled luminescent nanoparticles for biomedical applications*. *Journal of Luminescence*, 2015. **165**: p. 190-215.
58. Heffern, M.C., L.M. Matosziuk, and T.J. Meade, *Lanthanide Probes for Bioresponsive Imaging*. *Chemical Reviews*, 2014. **114**(8): p. 4496-4539.
59. Liu, J., et al., *Development of a microchip Europium nanoparticle immunoassay for sensitive point-of-care HIV detection*. *Biosensors and Bioelectronics*, 2014. **61**: p. 177-183.
60. Lechevallier, S., et al., *Gadolinium–Europium Carbonate Particles: Controlled Precipitation for Luminescent Biolabeling*. *Chemistry of Materials*, 2010. **22**(22): p. 6153-6161.
61. Zhao, Y., et al., *Preparation, Structure, and Imaging of Luminescent SiO₂ Nanoparticles by Covalently Grafting Surfactant-Encapsulated Europium-Substituted Polyoxometalates*. *Langmuir*, 2010. **26**(23): p. 18430-18436.
62. Xu, W., et al., *A T₁, T₂ magnetic resonance imaging (MRI)-fluorescent imaging (FI) by using ultrasmall mixed gadolinium–europium oxide nanoparticles*. *New Journal of Chemistry*, 2012. **36**(11): p. 2361-2367.
63. Chen, H., et al., *Magnetic and optical properties of multifunctional core–shell radioluminescence nanoparticles*. *Journal of Materials Chemistry*, 2012. **22**(25): p. 12802-12809.

64. He, L., et al., *Recent advances of cerium oxide nanoparticles in synthesis, luminescence and biomedical studies: a review*. Journal of Rare Earths, 2015. **33**(8): p. 791-799.
65. Li, L., et al., *Review of Oxygen Vacancies in CeO₂-doped Solid Solutions as Characterized by Raman Spectroscopy*. Acta Physico-Chimica Sinica, 2012. **28**(5): p. 1012-1020.
66. Dowding, J.M., et al., *Cellular Interaction and Toxicity Depend on Physicochemical Properties and Surface Modification of Redox-Active Nanomaterials*. ACS Nano, 2013. **7**(6): p. 4855-4868.
67. Piro, N.A., et al., *The electrochemical behavior of cerium(III/IV) complexes: Thermodynamics, kinetics and applications in synthesis*. Coordination Chemistry Reviews, 2014. **260**: p. 21-36.
68. Wadsworth, E., F.R. Duke, and C.A. Goetz, *Present Status of Cerium(IV)-Cerium(III) Potentials*. Analytical Chemistry, 1957. **29**(12): p. 1824-1825.
69. Rao, G.P. and A.R.V. Murthy, *Measurement of Formal Oxidation—Reduction Potentials of Cerium(IV)—Cerium(III) System in Acetonitrile*. The Journal of Physical Chemistry, 1964. **68**(6): p. 1573-1576.
70. Maverick, A.W. and Q. Yao, *The cerium(IV)/cerium(III) electrode potential in hydrochloric acid solution*. Inorganic Chemistry, 1993. **32**(24): p. 5626-5628.
71. Noyes, A.A. and C.S. Garner, *Strong Oxidizing Agents in Nitric Acid Solution. I. Oxidation Potential of Cerous—Ceric Salts*. Journal of the American Chemical Society, 1936. **58**(7): p. 1265-1268.
72. Yu, P.E., al., *The Phase Stability of Cerium Species in Aqueous Systems II. The Formula Systems. Equilibrium Considerations and Pourbaix Diagram Calculations*. Journal of The Electrochemical Society, 2006. **153**: p. 74.
73. Fernández-García, M., et al., *Nanostructured Oxides in Chemistry: Characterization and Properties*. Chemical Reviews, 2004. **104**(9): p. 4063-4104.
74. Huang, X. and M.J. Beck, *Surface structure of catalytically-active ceria nanoparticles*. Computational Materials Science, 2014. **91**: p. 122-133.
75. Esch, F., et al., *Electron Localization Determines Defect Formation on Ceria Substrates*. Science, 2005. **309**(5735): p. 752-755.
76. Khalifi, M.E., F. Picaud, and M. Bizi, *Electronic and optical properties of CeO₂ from first principles calculations*. Analytical Methods, 2016. **8**(25): p. 5045-5052.
77. Korsvik, C., et al., *Superoxide dismutase mimetic properties exhibited by vacancy engineered ceria nanoparticles*. Chemical Communications, 2007(10): p. 1056-1058.
78. Körner, R., et al., *Phase transformations in reduced ceria: Determination by thermal expansion measurements*. Journal of Solid State Chemistry, 1989. **78**(1): p. 136-147.
79. Ricken, M., J. Nölting, and I. Riess, *Specific heat and phase diagram of nonstoichiometric ceria (CeO_{2-x})*. Journal of Solid State Chemistry, 1984. **54**(1): p. 89-99.

80. Ray, S.P., A.S. Nowick, and D.E. Cox, *X-ray and neutron diffraction study of intermediate phases in nonstoichiometric cerium dioxide*. Journal of Solid State Chemistry, 1975. **15**(4): p. 344-351.
81. Sayle, T.X.T., S.C. Parker, and C.R.A. Catlow, *The role of oxygen vacancies on ceria surfaces in the oxidation of carbon monoxide*. Surface Science, 1994. **316**: p. 329-336.
82. Conesa, J., *Computer modeling of surfaces and defects on cerium dioxide*. Surface Science, 1995. **339**(3): p. 337-352.
83. Skorodumova, N.V., et al., *Quantum Origin of the Oxygen Storage Capability of Ceria*. Physical Review Letters, 2002. **89**(16): p. 166601.
84. Sayle, T.X.T., S.C. Parker, and D.C. Sayle, *Shape of CeO₂ nanoparticles using simulated amorphisation and recrystallisation*. Chemical Communications, 2004(21): p. 2438-2439.
85. Vyas, S., et al., *Structure, stability and morphology of stoichiometric ceria crystallites*. Journal of the Chemical Society, Faraday Transactions, 1998. **94**(3): p. 427-434.
86. Tsunekawa, S., J.T. Wang, and Y. Kawazoe, *Lattice constants and electron gap energies of nano- and subnano-sized cerium oxides from the experiments and first-principles calculations*. Journal of Alloys and Compounds, 2006. **408-412**: p. 1145-1148.
87. Kumar, A., et al., *Luminescence Properties of Europium-Doped Cerium Oxide Nanoparticles: Role of Vacancy and Oxidation States*. Langmuir, 2009. **25**(18): p. 10998-11007.
88. Renuka, N.K., *Structural characteristics of quantum-size ceria nano particles synthesized via simple ammonia precipitation*. Journal of Alloys and Compounds, 2012. **513**: p. 230-235.
89. Cafun, J.-D., et al., *Absence of Ce³⁺ Sites in Chemically Active Colloidal Ceria Nanoparticles*. ACS Nano, 2013. **7**(12): p. 10726-10732.
90. Zanella, R., *Metodologías para la síntesis de nanopartículas: controlando forma y tamaño*. Revista interdisciplinaria en Nanociencias y Nanotecnología, 2012. **5**: p. 69.
91. Lee, J.-S. and S.-C. Choi, *Crystallization behavior of nano-ceria powders by hydrothermal synthesis using a mixture of H₂O₂ and NH₄OH*. Materials Letters, 2004. **58**(3-4): p. 390-393.
92. Patil, S., et al., *Protein adsorption and cellular uptake of cerium oxide nanoparticles as a function of zeta potential*. Biomaterials, 2007. **28**(31): p. 4600-4607.
93. Shan, W., et al., *Controllable preparation of CeO₂ nanostructure materials and their catalytic activity*. Journal of Rare Earths, 2012. **30**(7): p. 665-669.
94. Li, L., et al., *Photoluminescence Properties of CeO₂:Eu³⁺ Nanoparticles Synthesized by a Sol-Gel Method*. The Journal of Physical Chemistry C, 2009. **113**(2): p. 610-617.
95. Tiseanu, C., et al., *Surface versus volume effects in luminescent ceria nanocrystals synthesized by an oil-in-water microemulsion method*. Physical Chemistry Chemical Physics, 2011. **13**(38): p. 17135-17145.


96. Yin, L., et al., *Sonochemical Synthesis of Cerium Oxide Nanoparticles—Effect of Additives and Quantum Size Effect*. Journal of Colloid and Interface Science, 2002. **246**(1): p. 78-84.
97. Xia, T., et al., *Comparison of the Mechanism of Toxicity of Zinc Oxide and Cerium Oxide Nanoparticles Based on Dissolution and Oxidative Stress Properties*. ACS nano, 2008. **2**(10): p. 2121-2134.
98. Jamshidijam, M., et al., *Effect of rare earth dopants on structural characteristics of nanoceria synthesized by combustion method*. Powder Technology, 2014. **253**: p. 304-310.
99. Lin, H.-L., C.-Y. Wu, and R.-K. Chiang, *Facile synthesis of CeO₂ nanoplates and nanorods by [1 0 0] oriented growth*. Journal of Colloid and Interface Science, 2010. **341**(1): p. 12-17.
100. Celardo, I., et al., *Pharmacological potential of cerium oxide nanoparticles*. Nanoscale, 2011. **3**(4): p. 1411-1420.
101. Deshpande, S., et al., *Size dependency variation in lattice parameter and valency states in nanocrystalline cerium oxide*. Applied Physics Letters, 2005. **87**(13): p. 1331B.
102. Pulido-Reyes, G., et al., *Untangling the biological effects of cerium oxide nanoparticles: the role of surface valence states*. Scientific Reports, 2015. **5**: p. 15613.
103. Takahashi, Y., et al., *Determination of the CeIV/CeIII Ratio by XANES in Soil Horizons and its Comparison with the Degree of Ce Anomaly*. Physica Scripta, 2005: p. 936.
104. Simon, P., et al., *Observation of surface reduction in porous ceria thin film grown on graphite foil substrate*. Materials Today: Proceedings, 2016. **3**(8): p. 2772-2779.
105. Manoubi, T., et al., *Curve fitting methods for quantitative analysis in electron energy loss spectroscopy*. Microsc. Microanal. Microstruct., 1990. **1**(1): p. 23-39.
106. Strydom, C.A. and H.J. Strydom, *X-ray photoelectron spectroscopy determination of the Ce(III)/Ce(IV) ratio in cerium compounds*. Inorganica Chimica Acta, 1989. **161**(1): p. 7-9.
107. Zhang, F., et al., *Cerium oxidation state in ceria nanoparticles studied with X-ray photoelectron spectroscopy and absorption near edge spectroscopy*. Surface Science, 2004. **563**(1): p. 74-82.
108. Rama Rao, M.V. and T. Shripathi, *Photoelectron spectroscopic study of X-ray induced reduction of CeO₂*. Journal of Electron Spectroscopy and Related Phenomena, 1997. **87**(2): p. 121-126.
109. Johnston-Peck, A.C., et al., *Dose-rate-dependent damage of cerium dioxide in the scanning transmission electron microscope*. Ultramicroscopy, 2016. **170**: p. 1-9.
110. Ferraro, D., et al., *Dependence of the Ce(III)/Ce(IV) ratio on intracellular localization in ceria nanoparticles internalized by human cells*. Nanoscale, 2017. **9**(4): p. 1527-1538.
111. Asati, A., et al., *Surface-Charge-Dependent Cell Localization and Cytotoxicity of Cerium Oxide Nanoparticles*. ACS Nano, 2010. **4**(9): p. 5321-5331.

112. Collin, B., et al., *Influence of Natural Organic Matter and Surface Charge on the Toxicity and Bioaccumulation of Functionalized Ceria Nanoparticles in Caenorhabditis elegans*. Environmental Science & Technology, 2014. **48**(2): p. 1280-1289.
113. Dahle, J.T., K. Livi, and Y. Arai, *Effects of pH and phosphate on CeO₂ nanoparticle dissolution*. Chemosphere, 2015. **119**: p. 1365-1371.
114. Grulke, E.A., et al., *Surface-controlled dissolution rates: a case study of nanoceria in carboxylic acid solutions*. Environmental Science: Nano, 2019. **6**(5): p. 1478-1492.
115. Briffa, S.M., et al., *Uptake and impacts of polyvinylpyrrolidone (PVP) capped metal oxide nanoparticles on Daphnia magna: role of core composition and acquired corona*. Environmental Science: Nano, 2018. **5**(7): p. 1745-1756.
116. Brydson, R., et al., *Analytical Transmission Electron Microscopy*. Reviews in Mineralogy and Geochemistry, 2014. **78**: p. 219.
117. Egerton, R.F. and M. Malac, *EELS in the TEM*. Journal of Electron Spectroscopy and Related Phenomena, 2005. **143**(2): p. 43-50.
118. Oleshko, V.P., M. Murayama, and J.M. Howe, *Use of Plasmon Spectroscopy to Evaluate the Mechanical Properties of Materials at the Nanoscale*. Microscopy and Microanalysis, 2002. **8**(4): p. 350-364.
119. Bearden, J.A., *X-Ray Wavelengths*. Reviews of Modern Physics, 1967. **39**.
120. Bearden, J.A. and B. A.F., *Reevaluation of X-Ray Atomic Energy Levels*. Reviews of Modern Physics, 1967. **39**.
121. Speakman, S.A., *Basics of X-Ray Powder Diffraction*. 2010, Massachusetts Institute of Technology.
122. Sartor, M., *Dynamic Light Scattering*. 2003, University of California. : San Diego.
123. Peng, L., et al., *Comparative Pulmonary Toxicity of Two Ceria Nanoparticles with the Same Primary Size*. International Journal of Molecular Sciences, 2014. **15**(4): p. 6072.
124. Goldburg, W.I., *Dynamic light scattering*. American Journal of Physics, 1999. **67**(12): p. 1152-1160.
125. Kaszuba, M., et al., *High-concentration zeta potential measurements using light-scattering techniques*. Philos Trans A Math Phys Eng Sci, 2010. **368**(1927): p. 4439-51.
126. Bhattacharjee, S., *DLS and zeta potential – What they are and what they are not?* Journal of Controlled Release, 2016. **235**: p. 337-351.
127. Vakurov, A., et al., *ZnO nanoparticle interactions with phospholipid monolayers*. Journal of Colloid and Interface Science, 2013. **404**: p. 161-168.
128. Vakurov, A., et al., *Significance of particle size and charge capacity in TiO₂ nanoparticle-lipid interactions*. Journal of Colloid and Interface Science, 2016. **473**: p. 75-83.
129. Nobanathi Wendy, M., G. Sandile Surprise, and M. Gugu Hlengiwe, *Voltammetry*. 2019. p. 116.
130. Elgrishi, N., et al., *A Practical Beginner's Guide to Cyclic Voltammetry*. Journal of Chemical Education, 2018. **95**(2): p. 197-206.

131. Reiger, P., *Electrochemistry*. 2nd Edition ed, ed. C. Hall. 1994.
132. Mohamadi, S., et al., *Electrochemical screening of biomembrane-active compounds in water*. *Analytica Chimica Acta*, 2014. **813**: p. 83-89.
133. Wang, H. and L. Pilon, *Accurate Simulations of Electric Double Layer Capacitance of Ultramicroelectrodes*. *The Journal of Physical Chemistry C*, 2011. **115**(33): p. 16711-16719.
134. Conway, B.E., *Electrochemical supercapacitors : scientific fundamentals and technological applications*. 1999, New York ;; Kluwer Academic/Plenum.
135. Streyer, L.L., Berg, J.M., Tymoczko, J.L. , *Bioquimica. Curso Basico*. 2014: Editorial Reverte.
136. Streye, L.T., J. Berg, J. , *Bioquimica. Curso Basico*. 2014: Editorial Reverte.
137. Miller, I.R. and D.C. Grahame, *Polyelectrolyte adsorption on mercury surfaces. Differential capacity in the presence of poly 2- and 4-vinyl pyridines*. *Journal of Colloid Science*, 1961. **16**(1): p. 23-40.
138. Zhang, S., et al., *Electrochemical modelling of QD-phospholipid interactions*. *Journal of Colloid and Interface Science*, 2014. **420**: p. 9-14.
139. Nelson, A., *Conducting gramicidin channel activity in phospholipid monolayers*. *Biophysical Journal*, 2001. **80**(6): p. 2694-2703.
140. G.Gouy, *Annales de Chimie et de Physique*, 1906. **8**.
141. Scheller, P.R., *Chapter 1.6 - Some Aspects of Electrochemistry of Interfaces*, in *Treatise on Process Metallurgy*, S. Seetharaman, Editor. 2014, Elsevier: Boston. p. 79-93.
142. Nelson, A. and N. Auffret, *Phospholipid monolayers of di-oleoyl lecithin at the mercury/water interface*. *Journal of Electroanalytical Chemistry and Interfacial Electrochemistry*, 1988. **244**(1): p. 99-113.
143. Nelson, A., *Electrochemistry of mercury supported phospholipid monolayers and bilayers*. *Current Opinion in Colloid & Interface Science*, 2010. **15**(6): p. 455-466.
144. Nelson, A. and A. Benton, *Phospholipid monolayers at the mercury / water interface*. *Journal of Electroanalytical Chemistry and Interfacial Electrochemistry*, 1986. **202**(1): p. 253-270.
145. Guminski, C., *The Hg-Pt (Mercury-Platinum) system*. *Bulletin of Alloy Phase Diagrams*, 1990. **11**(1): p. 26-32.
146. Nelson, A., *Electrochemical analysis of a phospholipid phase transition*. *Journal of Electroanalytical Chemistry* 2007. **601**: p. 83-93.
147. William, N., et al., *Hg-supported phospholipid monolayer as rapid screening device for low molecular weight narcotic compounds in water*. *Analytica Chimica Acta*, 2019. **1069**: p. 98-107.
148. Tanford, C., *The Hydrophobic Effect: Formation of Micelles and Biological Membranes*. 1980, New York: John Wiley & Sons.
149. Chen, Y.F., et al., *Differential dependencies on [Ca²⁺] and temperature of the monolayer spontaneous curvatures of DOPE, DOPA and cardiolipin: effects of modulating the strength of the inter-headgroup repulsion*. *Soft Matter*, 2015. **11**(20): p. 4041-4053.

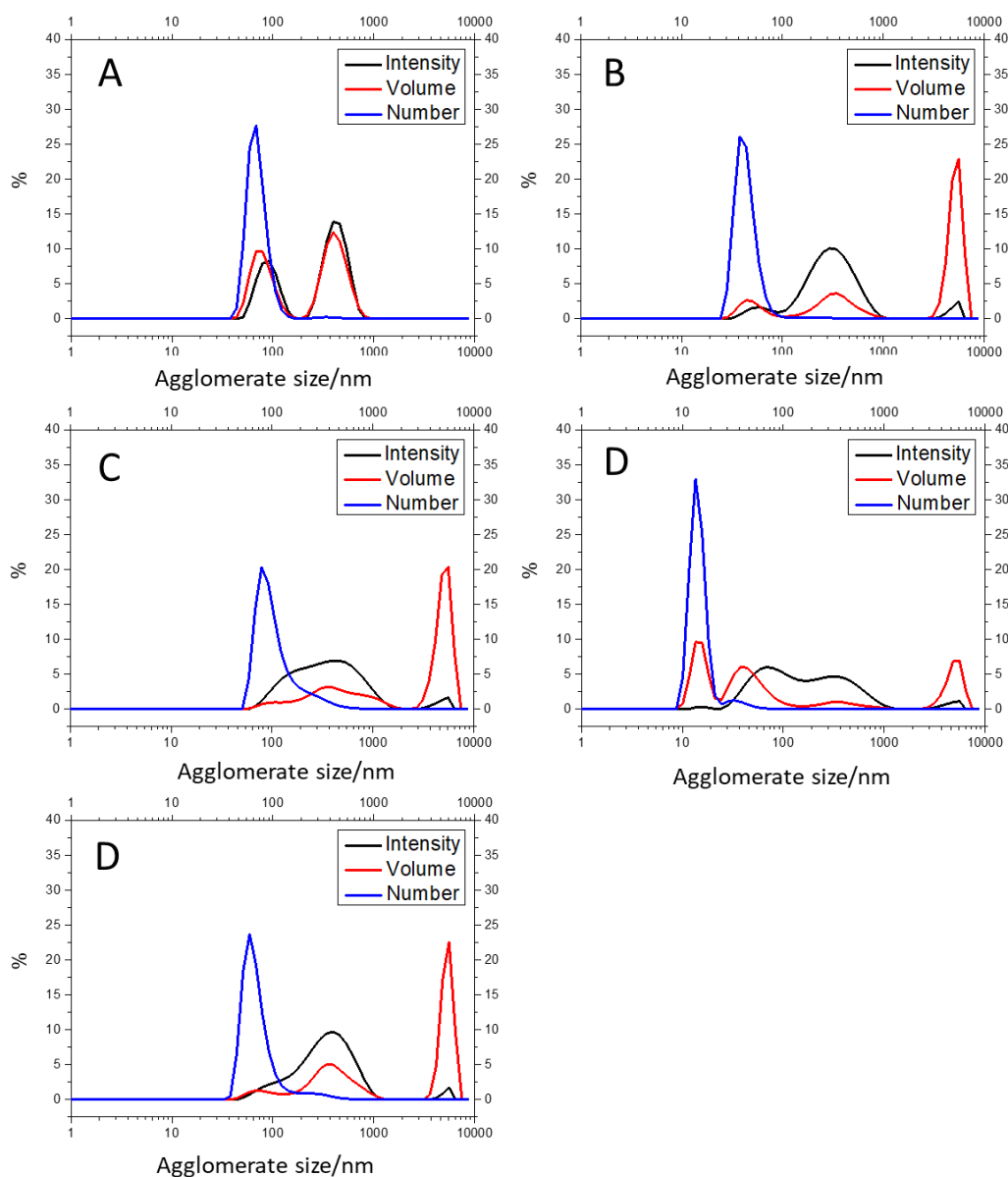
150. Eze, M.O., *Phase transitions in phospholipid bilayers: Lateral phase separations play vital roles in biomembranes*. *Biochemical Education*, 1991. **19**(4): p. 204-208.
151. McElhaney, R.N., *The use of differential scanning calorimetry and differential thermal analysis in studies of model and biological membranes*. *Chemistry and Physics of Lipids*, 1982. **30**(2): p. 229-259.
152. Hinz, H.J.S., J.M., *Calorimetric Studies of Dilute Aqueous Suspensions of Bilayers Formed from Synthetic L- α -lecithins*. *The Journal of Biological Chemistry*, 1972. **247**: p. 6071-6075.
153. Lipids, A. *Ionisation Constants of Phospholipids*. Available from: <https://avantilipids.com/tech-support/physical-properties/ionization-constants>.
154. Marsh, D., *Handbook of Lipid Bilayers*. 1990.
155. Ding, W., et al., *Effects of Lipid Composition on Bilayer Membranes Quantified by All-Atom Molecular Dynamics*. *The Journal of Physical Chemistry B*, 2015. **119**(49): p. 15263-15274.
156. Dawaliby, R., et al., *Phosphatidylethanolamine Is a Key Regulator of Membrane Fluidity in Eukaryotic Cells*. *J Biol Chem*, 2016. **291**(7): p. 3658-67.
157. van der Veen, J.N., et al., *The critical role of phosphatidylcholine and phosphatidylethanolamine metabolism in health and disease*. *Biochimica et Biophysica Acta (BBA) - Biomembranes*, 2017. **1859**(9, Part B): p. 1558-1572.
158. BEVERS, E.M., et al., *Generation of Prothrombin-Converting Activity and the Exposure of Phosphatidylserine at the Outer Surface of Platelets*. 1982. **122**(2): p. 429-436.
159. Koopman, G., et al., *Annexin V for flow cytometric detection of phosphatidylserine expression on B cells undergoing apoptosis*. *Blood*, 1994. **84**(5): p. 1415-1420.
160. Martin, S.J., et al., *Early redistribution of plasma membrane phosphatidylserine is a general feature of apoptosis regardless of the initiating stimulus: inhibition by overexpression of Bcl-2 and Abl*. 1995. **182**(5): p. 1545-1556.
161. Fadok, V.A., et al., *Exposure of phosphatidylserine on the surface of apoptotic lymphocytes triggers specific recognition and removal by macrophages*. 1992. **148**(7): p. 2207-2216.
162. Lemmon, M.A., *Membrane recognition by phospholipid-binding domains*. *Nature Reviews Molecular Cell Biology*, 2008. **9**(2): p. 99-111.
163. Buckland, A.G. and D.C. Wilton, *Anionic phospholipids, interfacial binding and the regulation of cell functions*. *Biochimica et Biophysica Acta (BBA) - Molecular and Cell Biology of Lipids*, 2000. **1483**(2): p. 199-216.
164. Kooijman, E.E., Carter, K.M., van Laar, E.G., Chupin, V., de Kruijff, B., *What Makes the Bioactive Lipids Phosphatidic Acid and Lysophosphatidic Acid So Special?* *Biochemistry*, 2005. **44**(51): p. 17007-17015.

165. Kooijman, E.E., Burger, K.N.J., *Biophysics and function of phosphatidic acid: A molecular perspective*. Biochimica et Biophysica Acta (BBA) - Molecular and Cell Biology of Lipids, 2009. **1791**(9): p. 881-888.
166. Zegarlińska, J.P., M. Sikorski, A.F. Czogalla, A., *Phosphatidic acid - a simple phospholipid with multiple faces*. Acta Biochimica Polonica, 2018. **65**.
167. Kooijman, E.E., Et.Al., *An Electrostatic/Hydrogen Bond Switch as the Basis for the Specific Interaction of Phosphatidic Acid with Proteins*. Journal of Biological Chemistry, 2007. **282**: p. 11356-11364.
168. Kooijman, E.E., et al., *Spontaneous Curvature of Phosphatidic Acid and Lysophosphatidic Acid*. Biochemistry, 2005. **44**(6): p. 2097-2102.
169. Träuble, H. and H. Eibl, *Electrostatic effects on lipid phase transitions: membrane structure and ionic environment*. Proceedings of the National Academy of Sciences of the United States of America, 1974. **71**(1): p. 214-219.
170. Verkleij, A.J., et al., *Divalent cations and chlorpromazine can induce non-bilayer structures in phosphatidic acid-containing model membranes*. Biochimica et Biophysica Acta (BBA) - Biomembranes, 1982. **684**(2): p. 255-262.
171. Cambrea, L.R. and J.S. Hovis, *Formation of three-dimensional structures in supported lipid bilayers*. Biophysical journal, 2007. **92**(10): p. 3587-3594.
172. Mohamadi, S., *Electrochemical screening of biological membrane active compounds*, in *School of Chemistry*. 2014, University of Leeds.
173. Vakurov, A., R. Brydson, and A. Nelson, *Electrochemical Modeling of the Silica Nanoparticle–Biomembrane Interaction*. Langmuir, 2012. **28**(2): p. 1246-1255.
174. Plakhova, T.V., et al., *Solubility of Nanocrystalline Cerium Dioxide: Experimental Data and Thermodynamic Modeling*. The Journal of Physical Chemistry C, 2016. **120**(39): p. 22615-22626.
175. Lemont, F. and A. Barbier, *Kinetics and mechanism of the reduction-dissolution of cerium oxide catalyzed by fluoride ions in hydrochloric acid solution*. Hydrometallurgy, 2019. **183**: p. 193-198.
176. Rajesh, K., et al., *High-Surface-Area Nanocrystalline Cerium Phosphate through Aqueous Sol–Gel Route*. Chemistry of Materials, 2004. **16**(14): p. 2700-2705.
177. Fang, J., et al., *Sequential microfluidic flow synthesis of CePO₄ nanorods decorated with emission tunable quantum dots*. Lab on a Chip, 2010. **10**(19): p. 2579-2582.
178. Höfer, R., *Industrial Biorefineries & White Biotechnology*. 2015: Elsevier.
179. Simoes, T.A., et al., *Evidence for the dissolution of molybdenum during tribocorrosion of CoCrMo hip implants in the presence of serum protein*. Acta Biomaterialia, 2016. **45**: p. 410-418.
180. Fortner, J.A., et al., *EELS analysis of redox in glasses for plutonium immobilization*. Ultramicroscopy, 1997. **67**(1): p. 77-81.
181. Sims, C., et al., *Approaches for the quantitative analysis of oxidation state in cerium oxide nanomaterials*. Nanotechnology, 2019. **30**.

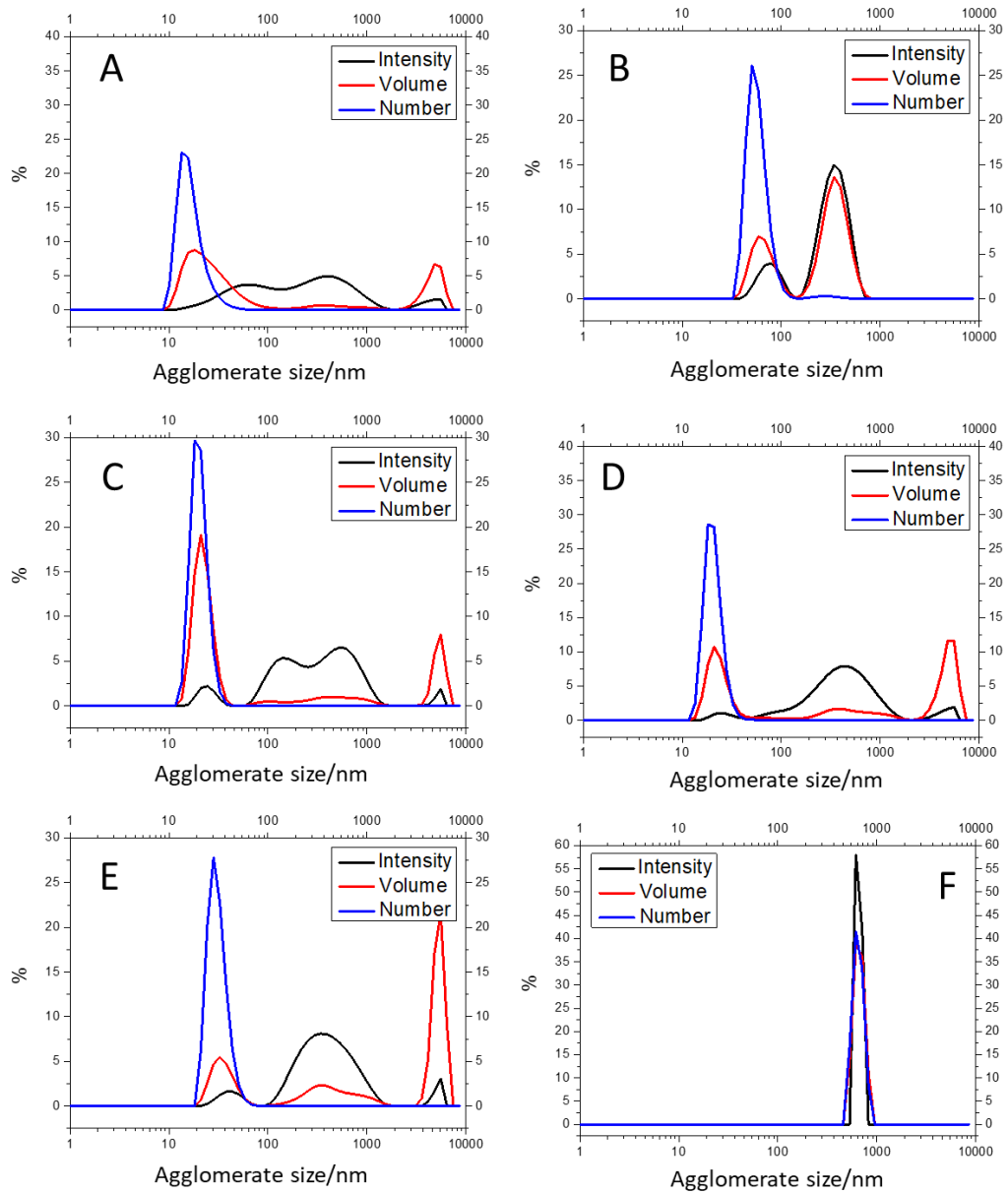
- 
182. Thole, B.T., et al., *3d x-ray-absorption lines and the $3d^{9}4f^{n+1}$ multiplets of the lanthanides*. Physical Review B, 1985. **32**(8): p. 5107-5118.
 183. Kaindl, G., et al., *M-edge x-ray absorption spectroscopy of 4f instabilities in rare-earth systems (invited)*. Journal of Applied Physics, 1984. **55**(6): p. 1910-1915.
 184. Alpaslan, E., et al., *pH-Controlled Cerium Oxide Nanoparticle Inhibition of Both Gram-Positive and Gram-Negative Bacteria Growth*. Scientific Reports, 2017. **7**(1): p. 45859.
 185. Pulido-Reyes, G., et al., *Internalization and toxicological mechanisms of uncoated and PVP-coated cerium oxide nanoparticles in the freshwater alga Chlamydomonas reinhardtii*. Environmental Science: Nano, 2019. **6**(6): p. 1959-1972.
 186. Shah, V., et al., *Antibacterial Activity of Polymer Coated Cerium Oxide Nanoparticles*. PLOS ONE, 2012. **7**(10): p. e47827.
 187. Arya A, G.A., Singh SK, Roy M, Das M, Sethy N, Bhargava K., *Cerium oxide nanoparticles promote neurogenesis and abrogate hypoxia-induced memory impairment through AMPK–PKC–CBP signaling cascade*. Int J Nanomedicine, 2016. **11**: p. 1159-1173.

APPENDIX

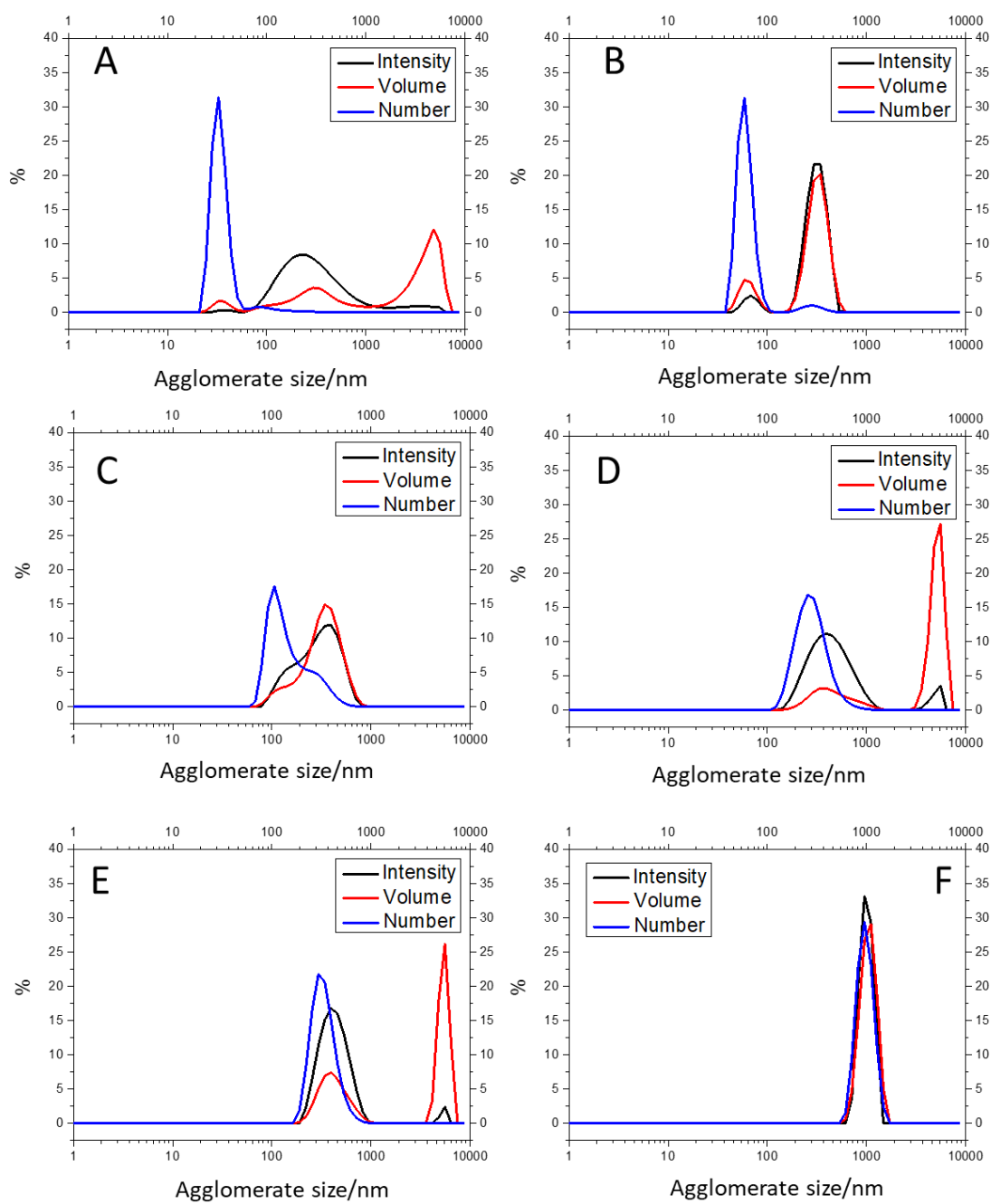
APPENDIX 4. CHAPTER 4



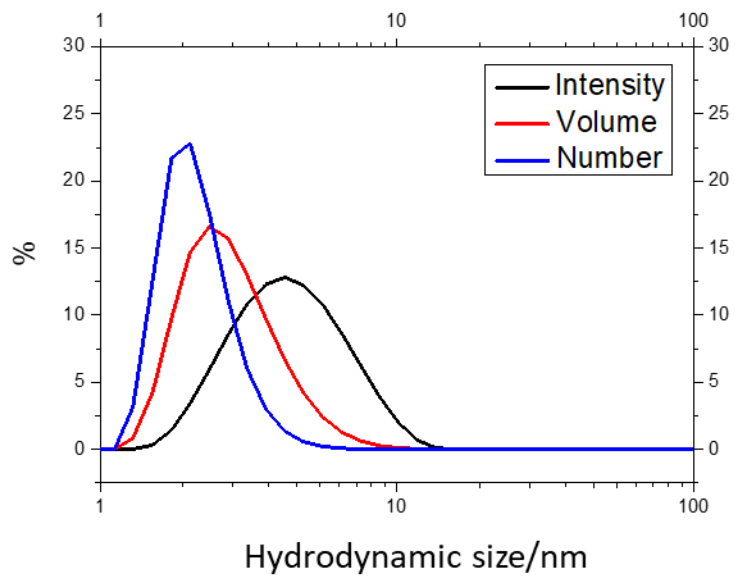
Appendix 4. 1: DLS plots showing percentage (%) in intensity (black lines), volume (red lines) and number (blue lines) versus size in nm of CeO₂ NPs (needles) in: A: GLY 3.0, B: CCB 3.0, C: CCB 4.0, D: CCB 5.0, E: CCB 6.0.



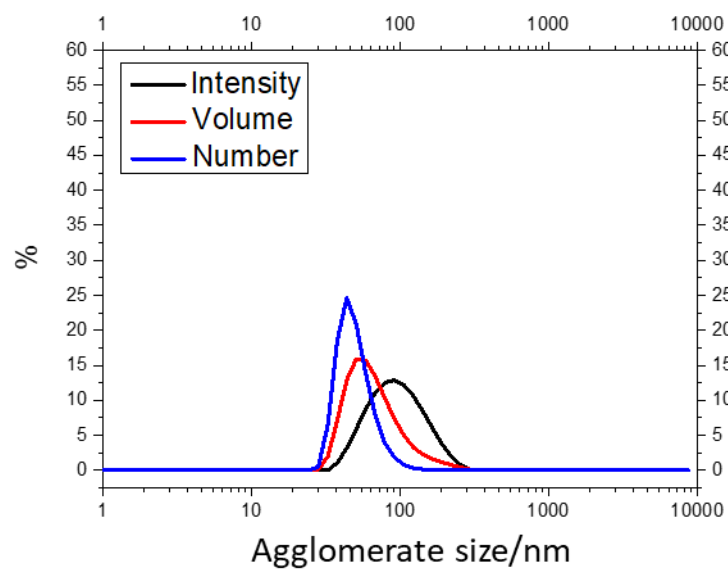
Appendix 4. 2: DLS plots showing percentage (%) in intensity (black lines), volume (red lines) and number (blue lines) versus size in nm of CeO₂ NPs (cubes) in: A: GLY 3.0, B: CCB 3.0, C: CCB 4.0, D: CCB 5.0, E: CCB 6.0 and F: PBS 7.4



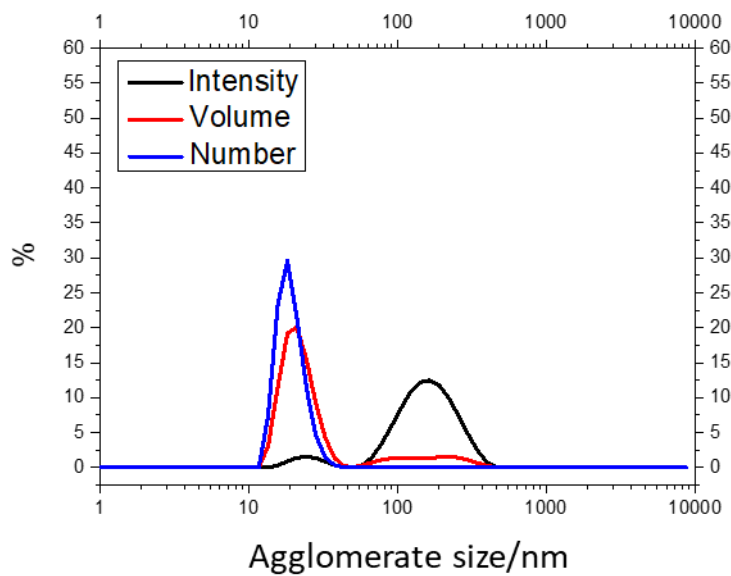
Appendix 4. 3: DLS plots showing percentage (%) in intensity (black lines), volume (red lines) and number (blue lines) versus size in nm of CeO₂ NPs (spheres) in: A: GLY 3.0, B: CCB 3.0, C: CCB 4.0, D: CCB 5.0, E: CCB 6.0 and F: PBS 7.4



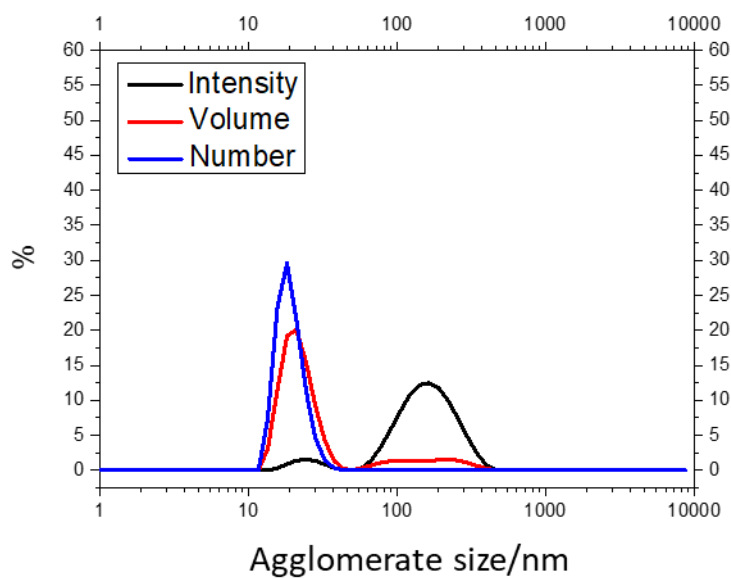
Appendix 4. 5: DLS plots showing percentage (%) in intensity (black lines), volume (red lines) and number (blue lines) versus size in nm of CeO₂ NPs (dots, commercial)



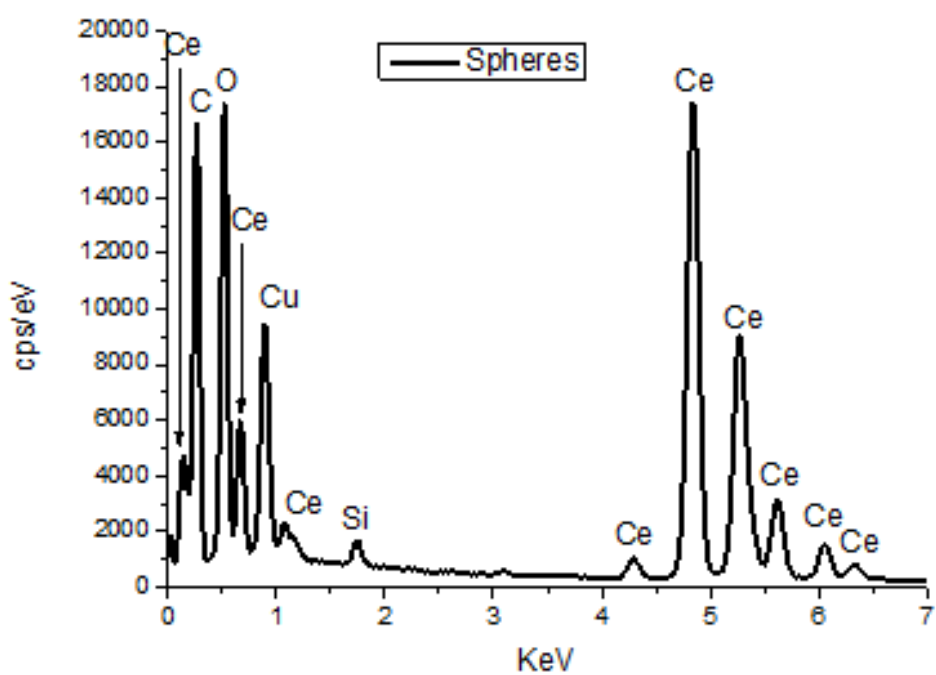
Appendix 4. 4: DLS plots showing percentage (%) in intensity (black lines), volume (red lines) and number (blue lines) versus size in nm of PVP-CeO₂ NPs



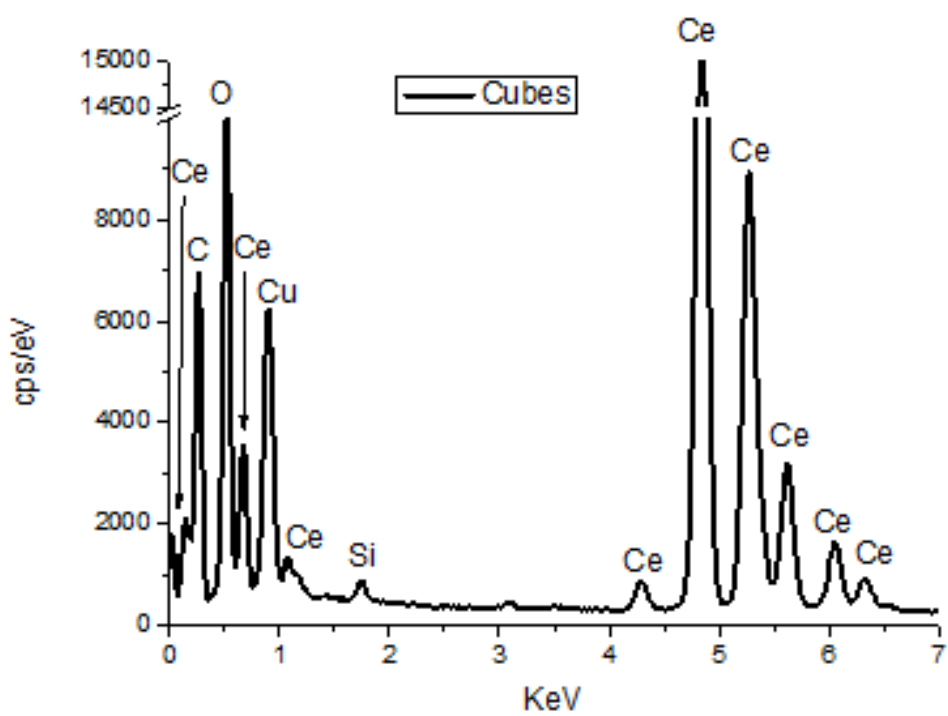
Appendix 4. 6: DLS plots showing percentage (%) in intensity (black lines), volume (red lines) and number (blue lines) versus size in nm of Dextran-CeO₂



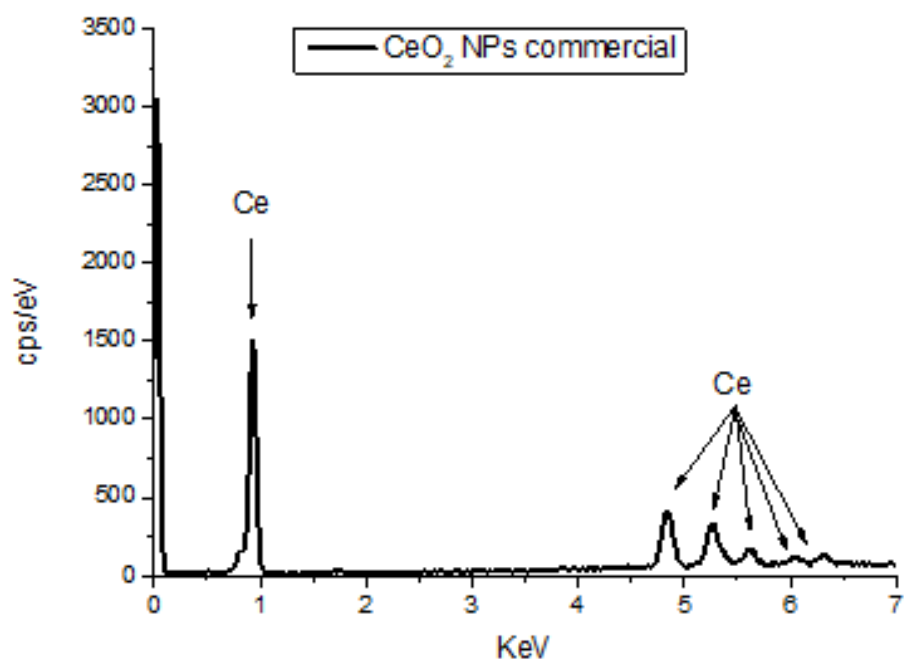
Appendix 4. 7: DLS plots showing percentage (%) in intensity (black lines), volume (red lines) and number (blue lines) versus size in nm of PEG-CeO₂



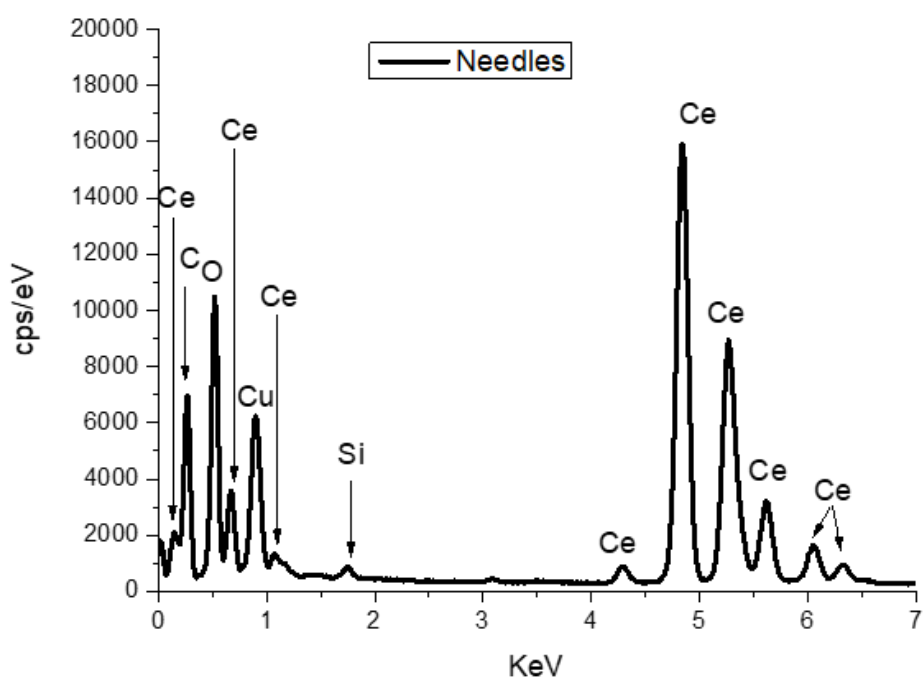
Appendix 4. 8: EDX spectrum of CeO₂NPs (spheres)



Appendix 4. 9: EDX spectrum of CeO₂NPs (cubes)



Appendix 4. 10: EDX spectrum of CeO₂ NPs (dots, commercial)



Appendix 4. 11: EDX spectrum of CeO₂ NPs (needles)

